Hydrodynamics and Dust Formation in the Circumstellar Shells of Miras and Long-Period Variables

von
Dipl.–Phys. A.J. FLEISCHER
aus Berlin

Vom Fachbereich 04 (Physik)
der Technischen Universität Berlin
zur Erlangung des akademischen Grades

Doktor der Naturwissenschaften (Dr. rer. nat.)

genehmigte Dissertation

Berlin 1994

D 83

Promotionsausschuß:

Vorsitzender: Prof. Dr. S. Hess
Berichter: Prof. Dr. E. Sedlmayr
Priv. Doz. Dr. J.P. Kaufmann

Tag der mündlichen Prüfung: 04.02.1994

To my parents

Zusammenfassung

Miras und Langperiodische Veränderliche (LPV's) sind weit entwickelte Sterne auf dem Asymptotischen Riesenast. Aufgrund der besonderen physikalischen Bedingungen dieser leuchtkräftigen pulsierenden Objekte, stellen ihre kühlen, ausgedehnten Hüllen eine ausgezeichnete Umgebung für die Bildung von kleinen Festkörpern (Staub) dar. Es bildet sich ein starker Massenabstrom oder Wind aus, der durch Strahlungsdruck auf Staub getrieben wird. Eine realistische Beschreibung der zirkumstellaren Staubhüllen (ZSH) von Miras und LPV's ist notwendig, um diese wichtige Station im kosmischen Materiekreislauf zu verstehen.

Die ZSH von Miras und LPV's sind komplexe, nichtlineare Systeme, die eine konsistente Beschreibung der Hydrodynamik, der Staubbildung, der Thermodynamik, sowie der Chemie erfordern, um eine verläßliche theoretische Modellierung zu erreichen. Es werden daher dynamische Modelle von ZSH präsentiert, die, konsistent gekoppelt, zeitabhängige Hydrodynamik, eine detailierte Beschreibung von Staubbildung, Wachstum und Verdampfung, sowie den Strahlungstransport und auch eine Behandlung der Chemie der Gasphase beinhalten.

Die Ergebnisse dieser Rechnungen unterstreichen die Notwendigkeit, alle als wichtig erkannten Wechselwirkungen auch in der theoretischen Modellierung zu berücksichtigen. Dabei zeigt sich, daß dem Staubkomplex die entscheidende Rolle für die Dynamik der ZSH zukommt. Es wird gezeigt, daß Strahlungsdruck auf Staub, unterstützt durch die Pulsation, den Wind treiben kann. Darüberhinaus kann der Staub selbst, starke Stoßwellen induzieren, die die Struktur der ZSH beherrschen. Dieser Mechanismus von *stauberzeugten Stößen* produziert eine zwiebelschalenartige radiale Struktur der ZSH und erzeugt dabei auch eine inhomogene Verteilung des Staubs.

Die Modellrechnungen zeigen, daß das Häufigkeitsverhältnis von Kohlenstoff zu Sauerstoff, ϵ_C/ϵ_O, ein zentraler Parameter ist. Für hinreichend hohe Werte des ϵ_C/ϵ_O Verhältnisses ergibt sich eine Zeitskala der ZSH, die gleich der durch die Pulsation vorgegebenen Zeitskala ist. Wird der Wert von ϵ_C/ϵ_O jedoch reduziert, so entwickelt die ZSH eine eigene Zeitskala, die um ein Vielfaches länger sein kann als die Pulsationszeitskala; daher wird dieser Effekt als *Multiperiodizität* bezeichnet. Weiterhin zeigt sich, daß durch eine Erhöhung von ϵ_C/ϵ_O auch die resultierende Ausströmgeschwindigkeit des Materials gesteigert wird. Als Folge dieser linearen Korrelation ist es im Prinzip durch die Messung der Ausströmgeschwindigkeit möglich, auf den ϵ_C/ϵ_O Wert des Objekts zu schließen. Bislang bereitet die direkte Bestimmung der photosphärischen Kohlenstoffüberhäufigkeit erhebliche Schwierigkeiten und konnte nur für relativ wenige Objekte durchgeführt werden.

Sind die Leuchtkräfte der Modelle hinreichend hoch, kann sich eine Instabilität einstellen. Sie wird in dieser Arbeit als *äußerer κ–Mechanismus* bezeichnet, da der Staubopazität eine Schlüsselrolle zukommt. In diesen Rechnungen erzeugt

der Strahlungsdruck auf Staub selbst dann Stoßwellen, wenn keine Pulsation des Sterns vorliegt. Durch Absorption von Sternstrahlung wird das Material einerseits beschleunigt, andererseits werden durch den backwarming–Effekt der Staubopazität in der inneren, staubfreien Region der Atmosphäre Wellen angeregt. Diese Wellen triggern dann wieder die Staubbildung und prägen so dem System eine Zeitskala auf. Es handelt sich somit um einen zyklischen und selbsterhaltenden Mechanismus.

Multiperiodizität und stauberzeugte Stöße manifestieren sich auch im optischen Erscheinungsbild der Staubhüllenmodelle. Die dabei auftretenden Effekte sind prinzipiell auch in den Beobachtungsergebnissen von Miras und LPV's vorhanden.

Abstract

Miras and Long–period Variables (LPVs) are highly evolved stars on the Asymptotic Giant Branch. Due to the peculiar physical conditions of these luminous pulsating objects, their cool, extended atmospheres are distinguished sites for the formation of small solid particles (dust). A massive outflow or wind develops, which is driven by radiation pressure on dust. Dust particles influence both, the internal structure of the circumstellar shell as well as the optical appearance of Miras and LPVs. A thorough description of the circumstellar dust shells (CDS) around Miras and LPVs is necessary for a comprehensive understanding of this important stage of the cosmic cycle of matter.

The CDS around Miras and LPVs have to be considered as complex nonlinear systems, which require a consistent treatment of hydrodynamics, dust formation, thermodynamics, and chemistry to achieve a reliable model description. Hence, dynamical models of CDS around carbon–rich Miras and LPVs are presented, which include, consistently coupled, time-dependent hydrodynamics and a detailed treatment of the processes of formation, growth and evaporation of dust grains as well as radiative transfer and a treatment of the chemistry of the gas phase.

The results stress the necessity of taking into account the relevant physical interactions. Thereby, the dust complex is revealed as the decisive component which dominates the dynamics of the CDS. Radiation pressure on dust, supported by the interior pulsation, is shown to drive the wind, but moreover, the dust complex is able to induce its own strong shock waves which travel through the atmosphere and predominate the circumstellar structure. Furthermore, due to this mechanism of *dust–induced shocks*, the radial structure of the CDS appears to have a discrete or onion–shell like structure, which also results in an inhomogeneously distribution of the dust grains.

The abundance ratio of carbon to oxygen turns out to be a key parameter for the model calculations. For sufficiently high values of the carbon overabundance the time scale of the CDS behaves in accordance with the time scale of the interior pulsation. However, if the overabundance of carbon is reduced the CDS develops a separate time scale, multiple times longer than the pulsational time scale, an effect which we call *multiperiodicity.* Furthermore, an increase of the abundance of carbon to oxygen results in an increased outflow velocity. As a result of this linear correlation the derivation of carbon overabundances from the measurement of final outflow velocities becomes, in principle, possible. A direct derivation of the photospheric overabundance from observations is a difficult task, which has been possible only for a rather limited number of objects.

For sufficiently luminous models an instability occurs. In this work this new effect is called *exterior κ–mechanism* since the dust opacity plays the key role. In these models, radiation pressure on dust induces strong shocks, even in the absence of an interior pulsation. The absorption of stellar radiation by the dust particles causes an acceleration of the material, and moreover, the generation of small amplitude waves in the inner dustfree region, due to the backwarming of the dust. In turn, these waves trigger dust formation and impose a time scale on the dynamical system, and thus they close the cyclic self–maintaining process.

Dust–induced shocks as well as multiperiodicity are shown to influence decisively the optical appearance of the dust shell models by effects, which, in principle, are also present in observations of the objects under consideration.

Résumé

Les variables à longue période (VLP) et les étoiles de type Mira Ceti sont des étoiles de type tardif qui évoluent sur la branche asymptotique des géantes rouges. En raison des conditions physiques particulières de ces objets lumineux et pulsants, leurs enveloppes froides et étendues constituent des lieux privilégiés pour la formation de petites particules solides (poussière). Dans les enveloppes de ces étoiles se manifeste un échappement de matière massif ou vent stellaire, qui est entretenu par la pression radiative exercée sur les grains de poussière. Ces particules de poussière ont une influence à la fois sur la structure interne de l'enveloppe et sur l'apparence optique des VLP et des étoiles de type Mira Ceti. Une description complète de l'enveloppe circumstellaire riche en poussière (ECRP) de ces étoiles est nécessaire afin de mieux comprendre le fonctionnement de cette étape de l'evolution de la matière interstellaire.

L'ECRP des étoiles de type Mira Ceti et des VLP sont des systèmes complexes non-linéaires qui requièrent un traitement *self-consistent* des équations hydrodynamiques, des équations décrivant la formation de la poussière, ainsi que des équations thermodynamiques et chimiques, afin de parvenir à une description théorique réaliste. Des modèles dynamiques des ECRP des étoiles de type Mira Ceti et des VLP riches en carbone sont présentés ici, qui renferment donc les équations temporelles de l'hydrodynamique, une description détaillée de la formation, de la croissance et de l'évaporation de la poussière, ainsi que les équations du transfert du rayonnement et un traitement de la chimie de la phase gaseuze. Les calculs effectués s'attachent à résoudre ce système couplé d'équations.

Les résultats de ces calculs font ressortir la nécessité de prendre en considération toutes les interactions physiques connues qui participent à l'évolution dynamique des ECRP. A travers ces résultats il s'avère que la poussière y joue le rôle décisif. Il est montré en effet que la pression radiative sur les grains de poussière, supportée par les pulsations stellaires, peut entretenir le vent stellaire. Par ailleurs, la poussière seule est également capable de produire de fortes ondes de chocs qui dominent la structure de l'enveloppe. Ce mécanisme de *chocs induits par la poussière* fait apparaitre une structure de l'enveloppe stellaire en pelure d'oignon et une distribution spatiale inhomogène de la poussière.

Le rapport des abondances du carbone sur l'oxygène ϵ_C/ϵ_O se révèle un paramètre-clé dans les résultats obtenus. Pour des valeurs suffisament élevées de ϵ_C/ϵ_O l'échelle de temps dans l'enveloppe est égale à la période des pulsations stellaires. En revanche, pour des valeurs plus petites de ϵ_C/ϵ_O l'enveloppe peut se comporter avec un temps caractéristique mutiple de la période des pulsations, un tel effet sera nommé *multipériodicité*. De plus une élévation de la valeur de ϵ_C/ϵ_O provoque une augmentation de la vitesse terminale du vent stellaire. Cette dépendance étant linéaire, il est en principe possible de déduire les valeurs de ϵ_C/ϵ_O pour les étoiles dont l'observation a permis d'estimer la vitesse terminale

du vent. La détermination directe du rapport ϵ_C/ϵ_O dans la photosphère est une tâche délicate et n'était jusqu'à présent possible que pour un nombre limité d'étoiles.

Lorsque la luminosité des modèles est suffisament élevée, une instabilité peut se développer dans les ECRP. Dans le présent travail cette instabilité sera désignée par l'appelation *κ–mécanisme externe*, puisque l'opacité de la poussière y joue le rôle prédominant. Dans une telle situation la pression radiative sur les grains de poussière induit de fortes ondes de choc, même en l'absence de pulsation de l'étoile. L'absorption des radiations de l'étoile par les particules de poussière provoque d'une part l'accélération de la matière circumstellaire, et d'autre part, en raison de l'augmentation de la température par le blocage des radiations, l'apparition d'ondes de faible amplitude dans la région interne de l'enveloppe privée de poussière. En retour ces ondes déclenche la formation de poussière et imposent au système une échelle de temps caractéristique. L'ensemble forme ainsi un processus cyclique et auto-entretenu.

La multipériodicité et les chocs induits par la poussière se manifestent aussi dans le spectre lumineux calculés à partir des modèles. Les effets qui y apparaissent sont en principe également présents dans les observations de VLP et d'étoiles de type Mira Ceti.

Contents

List of Figures

List of Tables

Prologue

Most people consider dust as a rather tiresome component of their everyday life. In fact, it could cause allergies and serves as host for various species of mites[1]. Understandably enough, these people question the relevance of an investigation dedicated to the *formation* of dust. However, also the fluffy aggregates forming in the corner of a slipshodly cleaned room could provoke the scientist to very sophisticated thoughts, for instance about the dimension of these clusters.

Indeed, *cosmic dust*, the prototype of the solid phase in the universe, which simply could be conceived as sandy grains, but exhibits a much greater variety of chemical compositions and physical structures than "domestic dust", is a major source for the enrichment of the interstellar matter with complex molecules, thus, providing an indispensable prerequisite for the development of life at all. Dust is an ubiquitous constituent of the cosmic cycle of the evolution of matter.

During the very early stages of star formation, when an amorphous dense interstellar cloud becomes gravitationally unstable and starts to collapse, the presence of dust hinders the development of a counteracting pressure. The dust particles ensure that the gravitational energy, which is set free by the collapse and partly is converted into thermal energy, is radiated away at infrared wavelengths for which the cloud is transparent. Thus, dust ensures that the collapse continues until a young star is born which maintains its stability by producing its own energy. In the inner region the temperatures become high enough to evaporate the dust, in the outer region, however, dust particles possibly coagulate and form a planetary system, where life could develop due to the presence of complex organic molecules. The central star, of which we assume that it has a mass less than 5 solar masses ($M_\odot$), spends most of the time of his life on the so called main sequence, a stable, unspectacular phase where it lives on its enormous store of hydrogen.

Once all hydrogen is burnt into helium in the core, the energy production processes become more structured, e.g. proceed in thin shells around the core, and the star reaches its final stages of life. During these stages the outer layers of the star become cool and dense enough to allow the formation of new dust particles. And now, dust again plays a key role. Dust ensures that before the star terminates

[1] e.g. Dermatophagoides Pteronyssinus

its life as a rather insignificant object, it undergoes a phase of substantial mass loss, where it donates much of its gas *and dust* to the surrounding interstellar medium, and thereby closes the cosmic cycle of matter. The enrichment of the interstellar medium with dust and complex organic molecules by dying low–mass stars marks the starting point of a new turn of the cosmic cycle.

Suppose now, we let the cosmic cycle of the evolution of matter be subject to a certain self–similar transformation Ψ, which brings us back to the level of the *mites*: we could end up with the food–chain of an ecosystem!

There, on the level of the unstructured interstellar cloud, we have various sorts of autotroph plants, which maintain their life by transforming the radiation from the sun. They serve as nutrient for herbivorous living creatures (corresponding to the peaceful beings on the main sequence), which gain their own energy by breaking up vegetable matter. These living beings in turn serve as nutrient for carnivorous life forms, e.g. mammals. These, sometimes, even more complicated and structured living beings maintain their life by producing energy which they gain from the break up of organic matter. Once, these creatures die, they give rise to a variety of microscopic diligent species, such as bacteria, mould, *and mites*, that transform the dusty remains into a manifold of anorganic and organic compounds, which serve as nutrient for the plants again, and provide the seed for new forms of life. Thus,

the presence of dust and the existence of life
are inevitably coupled

Chapter 1

Introduction

Ferner habe ich vor einigen Jahren gefunden, dass Mira Ceti eigentlich zu den Planetarischen Nebelflecken gezählt werden könne. Er lässt sich zwar nicht so stark vergrössern als jene, allein er erscheint doch als Scheibe mit einer geringen Blendung, und grösser wie andere Sterne. (...) Es leidet keinen Zweifel, dass Mira ein Stern ganz anderer Art sey als andere Fixsterne.

Erb–Landmarschal und Ritter von Hahn zu Remplin[1]

1.1 Some historical remarks

In August 1596 the friesian parish priest DAVID FABRICIUS observed a star in the constellation of Cetus of about second magnitude. He neither had noticed the star before nor could he find it in a star catalogue. He continued his observations for several weeks but the brightness of the star declined regularly, and already in October of the same year the star vanished. The belief of FABRICIUS that the change of light of a fixed star is something impossible prevented that he paid more attention to his discovery. That might explain why, although FABRICIUS rediscovered the star in February 1609, he did not start systematic observations. Meanwhile in 1603, JOHANNES BAYER had also found the star and gave him the greek letter o in his star catalogue. Due to the changes of light of the star it was also called "the wonderful in Cetus" (Mira Ceti).

[1] quoted from **Bodes Astronomischen Jahrbuch** of the year 1803, p. 106

It took until 1638, when HOLWARDA, a professor at the University of Franecken, again observed *o* Ceti, registered again the changes in its light, and initiated continuous observations. [GUTHNICK 1901] notes, that among those who subsequently observed Mira were also KEPLER, HEVELIUS, KIRCH and others. Unfortunately, FABRICIUS did not live to see the interest his star rose. He was beaten to death on the evening of May 17, 1617 with a peat spade by the farmer Frerik Hoyer [BERTHOLD 1894][2].

No longer before 1660, the periodicity of Mira was definitely established with a period of 11 months. Mira Ceti became the first member of a group referred to as *long–period variables*. No new variable stars were registered until 1784, apart from the discovery of the eclipsing binary β Persei (Algol) by MONTANARI 1667. In 1783 the Copley–medal was awarded to GOODRICKE by the english Royal Society: "...for his discovery of the period of the variation of light in the star Algol" [HAGEN AND STEIN 1921]. In 1784 GOODRICKE also revealed light variations of δ Cephei, which was to become the prototype of a further class of variable stars: *the Cepheids*.

Before the end of the 18^{th} century three more classes of variable stars have been established: *irregular* (α Herculis discovered by HERSCHEL in 1795), *semi–regular variables* (R Scuti discovered by PIGOTT also in 1795), and the peculiar object R Coronae Borealis (PIGOTT 1783). For a long time the number of variable stars remained fairly constant. The first catalogue of ARGELANDER published in Schumachers Jahrbuch of 1844, p.216, contains a list of 18 objects. Only six more objects than PIGOTTS catalogue of 1786 (cf. Phil. Trans. R. Soc. London **76**, p.189), which also contains 38 objects with questionable variability. [MÜLLER AND HARTWIG 1918] give a list of all important catalogues that followed up to 1915, see also the very intriguing Fig. 1 of [LEDOUX AND WALRAVEN 1958], which demonstrates the steeply rising number of discovered variables.

The use of photography and the development of spectroscopic techniques at the end of the 19^{th} century increased the number of discoveries dramatically, and led to the introduction of several observational classification schemes, e.g. [LUDENDORFF 1928].

In the following, however, we want to focus our attention to the theoretical approaches to explain the phenomenon of variable stars. For an extensive review of the different attempts and approaches to explain the changes of light of variable stars see [LEDOUX AND WALRAVEN 1958].

Basically, these early theories can be divided into two groups: the purely geometrical and mechanical approaches, and second those, which are more physically oriented. Some of the earliest attempts are based on the rotation of a solid body with a non–uniform surface brightness distribution, which is assumed constant in time, e.g. BOULLIAUD in 1667. These approaches have been refined by P.L

[2] Besides being a priest and astronomer FABRICIUS also was an astrologer, which gave rise to various rumors, that he had foreseen his death, and nevertheless could not escape his destiny.

MOREAU DE MAUPERTUIS (1732), who attributed the light variations to the precession of an ellipsoidal body under the influence of planets on highly eccentric orbits. In 1881 in the "Monatsberichte d. Kgl. Preuβ. Akad. d. Wiss.", p.48, H. BRUNS published a rather mathematical approach. He showed that each continuous and periodic lightcurve can be generated in infinitely many ways by a non–uniform brightness distribution on the surface of a sphere rotating around a fixed axis. Unfortunately, he oversaw the problem that the brightness distribution derived from lightcurves must be positive everywhere and cannot take negative values!

An experimental approach was presented by [GUTHNICK 1919]. In the laboratory, he observed a dark, 34 mm small, rotating sphere, on which he had drawn a spot with white chalk. By taking into account the limbdarkening, he could reproduce all hitherto observed types of lightcurves. However, [BOTTLINGER 1919] pointed out that the limbdarkening produced by the lamp in the laboratory had rather high values, which he considered as unrealistic for real objects, and therefore he refused the spot theory.

Slowly, the theories incorporated more and more physical mechanisms. Already ZÖLLNER in 1865 had attributed the light variation to the movement of superficial slag towards the equator and trajectories deviated against the rotation of the star.

Although rather fictitious at that time the so called *veil–theories* comprised remarkably interesting ideas, and still are relevant, of course in another sense, in these days. The forerunner of these theories was developed by BRESTER in 1889 with some ideas about the periodic evaporations and condensation of separate clouds in a layer of supersaturated vapor above the photosphere of a star. In his monograph "Spectra of long–period variables" (1940, p. 98) P.W. MERRILL writes:

> A (...) phenomenon which may increase the light ranges of long–period variables is the formation of a cloudy veil of solid or liquid particles condensed, at certain phases, from gases of the star's upper atmosphere. The existence of such a cloud is suggested by the low temperature of the photosphere (...); and by the apparent insufficiency of other hypotheses.

[O'KEEFE 1939] concluded from simple physical and chemical considerations, that the condensation of carbon particles out of atomic carbon gas is going to take place at a reasonable distance above the photosphere of R Coronae Borealis, which he assumed to be within $\approx 20\ R_\star$, and would then account for the light variations of this star. He suggested that the shape of the lightcurves as well as the spectral variation at minimum of R CrB could be attributed to the formation of these obscuring clouds. For a review of these early dust theories see [STRUVE 1955].

The preceding theories contained a purely mechanical point of view or physical considerations that were connected solely with the surface of the star. As an alternative to these theories EDDINGTON in 1917 proposed to apply the theory of pulsation, which he had developed for Cepheids, also to Miras. Later, this theory of purely radial pulsations has been refined by [JEANS 1929], p. 388, by proposing that the central, ellipsoidal core of the star was undergoing these pulsations. He considered the core to be surrounded by an extended atmosphere, rotating more slowly than the core, to which the motion of the core is transmitted through the action of gravitation and pressure in the form of a running wave that travels around the equator.

All these attempts cited above were aimed to explain the variations of light of the variable stars. At the beginning of the 20^{th} century almost nothing is known about the evolutionary status of variable stars, and in particular Miras and long–period variables. In a short section in his review devoted to the “Entwicklungsgang der Mira–Sterne” (Evolutionary sequence of Miras) [LUDENDORFF 1928] states, that Miras have to be considered as giants, and, based on the evolution theory of RITTER and RUSSEL, he concludes that Miras must be young stars.

Nowadays, many amateur astronomers monitor especially long–period variables in the visual as regular as possible, which is an important task for statistical purposes. However, it seems that the french astronomer LALANDE in 1792 saw things a little bit too optimistic, when he wrote (as quoted by [HAGEN AND STEIN 1921]):

> *Ces variations des étoiles sont bien dignes de l'attention des observateurs curieux. Le moyen le plus sûr de les découvrir serait d'observer de temps en temps toutes les étoiles, et d'en dresser des catalogues. Un jour viendra peut-être où les sciences auront assez d'amateurs pour qu'on puisse suffire à ses détails.*

1.2 Miras and Long–Period Variables

1.2.1 Evolutionary status

Low and intermediate mass stars, after leaving the main sequence, are thought to reach finally the Asymptotic Giant Branch (AGB) on which they evolve along the Hayashi–line towards higher luminosities until they end up as Planetary Nebulae (PN) leaving the remaining central object as a white dwarf. Miras and Long–period variables are considered as highly evolved objects at the end of the AGB–phase, a quite common stage of stellar evolution.

In the following, we give a brief description of this evolutionary sequence based on [Iben 1981, Iben and Renzini 1983, Iben 1987, Iben 1991], [Boothroyd and Sackmann 1988b], [Lattanzio 1989], [Weidemann and Schönberner 1990, Schönberner 1990].

Due to the difference in mass, the evolution of these objects shortly after the main sequence proceeds different. After the exhaustion of hydrogen in the core, intermediate mass stars (typical masses between 2 and 6 $M_\odot$)[3] ignite He–burning under nondegenerate conditions and evolve nearly horizontally in the Hertzsprung–Russel diagram (HR–diagram) from the main sequence directly to the red giant region, performing loops towards the hotter region of the HR–diagram and back to the red giants, while undergoing central helium burning.

In contrast, low mass stars ($1\ M_\odot \leq M \leq 2\ M_\odot$) develop, after hydrogen exhaustion on the main sequence and subsequent H–shell burning, a degenerate He–core and climb the Red Giant Branch (RGB) along the Hayashi–line. The increase of the H–shell burning strength causes the luminosity increase on the RGB, which is necessary to balance the gravity of the increasing degenerate He–core. Finally, at the end of the RGB phase, where low mass stars have reached luminosities of $\approx 3\,10^3\ L_\odot$, the He burning is ignited in a core flash, which lifts the degeneracy and causes the luminosity to drop to values about $1.8\ 10^3\ L_\odot$. Due to the high luminosities during the RGB-phase, the stars already lose substantial amounts of mass, which decisively influences their evolution. The helium core flash, however, first of all removes them from the red giant region.

Once, the central helium storage is exhausted both types of stars qualitatively evolve similarly. Again, they switch to shell–burning. An extensive He–burning shell causes the stars i) to expand, thereby cooling the outer regions which extinguishes the outer H–burning shell, ii) to increase their luminosity, and iii) to reach asymptotically the red giant region again. The stars consist of a degenerate increasing core consisting of carbon and oxygen, a He–burning shell, and a hydrogen–rich envelope. This evolutionary stage is called Early Asymptotic Giant Branch (E–AGB) phase.

At the end of the E-AGB phase, the outwards moving He–burning shell reaches the outer hydrogen-envelope. At temperatures exceeding 10^8K, due to He–burning, the H–shell is ignited again. This two–shell burning, together with the development of instabilities leads to an unsteadily burning of He in so called He–shell flashes or thermal pulses (TP). The TP occur rather periodically on timescales of 10^4 yrs. This second stage of AGB evolution is therefore called TP–AGB phase.

As a result of the 3α-process (He–burning) the core of an AGB star consists of $\approx 80\%\ ^{16}O$ and $20\%\ ^{12}C$. On top of this He–burning shell is material that has been processed by H–burning, thus contains primarily helium, with enhancements

[3]The numbers given in this paragraph depend on details of evolutionary calculations and are still a matter of debate. They should be conceived as a rough guidance.

of ^{14}N resulting from the CNO–cycle. Outside the hydrogen burning shell the envelope has a chemical composition, which is that of the main sequence, modified by abundance changes due to the so called first and second dredge up phases.

These changes are caused by the convective envelope which extends inward and "dredges up" material that has undergone hydrogen burning during preceding phases. Every star that becomes a red giant for the first time shows the first dredge–up phase. The second dredge–up phase occurs after the exhaustion of central helium and during the formation of a degenerated core. During the TP–phase the third dredge–up occurs. The pulses can reach a luminosity from helium burning up to $10^7 L_\odot$. The deposition of these large amounts of energy causes a convective zone to form at the base of the He–burning shell which extends almost to the H–burning zone. The temperatures at the base of the convective region can exceed 3 10^8K and causes reactions like $^{22}\mathrm{Ne}(\alpha,n)^{25}\mathrm{Mg}$ to take place, thus forming free neutrons, which can be captured by ^{56}Fe, and result in the formation of s–process elements.

After the pulse, the convective zone might reach as deep as into the ^{12}C–rich zone and carbon can be mixed to the surface. Whether this is the case or not yields a first classification of AGB–stars:

AGB–stars can be roughly classified according to their surface abundance of carbon to oxygen: $\epsilon_C/\epsilon_O > 1$: carbon-rich stars (C-stars), $\epsilon_C/\epsilon_O < 1$: oxygen-rich stars (M-stars) and the intermediate case of $\epsilon_C/\epsilon_O \approx 1$: S-stars.

To finish this evolutionary scenario, we give a few remarks on the final fate of AGB–stars. Mass loss is the dominating phenomenon which terminates the AGB evolution. Since the thermal pulses do not suffice to expel the outer layers of the star, other mechanisms, discussed below, are more likely to bring an end to the life of an AGB–star. The stellar core already is a hot pre–white dwarf with decreasing radius and constant luminosity. When the central object has reached $\approx$ 3 10^4K, its ultra–violet radiation is able to ionize the expelled shell. Due to recombination effects of the emitted radiation of the shell, it becomes visible as a planetary nebula. Finally, the hydrogen burning of the central star ceases and the luminosity steeply decreases. The temperature, which so far has reached values as high as 1.5 10^5K, decreases and the object cools down to become a white dwarf.

Although, the lifetime on the tip of the AGB is rather short, $10^4 \ldots 10^5$yrs, understanding the mass loss process of Miras and LPVs is of extreme importance, since the following post-AGB evolution is completely determined by their stellar structure on the AGB. Furthermore, since only $\approx 5\%$ of the stars on the main sequence have masses exceeding 6 $M_\odot$ and end their lives as supernovae, the AGB–phase is a common stage of stellar evolution.[4]

No final picture of the evolution from the main sequence to the planetary nebulae phase exists. Since there are no consistent theoretical calculations, only a qualitative, rather sketchy description, omitting many details, had to be given.

[4] Low– and intermediate–mass stars account for $\approx 50\%$ by mass on the main sequence.

Theoretical evolutionary model calculations are still contaminated with a lot of free parameters, which make quantitative statements rather uncertain. Although considerable progress has been achieved in the last 20 years, the calculation of consistent evolutionary tracks has still to be seen as a great challenge of modern astrophysics.

1.2.2 Characteristica and properties

Miras and LPVs are highly evolved objects, located at the upper region of the AGB in the Hertzsprung-Russel diagram, at luminosities of the order of $10^4 L_\odot$ and typical effective temperatures of less then 3000 K.

Due to these extremely low effective temperatures molecular bands are permanently present in their spectra. Stars of spectral type M show molecular bands especially of TiO, C–star (earlier classified as R and N) spectra are characterized by CN, CO or C_2 bands. The intermediate case of S–stars is characterized by the presence of ZrO bands [Hoffmeister *et al.* 1990]. The additional characteristic presence of emission lines in the spectra is indicated by an *e* after the spectral type: Me, Ce, Se.

Concerning the distribution of these stars in our own galaxis, there seems to be agreement among observers that the number density of C–stars shows no variation with the galactic radius, but that there seems to be a decided preference by M–stars for the direction of the galactic center [Thronson *et al.* 1987], and references therein. From the data of the IRAS Point Source Catalogue [Thronson *et al.* 1987] derive an exponential decrease of the number density of M-stars in the galaxy.

For the number ratio of cool carbon stars to M giants [Blanco 1989] gives a value ≤ 0.001 for the galactic bulge, ≈ 2 for the Large Magellanic Cloud and ≈ 20 for the Small Magellanic Cloud. To interpret these striking differences at first sight as a simple function of the mean metallicity of the galaxies leads to contradictions with other results from observations [Blanco 1989]. Although, the absolute numbers of the C–star – M–star ratios may vary, the general trend is well established. However, the explanation for the strong differences is still a matter of controversy.

Apart from the general distinction between C- and M-stars it seems to be difficult to determine the actual ratio of the photospheric abundance of carbon to oxygen e.g. for C-stars and the results show major discrepancies [Gow 1977], [Lambert *et al.* 1986], [Frantsman and Eglitis 1988], [Eglitis 1993].

During this important stage of stellar evolution, the appearance of these objects is dominated by two phenomena: **variability** and the presence of a **circumstellar dust shell** (CDS).

- **Variability**. More or less, all red giants show variability. The term Long–period Variables is somewhat misleading, since it stems from older classifications, and in principle, comprises Miras, Semi–regular and even Irregular varying objects.

Usually, the term *Mira* is used for objects varying with amplitudes larger than $2^m.5$ (up to $5^m \ldots 11^m$) in the visual with a well defined periodicity. *Semi–regular* variables (SR) are giants and supergiants who sometimes differ from Mira type variables only by their smaller light variations (less than $2^m.5$). They may also show changes in the amplitude and the shape of the light curve. Subtypes are SRa–d, see e.g. [KERSCHBAUM AND HRON 1992]. *Irregular* variables (Lb, Lc) show light variations which exhibit no or at most a rather poorly pronounced periodicity. Despite these distinctions, we will use a little bit sloppyly the phrase "Miras and LPVs", if we refer to this class of late–type stars.

In recent years, due to the results of e.g. the IRAS–mission, a further class of variable stars has been found: OH/IR stars. They can be considered as a subclass of the Mira variables for the following reasons [HABING 1990]: The amplitude of their light variation is almost the same, with periods even exceeding that of Miras (see below). In some cases distances could be measured which in combination with the measured fluxes yield luminosities of these objects between 4 10^3 and 6 10^4 $L_\odot$. Their kinematical properties and their galactic distribution are the same as those of Miras (see also below). OH/IR stars are thought to be surrounded by extremely thick dust shells, which prohibit to observe their photospheres. Due to the apparent similarities in period and luminosities, Miras are considered as the evolutionary progenitors of OH/IR stars, which in turn, as more evolved objects, are at the immediate transition to the planetary nebulae stage, see also [ENGELS *et al.* 1983, NYMAN *et al.* 1993, CHENGALUR *et al.* 1993].

Miras undergo large and mostly regular pulsations with a period range from $\approx$ 100 d up to $\approx$ 1000 d [WHITELOCK *et al.* 1991] with a maximum in the distribution by number around 350 d. Most of them are oxygen–rich Miras, in fact most cool stars are oxygen–rich. According to [HOFFMEISTER *et al.* 1990], p.59, in the period range between 350 and 400 days 113 of the Miras found were of spectral type M, 14 of C–type, and also 14 of the S–type. The numbers may change but the trend is evident. There seems also to exist a correlation between the period and the position of the objects in the galaxy. The Miras with periods less than 350 days seem to be concentrated in the galactic bulge [WHITELOCK *et al.* 1991].

These pulsations are presumably maintained by a modulated absorption of radiation in the interior, the κ– mechanism. [KEELEY 1970] has shown that this mechanism causes strong driving of the pulsation in the region outside the helium– and hydrogen–ionization zones. There has been a long lasting debate about the mode of these pulsations. [HILL AND WILLSON 1979] estimated that the first overtone pulsation is incapable in providing the observed pulsation velocities, and therefore Miras have to be fundamental mode pulsators. On a different analytic approach [WOOD 1986] argued that Miras are in fact first overtone pulsators. However recently, based on the calculations of [Bowen 1988a] (see Sec. 3 for a discussion), [Wood 1990] also claimed that Miras are fundamental mode pulsators, see [Tuchman 1991] for a derivation of the mode of the pulsation based on observations. Full nonlinear pulsation models for Miras are not yet available [Dorfi and Feuchtinger 1991] and the question cannot finally be answered.

In any case, pulsationally induced waves travel into the outer regions of the star where they steepen to become shocks. The presence of shock waves, revealed by emission line observations in LPVs, e.g. [Willson 1976, Gillet 1988], causes a levitation of the atmosphere, i.e. a dramatically increased density scale height compared to the corresponding hydrostatic value.

- **Circumstellar dust shells**. The presence of a circumstellar dust shell (CDS) is inferred from the IR-excess, i.e. the presence of a large amount of long–wavelength radiation in the spectra of the stars.

More than 30 years ago [Woolf and Ney 1969] attributed the observed emission in the 10 to 14 μm range to circumstellar emission rather than to be photospheric. They noticed that the observed spectra are similar to those of mineral grains. Very soon, it became clear that CDS are indeed a rather frequent phenomenon [Gehrz and Woolf 1971].

Because of the increased density due to the interior pulsation, effective condensation of solid particles becomes possible, if the temperature is sufficiently low. The possibility, that the dust is formed in the interior of the star can be rejected, since the temperatures are too high for the solids to exist. The presence of dust causes the observed large infrared excesses due to the absorption of short–wavelength radiative energy by the solid particles, internal thermal relaxation, and subsequent reradiation at longer wavelengths.

Based on data of the IRAS–mission, [Veen and Rugers 1989] constructed a two–color diagram ([12]–[25]/[25]–[60]) which they interpreted in terms of a sequence of decreasing dust temperature in *expanding* circumstellar shells, from Miras with relatively short periods via LPVs to non–variable sources and finally to the PN. However, that CDS are indeed a dynamical phenomenon has been known before. The terminal outflow velocities range from less than $10\,\mathrm{km\,s^{-1}}$ up to $45\,\mathrm{km\,s^{-1}}$ (e.g. [Knapp and Morris 1985], [Jura 1986a], [Zuckerman *et al.* 1986], [Barnbaum *et al.* 1991]).

[Zuckerman *et al.* 1986] have shown that carbon-rich stars exhibit a mean terminal outflow velocity around $17\mathrm{km\,s^{-1}}$ which is somewhat larger than in the oxygen-rich case.

The dust grains are also effective absorbers of radiative momentum which they transmit via frictional coupling to the surrounding gas particles. Thereby, they cause the acceleration of the material and drive a mass outflow or a so called wind. Since this material will finally not be gravitationally bound anymore, the

Table 1.1: Observed parameters of four typical carbon–rich Long–period Variables. The numbers in [.] denote the corresponding reference: [1] [Knapp and Morris 1985], [2] [Heske 1990], [3] [Heske 1989], [4] [Lambert *et al.* 1986], [5] [Gow 1977], [6] [Zuckerman and Dyck 1986a], [7] [Veen and Rugers 1989] to be continued on opposite page

Object*	ϵ_C/ϵ_O †	$T_\star$ ‡	P♣	$L_\star$ ♠
R Lep 04573–1452 GL 667 TMSS–10080 CCS 276 HD 31996	1.03 [4] 1.29 [5]	2390 [4]	423 [3] 432 [8] 427 [15]	0.87 [10]
R Scl 01246–3248 GL 215 TMSS–30015 CCS 68 HD 8879	1.34 [4]	2550 [4]	363 [8] 370 [15]	0.8 [10]
S Cep 21358+7823 GL 2785 TMSS+80048 CCS 3055 HD 206362	4.06 [5]	–	487 [8]	0.81 [10]
V Hya 10491–2059 GL 1439 TMSS–20218 CCS 1766 SAO 179278	1.05 [4] 2.33 [5]	2650 [4]	529 [8] 531 [15]	0.69 [10]

* different names, GL≡RAFGL, TMSS≡IRC
† Overabundance of carbon to oxygen
‡ Effective Temperature in K
♣ Pulsational Period in d
♠ Stellar luminosity in 10^4 $L_\odot$

Table 1.2: Tab. 1.1 continued. Properties of four typical carbon–rich LPVs. References continued: [8] [JURA 1986A], [9] [ROWAN-ROBINSON AND HARRIS 1983], [10] [CLAUSSEN *et al.* 1987], [11] [OLOFSSON *et al.* 1987], [12] [ZUCKERMAN *et al.* 1986], [13] [GROENEWEGEN *et al.* 1992], [14] [NYMAN *et al.* 1992], [15] [OLOFSSON *et al.* 1993A], [16] [LOUP *et al.* 1993]

u_∞ *		$\dot{M}$ †		d ‡		Spectral type		Variability type	
21.4	[14]	2.1(-6)	[1]	450	[1]	N6e	[1]	M	[4]
20.5	[1]	3.2(-7)	[8]	430	[13]	N6;C7,4	[4]		
17.6	[2]	3.2(-7)	[10]	480	[7]				
9.8	[6]	1.6(-6)	[13]	410	[8]				
9.8	[8]	2.0(-6)	[16]	430	[10]				
18.6	[13]			430	[15]				
12.8	[3]			480	[16]				
16.7	[15]								
17.3	[15]								
17.9	[16]								
18.0	[8]	3.1(-5)	[1]	400	[9]	C6,5	[9]	SRa	[4]
24.7	[1]	7.6(-7)	[10]	260	[13]	C6 II	[1]	SRb	[15]
17.5	[6]	3.5(-6)	[8]	840	[1]	Np;C6,5	[4]		
17.5	[13]	2.0(-6)	[13]	430	[10				
16.5	[15]	1.2(-5)	[16]	370	[7]				
15.2	[15]			420	[15]				
18.2	[16]			2080	[16]				
22.4	[6]	3.2(-7)	[10]	560	[9]	C6II	[9]	M	[6]
27.0	[13]	1.85(-6)	[13]	460	[7]	C	[6]		
31.3	[14]	4.0(-6)	[16]	390	[10]				
22.5	[15]	1.1(-6)	[15]	410	[13]				
21.5	[15]			440	[15]				
24.6	[16]			460	[16]				
16.0	[8]	4.0(-6)	[1]	390	[8]	C6	[9]	SRa	[4]
20.9	[1]	9.5(-7)	[10]	400	[1]	C6,3e	[1]		
14.2	[7]	1.7(-6)	[8]	330	[7]	N;C7,5	[4]		
14.9	[13]	3.1(-6)	[16]	280	[13]				
15.8	[14]			350	[15]				
13.7	[15]			330	[16]				
27.8	[15]								
18.7	[16]								

* final outflow velocity in km s^{-1}
† mass loss rate in $M_\odot$ yr^{-1}, a(-b) denotes a 10^{-b}
‡ distance in pc, 1 pc = 3.08 10^{16} m

star undergoes a mass loss. The mass loss rates range from $10^{-8} M_\odot\,\mathrm{yr}^{-1}$ up to $10^{-4} M_\odot\,\mathrm{yr}^{-1}$, e.g. [Olofsson *et al.* 1993a] and references therein.

Furthermore, there exist certain correlations derived from observations, which underline a close linkage of mass loss to pulsation: A relationship was found between the observed infrared excess and the period, both for oxygen- and carbon-rich Miras [DeGioia-Eastwood *et al.* 1981, Jura 1986a]. It indicates particularly high mass loss rates for stars with periods $P > 400\,\mathrm{d}$. [Heske 1990] has found evidence for a correlation between the final outflow velocity $v_{\rm exp}$ and the period. Stars with periods between 100 d and 500 d appear to have a value $v_{\rm exp} \approx 10\,\mathrm{km\ s^{-1}}$ while stars with periods between 600 d and 2000 d have $v_{\rm exp} \approx 20\,\mathrm{km\ s^{-1}}$ with a narrow transition zone between both regions.

As stated already earlier the high mass loss of Miras and LPVs has severe consequences for them and for the interstellar medium:

i) mass loss extremely accelerates the final AGB–evolution [Schönberner 1990],

ii) Miras and LPVs serve as important sources for the enrichment of the interstellar matter with molecules and dust [Gehrz 1989, Lafon and Berruyer 1991].

Summarizing, LPVs can be considered as highly evolved AGB–objects which possess a massive, slow wind, which is a place for copious dust formation. As an example, we list in Tabs. 1.1 and 1.2 derived properties of some fairly good observed objects, where, nevertheless, various authors arrive at considerable different results.

The details of the **mass loss mechanism** are still a matter of debate. Since the present work investigates the interplay between interior pulsation and radiation pressure on dust particles and its contribution to the wind generation (and favours this mechanism as the dominating one), we would nevertheless in this introductory section describe some alternative mechanisms. Although never stated explicitly by other authors, there is a general agreement, that once the dust is present, it completely dominates the dynamics and the optical appearance of the CDS. The problem reduces to the question, which mechanism provides the physical conditions (low enough temperatures and simultaneously high enough densities) that dust can form?

Some of the mechanisms listed below were constructed to drive the winds from cool stars even without radiation pressure on dust:

Radiation pressure on molecules. Since the considerable mass loss of O and B stars is caused by radiation pressure on atoms, it is natural to investigate the question whether the corresponding mechanism, radiation pressure on molecules, also works for late–type stars, supporting the atmospheric levitation.

Therefore, [Jørgensen and Johnson 1992] investigated the absorption and scattering of photons by molecules in the photosphere of cool giants. They extended previous work, [Jørgensen and Johnson 1992] and references therein, which were confined to oxygen–rich atmospheres, also to the case of carbon–rich atmospheres.

They calculate the radial structure of radiation pressure on molecules for a representative grid of photospheric models. In general, [Jørgensen and Johnson 1992] find the radiative acceleration to be a few percent of the corresponding gravitational acceleration. While comparing their calculations for the carbon–rich case with those of the oxygen–rich case, they find approximately equal values for the radiation pressure on molecules for a carbon–rich atmosphere of $C/O \approx 1.35$, and an oxygen–rich atmosphere of the solar value, i.e. $C/O = 0.43$. Models with higher values of C/O show a greater levitation, and models with lower C/O have a lower levitation, compared the the model with solar C/O. The radiation pressure increases with increasing stellar temperature, but is almost independent of the gravity of the model and the stellar mass.

Radiation pressure on molecules seems to be a good candidate to support the levitation of the atmosphere, and to provide appropriate physical conditions for dust formation, which, then, is much more efficient and dominates the atmospheric behaviour.

Sound waves. In series of papers the dutch group investigated the role of acoustic waves for driving the winds of various astrophysical objects [Pijpers and Habing 1989, Pijpers and Hearn 1989, Pijpers 1990, Koninx and Hearn 1992, Koninx and Pijpers 1992].

With respect to AGB–stars they find, that sound waves can drive winds with mass loss rates between 10^{-7} and 10^{-4} $M_\odot$ yr^{-1}, and they claim that acoustic wave driven stellar winds reproduce the overall structure of the winds of Miras and OH/IR stars. However, their models are contaminated with some arbitrary parameters and completely neglect the effects of dust. Therefore, the role of sound waves seems to be overestimated. In addition, it is questioned [Wood 1990] whether sound waves are actually able to leave a pulsating Mira or whether they are blocked and reflected by the strong shock front.

The role of sound waves, which are generated in the convective interior of the star and undoubtedly should be present somewhere in late–type atmospheres, will primaryly be in supporting than in driving the stellar wind.

Alfvén waves. The contribution of Alfvén waves to the levitation of the atmosphere is discussed by e.g. [Hartmann and MacGregor 1980, Holzer *et al.* 1983, Holzer and MacGregor 1985, Holzer 1987].

They consider the energy transport by small amplitude waves in general, which, in the presence of magnetic fields, can be non–compressive Alfvén waves. Since they are non–compressive, these waves are much less readily damped as e.g. acoustic waves, and thus Alfvén waves are able to extend a stellar atmosphere over a much larger radius interval and lift the material out of the gravitational field. The calculations show, that completely undamped Alfvén waves indeed cause a stellar outflow with mass loss rates of $\approx 10^{-7}$ $M_{\odot}$ yr^{-1} but with unrealistic high outflow velocities. If damping is introduced, the outflow velocity is considerably reduced, but the problem remains that too much energy is transferred to the wind in the supersonic region, and the wind still is too fast.

Since in addition, less is really known about magnetic fields in late–type stars, the Alfvén wave theory has to deal with considerable uncertainties.

However, pulsation seems to be generally accepted as the dominant and most likely levitation mechanism [Gail 1990] in the atmospheres of cool late–type stars. Whether pulsation contributes alone to the levitation or in combination with other mechanisms is still under investigation.

Considerable progress, due to new observational and computing facilities, has been made in the last 15 years to understand the processes reigning these complex as well as important objects. On the theoretical part, modelling has been focused on the interior of the LPVs and on the pulsation driving region, while less effort has been made to produce a detailed model of the outer atmosphere.

The pioneering work in modelling circumstellar dust shells (CDS) by [Willson and Hill 1979, Wood 1979] has been substantially improved by the work of [Bowen 1988a, Bowen and Willson 1991] who include parametrized cooling laws which yield a more realistic modelling of the post-shock relaxation both in the inner and outer region of the atmosphere. These calculations represent the largest grid of dynamical model calculations of CDS around LPVs that has been presented so far. Nevertheless, these models severely lack a detailed treatment of dust formation, growth and destruction. Instead, only a kind of step function is assumed to simulate the acceleration by radiation pressure on dust. This function jumps from zero to a value of the order of one (in units of the gravitational acceleration) when the temperature drops below a suitable chosen, critical value, called the condensation temperature. These calculations will be discussed in detail in Chap. 3.

This approach neglects the interaction between the hydrodynamical and thermodynamical conditions and the dust complex and thus is insufficient to reveal the key role of the solid particles in determining the structure of the CDS as has been pointed out already by [Fleischer *et al.* 1990, Fleischer *et al.* 1991]. Nevertheless, Bowen's calculations stress the importance of radiation pressure on dust for the dynamics of CDS around LPVs. His purely pulsationally driven models without dust, i.e. without consideration of the step function, cannot account for the observed mass loss rates.

1.3 The aim of this work and its structure

It is the very aim of this investigation to achieve a reliable theoretical description of the expanding circumstellar dust shells (CDS) around Miras and Long–period variables (LPVs). Thereby, we do not intend to improve the microscopic description of various physical processes, but to unite them in a numerical tool which provides a comprehensive description of a dust forming atmosphere as a whole.

CDS around Miras and LPVs have to be considered as nonlinear dynamical systems whose local physical conditions and global structure can only be understood if the interaction of hydrodynamics, thermodynamics, radiative transfer, chemistry, and dust formation are taken into account in an appropriate manner. However, these systems have never been studied in this complexity before, and thus, severe problems could never be addressed to consistently, e.g. the questions where and at which amount the dust forms, or how it influences the dynamical structure.

Hence, this work is aimed at a more physical understanding of CDS around LPVs, which in addition shall provide a reliable basis for further theoretical model calculations as well as a trustworthy explanation for existing and planned observations of these fascinating objects.

This work is organized as follows:

Chapter 2 contains a concise description of the physical problem we face, when dealing with dust forming stellar atmospheres. The physical ingredients are discussed and special emphasis is given to the different interaction mechanisms. Furthermore, Chapter 2 contains a brief description of the numerical method as well as some technical details that turned out to be important during the development of the code.

Chapter 3 gives an overview about previous calculations of other authors concerned with the numerical modelling of circumstellar dust shells around long–period variables. It is shown, that our code reproduces these results, if we apply the oversimplifying method to treat the dust component, which was used in the literature so far. Some emphasis is given to study the development of the hydrodynamical structure in the innermost dust–free region of the atmosphere.

Chapter 4 demonstrates that completely new, nonlinear effects and a complex structure of the circumstellar dust shell arise, if dust formation, growth and evaporation are taken into account and treated with an appropriate physical method. Dust is revealed as the key component which determines the dynamics of the circumstellar shell as well as its structure.

Chapter 5 shows that in certain regions of the parameter space an instability occurs, which causes the development of strong shock waves even in the absence of an interior pulsation. Neglecting the influence of the dust complex on the thermodynamical structure yields the limit case of a stationary purely dust driven wind.

Chapter 6 is an extension of Chapter 4 to an enlarged range of model parameters. The systematic variation of certain model parameters turns out to have severe influences on the dynamical behaviour of the circumstellar dust shell.

Chapter 7 gives a first investigation whether the new effects presented in the previous chapters have consequences that, in principle, can be verified by detailed observations of the objects under consideration.

Chapter 8 comprises some preliminary results that are relevant for an extension of the method presented here e.g. to the nucleation of more complex forms of dust or to the application of the scheme to other types of astrophysical objects.

Chapter 9 is devoted to a discussion of the approximations inherent in the modelling approach, and to their influence on the results which were presented.

Chapter 10 contains a concise summary of the main results of this work.

Chapter 11 points out some possible directions of further investigations based on the present work, and shows up extensions of the current version of the code. Furthermore, some concluding remarks are given.

A lot remains to be done, but this work provides a comprehensive description and analysis of the present state of the art of the dynamical modelling of circumstellar dust shells around late–type pulsating stars:

Es wird aber nöthig sein, einen festen Boden schon unter den Füssen zu haben, auf dem dann weiter gebaut werden kann, und mir würde es dann zur grössten Genugthuung gereichen, wenn diese Untersuchungen einen solchen geliefert haben würden.

[Guthnick 1901], p. 22

Chapter 2

The Modelling Method

2.1 The physical problem

The "classical" stellar atmosphere problem consists of the solution of the coupled system of differential equations describing the hydrodynamical and thermodynamical structure as well as the chemical stratification of the atmosphere. This part of the problem is represented by the blue parts (or solid arrows[1]) of Fig. 2.1. The additional presence of dust, however, introduces some decisive consequences which have to be taken into account in the description of a dusty atmosphere. Due to its large cross section for the interaction with photons and with the particles from the gas phase dust decisively affects the local transport coefficients and thus, the global structure of the atmosphere. As a macroscopic solid particle it essentially influences the physics of the system:

- As a solid, dust is able to thermalize energy. By the absorption of short wavelength photons and reemission at longer wavelengths the dust component is a very effective energy transmitter. Thereby, it influences the thermal structure of the object by its absorption coefficient κ_ν^d and its IR–emission as well as the characteristic spectral appearance of the object, e.g. IR–excess. The energy thermalisation results in an internal heating of the dust grains compared to the ambient gas, and thus, in a thermally decoupling of the dust particles from the gas component.

- The solid particles effectively absorb radiative momentum which they transmit via frictional coupling to the surrounding gas, i.e. dust grains are also effective momentum transmitters with essential influence on the hydrodynamical structure. Due to this efficient acceleration mechanism dust is able to accelerate the bulk of material to supersonic velocities, thereby driving the massive and slow outflows which characterize late–type stars. A further complication could be expected if also the strength of the coupling is

[1] if Fig. 2.1 is contained only in its black/white version

taken into account. Then, larger dust particles could "drift" relative to the mean motion of the gas and hydrodynamical description could require the separate solution of an equation of motion for the dust grains.

- As a macroscopic solid in a reactive flow, the surface of the grain gives rise to further chemical reactions which would not occur without the surface. By the absorption of special species the reaction probability with appropriate partners is enhanced and the dust grains possibly catalyse the formation of complex molecules.

The extension of the classical atmosphere problem due to the presence of dust is roughly depicted by the red parts (or dashed arrows) of Fig. 2.1. In the following, we want to describe the resulting nonlinearly coupling of the extended system in some more detail; the respective equations are summarized in Sec. 2.2.

A realistic treatment of an atmosphere which contains dust also requires the treatment of the phase transition from the gas phase to the solid phase. The solution of the chemical equations yields the particle densities of all species including e.g. molecules and ions, and provides in particular the densities of the species relevant for dust formation. Given the cross sections of the species with respect to the stellar radiation completely determines the opacity of the gas.

From the nucleating species critical clusters can be formed which subsequently grow to macroscopic particles. During the formation and growth process molecules are extracted from the gas phase, which means a strong feedback of the dust on the gas phase chemistry.

An appropriate description of dust growth yields the chemical composition of the dust particles as well as their size distribution function. The interaction of solids and radiation is described by the Mie-theory. Once the monochromatic extinction and scattering cross sections and the size distribution are known the extinction and scattering coefficients (χ_ν^d, s_ν^d) and hence the absorption coefficient κ_ν^d are readily calculated.

These transport coefficients are now used to calculate the thermodynamical structure of the atmosphere which is determined by the propagation of the stellar radiation through the atmosphere. The solution of the equation of radiative transfer yields the value of the monochromatic specific intensity I_ν at every radial position, and hence also the energy flux, i.e. the emergent spectrum of the dustforming object. The energy equation, which describes the energy exchange between the radiation field and the circumstellar material is used to derive a temperature stratification, where of course, conservation of energy is assumed. Since in turn, already the solution of the equation of radiative transfer is based on the knowledge of the temperature structure, the determination of the thermodynamical structure usually results from an iteration between the energy equation and the equation of radiative transfer. The resulting temperature structure essentially influences the dust complex.

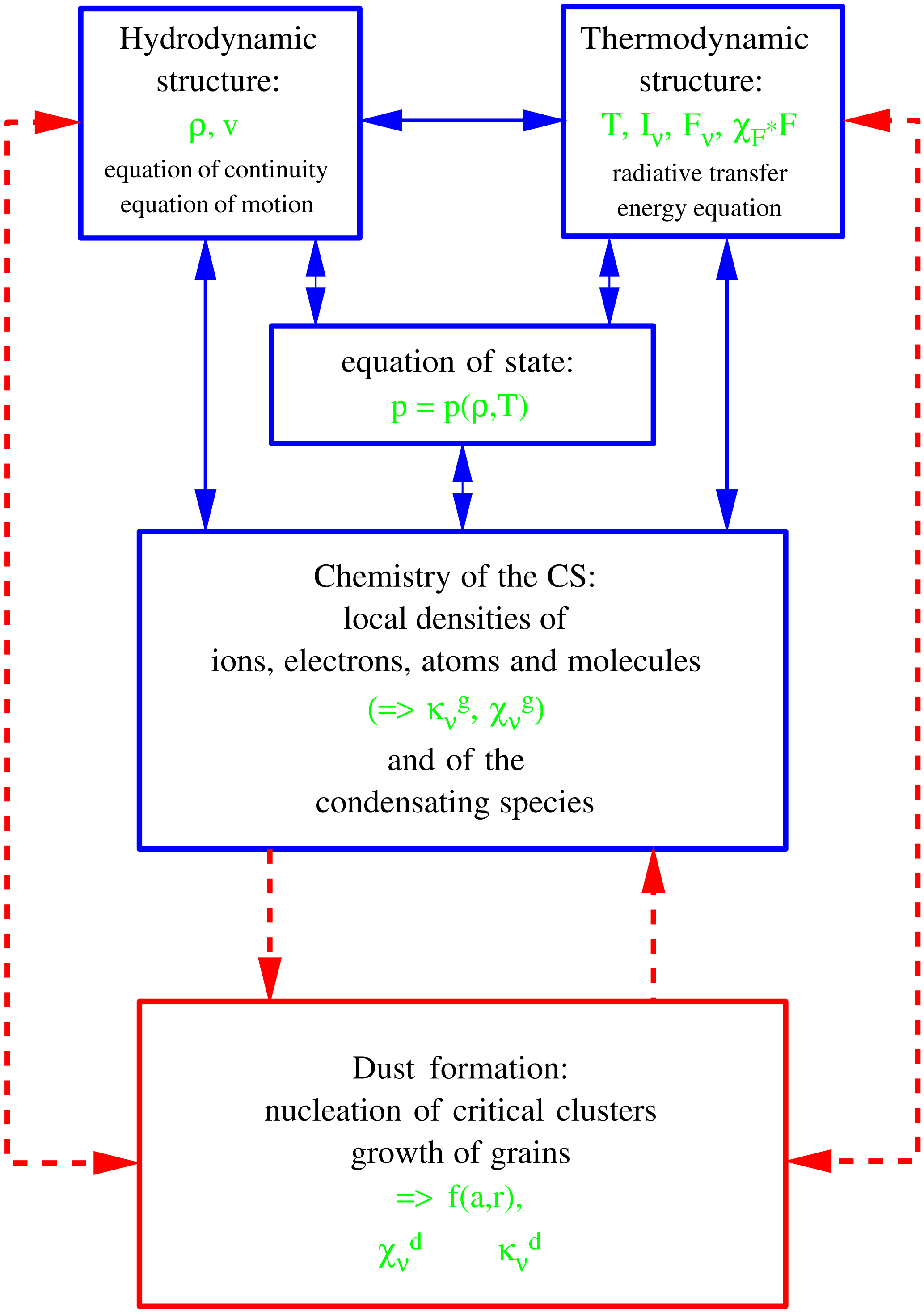

Figure 2.1: The physical problem of a dust forming stellar atmosphere and extension of the classical stellar atmosphere problem, adopted from [WINTERS *et al.* 1994A]

Since the nucleation rate, i.e. the quantity which describes the formation of new dust grains, depends very sensitively on the temperature, the thermodynamical structure determines where and how efficiently new dust grains are formed.

The radiation field also effectively couples to the chemistry of the circumstellar shell. The stellar radiation field is the source of ionization and photodissociation and thereby plays a crucial role in determining the character of the chemistry. For instance, the presence of a strong chromospheric UV–field and oscillations of the gas temperature could cause strong deviations from chemical equilibrium. Furthermore, also the collision rates between the reacting species are a function of the temperature which results in a preference of certain reaction channels in specific temperature regimes.

The radiation pressure, calculated as the product of the extinction coefficient χ of the circumstellar material and the frequency–integrated radiation flux, is the important contribution to the hydrodynamical equation of motion. It will be one result of the present investigation that this term, even in the presence of other energy sources, completely determines the equation of motion and hence the dynamical behaviour of the circumstellar shell.

The density stratification, resulting from the equation of continuity, essential affects the instant of time when new dust is formed and how effectively it subsequently grows. The velocity structure also regulates this growth process since it determines how long the material rests at a certain position in the atmosphere. Furthermore, the velocity limits the dust forming region since it causes a depletion effect in the chemistry and hence a reduced concentration of the dustforming molecules.

It is remarkable that the whole system can be self–consistently solved by the prescription of only four stellar parameters: the stellar luminosity $L_\star$, which describes the radiative energy input of the star, the stellar mass $M_\star$, which describes the gravitational deceleration, the stellar temperature $T_\star$, which is the boundary condition that fixes the temperature stratification, and the element abundances ϵ_i, that describe the initial chemical composition of the gas phase. If energy input, e.g. due to the dissipation of strong shock waves, has to be considered, additional parameters could arise, e.g. the so called piston approximation needs the prescription of the period and the amplitude of the piston, for details see Sec. 2.3 .

2.2 Basic Equations

Firstly, we summarize the basic equations underlying our model calculations. After a short description of the hydrodynamical equations, we give a brief introduction to the theory of dust formation and growth, mainly designated to introduce the basic quantities. This discussion is followed by a short description of our approach to treat the chemistry as well as the radiative transfer problem.

Secondly, we discuss the boundary conditions needed to solve the basic equations.

To start the calculations an initial model is needed. In Section 2.4 the procedure to construct an initial hydrostatic model is described.

The discretized basic equations as well as some technical details concerning time step control, remapping, artificial viscosity etc. are given in Section 2.5.

The procedure to construct the final dynamical models is presented in Section 2.5.3.

2.2.1 Hydrodynamical equations

Motivated by the pioneering work of [Gauger *et al.* 1990], who investigated dust formation, growth, and evaporation in a volume element of gas under time–dependent conditions, we chose the Lagrangian formulation of hydrodynamics for the present model calculations.

In contrast to the field description of the Eulerian approach, the Lagrangian formulation treats the individual paths of an ensemble of small fluid elements, e.g. [Chorin and Marsden 1979]. Thereby, the radial position R of a certain fluid parcel is described as a function of the Lagrangian variable r, such that at an instant of time t_1 we have $R = R(r, t_1)$, and $r = R(r, t_0)$, which denotes the initial or so called reference configuration. Individual fluid elements are distinguished by different Lagrangian variables in the initial configuration. A very convenient way to choose r is e.g. to arrange the initial position of the elements such that each volume element has a unique density ρ_0. In any case we denote by ρ_0 the density distribution of the reference configuration.

The time development along the path of the fluid is governed by the equation

$$\frac{\partial R}{\partial t} = u \quad , \tag{2.1}$$

which simply states, that the larger the fluid velocity u the larger is the change of the radial position of the fluid element.

The *continuity equation* usually is expressed in the Eulerian form as

$$\frac{D\rho}{Dt} + \rho \,\mathrm{div}\, u = 0 \quad , \tag{2.2}$$

where ρ denotes the mass density and $\frac{D}{Dt}$ denotes the material derivate, which is related to the spatial derivative $\frac{\partial}{\partial t}$ via

$$\frac{D}{Dt}(.) = \frac{\partial}{\partial t}(.) + u\, \mathrm{grad}(.) \quad . \tag{2.3}$$

Assuming spherical geometry and multiplying Eq. (2.2) with the Jacobian $J = \frac{R^2 \partial R}{r^2 \partial r}$ of the transformation $r \rightarrow R$, and obeying the property of Jacobians that $DJ/Dt = J \operatorname{div} u$ yields two forms of the equation of continuity in Lagrangian coordinates [Serrin 1959]

$$\frac{D}{Dt}(\rho J) = 0 \; ; \; \rho J = \rho_0 \quad . \tag{2.4}$$

Inserting J in the right hand form yields a very intuitive representation of mass conservation

$$\begin{aligned} \rho R^2 dR &= \rho_0 r^2 dr \qquad \Longleftrightarrow & (2.5)\\ V &= V_0 \left(\frac{R}{r}\right)^2 \frac{\partial R}{\partial r} \quad , & (2.6) \end{aligned}$$

where we have introduced the specific volume $V = 1/\rho$.

In Eulerian notation the *equation of motion* reads

$$\frac{Du}{Dt} = -\frac{1}{\rho} \operatorname{grad} p + \mathcal{F} \quad , \tag{2.7}$$

where $\mathcal{F}$ and p denote an exterior force and the thermal pressure, respectively. Assuming spherical symmetry and taking into account only one spatial dimension Eq. (2.7) can be readily transformed into its Lagrangian form:

$$\begin{aligned} \frac{\partial u}{\partial t} + \left(u \frac{\partial}{\partial R}\right) \frac{\partial R}{\partial t} &= -\frac{1}{\rho} \frac{\partial p}{\partial R} + \mathcal{F} & (2.8)\\ \frac{\partial u}{\partial t} + \left(u \frac{\partial}{\partial t}\right) \frac{\partial R}{\partial R} &\overset{(2.5)}{=} -\frac{1}{\rho_0} \left(\frac{R}{r}\right)^2 \frac{\partial p}{\partial r} + \mathcal{F} & (2.9)\\ \frac{\partial u}{\partial t} &= -V_0 \left(\frac{R}{r}\right)^2 \frac{\partial p}{\partial r} + \mathcal{F} & (2.10) \end{aligned}$$

The exterior forces acting on a fluid element are gravitational deceleration and acceleration due to radiation pressure:

$$\mathcal{F} = -\frac{GM}{R^2} + \frac{4\pi}{c} \frac{\kappa_H}{\rho} H \quad , \tag{2.11}$$

where κ_H denotes the flux weighted mean of the mass extinction coefficient, G the gravitational constant, and c the speed of light. Since the mass contained in the region under consideration, i.e. the circumstellar shell, is small compared to the mass of the star we assume $M = M_\star$. In radiative equilibrium the conservation of the radiative flux H can be expressed as

$$H = H_\star \left(\frac{R_\star}{R}\right)^2 \quad , \tag{2.12}$$

where $R_\star$ is the stellar radius and $H_\star$ is defined as

$$H_\star = \frac{L_\star}{16\pi^2 R_\star^2} \quad , \tag{2.13}$$

and $L_\star$ denotes the stellar luminosity. Inserting Eqs. (2.12) and (2.13) allows to write Eq. (2.11) in a very concise way

$$\mathcal{F} = -\frac{GM_\star}{R^2}(1-\alpha) \quad , \tag{2.14}$$

where

$$\alpha = \alpha_0 \kappa_\mathrm{H}, \tag{2.15}$$

with

$$\alpha_0 = \frac{L_\star}{4\pi c G M_\star} \quad . \tag{2.16}$$

The quantity α is the ratio of radiative to gravitational acceleration. In writing only one equation of motion for the gas–grain mixture, we assume complete momentum coupling between the grains and the surrounding gas. Thus, we end up with the final form of the equation of motion

$$\frac{\partial u}{\partial t} = -V_0 \left(\frac{R}{r}\right)^2 \frac{\partial p}{\partial r} - \frac{GM}{R^2}(1-\alpha) \quad . \tag{2.17}$$

As the *equation of state* of the system we use the ideal gas law

$$pV = \frac{kT_\mathrm{g}}{m_\mathrm{H}\mu} \quad . \tag{2.18}$$

The quantity k is the Boltzmann constant, m_H is the mass of the hydrogen atom, and T_g is the gas temperature. We adopt a constant molecular weight of $\mu = 1.27$, which results from a H/He ratio by number of 10:1 and the assumption that all hydrogen is available in atoms rather than in H_2.

The system of equation is completed by the *gas energy equation*

$$\frac{\partial U}{\partial t} = -\,p\,\frac{\partial V}{\partial t} + Q \quad , \tag{2.19}$$

where U and Q denote the internal energy per unit mass, and the net heating rate, respectively. The quantity Q is the net energy gain of the gas per unit mass and unit time by absorption of radiative energy and by collisions with dust grains.

In most parts of this work we deal only with isothermal processes, in the sense that T_g equals the local radiative equilibrium temperature T_eq (cf. Sec.

2.2.4) at every instant of time throughout the atmosphere. Thus, we treat shocks in the isothermal limit case, i.e. cooling behind shock fronts is assumed to take place instantaneously. Therefore, we list the energy equation mainly for the sake of completeness, since the inclusion of cooling-functions is a subject of current investigations [GAUGER *et al.* 1994A]. As an exception we present some calculations in the adiabatic limit case. Then, $Q = 0$ and Eq. (2.19) together with the equation of state are used to determine the gas temperature stratification, where $U = p/[\rho(\gamma - 1)]$ and an adiabatic index γ of 5/3 are used.

To summarize, we consider a spherically symmetric shell around a pulsating red giant in (most cases) the limit case of isothermal shocks governed by the equations (2.1), (2.6), (2.17), and (2.18),in the case of non–isothermal shocks complemented by Eq. (2.19). The physical input parameters so far are only the stellar mass $M_\star$, effective temperature $T_\star$, and the stellar luminosity $L_\star$. For the treatment of the pulsation we assume the so called piston approximation which is described in Sec. (2.3).

2.2.2 The equations of dust formation, growth, and evaporation

Dust formation, growth, and evaporation are treated by means of a moment method developed by [GAIL AND SEDLMAYR 1988].

Thereby, the moments K_i of the local size distribution function of the dust grains $f(N,t)$ are defined by

$$K_i(N,t) = \sum_{N=N_\mathrm{l}}^{\infty} N^{i/d} f(N,t) \,/\, n_{<\mathrm{H}>}, \tag{2.20}$$

where the number of monomers contained in a dust particle defines the particle size N. N_l is the lower limit size of particles contributing to the size distribution, d is the spatial dimension of the particles and $n_{<\mathrm{H}>}$ denotes the total number of H-atoms per unit volume.

In our calculations we consider spherical particles, i.e. $d = 3$. As scattering is neglected in the radiative transfer the moments only have to be calculated up to $i = 3$, because the highest moment required to determine the absorption coefficient as well as the consumption of the condensable material is the third moment (cf. Eq. (2.42)).

The time evolution of the dust component is described by the following coupled system of equations [GAUGER *et al.* 1990]:

$$\frac{\mathrm{d}K_0}{\mathrm{d}t} = J(N_\mathrm{l},t), \tag{2.21}$$

$$\frac{\mathrm{d}K_i}{\mathrm{d}t} = N_\mathrm{l}^{i/d} J(N_\mathrm{l},t) + \frac{1}{\tau}\frac{i}{d}K_{i-1}, \quad i = 1,2,3 \tag{2.22}$$

The quantities K_0, K_i and J are normated to $n_{<\mathrm{H}>}$ (For simplicity we have omitted "the hat" on these quantities normated to $n_{<\mathrm{H}>}$ in contrast to the notation of [Gauger *et al.* 1990]).

While writing the moment equations in the form of Eqs. (2.21), (2.22) one should bear in mind that this is not the most general system of difference equations describing the time evolution of the i-th moment but already some simplifications and assumptions have been introduced:

- the time evolution for the dust is considered in the region of macroscopic particles, i.e. above a certain lower limit for the particle size N_l, where N_l typically can be chosen between $10^2 \ldots 10^3$. Within this region a thermodynamical treatment of the quantities depending explicitly on the particle size N becomes applicable and allows to determine reliable values of these quantities.

- For particle sizes well above N_l the association or dissociation of an i-mer does not change the particle size distribution $f(N,t)$ too much and it is justified to assume in a certain interval -I, I around N

$$f(N+i,t) \approx f(N,t), \quad -I \leq i < I \ . \tag{2.23}$$

- The temperature of a macroscopic dust grain is solely determined by the equilibrium between the absorption of radiation and thermal reemission at the temperature $T_d(N)$. It can be shown that energy exchange processes between the dust particles and the surrounding gas can be neglected compared to the energy exchange with the radiation field [Gauger *et al.* 1990]. Thus, if the grains are assumed to be sufficiently small such that the absorption efficiency can be calculated in the small particle limit of Mie-theory, the dust temperature T_d becomes independent of the particle size

$$T_d(N) = T_d \ . \tag{2.24}$$

- Furthermore, quantities such as the relative velocities u_{th} due to thermal motion between an i-mer and a macroscopic particle or the averaged sticking efficiency α are assumed to be independent of N.

- It is also assumed that the surface of a dust particle A_N varies with N as

$$A_N = A_1 N^{\frac{d-1}{d}} \ , \tag{2.25}$$

  with a constant A_1 depending on the shape of the (dust) particle.

The source term $J(N_l, t)$ in Eq. (2.21) is given by

$$J(N_l, t) = N_l^{\frac{d-1}{d}} \frac{1}{\tau} f(N_l, t) \ . \tag{2.26}$$

and will be discussed in some detail below.
The quantity $1/\tau$ appearing in the Eqs. (2.22) and (2.26) is the number of monomers per second, per dust particle and per monomer surface on the dust particle, which are associated onto or dissociated from the dust particle

$$\begin{aligned} \frac{1}{\tau} &= \sum_{i=1}^{I} i A_1 u_{th}(i) \alpha(i) f(i,t) \left\{ 1 - \frac{1}{S^i} \frac{1}{b^i} \alpha_\star(i) \right\} \\ &+ \sum_{i=1}^{I'} i A_1 \sum_{m=1}^{M_i} u_{th}(i,m) \alpha_m^c(i) n_{i,m} \left\{ 1 - \frac{1}{S^i} \frac{1}{b_{i,m}^c} \alpha_\star^c(i,m) \right\} \ . \end{aligned} \tag{2.27}$$

Thereby, we have introduced the following quantities:

- S, the supersaturation ratio, defined by

$$S = \frac{p(1)}{p_V(1)} \ , \tag{2.28}$$

  the ratio of the actual partial pressure of monomers of the condensing species in the gas phase $p(1)$ to the vapor saturation pressure with respect to the dust temperature $p_V(1)$.

- $b_i, b_{i,m}^c$ generalized departure coefficients. They describe departures of the actual particle densities of the i-mers due to chemical and thermodynamical non-equilibrium between the solid phase and the gas phase or due to chemical reactions, respectively.

- $\alpha_\star$ comprises non-TE effects caused by a non-TE population of states of the i-mers *or* by a TE-population of states of the i-mers with an excitation temperature different from T_d *or* by the difference of the thermal velocities of the particles at the dust temperature and the actual gas-kinetic temperature.

- $\alpha_\star^c$ comprises non-TE effects caused by deviations from a TE-population of states of the reacting molecules in the forward and backward direction.

The net growth rate can be divided into two parts

$$\frac{1}{\tau} = \frac{1}{\tau_{\rm gr}} - \frac{1}{\tau_{\rm ev}}, \tag{2.29}$$

with $1/\tau_{\rm gr}$ being the growth rate, i.e. the number of monomers which are associated to a dust particle per unit time and unit surface, and $1/\tau_{\rm ev}$ is the corresponding evaporation rate, i.e. the number of monomers which are dissociated.

According to the sign of $1/\tau$ the quantity $J(N_{\rm l},t)$ denotes the local rate of formation and destruction of dust particles at size $N_{\rm l}$, respectively.
For $1/\tau_{\rm gr} > 1/\tau_{\rm ev}$ Eqs. (2.21) and (2.22) describe grain nucleation and growth. Since condensation at sizes $N < N_{\rm l}$ can be considered as a stationary process for conditions typical in circumstellar shells [Gail and Sedlmayr 1988] the rate of formation $J(N_l,t)$ at any time t is equal to a constant value $J_\star$, the stationary nucleation rate, which is determined from classical nucleation theory according to the set of equations given in [Gail *et al.* 1984], cf. also below.

For $1/\tau_{\rm gr} < 1/\tau_{\rm ev}$ Eq. (2.29) yields a negative net "growth rate". In this case Eqs. (2.21) and (2.22) describe dust destruction due to thermal evaporation and chemical sputtering. Then $J(N_{\rm l},t)$ is the destruction rate of the dust particles which depends on the actual value of the grain size distribution function at the lower size limit $N_{\rm l}$.

In order to obtain an expression for $f(N_{\rm l},t)$ it is advantageous to introduce the dimensionless particle radius [Gauger *et al.* 1990]

$$\tilde{a} = N^{1/d} \tag{2.30}$$

and the function

$$g(t) = J_\star(t)\,\tau(t)\,d. \tag{2.31}$$

Since the time evolution of N is simply given by

$$\frac{{\rm d}N}{{\rm d}t} = \frac{1}{\tau}\,N^{\frac{d-1}{d}}. \tag{2.32}$$

it follows with Eq. (2.30)

$$\frac{{\rm d}\tilde{a}(t)}{{\rm d}t} = \frac{1}{\tau\, d}\ . \tag{2.33}$$

The net rate does not depend on $\tilde{a}$, thus the change of $\tilde{a}$ is the same for all dust particles independent of their size. Since $\tilde{a}$ is a uniquely determined function of t, the independent variable t can be substituted by $\tilde{a}$. It is an important result of Gauger et al. that the actual value of the size distribution function $f(\tilde{a}_{\rm l},t)$ during a phase of evaporation is given by the value of the function g for the actual maximum particle radius, i.e. $g(\tilde{a}_{\rm max})|_{\tilde{a}_{\rm max}(t)}$. Then the destruction rate is determined by

$$J(N_{\rm l},t) = \frac{1}{\tau\, d}\,g(\tilde{a}_{\rm max})|_{\tilde{a}_{\rm max}(t)}. \tag{2.34}$$

Hence, if the moment equations, Eqs. (2.21) and (2.22), are supplemented by Eq. (2.33) written for the change of $\tilde{a}_{\rm max}$, cf. [Gauger *et al.* 1990], and the definition (2.31) of the function g, the values of the moments during evaporation are always known once nucleation and growth have been calculated.

This generalized system of moment equations does include dust destruction due to thermal evaporation and chemical sputtering which might be important destruction mechanisms for dust grains in CDS around LPVs. In addition, it provides us with the knowledge of the size distribution function of the dust particles at every site in the atmosphere and at every instant of time. For further details see [Dominik *et al.* 1989] and [Gauger *et al.* 1990].

The moments defined by Eq. (2.20) are closely related to important dust properties cf. [Gail *et al.* 1984], which will be used frequently in the discussion of our results in the next section:

a) $n_{\rm d}/n_{<{\rm H}>} = K_0$ is the number of dust particles per H-atom,

b) $f_{\rm c} = K_3 \,/\, n_{cond}$ is the degree of condensation, i.e. the amount of material actually condensed into grains divided by the number density of condensable material in the pure gas phase,

c) $r_{\rm m} = a_0\, K_1/K_0$ is the mean particle radius, where a_0 is the (hypothetical) radius of a monomer constituting the solid particle. In the present case a_0 is assumed to be $a_0 = 1.28\,10^{-8}$cm, cf. [Gail *et al.* 1984].

The nucleation rate $J_\star(t)$: A crucial ingredient to the procedure described above is the source term $J(N_l, t)$, such that a few remarks concerning the calculation of this term seem to be appropriate. For a recent review of the processes that lead from molecules to grains see [Sedlmayr 1994].

Basically, there are two distinct approaches to deal with the problem of formation of clusters from the gas phase:

a) The so called "classical nucleation theory" describes the formation of critical nuclei in a supersaturated vapor by means of thermodynamical quantities. In this approach it is assumed that the clusters in the nucleation regime can be conceived as small solid particles whose properties can be calculated by

- **i)** the extrapolation of the bulk properties even into the domain of very small clusters,
- **ii)** the interpolation of the thermodynamic properties between those of molecules and those of solid particles, e.g. [Draine and Salpeter 1977, Draine 1979].

Once the material properties are known, the evolution in the discrete cluster space can be described by means of a master equation for the cluster size distribution function [Gail *et al.* 1984, Gail and Sedlmayr 1988]. Furthermore we can distinguish between different clustering mechanisms. The *homomolecular homogeneous nucleation* describes the formation of chemically homogeneous clusters by the condensation of molecules of one type, e.g. the formation of SiO or Fe to the respective clusters in the winds of M–stars. *Heteromolecular homogeneous nucleation* describes the formation of homogeneous clusters by reaction of various contributing molecules, i.e. the condensation of amorphous carbon clusters by the contribution of carbon–bearing compounds such as C_N, C_2H, C_2H_2, ..., etc. Also under the consideration of non–equilibrium effects the nucleation rate for heteromolecular homogeneous condensation can be readily calculated within the framework of classical nucleation theory [Gail and Sedlmayr 1988, Gauger *et al.* 1990]. We use this approach for the present investigation with the respective data given in [Gail *et al.* 1984].

b) The *chemical pathway method* aims to describe the transition from molecules to grains by the construction of a realistic reaction chain. As a purely microscopic approach this method is freightened with the necessity of knowing the relevant reaction steps and furthermore the respective input data describing these steps. Since in principle the reaction network can be made arbitrarily complex it is a difficult task to define an upper limit size of the network which on the one hand ensures to describe the chemical situation in a reliable manner and on the other hand is still numerically treatable. Attempts of reduction have been undertaken by [Cherchneff *et al.* 1991, Cherchneff and Barker 1992, Cherchneff *et al.* 1992, Cherchneff *et al.* 1993] with the so called *lumping* procedure, where the network is artificially reduced by the fusion of similar reaction channels. Unfortunately, truncated networks seem to overestimate the nucleation rate. An alternative method is aimed to find the most efficient reaction in the network, i.e. the one, which provides the shortest travel time in the N–cluster space for a small molecule to develop into the growth regime, and thus essentially dominates the nucleation rate. Based on this approach [Keller 1987, Gail and Sedlmayr 1987a, Goeres 1993] have described the carbon nucleation in C–stars by a chemical pathway, which starts with the most abundant condensable species, acetylene, and leads by a series of polycyclic aromatic hydrocarbons (PAHs) to macroscopic structure of flat or curved geometry. Unfortunately, these pathways are still under investigation and we can only present a test calculation with a rather preliminary version [Keller 1987] of the nucleation rate, cf. also Secs. 8.3.1 and 8.3.2.

Despite considerable shortcomings of the classical nucleation theory (e.g. clusters are treated as macroscopic systems, the application of the surface tension concept, the geometrical shape is restricted to spherical particles, cf. [Sedlmayr 1989] for details) it is and will be frequently used in astrophysics until reliable data are available that allow the application of the chemical pathway concept in consistent model calculations.

2.2.3 The chemistry of the gas phase

For the calculation of the nucleation rate $J_\star$ and the net rate $1/\tau$ it is necessary to know the chemical composition of the gas phase. Since we want to consider C–stars in the present paper we use the same reduced set of hydrocarbons in chemical equilibrium, containing H, H_2, C, C_2, C_2H, C_2H_2 as described in detail in [Gauger *et al.* 1990] to calculate the particle densities of the species contributing to the growth of carbon grains, i.e. every reaction is balanced by its own reverse reaction.

Assuming chemical equilibrium the concentrations become independent of time, i.e. of the previous conditions, and therefore are functions of the temperature T, the density $n_{<H>}$, and of the chemical abundances ϵ_i relative to hydrogen of the elements only. Since we have also assumed that the ideal gas law holds as the equation of state for the system, the assumption of chemical equilibrium leads the law of mass action:

Consider the following general reaction:

$$E^1_{e_{l,1}} + E^2_{e_{l,2}} + \ldots + E^J_{e_{l,J}} \longrightarrow E^1_{e_{l,1}} E^2_{e_{l,2}} \cdots E^J_{e_{l,J}} \quad , \tag{2.35}$$

where from the constituents $E^1, E^2, \ldots, E^J$ a molecule M_l with the chemical formula $E^1_{e_{l,1}} E^2_{e_{l,2}} \cdots E^J_{e_{l,J}}$ is formed. The superscript labels the elements, e.g. $E^1 = H$, $E^2 = C$, $e_{l,j}$ gives the number that describes how many constituents of species E^j are contributed to the l–th molecule. The partial pressure of a molecule M_l with the chemical compounds $E^1 \cdots E^J$ is given by

$$\overset{\circ}{p}_{M_l} = \kappa_{M_l} \prod_{j=1}^{J} \left(\overset{\circ}{p}_j\right)^{e_{l,j}} \quad , \tag{2.36}$$

where

$$\kappa_{M_l} = \exp\left\{-\frac{\Delta G_l}{kT}\right\} \tag{2.37}$$

is the dissociation constant, described by the Gibbs energy (free enthalpy) difference ΔG_l between molecule and constituting elements. Without nuclear reactions the total number of every species is a constant in a closed system and we can write the conservation law, which is the so called mass action law:

$$\sum_{l=1}^{L} e_{l,j} \, \overset{\circ}{p}_{M_l} = \sum_{l=1}^{L} e_{l,j} \kappa_{M_l} \prod_{j=1}^{J} \left(\overset{\circ}{p}_j\right)^{e_{l,j}} = \epsilon_j n_{<H>} kT \quad , \tag{2.38}$$

where L denotes the maximum number of molecules present, cf. also [Dominik 1992].

The so described general case yields a system of J equations for the partial pressure of the atoms of the L elements. The solution of the general case with a large number of molecules is done with Newton–Raphson iteration, e.g. [Gail and Sedlmayr 1987a], but could be rather time consuming. Under certain conditions it is possible to decouple the equations and solve them analytically [Gail and Sedlmayr 1987a, Dominik 1992].

For the present case with $J = 2$ the system reduces to the solution of two quadratic equations. If we would take into account molecules containing C_3 it would result in the solution of a cubic equation and could also be done analytically. C_3H is, besides C_2H and C_2H_2, the third abundant molecule by number. Thus, the neglect of C_3H as a molecule contributing to the nucleation rate leads to an underestimation of $J_\star$.

We assume solar abundances, cf. [Allen 1973], for all elements except for the abundance of carbon $\epsilon_{\rm C}$ which we consider as a free model parameter in order to account for a carbon rich element composition ($\epsilon_{\rm C} > \epsilon_{\rm O}$).

2.2.4 The radiative transfer problem

The radiative transfer problem is treated with the semi-analytical method of [Lucy 1976] appropriate for extended stellar atmospheres, which is based on his procedure to close the moment equations of the radiation field [Lucy 1971] and yields an expression for the temperature structure in radiative equilibrium.

The key idea of Lucy was to split the monochromatic specific intensity into two contributions. At a certain distance r from the star one part, I^+, comprises the part of the radiation field that emerges directly from the angle under which the photosphere is seen, whereas the other part, I^-, comprises the rest of the solid angle, i.e. the contribution that results from scattering and emission outside the photosphere. He further assumes that I^+ and I^- are a function of r only, and that they are independent of the angle. With so defined specific intensity the moments can be expressed in terms that are linear in $I^+ + I^-$ and $I^+ - I^-$. These expressions can be eliminated from the equations for the first two moments (in Eddington variables J and H) and an expression for the third moment is gained, which closes the coupled system and equals the known Eddington-approximation for $r = R_\star$.

Further assuming radiative equilibrium, the moment equations can be integrated analytically and the local radiative equilibrium temperature $T_{\rm eq}$ is determined by

$$T_{\rm eq}^4(r) = T_\star^4 \left(W + \frac{3}{4}\tau_{\rm L} \right) , \tag{2.39}$$

where the geometrical dilution factor

$$W = \frac{1}{2}\left(1 - \sqrt{1 - \left(\frac{R_\star}{r}\right)^2}\right) \tag{2.40}$$

and the modified optical depth

$$\tau_{\rm L}(r) = -\int_\infty^r \left(\frac{R_\star}{r'}\right)^2 \kappa_H\, \rho dr' \quad \text{, with } \tau_{\rm L}(\infty) = 0 \ . \tag{2.41}$$

Thereby, and also further, we assume that the gas–dust mixture absorbs grey, i.e. the respective coefficient weighted by the mean intensity equals that weighted by the Planck function B_ν, $\kappa_J = \kappa_B$. Otherwise Eq. (2.39) would have to be supplemented by an additional factor κ_B/κ_J (where the respective scattering coefficients cancel due to the assumption of radiative equilibrium).

The general form of Eq. (2.41) contains the flux–weighted extinction coefficient χ_H instead of the absorption mean κ_H. However, due to the following assumptions it is justified to neglect scattering.

The mean mass absorption coefficient κ_H is the sum of the dust opacity $\kappa_{\rm d}$ and of the gas opacity $\kappa_{\rm g}$. The gas opacity is assumed to be constant throughout the atmosphere and a value of $\kappa_{\rm g} = 2\,10^{-4}{\rm cm}^2{\rm g}^{-1}$ is taken which is based on the calculation of Rosseland mean opacities of [Alexander *et al.* 1983] (cf. [Bowen 1988a] for a further discussion of this assumption).

For the calculation of the extinction coefficient of the dust $\kappa_{\rm d}$ we assume the size of the grains to be small compared to the mean wavelength of the radiation field, cf. [Dominik *et al.* 1989]. Thus, we can calculate $\kappa_{\rm d}$ in the small particle limit of Mie theory according to the equation given in [Gail and Sedlmayr 1987b]

$$\kappa_{\rm d} = \frac{3}{4} V_0 K_3 Q'(T) \ , \tag{2.42}$$

where V_0 denotes the volume per monomer of the grains and $Q'(T)$ is the extinction efficiency of the grain material divided by the grain radius [Lucy 1976].

For simplicity we replace the flux weighted mean absorption coefficient κ_H by its Rosseland mean κ_R. We use the extinction data of amorphous carbon condensates measured by [Koike *et al.* 1980]. Using these data according to [Gail and Sedlmayr 1985] the temperature dependence of the Rosseland mean can be approximated by

$$Q'(T) \approx Q'_R = 5.9T \ . \tag{2.43}$$

2.3 Boundary conditions

Our model is determined by Eqs. (2.1), (2.6), (2.17), (2.18), (2.21),(2.22),(2.33), and (2.39), which are subject to the following boundary conditions:

a) The radius of the inner boundary $R_{\rm inner}$, located a few scale heights below the photosphere, is assumed to vary sinusoidally with time

$$R_{\rm inner} = R_0 + \Delta u \, \frac{P}{2\pi} \, \sin\left(\frac{2\pi}{P}\, t\right) \quad . \tag{2.44}$$

Therefore, it follows from Eq. (2.1) that

b) the velocity at the inner boundary $u_{\rm inner}$ varies like

$$u_{\rm inner} = \Delta u \cos\left(\frac{2\pi}{P} t\right) \quad . \tag{2.45}$$

The velocity amplitude Δu, which simulates the interior pulsation of the star, as well as the pulsation period P are input parameters. At time $t = n\,P$ $(n = 0, 1, 2, \ldots)$ according to Eq. (2.44) the inner boundary (the "piston") takes its initial position R_0 and according to Eq. (2.45) moves outwards with maximum velocity Δu. We define these instant of time as *phase zero of the pulsation cycle* or as the beginning of the hydrodynamical cycle, respectively.

c) The discretization scheme requires a fictitious value of the pressure variable p^{n+1}_{jmax} for the zone beyond the outer boundary j_{max}, cf. [Richtmyer and Morton 1967]. The subscript j of the discretized quantities refers to the spatial grid and the superscript n to the discrete time variable. If rezoning is not necessary we apply the constant gradient condition: $p^{n+1}_{jmax}/p^{n+1}_{jmax-1} = p^{n}_{jmax}/p^{n}_{jmax-1}$, for calculating the value of p^{n+1}_{jmax}. Otherwise the grid has evolved beyond the prescribed radius of the outer boundary and we use the calculated pressure for this zone beyond j_{max}, cf. Sect. 2.5.1.

Instead of prescribing a fictitious pressure at the outer boundary, alternatively the so called free boundary condition can be used [Mihalas and Weibel Mihalas 1984], p.279, where $u^n_{jmax} = u^n_{jmax-1}$, since to fictitious pressure is only needed to calculated the velocity of the outer boundary.

d) For consistency we require $T(R_\star) = T_\star$ which results in the boundary condition of Eq. (2.41)

$$\tau_{\rm L}(R_\star) = \frac{2}{3} \quad . \tag{2.46}$$

This condition defines the photospheric radius $R_\star$.

e) The moment equations for the dust component are solved subject to the following initial conditions. The initial hydrostatic model is dust free. In principle, condensation becomes possible if the supersaturation ratio S, defined as the ratio of the partial pressure of carbon atoms in the gas phase divided by the vapour pressure of solid carbon, exceeds unity. However, the onset of relevant condensation requires that S exceeds some critical value S_c. Therefore we start the calculation of dust formation with the moment equations within a certain dust free mass shell when $S \geq S_c$ in this shell. A value of $S_c = 3$ has been adopted for our calculations [Draine and Salpeter 1977].

2.4 The initial hydrostatic model

To start the calculations an initial stratification of the hydrodynamical quantities is needed. This initial model is dust–free. We start most of all calculations from an initially *hydrostatic* model. To avoid spurious effects in the beginning it is absolutely necessary to solve the hydrostatic equations in the identical discrete form as the hydrodynamical equations in the dynamical code. Inserting the hydrostatic model into the dynamical code and integrating in time (without dust and piston approximation) should conserve the hydrostatic state.

Due to the assumption of a constant gas opacity and a constant mean molecular weight the construction of the hydrostatic model reduces to the solution of an initial value problem. Specifying $M_\star$, $T_\star$, $R_\star$ (or instead of $R_\star$, $L_\star$) immediately yields the values of p and ρ at $R_\star$. Assuming $\tau(R_\star) = 2/3$, $\tau(r \to \infty) = 0$, and $p(r \to \infty) = 0$ and applying the finite difference scheme according to [Richtmyer and Morton 1967] for the dimensionless variables yields $\tau_{j+1/2} = p_{j+1/2}$ and an implicit equation for the pressure. Once the p–structure is known also the temperature stratification can be calculated immediately. The integration is performed on an equidistant spatial grid.

The generalization of the scheme presented above, to non–constant gas opacities, can easily be done, cf. [Gauger *et al.* 1994a], but is omitted here.

2.5 The numerical method and some technical details

2.5.1 The numerical method

The equations of hydrodynamics (2.1), (2.6), (2.17), (2.18), and the Eqs. (2.21), (2.22) and (2.33) describing dust formation, growth and evaporation and the temperature equation (2.39) are written in standard finite difference form on a staggered mesh and solved by explicit integration analogous to the scheme given in [Richtmyer and Morton 1967], p.318. In the case of the moment equations this is readily done since they have the form of continuity equations with source functions. This 1^{st} order accurate scheme, given in [Richtmyer and Morton 1967], is referred to as an *upwind* scheme, since the determination of a quantity A_j^{n+1} uses information from an upwind node $(n, j-1)$. In the present form it can readily be changed to a *leapfrog* in time scheme, cf. [Mihalas and Weibel Mihalas 1984, Fletcher 1991], which is of higher accuracy, but has not turned out to change the results in any way.

Shock fronts are broadened using the artificial tensor-viscosity of [Tscharnuter and Winkler 1979]. This is a generalisation of the classical v.Neumann–Richtmyer viscosity. It is still frequently used, e.g. [Bowen 1988a], and can be optionally included to allow a comparison with results from the literature. The basic idea of v.Neumann–Richtmyer was to introduce a dissipative mechanism which prohibits the overtaking of the zones behind the shock and provides a smooth transition from the quantities behind the shock front to the quantities in front of the shock over an radial interval of only a few grid zones. Thus, shocks show up as quasi–discontinuities which nearly fulfil the Rankine–Hugoniot conditions and travel approximately at the right speed. In contrast, exact methods to treat shock fronts, e.g. shock–fitting [Richtmyer and Morton 1967], turn out to be rather feasible for realistic physical situations.

To provide stability of the code and to insure a sufficiently fine-grained modelling we have to choose a properly determined time step Δt. In order to achieve an appropriate temporal resolution for the various processes, which underly different time-scales, at each time level t the minimum of the values calculated from the following criteria is taken as the new time step Δt:

a) $\Delta t = P/200$. This criterion provides the minimum number of time-steps per period.

b) $\Delta t = [\delta \Delta r / c_s]$, where c_s is the local sound velocity and Δr is the thickness of the mesh zone. This is the well-known Courant-Friedrichs-Levy (CFL) condition. In our case the CFL-factor δ is typically of the order of 10^{-2}.

c) Δt has to be chosen such that the temporal change of the relative specific volume $(\Delta V/V)$ is always smaller than 0.2.

d) Δt has be to sufficiently small, such that the change of a certain dust quantity q within a time step is limited to a certain fraction of its actual value
$$q^{n+1} - q^n \leq \epsilon_{\rm rel} q^n \ .$$
This criterion is necessary to guarantee an accurate calculation of the dust complex. It is of particular importance for the time evolution of the grain density, the degree of condensation and of the maximum particle radius. The application of this criterion to the maximum particle radius ensures an

accurate storage of the particle size distribution function during the phase of dust formation and growth, which according to Sect. 2.2.2 is necessary for calculating evaporation. In our calculation a value of $\epsilon_{\rm rel} = 0.1$ has turned out to be reasonable.

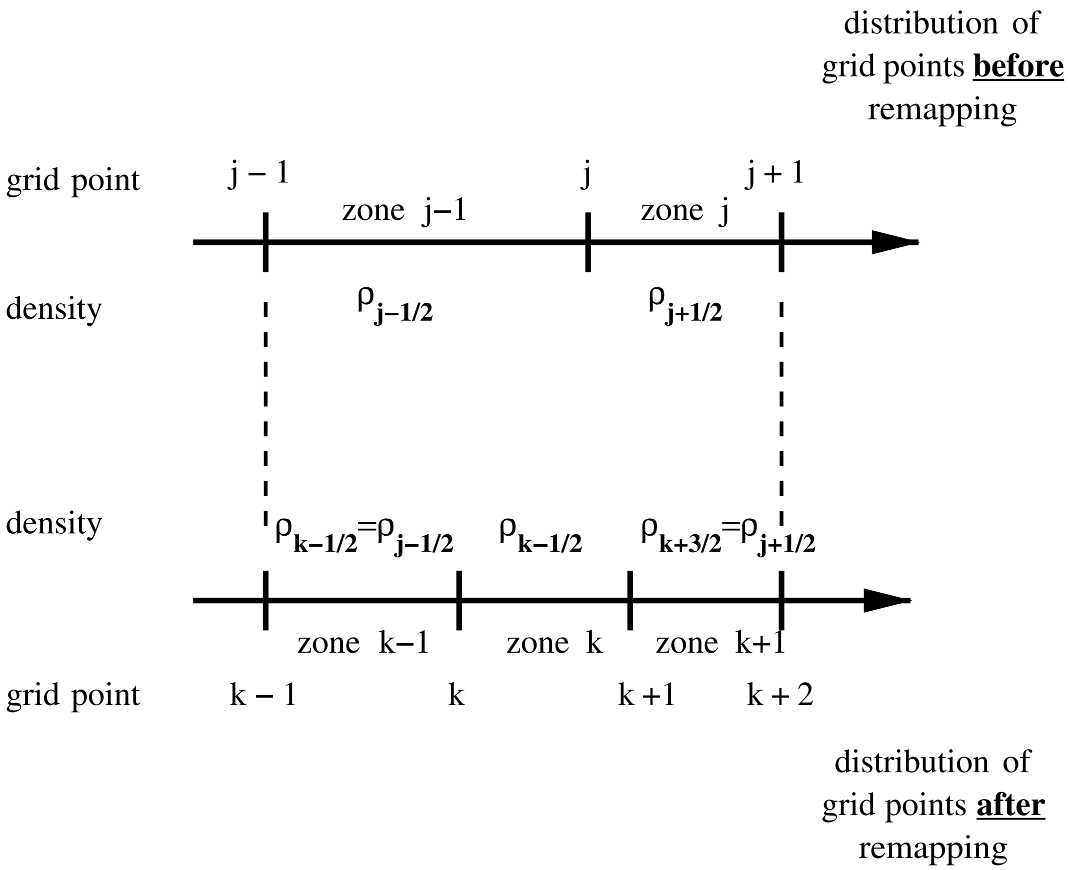

Figure 2.2: Insertion of new grid points during rezoning. For the definition of the density $\rho_k$in the new zone (k) see text

---

2.5.2 The rezoning scheme

To keep a sufficiently fine resolution of the radial grid our numerical scheme requires rezoning or remapping, i.e. the insertion of grid points where the width of the Lagrangian zones has become too large.

We have developed a rezoning procedure which, in principle, ensures the conservation of *all* physical quantities in the zone to be divided and avoids artificial oscillations of the redistributed grid. Since this remapping procedure is essential for the modelling we describe in some detail how the new Lagrangian grid points are determined and, as an example, which mass densities are assigned to the new zones. The basic idea is outlined in Fig. 2.2. If the zone $(j-1)$, i.e. the mass shell between the grid point R_{j-1} and the grid point R_j, has become too large, a new zone is introduced by removing the grid point R_j and by inserting two new grid points R_k and R_{k+1}. From the requirement of mass conservation the sum of the masses of the two old zones M_{j-1}^{j} is equal to the sum of the masses of the three new zones. Thus, we get the following equation

$$
\begin{aligned}
M_{j-1}^{j} &= \rho_{j-1/2}(R_j^3 - R_{j-1}^3) + \rho_{j+1/2}(R_{j+1}^3 - R_j^3) \\
&= \rho_{k-1/2}(R_k^3 - R_{k-1}^3) + \rho_{k+1/2}(R_{k+1}^3 - R_k^3) \\
&\quad + \rho_{k+3/2}(R_{k+2}^3 - R_{k+1}^3) \quad .
\end{aligned}
$$

The volume of the three new zones is determined according to

$$
\begin{aligned}
(R_k^3 - R_{k-1}^3) &= \frac{2}{3}(R_j^3 - R_{j-1}^3) \\
(R_{k+1}^3 - R_k^3) &= \frac{1}{3}(R_j^3 - R_{j-1}^3) + \frac{1}{3}(R_{j+1}^3 - R_j^3) \\
(R_{k+2}^3 - R_{k+1}^3) &= \frac{2}{3}(R_{j+1}^3 - R_j^3) \quad .
\end{aligned}
$$

Together with the conditions

$$
\begin{aligned}
\rho_{k-1/2} &= \rho_{j-1/2} \\
\rho_{k+3/2} &= \rho_{j+1/2} \\
R_{k-1} &= R_{j-1} \\
R_{k+2} &= R_{j+1}
\end{aligned}
$$

we get after some algebra the equations for the new zone boundaries and the corresponding density

$$
R_k = \left(\frac{2}{3}R_j^3 + \frac{1}{3}R_{j-1}^3\right)^{1/3} \tag{2.47}
$$

$$
R_{k+1} = \left(\frac{2}{3}R_j^3 + \frac{1}{3}R_{j+1}^3\right)^{1/3} \tag{2.48}
$$

$$
\rho_{k+1/2} = \frac{\rho_{j-1/2}(R_j^3 - R_{j-1}^3) + \rho_{j+1/2}(R_{j+1}^3 - R_j^3)}{R_{j+1}^3 - R_{j-1}^3} \quad . \tag{2.49}
$$

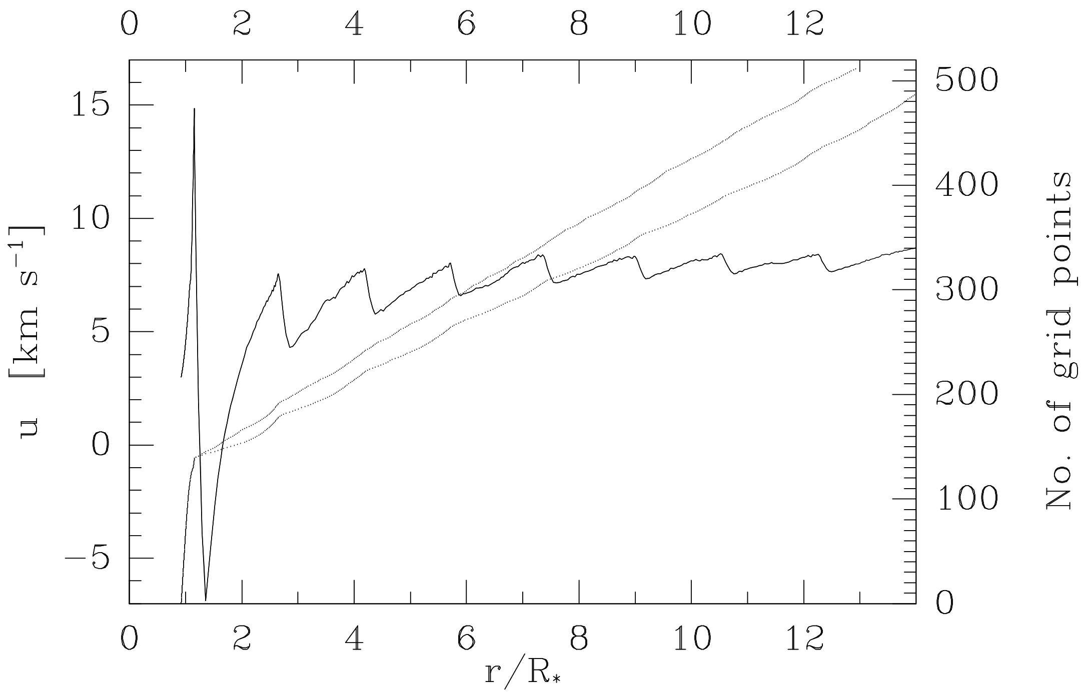

Figure 2.3: The resultant radial velocity structure and distribution of grid points before and after rezoning for a typical model calculation

---

This scheme is also applied to the conservation of the internal energy of the gas, which yields new values for the temperature and the pressure, to the conservation of the number of dust particles and to the amount of dust, which yields new values for the moments. In principle, this scheme could also be applied to the conservation of kinetic energy in order to determine the new velocities of the boundaries of the various zones, but it turned out that this induces numerical instabilities. Instead, we apply a linear interpolation for the velocities.

Since the total number of zones per model is held constant, the number of zones to be inserted is determined by the number of zones that have moved across a certain outer boundary, which usually is assumed to be situated between $15 - 20R_{\star}$. Then, the zone with maximal thickness is determined, the first zone is inserted and the physical quantities in this zone are calculated as described above. The zone with maximal thickness is redetermined and the next zone is inserted, this procedure is repeated until all grid points that moved across the outer boundary have been redistributed. The remapping procedure is performed twice each hydrodynamical cycle to maintain the desired resolution.

The resulting distribution of the grid points before and after applying the remapping scheme is depicted in Fig. 2.3. The r.h.s. ordinate shows the number of grid points. In this case, the individual data points are not connected by a line but are marked as dots. The upper distribution, of course, shows the grid points *after* the rezoning procedure. In addition, we have also shown the course of the velocity before and after rezoning. A difference can hardly be seen. Before the remapping the grid points are concentrated behind the shock front. After rezoning, the distribution of the grid points is almost linear in the outer layer and the number of points in the innermost region, where strongly varying dynamics occurs, is increased to ensure a sufficient resolution. The remapping procedure works stable and without spurious effects.

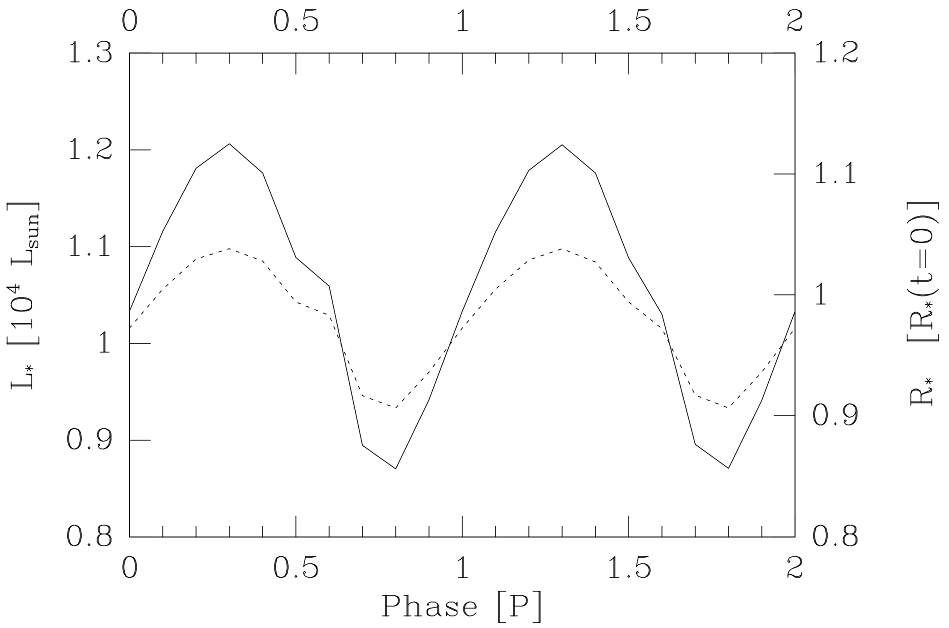

Figure 2.4: Time development of the stellar luminosity in units of the solar luminosity and the stellar radius in units of the stellar radius of the initial hydrostatic model, shown for Model E, cf. Table 4.1

2.5.3 The modelling procedure

Our dynamical models are produced as follows.

1. For given stellar parameters $(M_\star, R_\star, T_\star, \epsilon_i)$ or $(M_\star, L_\star, T_\star, \epsilon_i)$ a static initial model with a selected number of grid points (usually 512) is constructed. This is done by integrating Eq. (2.17) where the time derivative is set zero. If an initial stellar radius is to be prescribed, it is calculated from a

period-mass-radius relation

$$\log P_0 = -1.92 - 0.73 \log M_\star + 1.86 \log R_\star \tag{2.50}$$

cf. [Ostlie and Cox 1986], where P_0 stands for the fundamental mode pulsation period and equals our P. Then $L_\star$ is derived from Eq. (2.51). If $L_\star$ is chosen as initial parameter, $R_\star$ is calculated with Eq. (2.51).

2. The velocity amplitude of the piston is increased *slowly*, see p.36 Eq. (2.45), to the specified maximum value in order to avoid the destruction of the model by the first wave which moves into the exponential density gradient and therefore would steepen into an enormous shock wave. The calculation of dust formation and growth is started simultaneously.

3. The time development of the model is followed until a cyclic radial profile of all quantities is produced.

For certain model parameters the calculation of the dust component cannot be started under static conditions due to numerical reasons. In these cases step 2 has to be replaced by step 2'.

2'. A model with an assumed radiation pressure on dust grains is constructed, cf. [Bowen 1988a], because it is numerically easier to start the dust calculation within a levitated density structure. At first, the back reaction of the dust complex on the hydrodynamical quantities is taken into account in the schematic way proposed by [Bowen 1988a]. Then, the effective radiative acceleration on the grains is shifted slowly from the assumed value to the one that follows from the detailed treatment of the dust complex until full coupling to the hydrodynamical equations is realized.

Of course, those models, which can be calculated either with step 2 or with 2', show identical results.

During the calculation the effective temperature $T_\star$ is held constant and the stellar radius $R_\star$ is recalculated within each time step from Eq. (2.41) by the requirement $\tau_{\rm L}(R_\star) = 2/3$. Thereby, a new temperature structure is determined. Then the luminosity is determined by the equation

$$L_\star = 4\pi R_\star^2 \sigma T_\star^4 \ , \tag{2.51}$$

where σ is the Stefan-Boltzmann constant. The resulting time development of the stellar luminosity and of the stellar radius due to the variation at the inner boundary are shown in Fig. 2.4 for model E, cf. Table 4.1 in Sect. 4.2. The dips in the structure of the stellar radius and the luminosity at $t = 0.6P$ and $t = 1.6P$ are caused by the formation of a new discrete dust layer at these instants which is discussed in detail in the Chapter. 4.

Summarizing, the adopted numerical method for the developed code turns out to be suitable for addressing the problems under consideration. The method is simple and stable enough to allow a reasonable time of code development. Furthermore, the method is flexible to enough to exchange certain routines, thus, e.g. allows readily the implementation of an improved routine for the nucleation rate, i.e. the improvement of the input physics can readily be done. Since we start with an initial hydrostatic model, there is always an initial (on–set) phase of relaxation until the final solution is reached. It typically lasts 30 P, were $P = 650d$, with at least 10^4 time steps per P. Although, this phase consumes a large amount of computing time, the flexibility of this numerical method outweighs this disadvantage.

Furthermore, the explicit upwind scheme, although it is "classical", turns out to be accurate enough to address the nonlinear, dynamical problems. This is shown by a detailed comparison with the sophisticated radiation hydrodynamics code of the Vienna group [Dorfi and Höfner 1991, Höfner and Dorfi 1992, Feuchtinger *et al.* 1993]. They discretize the conservation form of the differential equations time centered and first order in space for a freely moving coordinate system. The adaptive grid technique [Dorfi and Drury 1987] requires to take into account the solution of a grid equation, which ensures a proper distribution of the grid points. The discretized system is solved implicitly by a Newton–Raphson method. The drawback of this implicit method is the *generation* of an initial model with appropriate distributed grid points.

Hence, both approaches, explicit as well as implicit, have their shortcomings during the phase of the model run. However, even a quantitative comparison, which will be subject of a forthcoming paper, shows the results in excellent agreement.

Chapter 3

Models with an assumed radiation pressure on dust – comparison with previous work

3.1 Introduction

In this section we would like to review in some detail the work of other authors on dynamical modeling of Mira and long-period variables. Thereby we concentrate on investigations aimed to present time-dependent circumstellar structures to study dynamical interactions. Furthermore we would like to focus our attention to those authors investigating the interplay between *pulsation* and *dust formation* and the role of these processes for the extensive mass-loss going on in these late stages of stellar evolution.

Other mass loss mechanisms are discussed in Chapter 1.

A pioneering work on this field of research has been performed by [Wood 1979]. In this paper he presented model atmospheres for a typical Mira variable star ($T_\star = 2750K$, $L_\star = 10^4 L_\odot$, $M_\star = M_\odot$, $P = 372d$) either in the adiabatic or in the isothermal limit case. To deal with the problem of dust formation he introduced an equation for the opacity of the grains which might be interpreted as follows: he assumed that all grains condense out at a prescribed condensation temperature T_{cond} over a small temperature interval ΔT and immediately reach their final and constant degree of condensation such that the opacity of the grains κ_d could be approximated by

$$\kappa_d = \frac{\kappa_{max}}{1 + exp\left[\left(T - T_{cond}\right)/\Delta T\right]} \quad . \tag{3.1}$$

Here, κ_{max} is a constant chosen to give a specified ratio of the force per unit mass due to radiation pressure $(F/m)_{rad}$ to that due to gravity. Usually, this constant is chosen to give $(F/m)_{rad} = 0.95g$. In other words, due to the lack of a treatable theory of dust formation and growth [WOOD 1979] attempted at least to include the dynamical effects of the dust grains on the circumstellar structure.

Woods modelling procedure differed from the present work, apart from the dust complex, mainly in two further ways. He solved the hydrodynamical equations in Eulerian coordinates and, to simulate a first overtone pulsation of the star, he assumed a sinusoidal variation of the *pressure* at the inner boundary. For a discussion of the mode of pulsation of cool red giants, which is still a matter of debate, see Chapter 1.

Woods models for the *adiabatic limit case without* the consideration of *dust formation* according to Eq. (3.1) showed unsatisfactorily high mass loss rates of $\approx 10^{-2} M_\odot\, yr^{-1}$ but reasonable outflow velocities of $5 - 10 km\, s^{-1}$.

The reason for these large mass loss rates is the high gas density in the wind which could be lowered by a reduction of the mechanical energy input at the inner boundary. However, Wood argued, this would result in a photospheric pressure and density too low compared to observed values [1].

A further severe problem of these models is the high gas temperature produced by the pulsation due to a lack of cooling mechanisms. In the inner region just above the photosphere, the gas temperature remains larger than $10^4 K$ over a considerable radius interval behind the shocks which would cause effects, e.g. on the course of the hydrogen emission line velocity, which are not observed.

The *isothermal* models presented by [WOOD 1979] showed only sporadic mass loss events with an averaged rate of $\approx 10^{-12} M_\odot\, yr^{-1}$, i.e. much too low to explain the observed values. The inclusion of radiation pressure on dust grains according to Eq. (3.1) in these isothermal models however, raised the mass loss rate dramatically to $\approx 10^{-7} M_\odot\, yr^{-1}$ due to an increased density in the subsonic region.

In conclusion, Woods work demonstrated that pulsation alone cannot account for the observed mass loss rates of Miras and LPVs but that a second mechanism, favourably radiation pressure on dust grains, has to be involved.

The previous model calculations have been extended by [DRINKWATER AND WOOD 1985] also to fundamental mode pulsations without altering the above conclusions.

Woods results were confirmed by [WILLSON AND HILL 1979, HILL AND WILLSON 1979] who presented an analytic approach for strictly periodic shocks in an isothermal atmosphere and also corresponding numerical models. In addition, they showed that an aperiodic moving piston at the inner boundary has only minor effects on enhancing the mass loss rate.

So far, the knowledge on the atmospheric structure of Miras and LPVs, the approaches of a theoretical understanding, either by numerical models or ana-

[1] From an extensive curve-of-growth analysis [FUJITA 1970], p.89, derived a photospheric gas pressure of $p_g \approx 10^2 dyn\, cm^{-2}$, depending on the object.

lytically by a time averaged description, have been summarized in the review of [Willson and Bowen 1985].

The limitation of Wood's [Wood 1979] model calculations to either instantaneous or no energy exchange between matter and radiation has been substantially improved by the work of Bowen [Bowen 1988a, Bowen 1988b, Bowen 1990, Bowen and Willson 1991]. Additionally to the hydrodynamical equations, he solved simultaneously the energy equation under the assumption of a parametrized radiative energy exchange Q per unit mass during a time interval Δt, with a parametrization depending on the different temperature intervals.

Basically, these relaxation laws have a form $\propto (T - T_{eq})\rho$ which is motivated by the following consideration: The emission of radiation depends on collisional excitation. Hence, the amount of radiation emitted per unit mass is proportional to the collision rate per unit volume (proportional to ρ^2) divided by the density.

Alike the present work [Bowen 1988a] used an explicit scheme to solve the hydrodynamical equations in Lagrangian coordinates and assumed a sinusoidal variation of the velocity at the inner boundary to simulate the interior pulsation.

With these improvements [Bowen 1988a] and [Bowen and Willson 1991] calculated a large grid of models for typical parameters of LPVs to study e.g. the development of mass loss rates during the evolution of a star.

Very recently [Feuchtinger *et al.* 1993] have overcome the problem of parametrized cooling laws by solving the complete set of the equations of radiation hydrodynamics. Thereby, they could avoid another problem inherent in Bowens calculations: the development of an unrealistic "chromosphere" especially behind the large innermost shock. Since the correct energy exchange term in the energy conservation equation of the gas and in the radiation energy equation is proportional to $\rho(J - S_g)$, where J denotes the zeroth moment of the radiation field and S_g denotes the source function of the gas, this exchange term yields in the LTE approximation of the source function a term proportional to $\rho(T_{rad}^4 - T_g^4)$, and thus yields a much more efficient cooling behind the shocks than Bowens approach. In fact, due to this efficient cooling, it turns out that the temperature structure in [Feuchtinger *et al.* 1993] shows an almost isothermal behaviour with very narrow peaks in the radial course of the temperature behind the shocks.

[Feuchtinger *et al.* 1993] discretized the equations of radiation hydrodynamics using a 2^{nd} order advection scheme and solved the resulting algebraic equations by a modified Newton-Raphson technique.

All the aforementioned approaches have in common that they use the simple formula (3.1) first introduced by [Wood 1979] to account for radiation pressure on dust.

Although, it will become clear in the next sections that this approximation is rather crude and cannot account for a detailed description of the CDS, this approach, nevertheless, serves as a test ground to study the influence of certain parameters which are otherwise obscured by other effects. Besides, since no analytic solution of the whole problem of a dynamically variable star atmosphere is known to exist [2], a new code always has to be tested by comparison with existing numerical solutions.

It is the aim of this section to demonstrate that our model calculations under the assumption of the simple dust opacity (3.1) and in the isothermal or adiabatic limit case are, at least qualitatively, in excellent agreement with the literature. A quantitative comparison is only possible for global quantities such as the final wind velocity or the mass loss rate since a complete data set of the other model calculations is of course not available to the author. In this restricted sense of comparison, we also find very good quantitative agreement.

3.2 A typical model calculation

To illustrate some of the results mentioned in the previous section we present typical model calculations with an assumed radiation-pressure-on-dust-term either in the limit case of adiabatic or isothermal shocks and for the case without radiation pressure on dust at all. The radial structure is discussed in some detail for one set of parameters. The influence of the variation of the stellar parameters is discussed in the next section where a grid of such models is presented.

For the demonstrative example we have chosen the following set of parameters:

$$\begin{aligned} T_\star &= 3000K \\ M_\star &= 1M_\odot \\ L_\star &= 5330L_\odot \\ P &= 400d \\ \Delta u_p &= 3kms^{-1} \quad , \end{aligned}$$

henceforth called **Model A**.

3.2.1 The limit case of isothermal shocks

Fig. 3.1 shows a time sequence of the radial structure of the typical model (Model A) with an assumed radiation pressure on dust in the limit case of isothermal shocks.

[2] In this sense we include the problem of dust formation and, therefore, have to exclude the analytic approaches of [Bertschinger and Chevalier 1985, Bertschinger 1986, Bertschinger 1989] and [Hill and Willson 1979, Willson and Bowen 1985]

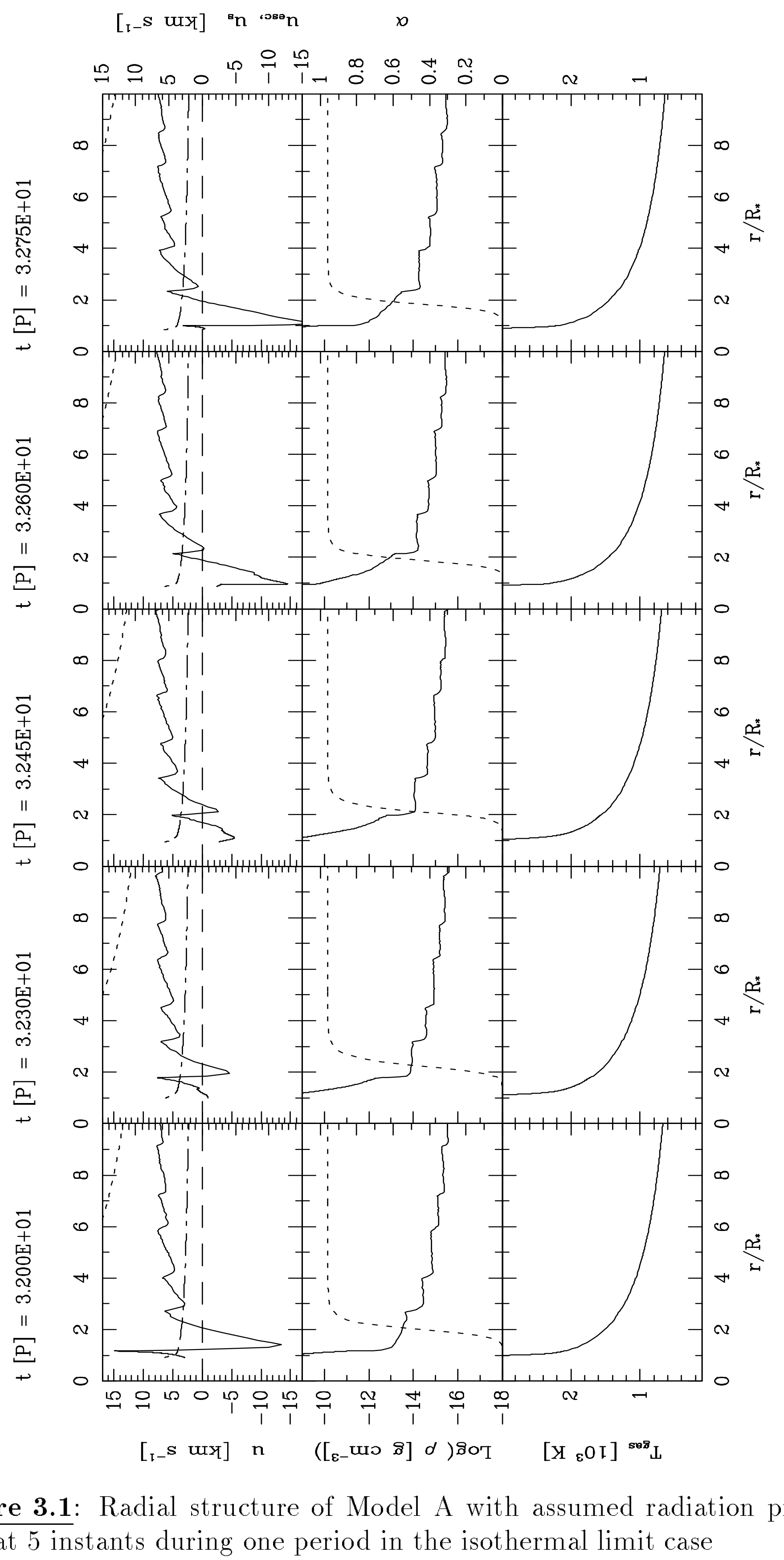

Figure 3.1: Radial structure of Model A with assumed radiation pressure on dust at 5 instants during one period in the isothermal limit case

In addition to the hydrodynamical quantities flow velocity u, gas density ρ, radiative acceleration in units of the gravitational acceleration α and gas temperature T_{gas} the upper panel also shows the velocity of sound u_s (long dashed – dotted line) and the escape velocity u_{esc} (short dashed line).

The course of the velocity and the density indicate several shock waves travelling through the atmosphere. At phase 0.0 (left column) the innermost shock reaches its maximum strength, i.e. a maximum velocity amplitude of about $29 km\, s^{-1}$.

Around $2R_\star$ the temperature drops below $1500K$ and marks the onset of dust formation according to Eq. (3.1). Thus, radiation pressure on dust is responsible for accelerating the material to supersonic flow velocities and driving a mass outflow at a rate of $1.6\,10^{-6} M_\odot\, yr^{-1}$ with a final velocity around $7.9 km\, s^{-1}$.

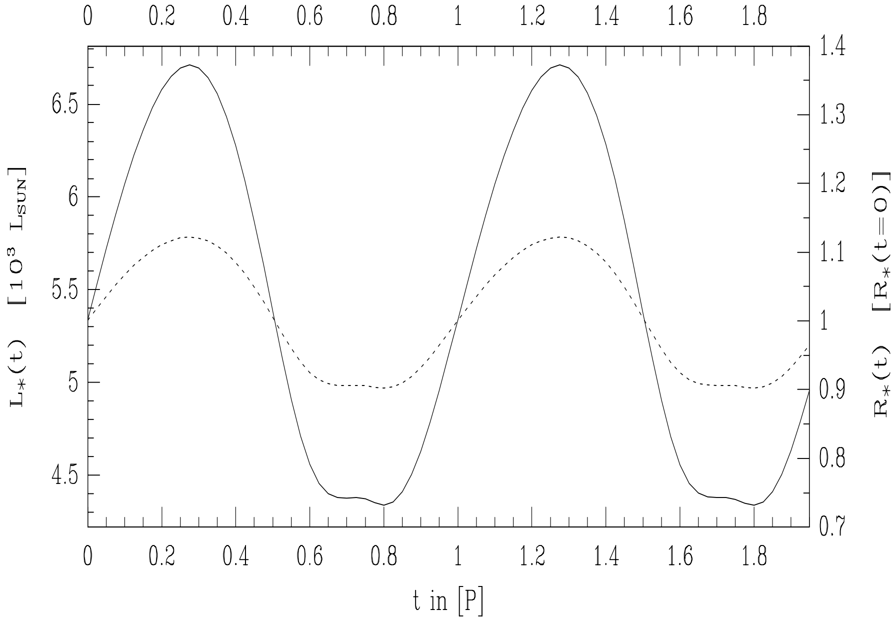

Figure 3.2: Stellar luminosity (solid line) and radius (dotted line) plotted against phase for Model A with assumed radiation pressure on dust in the limit case of isothermal shocks

---

Fig. 3.2 shows the temporal course of the stellar luminosity $L_\star$ (solid line) and the stellar radius $R_\star$ (dotted line) for Model A over an interval of 2 periods. In contrast to the sinusoidal movement of the piston, $L_\star$ and $R_\star$ show a plateau-like structure around phase 0.7 and 1.7, respectively. This gives a first hint to a dynamical phenomenon which we now like to discuss: the formation of "preliminary" shocks.

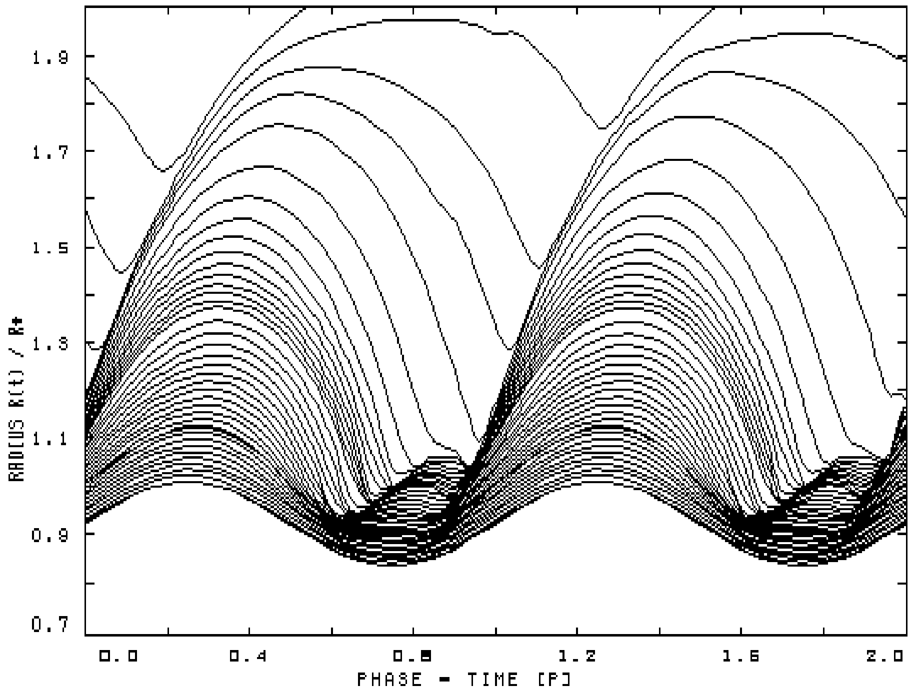

Figure 3.3: Radius of selected shells of the innermost region plotted against phase for Model A with assumed radiation pressure on dust in the limit case of isothermal shocks

---

To get a better idea of what is meant by "pre-shocks" we have plotted in Figs. 3.3 and 3.4 the radius and the corresponding density of selected inner shells as a function of phase; the line with the smallest radius is the piston. At phase 0.6 and 1.6, respectively, a (pre-) shock forms, coalescing at phase 0.9 (1.9) with the main shock which then travels out in the atmosphere.

This phenomenon can be explained by means of a time sequence of the enlarged radial structure of the inner region, which is shown in Fig. 3.5.

The sequence starts at $t = 32.55P$ (left panel), at this time the piston has just passed the position with maximum inward directed velocity and is now moving inwards with decreasing velocity. The material between $r \approx 1R_\star$ and $r \approx 2\,R_\star$ has been shocked in the previous cycle and is now falling inwards, thereby forming an accretion shock front, cf. $t = 32.65P$. Due to the steeply increasing density gradient this shock front encounters very dense inner regions just beneath the photosphere where it is reflected and subsequently moves outward. During this outward directed movement the front still steepens, cf. plots at $t = 32.65P$ and $t = 32.75P$.

Beginning at $t = 32.75P$ the piston is moving outwards again and thus causes the formation of the next compression wave. Since it is formed in the innermost

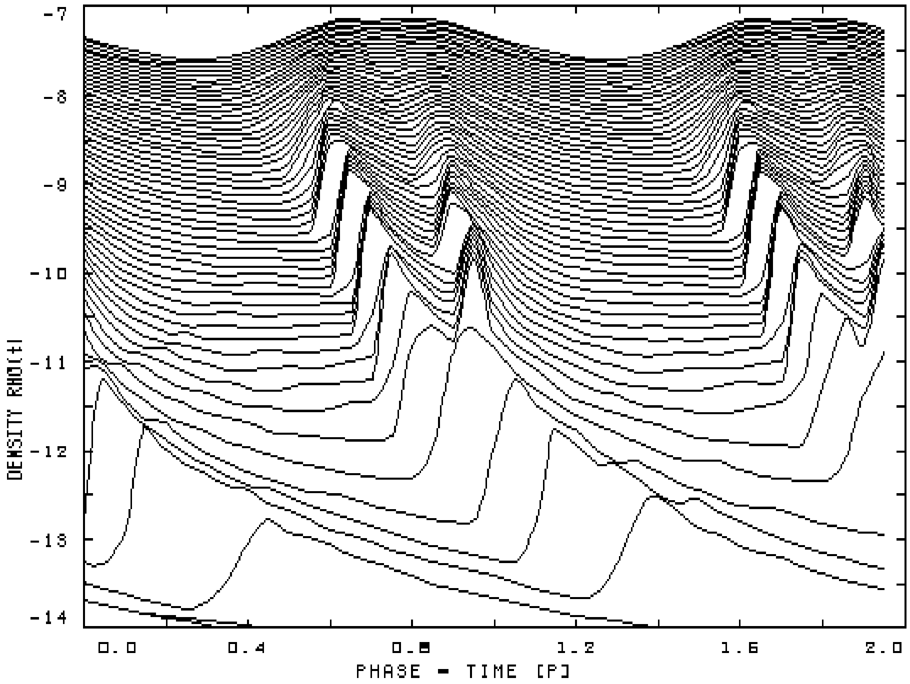

Figure 3.4: Density in selected shells of the innermost region plotted against phase for Model A with assumed radiation pressure on dust in the limit case of isothermal shocks

---

region this compression shock front runs down the almost exponential density gradient and thus has a higher propagation velocity than the former accretion front which runs into the wake of the shock front of the previous cycle. These different propagation velocities can also be seen in the radius vs. phase plot of Fig. 3.3.

Hence, the new compression wave overruns the former "accretion" wave, they merge between $t = 32.85P$ and $t = 32.95P$, and a new shock front runs out in the upper atmosphere.

It remains to explain why the innermost zones, after being pushed outwards by a shock wave, return asynchronous to the movement of the piston, i.e. they return earlier, thereby are unaffected by the piston and have a short time interval to form the accretion shock front.

The formation of these pre–shocks is an inherent phenomenon in all of our calculations. It even shows up in models with a consistent treatment of dust formation and growth because the mechanisms of its generation are located around and below the photosphere where no dust is present at all. Therefore, we will discuss in some detail in Sec. 3.2.4 the formation of the pre–shocks from a slightly

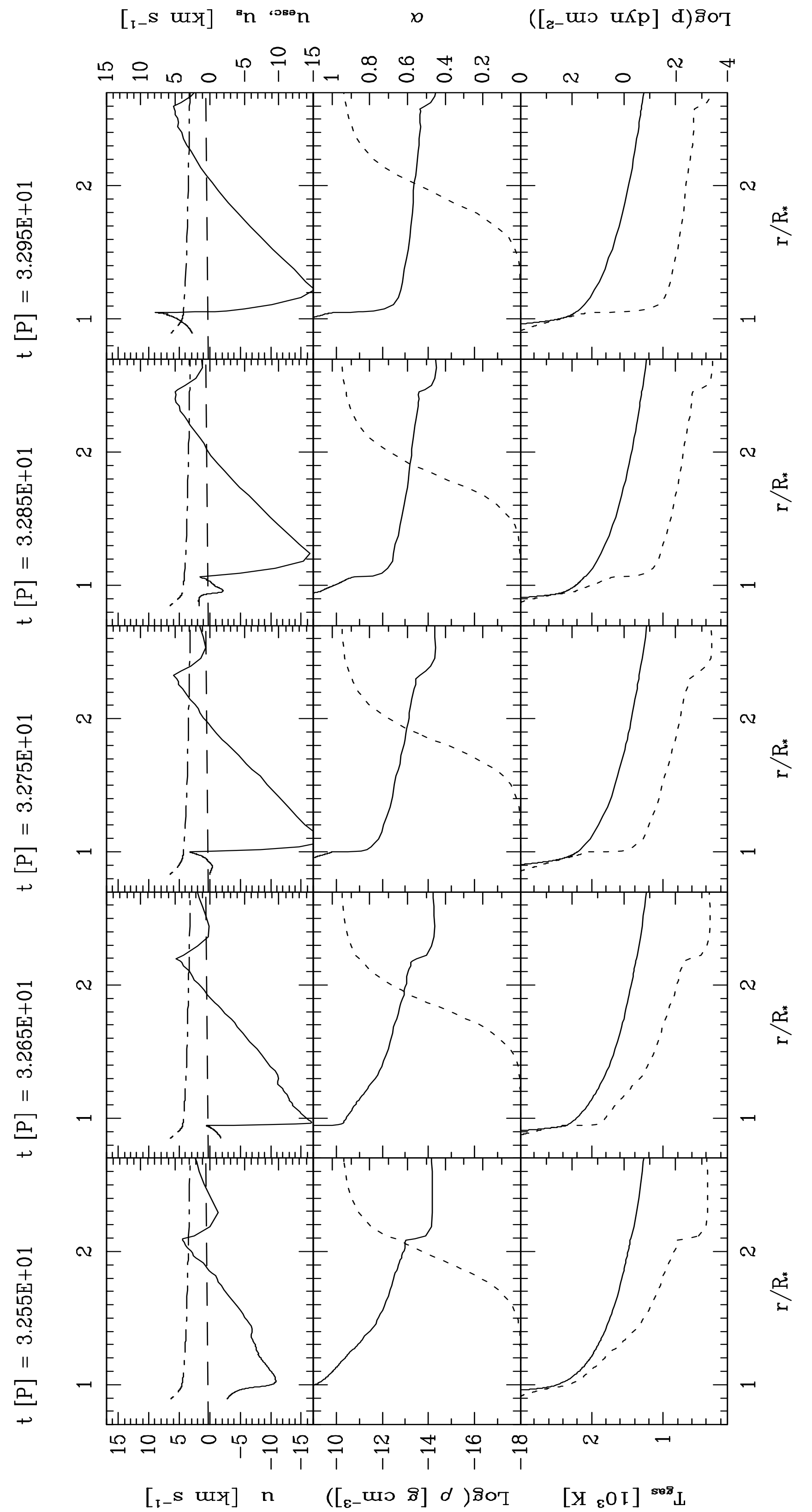

Figure 3.5: Radial structure of the innermost region of Model A with assumed radiation pressure on dust at 5 instants during one period in the isothermal limit case

more general point of view.

3.2.2 The limit case of adiabatic shocks

Fig. 3.6 shows a time sequence of the radial structure of Model A calculated with an assumed radiation pressure on dust in the limit case of adiabatic shocks.

In addition to the quantities shown in Fig. 3.1 for the isothermal case we have also plotted the radiative equilibrium temperature T_{eq}.

The course of the gas temperature shows that the material is strongly heated due to the compression of the shocks. Especially, the innermost shock which is formed once per period heats up the material to more than $10^4 K$.

Alike the calculation in the isothermal limit case, the model in the limit of adiabatic shocks shows a radial structure which is regularly passed by shock waves and undergoes a steady mass-loss whose rate is about $1.2\,10^{-4} M_\odot yr^{-1}$. The reason why we do not get a mass loss rate as disastrous as Woods $10^{-2} M_\odot yr^{-1}$ [Wood 1979] is given by the position of the inner boundary. Since the mechanical energy input by the piston can be conceived as $p\,\Delta V$, where ΔV denotes the variation of the volume, an outward shift of the rest position of the piston increases ΔV but is more than counterbalanced by the extremely steep increase of the gas pressure p in the vicinity of the piston. Thus, since the rest position of the piston in Woods calculations is far inside the photosphere compared to our calculations, the deposition of mechanical energy in Woods calculations is much higher than in ours which yields these enormous mass loss rates of his models. The influence of the rest position of the piston on the mass loss rate is also confirmed by [Feuchtinger *et al.* 1993], see also Sec. 3.3.

Subsequent cooling after the passage of a shock wave appears rather slowly due to expansion. Note, that despite the different scales of the temperature axis' in Fig. 3.6, the gas temperature remains well above the radiative equilibrium temperature.

A careful study of a time sequence of the radial structure of Model A in this limit case, which we would like to omit here, would again show the formation of a pre-shock in the inner region just above the photosphere. Instead, we refer to Fig. 3.7 were these pre-shocks can clearly be seen.

Since the dust is assumed to be in equilibrium with the radiation field, the radiative equilibrium temperature enters the equation (3.1) to calculate the radiative acceleration whose course is thus unaffected by the different treatment of thermodynamical behaviour of the post-shock gas.

Due to the high mass loss rates (cf. Tab. 3.5) and the temperature structure adiabatic models are not able to give a reliable explanation of the observed mass loss phenomena of LPVs.

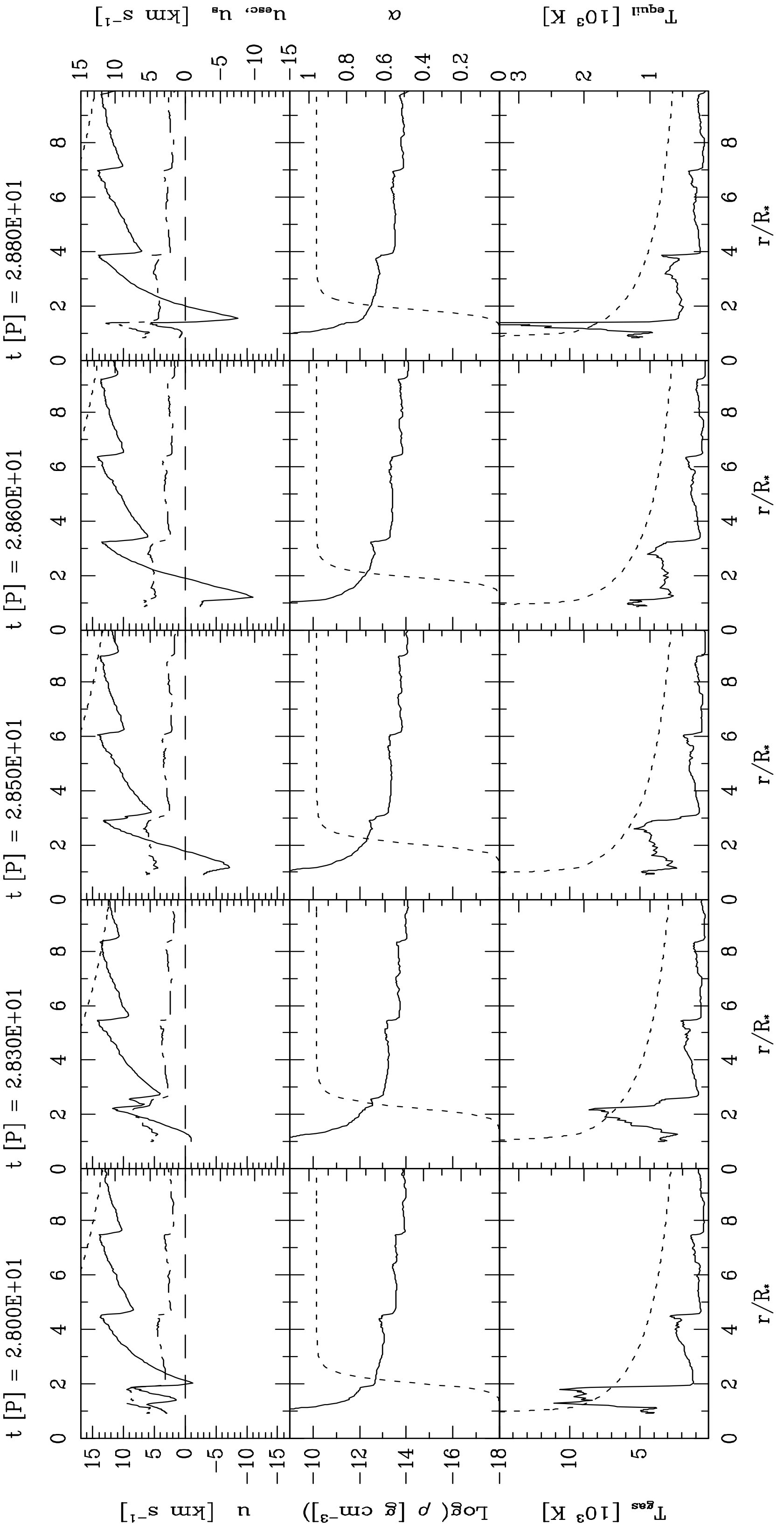

Figure 3.6: Radial structure of Model A with assumed radiation pressure on dust at 5 instants during one period in the adiabatic limit case

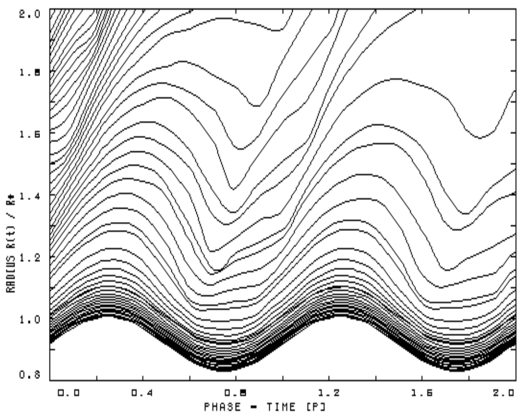

Figure 3.7: Radius of selected shells of the innermost region plotted against phase for Model A with assumed radiation pressure on dust in the limit case of adiabatic shocks

---

3.2.3 The case without radiation pressure on dust

To finish this section of individual models we would like to discuss models calculated without radiation pressure on dust.

Fig. 3.8 shows the resulting radial structure calculated for Model A in the isothermal limit case.

The temporal behaviour of these models can be characterized by a continued coalescing of shocks above the photosphere and an aperiodic build up of a single shock wave which traverses the outer boundary of the model but does not necessarily need to exceed the escape velocity. Thus, pulsation alone cannot drive a substantial mass loss and most of the material temporarily driven out by a shock wave is falling back towards the star. This can also immediately be seen from the velocity structure in Fig. 3.8, where the average velocity value is even less than the value of the local sound velocity.

Hence, the "mass loss rate" and the "outflow velocity" given for this kind of models in Tab. 3.6 are rather artificial, since they were calculated by averaging the outer region of a given radial structure. The "real mass loss rate" is orders of magnitudes less than the value given in Tab. 3.6 because it takes several cycles to build up a radial structure with an – on the average – positive velocity in the outer parts of the model, and to determine the mass lost one should take the

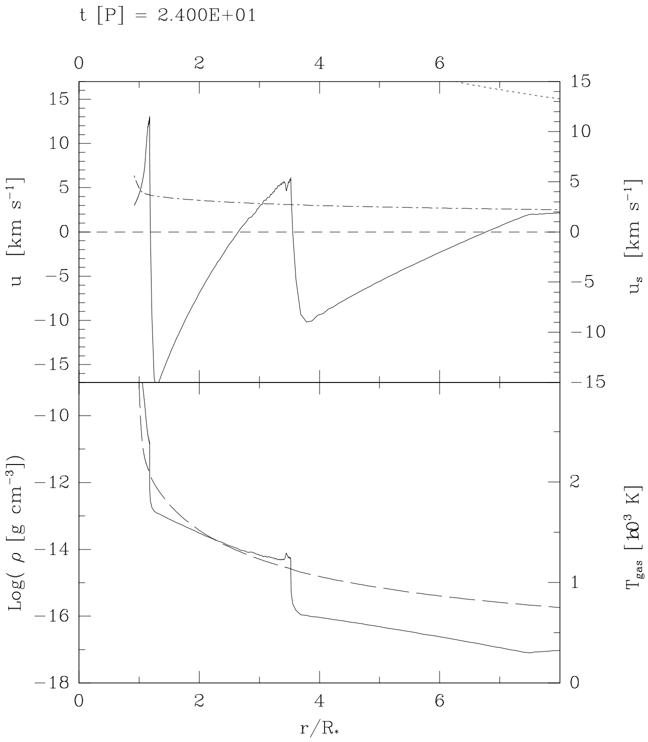

Figure 3.8: Radial structure of Model A without dust in the isothermal limit case

---

average over this time interval of several cycles.

Even if the velocity amplitude at the inner boundary is drastically increased a continuous outflow driven solely by pulsation is not achieved. The radial structure given in Fig. 3.8 is then only altered quantitatively without producing mass loss rates within the observed range. This finding confirms the results of [Wood 1979] for his isothermal model calculations without dust.

To conclude this section we would like to emphasize the result that pulsation alone *cannot* drive the outflow observed at Miras and LPVs but a second mechanism must come into play to support the final acceleration of the material above the photosphere. Therefore, radiation pressure on dust grains formed in the density enhanced atmosphere is likely to be a good candidate for this second mechanism, see also the introduction Chapter 1.

3.2.4 The formation of pre–shocks

The formation of pre–shocks, apparent in Fig. 3.3, can be understood within the framework of the linearized fluid equations, cf. [Mihalas and Weibel Mihalas 1984, Stein and Leibacher 1974].

Thereby, the propagation of small disturbances under the combined action of

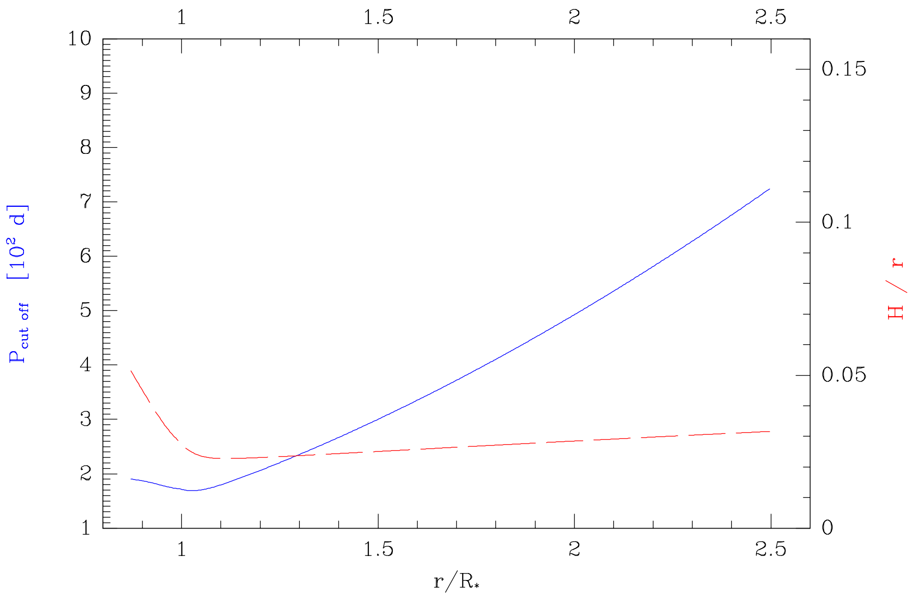

Figure 3.9: Cut–off period and density scale height as a function of the radius for the initial hydrostatic model of Model A

---

pressure and gravity in an isothermal medium is studied. Considering monochromatic plane waves, the respective wave equation is used to derive a dispersion relation. Then, two limiting frequencies, ω_{acc} and ω_g, can be derived which separate the regimes were either acoustic or gravity waves exist under the influence of gravity or pressure, respectively. Even under the combined action acoustic and gravity wave modes are still distinct. Between these regions, for $\omega_g \leq \omega \leq \omega_{ac}$, no progressive, i.e. no propagating waves exist.

The quantity

$$\omega_g := \sqrt{\gamma - 1}\,\frac{g}{u_s} = \sqrt{\gamma - 1}\,\frac{u_s}{\gamma\,H} \tag{3.2}$$

is the *Brunt–Väisälä* frequency, where

$$H = \frac{p}{\rho\,g} = \frac{R\,T}{\mu\,g} = \frac{u_s^2}{\gamma\,g} \tag{3.3}$$

is the density scale height.

If a fluid element in a gravitational field is displaced from the equilibrium position but remains in equilibrium with the pressure it will oscillate with the frequency ω_g (buoyancy oscillation). Under the combined action of both gravity

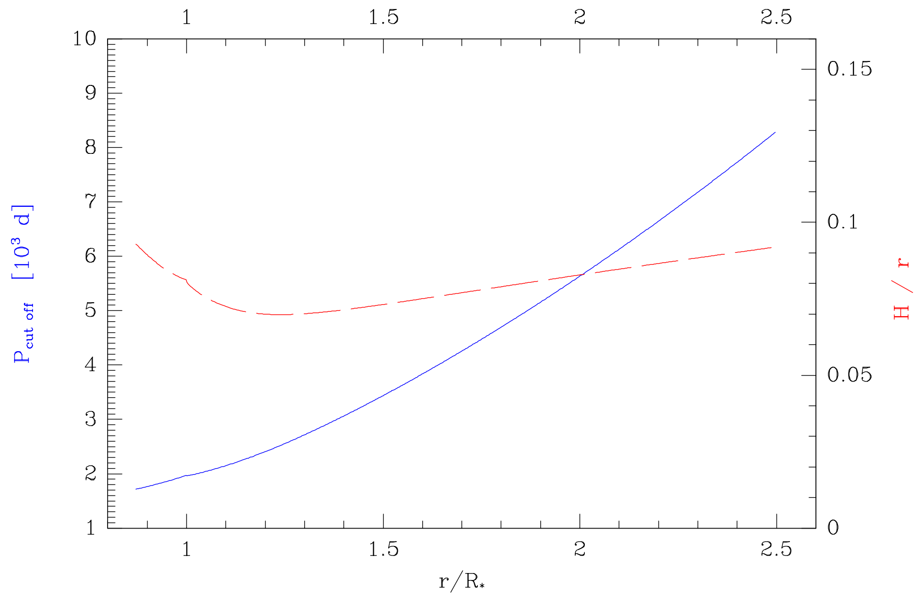

Figure 3.10: Cut–off period and density scale height of the initial hydrostatic model with $L_\star = 3\,10^4 L_\odot$, $M_\star = M_\odot$, $T_\star = 2450K$

---

and pressure ω_g marks the region were gravity mode oscillations prevail under the influence of pressure.

The quantity

$$\omega_{ac} := \frac{\gamma\, g}{2\, u_s} = \frac{u_s}{2\, H} \tag{3.4}$$

is called the acoustic cut–off frequency, below which acoustic waves cannot propagate in a stratified medium. The case $\omega >> \omega_{ac}$ represents the limit case of the propagation of *pure* acoustic waves. The corresponding cut–off period P_{ac} is

$$P_{ac} = \frac{4\pi\ H}{u_s} = \frac{4\pi\ u_s}{\gamma\, g} \quad . \tag{3.5}$$

Wave propagation is possible for $P < P_{ac}$.

In Figs. 3.9 and 3.10 we have plotted the radial structure of the cut–off period and the density scale height according to Eqs. (3.3) and (3.5) for Model A and a more luminous model. Although the plots look very similar, note the different scaling of the cut–off period ordinate. Around the stellar radius the cut–off period is almost constant, until further out the u_s–term in Eq. (3.5) dominates and P_{ac} increases. To get an idea how the cut–off period and the density scale height develop as a function of temperature and luminosity, we have listed in Tab. 3.1

Table 3.1: Cut–off period and density scale height as a function of stellar temperature and luminosity for the initial hydrostatic situation for a 1 $M_\odot$ model.

$T_\star$ [K]	$L_\star$ [10^4 $L_\odot$]	$P_{ac}[d]$	$H/R_\star$
3000	3.0	968	0.06
3000	1.0	322	0.03
3000	0.5	160	0.02
2500	3.0	1833	0.08
2500	1.0	610	0.05
2500	0.5	304	0.03
2000	3.0	4004	0.10
2000	1.0	1333	0.06
2000	0.5	666	0.04

the corresponding values for the typical range of parameters for a 1 $M_\odot$ model. The more luminous and cooler the model, the longer is the cut–off period and the larger is the value of the density scale height, i.e. the softer is the density gradient in the atmosphere. In general, i.e. also for other stellar masses, the cut–off period scales with R^2/M.

The cut–off period for Model A according to Tab. 3.1 is $\approx$ 160 days. The model is driven with a period of the piston of 400 days, i.e. well above the cut–off frequency, or the respective cut–off period. However, as depicted in Fig. 3.3, this does not mean that no waves can escape from the sub–photospheric region. Total reflection below the photosphere does not occur. The reason for this behaviour is that the waves that reach this region are not purely sinusoidal. The plot of the Lagrangian radius as a function of phase for Model A shown in Fig. 3.3 shows the presence of a standing wave between piston and photosphere. All Lagrangian shells reach their maximum outward position at nearly the same time and fall back synchronously, since the driving period is almost twice the cut–off period in this region. Above the photosphere, where the value of the cut-off period increases, there is still reflection of the waves but these are now travelling waves. The reflection in this region causes the material to fall back, thereby producing the pre–shock. Only little further outwards, around 1.4 $R_\star$, the cut–off period becomes comparable with the driving period, cf. Fig. 3.9, strong shock waves can form and travel outwards.

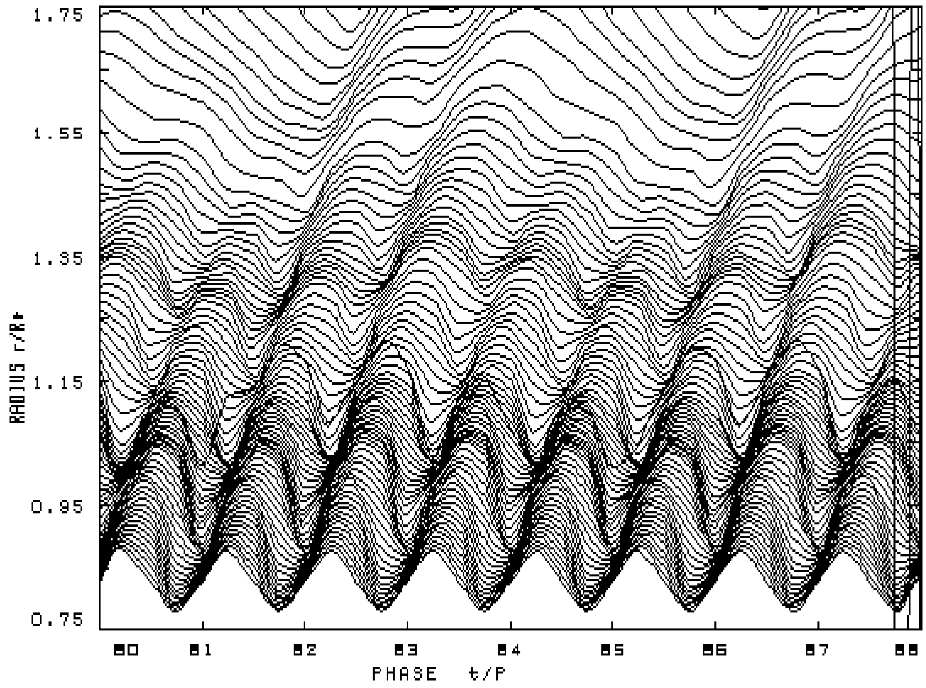

Figure 3.11: Radius of selected shells of the innermost region plotted against phase for a model with $M_\star = M_\odot$, $L_\star = 3.0\,10^4 L_\odot$, $T_\star = 2450K$ driven with a period of 776d, which is well below the cut–off period

---

We have found this behaviour to be independent of the rest position of the piston as well as independent of the amplitude of the piston, cf. [Bowen 1990] for similar results.

For comparison, we have also plotted the Lagrangian radii as a function of time for two models driven with a period considerably shorter than the cut–off period, Fig. 3.11, and with a period comparable with the cut-off period, Fig. 3.12. [3]

The model in Fig. 3.11, driven with $P = 776d << P_{ac}$, shows the development of propagating waves in the innermost region, i.e. up 1.35 $R_\star$. In the region beyond this, the waves are gradually damped after depositing their energy in the surrounding gas. The model in Fig. 3.12, driven with $P = 2988d$, which only slightly greater than the cut–off period, shows the development of a standing wave in the region just above the piston. The solid line shows the temporal behaviour of the stellar radius. In the region around the photosphere the waves have changed into propagating waves, since the cut–off period is now considerably larger than the driving period, cf. 3.10.

[3] The vertical bars in Figs. 3.11 and 3.12 are artifacts of the graphic program

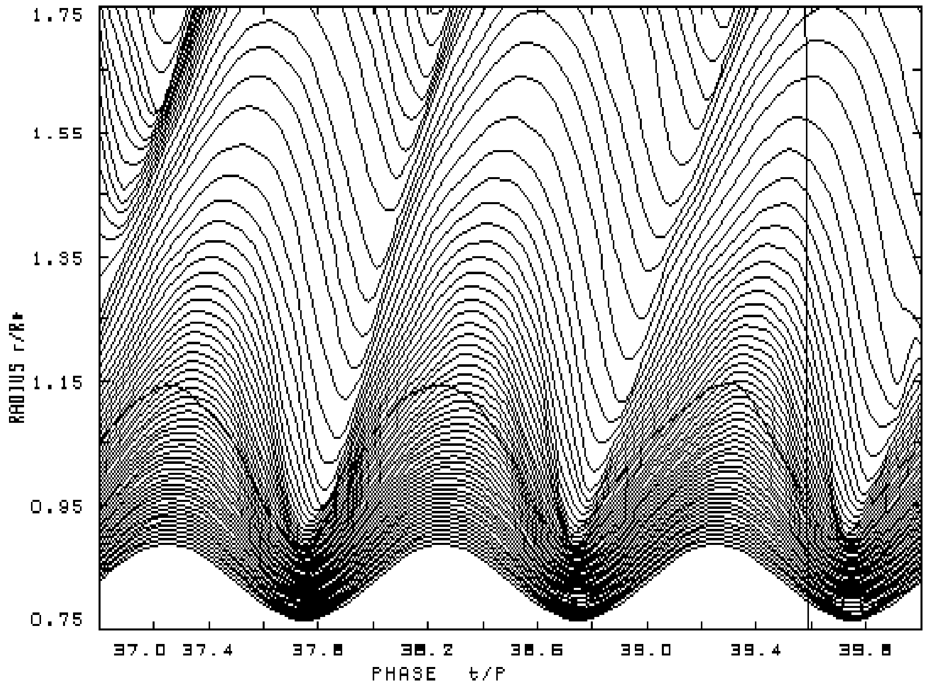

Figure 3.12: Radius of selected shells of the innermost region plotted against phase for a model with $M_\star = M_\odot$, $L_\star = 3.0\,10^4 L_\odot$, $T_\star = 2450K$ driven with a period of 2988d, which is above the cut–off period of 2166 days for this case

---

While comparing Figs. 3.3, 3.11, and 3.12 note the different scaling of the time–axis.

Summarizing, this effect is an example of the general rule that wave reflection occurs if the properties of the medium, i.e. in our case the density, change rapidly compared to the time scale given by the wavelength. Thus, an early reflection of waves could occur and fluid elements return asynchronously, thereby producing one or even more so called pre- or *intra–period* shocks [Bowen 1990], depending on the period of the driving piston. Despite its shortcomings (isothermal medium, linearized theory) this approach provides a satisfactorily explanation for the hydrodynamical behaviour in the innermost region of the circumstellar shell.

3.3 Results

We would like to end this chapter with a presentation of a large sample of models calculated including radiation pressure on dust according to Eq. (3.1) to analyse the dependence of the main observable quantities, namely the mass loss rate and the outflow velocity, on the model parameters $T_\star$, $M_\star$, Δu_P and P. Usually, heating and cooling of the gas is treated in the isothermal limit case, if not otherwise indicated.

Since most of the models, as indicated in the following tables, are calculated using the period-mass-radius relation of [OSTLIE AND COX 1986] to determine the stellar luminosity $L_\star = 4\pi R_\star^2 \sigma T_\star^4$, $L_\star$ is not treated as a separate parameter. In addition we have also investigated the influence of the position of the inner boundary R_{inner} and the influence of a variation of the assumed maximum opacity value κ_{max} in Eq. (3.1).

Qualitatively, the general shape of the radial structure and even the slope, e.g. of the density, at larger radii for many different models are very similar to those shown in Fig. 3.1. Apart from time-dependent changes due to the formation and propagation of shocks, the radial structure of the density can always be clearly divided into two different parts:

- the innermost region, inside the first large shock is characterized by an almost exponential decrease of the density,
- the outer region, outside the innermost shock characterized by a rather large scale height, i.a. a soft density decrease.

The following consideration gives a simple explanation for this behaviour [BOWEN 1988B]. In an atmosphere in hydrostatic equilibrium the pressure, which is proportional to the density, must increase towards smaller radii to balance the increase of weight, such that the density *gradient* is proportional to the density and an exponential slope of the density results. This is, of course, in contrast to dynamical atmosphere. We do not have this balance of forces in a dynamical situation but for an evolved and quasi-stationary model the average mass flow, $<\dot{M}>=<4\pi r^2 \rho u>$, must be constant in the wind. Assuming the outflow velocity to be constant (which is on the average correct for the wind region), the density must increase proportional to r^{-2}, which gives a density scale height $H_\rho = r/2$, with $1/H_\rho := 1/\rho \; d\rho/dr$ and approximately matches the plots of the density shown in the previous sections.

In the following tables we have compiled different series of models with varying stellar parameters. An "i" or "a" denotes a calculation in the isothermal or adiabatic limit case, respectively. The quantity $T_\star$ is given in $[K]$, $L_\star$ in $[L_\odot]$, $M_\star$ in $[M_\odot]$, P in $[d]$, Δu the amplitude of the piston in $[kms^{-1}]$, $\dot{M}$ in $[M_\odot yr^{-1}]$, u_∞ in $[kms^{-1}]$, $R_\star$ in $[R_\odot]$ and R_{inner} in $[R_\star]$ of the initial hydrostatic model.

Tab. 3.2 shows two short sequences of models with varying stellar mass. The compilation immediately shows the decrease of the mass loss rate with increasing stellar mass. This is not difficult to understand. Since all parameters except the stellar mass are held constant, the combined force of stellar pulsation and radiation pressure on dust has to surmount an increasing gravitational deceleration which yields, as indicated in Tab. 3.2, a decreasing outflow velocity, and hence, a decreasing mass loss rate.

In Tab. 3.3 we have compiled four models with increasing period of the variation of the piston at the inner boundary. This increase of the period leads according to the period-mass-radius relation to an increase of the stellar radius, thereby also of the luminosity, and hence to a decreased density scale height of the evolved model in the region below the innermost shock. This is the reason for the increase of the mass loss rate with the period, in contrast to the sequence with varying stellar mass in Tab. 3.2. Although the models in Tab. 3.2 underly the same variation of stellar parameters due to the period-mass-radius relation the effect of an increase of the luminosity is counterbalanced in the evolved models by the gravitational deceleration and the increase of mass-loss is due to the slight increase of the outflow velocity with decreasing mass. Increasing the pulsational period leaves the outflow velocity almost unaffected, but the resulting transition to the wind region, occuring at higher densities, is the effect, which is responsible for the increase of the mass loss rate.

Table 3.2: Sample of evolved models with varying stellar mass. The units are explained in the text

No.	gas	$T_\star$	$L_\star$	$M_\star$	P	Δu	$\dot{M}$	u_∞	$R_\star$	R_{inner}	Rem.
1	i	3000	4620	1.0	350	3.0	1.9-07	7.1	251	0.96	
2	i	3000	5331	1.2	350	3.0	7.8-08	6.9	269	0.97	
3	i	2750	7238	0.4	400	3.0	1.9-03	8.6	374	0.82	
4	i	2750	8595	0.7	400	3.0	5.0-04	8.3	407	0.82	
5	i	2750	10080	2.0	400	3.0	1.4-05	4.5	441	0.82	
6	i	2750	9064	1.0	400	3.0	1.7-04	8.1	418	0.82	

Table 3.3: Sample of evolved models with varying period of the piston at the inner boundary. The units are explained in the text.

No.	gas	$T_\star$	$L_\star$	$M_\star$	P	Δu	$\dot{M}$	u_∞	$R_\star$	R_{inner}	Rem.
1	i	3000	2526	1.0	200	3.0	1.6-07	2.2	184	0.92	
2	i	3000	3917	1.0	300	3.0	6.2-07	7.3	231	0.92	
3	i	3000	5342	1.0	400	3.0	1.5-06	7.6	270	0.92	
4	i	3000	6784	1.0	500	3.0	3.2-06	7.8	304	0.92	
5	i	3000	8190	1.0	600	3.0	1.2-04	8.5	334	0.92	

In Tab. 3.4 we have compiled several series of models with varying amplitude of the piston at the inner boundary. Fig. 3.13 shows a comparison between two models driven with $\Delta u_P = 1 kms^{-1}$ and $10 kms^{-1}$, respectively. The stellar parameters of the initial hydrostatic model of these calculations are $T_\star = 2750K$, $M_\star = 1.0 M_\odot$, $L_\star = 1.0\ 10^4 L_\odot$ and $P = 400d$.

The higher input of mechanical energy in the model with $\Delta u_P = 10 kms^{-1}$ can be immediately seen from the more than doubled amplitude of the innermost shock compared to the model with $\Delta u_P = 1 kms^{-1}$. Since the density scale height is the same for both models in the inner region, the higher energy input yields a less steeper transition to the wind region, i.e. a more levitated atmosphere and thus a higher mass loss rate. The final outflow velocity is unaffected by the increase of the mechanical power input in these models since the assumed equation for the radiation pressure on dust is only a function of the temperature and does not take into account the increased density of the model with $\Delta u_P = 10 kms^{-1}$.

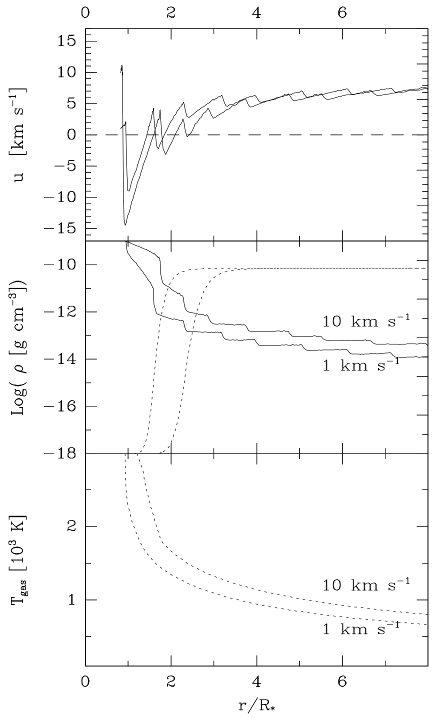

Figure 3.13: Radial structure of two Models driven with $\Delta u_P = 1 kms^{-1}$ and $10 kms^{-1}$, respectively, in the isothermal limit case

Table 3.4: Sample of evolved models with varying amplitude Δu_P of the piston at the inner boundary. The units are explained in the text.

No.	gas	$T_\star$	$L_\star$	$M_\star$	P	Δu	$\dot{M}$	u_∞	$R_\star$	R_{inner}	Rem.
1	i	3000	8190	1.0	600	3.0	1.2-04	8.5	334	0.92	
2	i	3000	7944	1.0	600	4.0	4.5-04	8.8	329	0.92	
3	i	3000	7757	1.0	600	5.0	6.2-04	8.4	325	0.92	
4	i	3000	6051	1.0	450	0.5	4.6-09	7.6	287	0.96	
5	i	3000	6048	1.0	450	2.0	5.5-07	7.5	287	0.96	
6	i	3000	6036	1.0	450	4.0	6.3-06	7.6	287	0.96	
7	i	3000	6025	1.0	450	6.0	2.8-05	7.5	286	0.96	
8	i	3000	5964	1.0	450	8.0	1.0-04	7.5	285	0.96	
9	i	3000	5315	1.0	400	1.0	9.5-08	7.7	269	0.92	
10	i	3000	5311	1.0	400	2.0	1.0-06	7.7	269	0.92	
11	i	3000	5342	1.0	400	3.0	1.5-06	7.6	270	0.92	
12	i	3000	5375	1.0	400	4.0	6.8-07	7.4	270	0.92	
13	i	3000	5252	1.0	400	5.0	2.3-05	7.5	267	0.92	
14	i	3000	5271	1.0	400	6.0	3.0-05	7.1	268	0.92	
15	i	3000	5234	1.0	400	7.0	6.0-05	7.1	267	0.92	
16	i	3000	5156	1.0	400	8.0	7.9-05	7.0	265	0.92	
17	i	3000	5108	1.0	400	9.0	1.0-04	7.0	264	0.92	
18	i	3000	5037	1.0	400	10.0	1.2-04	6.9	262	0.92	
19	i	3000	4616	1.0	350	1.0	1.5-08	7.5	251	0.96	
20	i	3000	4620	1.0	350	3.0	1.9-07	7.1	251	0.96	
21	i	3000	4600	1.0	350	5.0	3.9-06	7.5	250	0.96	
22	i	3000	4589	1.0	350	7.0	1.9-05	7.4	250	0.96	
23	i	3000	4567	1.0	350	9.0	5.6-05	7.2	249	0.96	
24	i	3000	4129	1.0	325	1.0	2.2-05	8.8	237	0.84	
25	i	3000	4045	1.0	325	3.0	1.3-04	8.6	235	0.84	
26	i	3000	4340	1.0	325	5.0	2.6-04	8.3	243	0.84	
27	i	3000	3753	1.0	325	7.0	1.2-03	8.3	226	0.84	
28	i	3000	4461	1.0	325	9.0	1.7-03	8.5	246	0.84	
29	i	2900	3686	1.0	322	2.0	1.7-07	5.3	240	0.96	
30	i	2900	3686	1.0	322	4.0	1.4-06	7.7	240	0.96	
31	i	2900	3677	1.0	322	6.0	1.7-05	4.3	239	0.96	

continued on next page

No.	gas	$T_\star$	$L_\star$	$M_\star$	P	Δu	$\dot{M}$	u_∞	$R_\star$	R_{inner}	Rem.
continued from previous page											
32	i	2900	3663	1.0	322	8.0	9.5-05	3.2	239	0.96	
33	i	2900	3687	1.0	322	0.5	1.0-09	7.3	240	0.96	
34	i	2750	9154	1.0	400	0.5	4.8-05	8.2	420	0.82	
35	i	2750	8824	1.0	400	1.0	1.0-04	8.1	413	0.82	
36	i	2750	8747	1.0	400	2.0	1.4-04	8.1	411	0.82	
37	i	2750	9064	1.0	400	3.0	1.7-04	8.1	418	0.82	
38	i	2750	10440	1.0	400	4.0	2.0-04	7.8	449	0.82	
39	i	2750	11940	1.0	400	5.0	2.7-04	7.6	480	0.82	
40	i	2750	13590	1.0	400	6.0	3.4-04	7.3	512	0.82	
41	i	2750	14740	1.0	400	7.0	3.9-04	7.0	534	0.82	
42	i	2750	16240	1.0	400	8.0	5.1-04	6.7	560	0.82	
43	i	2750	17560	1.0	400	9.0	5.4-04	6.5	583	0.82	
44	i	2750	18490	1.0	400	10.0	3.1-04	7.9	598	0.82	
45	i	2750	19500	1.0	400	11.0	3.4-04	7.8	614	0.82	
46	i	2750	19990	1.0	400	12.0	3.9-04	7.5	622	0.82	
47	i	2600	2911	1.0	388	2.0	7.9-07	8.0	265	0.90	
48	i	2600	2901	1.0	388	4.0	1.9-05	7.8	265	0.97	
49	i	2600	2898	1.0	388	6.0	6.3-05	7.4	264	0.97	
50	i	2600	2851	1.0	388	8.0	2.1-04	7.1	262	0.97	

The models in Tab. 3.5, p. 69, demonstrate a point of major concern connected with Eq. (3.1): the arbitrariness of the maximum dust opacity. In [Bowen 1988a] no really convincing arguments can be found why κ_{max} should have the value 0.95. The quantity κ_{max} directly increases the acceleration due to radiation pressure on dust, thereby increases the final outflow velocity and thus scales the mass loss rate. Therefore, the mass loss rates obtained with $\kappa_{max} = 0.95$ can only represent a qualitative trend and should be taken with care when used for quantitative interpretations.

Furthermore, as shown in Tab. 3.6, see p. 69, there is a general tendency in the models with an assumed radiation pressure on dust, that, if the value of $\kappa_{max} = 0.95$ is taken for real, the values of the final outflow velocities are confined to a rather narrow interval. Even if the models are calculated in the adiabatic limit case, and a rather high luminosity is assumed the values of the outflow velocity do not exceed 10 km s^{-1} too much. However, as stated in Sec. 1.2.2, the observed values of the final outflow velocity show a larger scattering and values of ≈ 20 km s^{-1} are common. In the models presented in this section, these values can only be reached by an arbitraryly scaling of κ_{max}, cf. Tab. 3.5, p. 69.

Radiation pressure on dust is responsible for accelerating the material to supersonic velocities. This mechanism is simulated by a simple step function, which is primarily governed by the course of the temperature. In turn, the temperature structure, given by the Lucy–approximation is rather insensitive to changes in the other quantities. Hence, the radial course of the radiation pressure on dust is more or less the same for all these models, i.e. the region where the maximum value of the acceleration is reached is always around 2 $R_{\star}$. As the acceleration is so similar for various kinds of parameters, the models exhibit a rather unique structure, and show only a narrow distribution of the final outflow velocities.

In conclusion we state, that the models presented in this section stress the necessity of taking into account the important interaction mechanisms and physical processes for the modelling of CDS around LPVs. Since these models neglect, e.g. the interaction of hydrodynamics and dust formation, and neglect a detailed treatment of dust formation and growth at all, they turn out to be unsatisfactorily for a comprehensive understanding of the objects under consideration and a quantitative comparison with observations.

Table 3.5: Sample of evolved models with assumed radiation pressure on dust and varying κ_{max}. The stellar temperature $T_\star$ is given in [K], the stellar luminosity $L_\star$ is given in [$L_\odot$], the stellar mass $M_\star$ in [$M_\odot$], the period P in days, the piston amplitude Δu in [km s^{-1}], the mass loss rate $\dot{M}$ in [$M_\odot yr^{-1}$], the final outflow velocity u_∞ in [km s^{-1}], the initial stellar radius $R_\star$ in [$R_\odot$], the position of the inner boundary is given units of the initial stellar radius.

No.	gas	$T_\star$	$L_\star$	$M_\star$	P	Δu	$\dot{M}$	u_∞	$R_\star$	R_{inner}	Rem.
1	i	3000	5340	1.0	400	3.0	3.6-07	0.47	270	0.92	$\kappa_{max} = 0.7$
2	i	3000	5340	1.0	400	3.0	1.1-05	25.7	270	0.92	$\kappa_{max} = 2.0$
3	i	3000	5344	1.0	400	3.0	6.7-06	19.6	270	0.92	$\kappa_{max} = 1.5$

Table 3.6: Sample of evolved models with assumed radiation pressure on dust. The units are explained in the text and in the caption of the previous Tab. 3.5

No.	gas	$T_\star$	$L_\star$	$M_\star$	P	Δu	$\dot{M}$	u_∞	$R_\star$	R_{inner}	Rem.
1	i	2900	4394	1.25	322	3.0	4.6-08	6.1	262	0.97	
2	i	2500	2365	1.0	370	3.0	5.6-06	7.7	258	0.96	
3	i	2390	2300	1.0	427	3.0	2.8-05	7.5	279	0.96	
4	i	3000	4045	1.0	325	3.0	1.3-04	8.6	235	0.84	
5	a	2450	12360	1.0	388	1.0	5.3-03	10.0	616	0.82	
6	a	2450	3771	1.0	388	1.0	2.6-04	9.4	340	0.82	
7	a	2450	26130	1.0	388	1.0	3.2-05	9.9	895	0.82	
8	a	2450	7073	1.0	388	1.0	2.3-03	11.7	466	0.82	
9	a	3000	5443	1.0	400	3.0	1.0-04	12.8	272	0.92	
10	i	3000	5340	1.0	400	3.0	1.2-08	2.2	270	0.92	no dust

Chapter 4

Dynamical models of CDS including a consistent treatment of dust formation

4.1 The range of the model parameters

Our models are defined by the prescription of the 4 fundamental stellar parameters: $(M_\star, L_\star, T_\star, \epsilon_C/\epsilon_O)$, the stellar mass, the stellar luminosity, the effective temperature, the overabundance of carbon to oxygen, respectively, and two additional parameters describing the pulsation of the underlying star: (P, Δu), the period of the piston, and the amplitude of the piston. The other elements are assumed to have a solar abundance.

Alternatively, instead of prescribing $L_\star$, it is also possible to choose $R_\star$ by Eq. (2.50) as an initial parameter and to derive $L_\star$ by Eq. (2.51).

The sets of parameters we have chosen for the exemplary model calculations to be presented in the *first part* of this chapter are listed in Tab. 4.1. It should be kept in mind that the parameters are chosen with regard to the study of the interaction of the various processes and therefore some are chosen perhaps somewhat extreme to underline the effects of certain interactions or to avoid the occurrence of other effects, namely *multiperiodicity*, which are discussed in succeeding chapters. During the stage of performing the numerical calculations it has been proved to be a rather feasible task to find combinations of model parameters for models which reveal a periodic behaviour from one period to the next. Most of the models that we calculated are in fact multiperiodic and in the Chapters 5 and 6 it will become clear why this is indeed true. A slightly extended grid of model calculations contains Tab. 4.3 in the *second part* of this chapter.

Before, however, some remarks concerning the determination of the fundamental parameters from observations seem to be appropriate.

Table 4.1: Parameters of the initial hydrostatic models, already presented in [FLEISCHER *et al.* 1992]. $R_\star(t=0)$ is calculated using the period-mass-radius relation Eq. (2.50). Then, $L_\star$ is derived from Eq. (2.51), except otherwise stated

Model	A	B	C**	D	E**	F**	G**	H**	I*
$T_\star$ [K]	3000	2900	2800	2800	2600	2600	2500	2800	3000
ϵ_C/ϵ_O	2.8	3.0	2.0	2.4	1.8	1.55	1.95	2.5	–
$L_\star$ [$10^3\,L_\odot$]	4.59	4.31	6.50	4.03	10.0	7.5	7.5	7.0	4.59
$R_\star(t=0)$ [$R_\odot$]	251.2	262.2	355.6	269.9	508.4	437.1	470.6	355.0	251.2
$M_\star$ [$M_\odot$]	1.0	1.25	1.0	1.0	1.0	1.0	1.0	1.0	1.0
P [d]	350	322	400	400	650	900	450	500	350
Δu [km s^{-1}]	3.0	3.0	2.0	3.0	2.0	2.0	2.0	2.0	3.0

* model calculation with an assumed radiative acceleration
** $L_\star$ taken as initial model parameter, $R_\star$ calculated with Eq. (2.51)

4.1.1 Derivation of stellar masses from observations

The masses of cool late-type stars, which are not directly measurable in the single star case, are not known very accurately, and are still a matter of debate. All attempts to deduce stellar masses from observations rely e.g. on evolutionary scenarios, models of the galactic rotation or on other observable quantities, e.g. distances and luminosities, and are therefore rather uncertain.

In a series of papers [ZUCKERMAN AND DYCK 1986A], [ZUCKERMAN *et al.* 1986], [ZUCKERMAN AND DYCK 1986B] and [ZUCKERMAN AND DYCK 1989] established a correlation between the outflow velocity u_∞ of red giant stars and their galactic latitude: There is a clear evidence that stars with large outflow velocities are located near the galactic plane. They infer that AGB carbon stars wit $u_\infty \geq 19 kms^{-1}$ should have main–sequence masses $M_{ms} \geq 3M_\odot$, those with u_∞ between 9 and 18 kms^{-1} had M_{ms} between 1 and 3 $M_\odot$ and those objects with $u_\infty < 9kms^{-1}$ had $M_{ms} \approx 1M_\odot$. Assuming the mass of their final state as a white dwarf to be $\approx 0.6M_\odot$ gives an estimate of their present mass. The results of Zuckerman et al. are different from the results of [CLAUSSEN *et al.* 1987] who found a rather narrow range of main-sequence masses, between 1.2 and 1.6 $M_\odot$. In contrast, [THRONSON *et al.* 1987] claimed a mass interval between 3 and 5 $M_\odot$. Very recently [BARNBAUM *et al.* 1991] found mounting evidence that the mass range of carbon star progenitors is rather large similar to the earlier results of Zuckerman et al.

Summarizing, values around 1.0 $M_\odot$ seem to be a reasonable choice for C-stars, furthermore since it will turn out that the stellar mass is not a sensitive parameter for our model calculations.

4.1.2 Derivation of stellar luminosities from observations

Since the determination of the distance of Miras and LPVs underlies considerable uncertainties their luminosities are not known very accurately.

Based on broad-band infrared photometry of 89 stars in the LMC and 21 sources in the SMC [Cohen *et al.* 1981] derived a mean luminosity of $\approx 6400 L_\odot$ for their sample, fainter than expected [Blanco 1989].

Using statistical parallaxes, which is described in [Clayton and Feast 1969], [Robertson and Feast 1981] present luminosities of individual objects in different environments, e.g. R Hya $12000 L_\odot$, R Leo $14700 L_\odot$ or o Ceti $2550 L_\odot$. Furthermore, [Robertson and Feast 1981] derived a M_{bol}–period relation for galactic Miras, cf. their Fig. 1. This relation shows a near linear correlation between the luminosities and the periods in the range from 150 to 400d.

[Wood 1986] reviews period–luminosity laws derived from infrared observations of the Galactic Bulge and the Magellanic Clouds. Usually all these laws show an increase of luminosity with period. For AGB-stars Fig. 1 of [Wood 1986] shows a maximal luminosity of $\approx 48000 L_\odot$ at periods around 600d.

[Claussen *et al.* 1987] find for a sample of 215 carbon stars a range of luminosities from $6\,10^3 L_\odot$ to $4\,10^4 L_\odot$ with a mean value of $L_\star \approx 1.0\,10^4 L_\odot$. They find the luminosities to be independent of the period, cf. [Claussen *et al.* 1987] Fig 8, which they assign to the assumption of a constant $M(K)$ value for all stars of their sample.

The luminosity values we have chosen for our calculations (see Tabs. 4.1 and 4.3) cover, if taken at phase zero, the whole observed range of typical luminosities of Miras and LPVs.

4.1.3 Derivation of effective temperatures from observations

To derive effective temperatures from observations there are in principle at least two methods available.

The *lunar occultation method* yields the angular diameter θ of the source, and together with the bolometric flux f_{bol} at the earth the effective temperature : $T_{eff} = (4 f_{bol}/\sigma\theta^2)^{1/4}$, where σ is the Stefan–Boltzmann constant. E. g. [Ridgway *et al.* 1980a] and [Ridgway *et al.* 1980b] used this method to determine angular diameters and effective temperatures of late-type stars.

The *infrared flux method*, as used e.g. by [Blackwell *et al.* 1980] and [Tsuji 1981], in addition needs the measurement of a monochromatic stellar flux f_λ at an infrared wavelength and it is assumed that f_λ can be taken as the continuum flux at this wavelength. Then $f_\lambda = \theta^2 F_\lambda/4$, which must be solved iterationally together with the previous equation for the effective temperature, since the emergent stellar flux F_λ is not a priori known and furthermore is a function of the effective temperature and other stellar parameters.

For sources where both methods are applicable the results are in good agreement, cf. [Tsuji 1981] Tab. 3, where the maximal temperature difference is about 10% .

The result of these investigations is that the majority of carbon stars of spectral type N, classified as SRb or Lb variables, i.e. as small amplitude or even irregular variables, are confined to a temperature range between 2400 and 3200 K. M-giants of the spectral type between M0 and M6, in contrast, mostly occupy the temperature range between 3200 and 3900 K. The sample of [Tsuji 1981] contained no Miras or SRa stars. From [Lambert *et al.* 1986] Table 3 it can be seen that they are confined to temperatures between 2400 and 3000 K.

Photometric observations from $0.35\mu m$ to $10\mu m$ performed by [Mendoza and Johnson 1965] of 39 Carbon stars and 6 LPVs yield an effective temperature range from 2270 to $5550K$.

4.1.4 Derivation of the overabundance of carbon to oxygen

An important parameter of our calculations is the overabundance of carbon to oxygen, $\epsilon_C/\epsilon_O > 1$, for C-stars which are to be considered in the present investigation. While it seems to be relatively easy to make a general distinction between C- and M-stars, since their spectra show many characteristic peculiarities, only a few authors have undertaken the difficult task to determine the actual value of the ratio ϵ_C/ϵ_O. Unfortunately, there are major discrepancies. Based on high-resolution infrared observations and on model atmospheres [Lambert *et al.* 1986] derived from their sample of 30 cool carbon stars an average value of $\epsilon_C/\epsilon_O = 1.15$. This sample contains almost exclusively non-Mira stars with rather low mass loss rates [Olofsson *et al.* 1987] and it may be biased towards low ϵ_C/ϵ_O ratios [Lambert *et al.* 1986]. Very recently [Eglitis 1993] reanalyzed Lamberts sample of stars and more or less confirmed their abundance ratios.

In contrast, [Gow 1977] based on spectrophotometry derived rather high ϵ_C/ϵ_O ratios, most of the 61 stars of his sample have a value of ϵ_C/ϵ_O between 1.3 and 4.0 and the average value is 2.14. Using the same method as Gow, [Frantsman and Eglitis 1988] derived an average ϵ_C/ϵ_O ratio of 1.7 for their sample of 64 stars.

Tables 4.1 and 4.3 show our ϵ_C/ϵ_O ratios mostly chosen in the range deduced by [Gow 1977] and [Frantsman and Eglitis 1988] to account for stars with significant amounts of carbon dust.

4.1.5 Derivation of periods and pulsational amplitudes

Probably the best determined parameter of Miras and LPVs is the period. Extensive observational material of visual lightcurves is compiled e.g. in [KHOLOPOV *et al.* 1985] and also by amateurs in e.g. [KOWALSKY *et al.* 1986]. Except for a few "test" calculations, we chose periods typical for Miras and LPVs.

Comparatively little is known on the amplitude of the pulsation. E.g. [WOOD 1986] adjusts the variable pressure at the inner boundary of his models to give a certain photospheric density which is deduced from observations. This results in a velocity amplitude of a few kilometers per second at the inner boundary. Similar values are applied by [BOWEN 1988A], thus, we chose the same range of amplitude values.

4.2 The models

In this section we present eight exemplary models (most of them already presented in [FLEISCHER *et al.* 1992]), which include a consistent treatment of the dust complex according to the moment method outlined in Chapter 2 (An extended grid of models is presented in Sec. 4.4). The parameters of the initial hydrostatic models are shown in Table 4.1. For comparison, we listed in the table an additional model (Model I) with an assumed radiation pressure on dust according to the formula given in [BOWEN 1988A], whose parameters correspond to Model A.

Again, with regard to a consistent modelling approach, we would like to point out that besides the four fundamental parameters $(M_\star, R_\star, T_\star, \epsilon_\mathrm{C}/\epsilon_\mathrm{O})$ or $(M_\star, L_\star, T_\star, \epsilon_\mathrm{C}/\epsilon_\mathrm{O})$, respectively, there are only two additional parameters $(\Delta u, P)$ describing the pulsation.

For model I no overabundance of carbon to oxygen has to be specified since this is the model calculated with an assumed radiation pressure on dust. Therefore, it is not necessary to calculate the chemical composition of the gas.

Figures 4.1 and 4.2 show the radial structure of the models with a consistent treatment of the dust complex. For the radial structure of a model calculated with an assumed radiation pressure on dust we refer to the previous Chapter. The capitals A, B, ... refer to the models listed in Table 4.1. All models are plotted at phase zero of the pulsation cycle. Model E, which is not shown in Figs. 4.1 and 4.2, is discussed in detail in Sect. 7.3.3.

Each row in Figs. 4.1 and 4.2 belongs to one model. The left plot of each row shows

a. the velocity structure u (solid line) and the velocity of sound u_s (short dashed line) and

b. the temperature structure T (long dashed line).

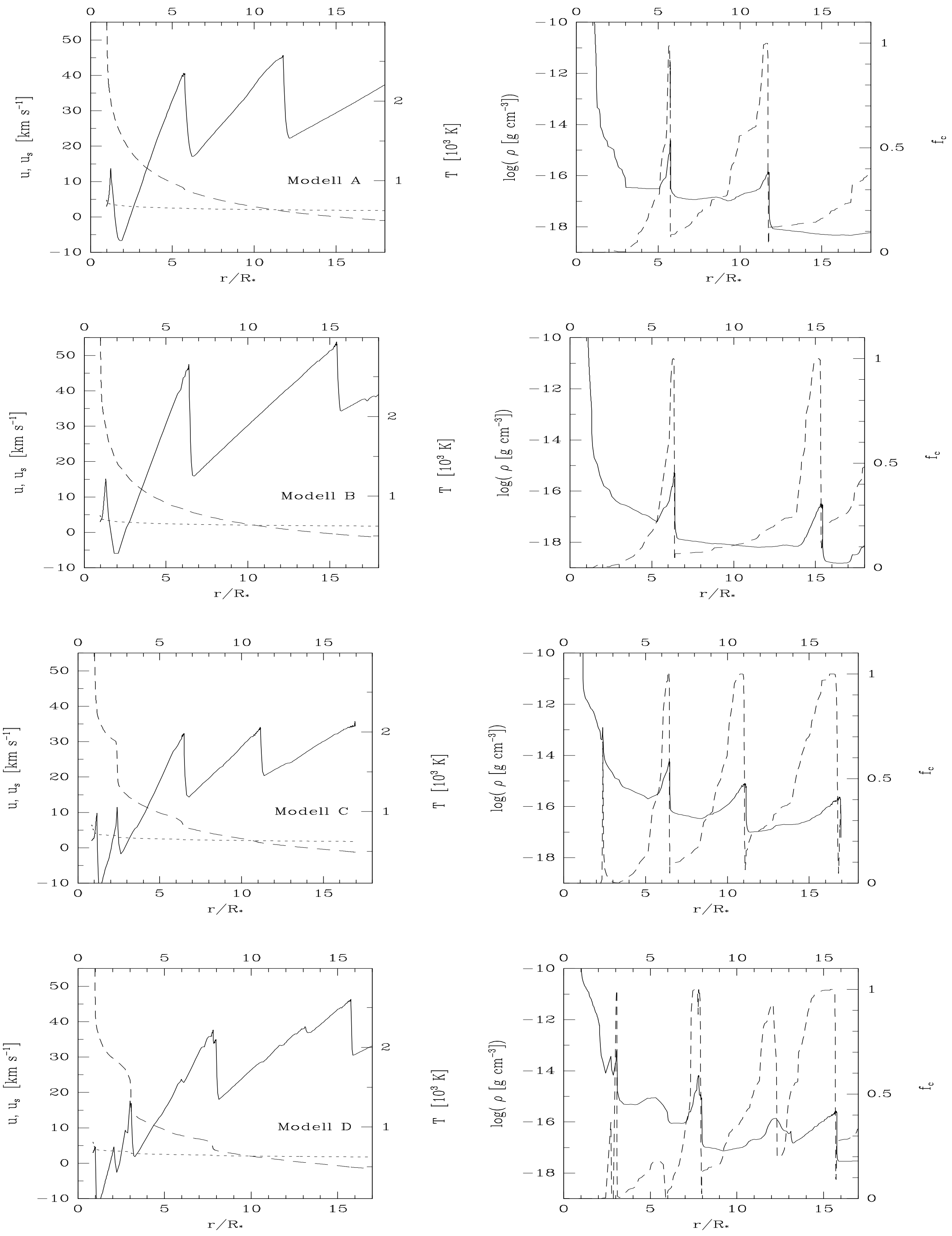

Figure 4.1: Radial structure of four exemplary models at the beginning of the pulsational cycle. The quantities are explained in the text. For the model parameter refer to Tab.4.1

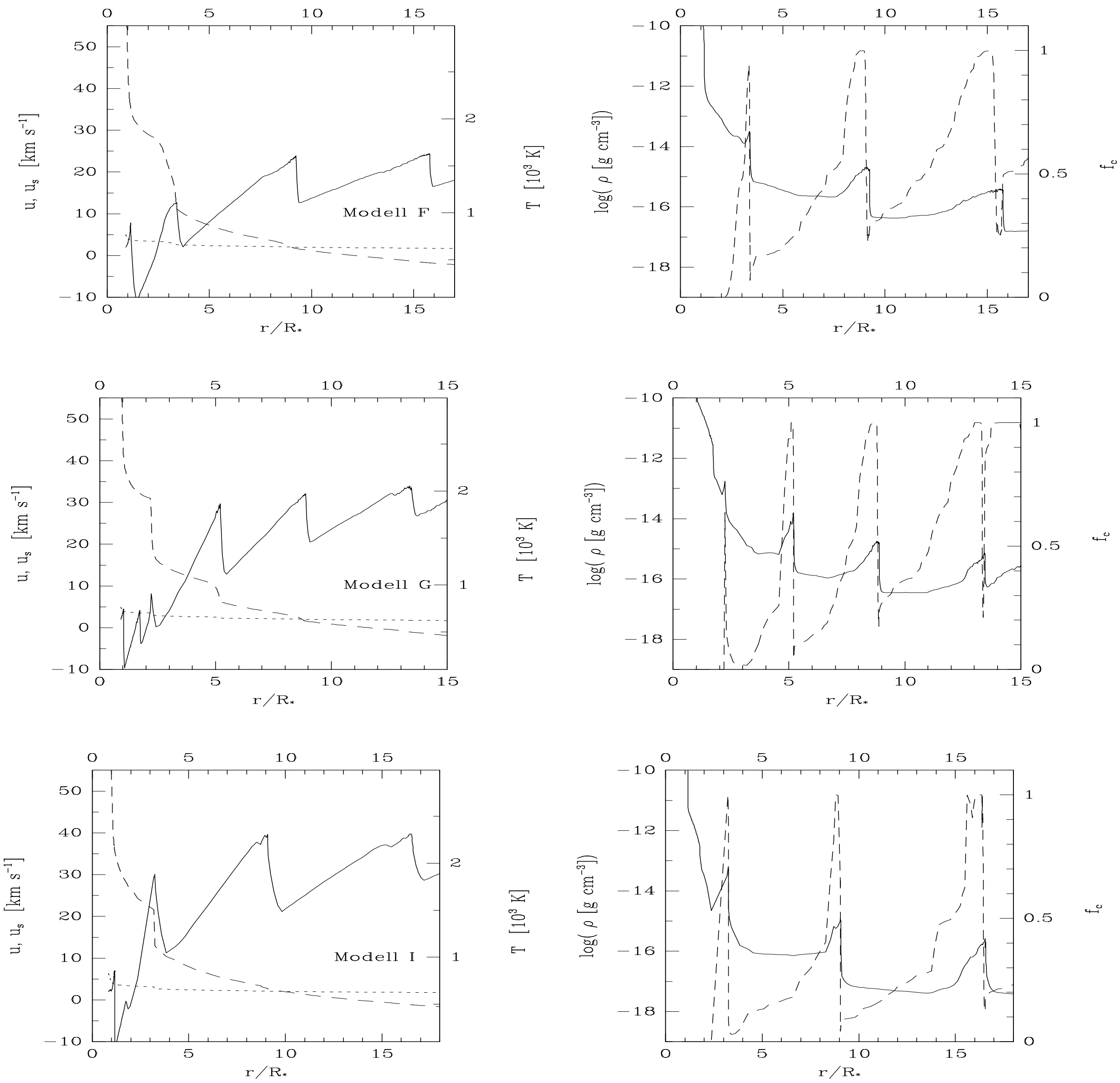

Figure 4.2: Radial structure of three more models with consistent treatment of dust formation growth and evaporation. For the model parameter refer to Tab. 4.1

The right hand plot of each row shows

a. the logarithm of the density ρ (solid line) and

b. the course of the degree of condensation f_c, i.e. the degree of condensable material actually condensed into grains (long dashed line). The value 1 denotes maximum degree of condensation, 0 no condensation.

A direct comparison of the models containing a simultaneous treatment of dust formation, growth and evaporation (Models A – H) with the calculations including the simplified description of the dust complex (cf. Chap 3) shows four major differences:

1) The maximum value of the radiative acceleration on dust dramatically exceeds the maximum value assumed by [Bowen 1988a] and is strongly correlated to the hydrodynamical structure, also in contrast to Bowen's models.

2) The second striking feature of models A – H, inherent in all our calculations, is an inhomogeneous distribution of the dust particles. This can be seen from the plot of the degree of condensation. The dust grains are concentrated in distinct layers, equidistant for each model, and the CDS exhibits a shell or onion like structure.

3) The models are passed periodically by strong shock waves. A direct comparison, e.g between Model A and the corresponding model with an assumed radiation pressure on dust (Model I), shows, that there are less shocks per radius interval in Model A, which means, that the shock waves propagate with a higher velocity through the atmospheres of these models.

4) At that instant of time shown in Fig. 4.1, especially for models C, D, E, F, G and H, the determining influence of the dust on the thermodynamical structure can be seen. The jump in the temperature structure occuring at $r \approx 2.5\ R_\star$ coincides with the spike of the radiative acceleration α located at $r \approx 2.5 R_\star$. This temperature jump of more than 500K, which also shows up in the models A and B at later phases, results from the opacity of the newly formed dust which is taken into account in the determination of the temperature $T_{\rm eq}$, according to Eq. (2.39).

The reason for these differences is the close coupling of dust formation to hydrodynamics and thermodynamics. This can be seen, especially for the dynamics, from the radial structure of the velocity in model C. The peak of the velocity around $r = 2.5\,R_\star$, coincides with the innermost maximum of the radiative acceleration on the dust grains α. Obviously, α induces a perturbation in the velocity structure which subsequently steepens to become a new dominating shock.

Table 4.2: Values of the averaged mass loss rate, the averaged outflow velocity, the averaged dust to gas ratio, the maximum and minimum of the monochromatic optical depth at $\lambda = 1\mu m$, the maximum and minimum of the stellar luminosity, the maximum velocity jump at the shock front. All values are calculated from the evolved models. $< \dot{M} >$ is given in $M_\odot$ yr^{-1}, $< u_\infty >$ is given in [km s^{-1}], the luminosities are given in [$10^3 L_\odot$] and Δu_{max} is given in [km s^{-1}], a(-b) means a 10^{-b}.

Model	A	B	C	D	E	F	G	H	I
$< \dot{M} >$	3.9(-7)	1.2(-7)	4.0(-6)	3.3(-7)	1.0(-5)	1.2(-5)	6.4(-6)	2.2(-6)	1.9(-7)
$< u_\infty >$	36.8	39.1	28.1	29.4	28.5	19.6	28.5	33.6	7.1
$\rho_d/\rho_g * 10^{-3}$	3.3	3.3	3.4	3.6	2.9	2.1	3.4	3.3	–
$\tau_{1\mu,\mathrm{max}}$	2.6	1.6	10.2	6.0	19.2	17.5	21.4	–	–
$\tau_{1\mu,\mathrm{min}}$	0.8	0.3	5.2	2.0	10.1	8.0	13.1	–	–
$L_{\star,\mathrm{max}}$	5.46	5.12	7.62	4.82	12.01	9.35	9.43	8.75	5.44
$L_{\star,\mathrm{min}}$	3.90	3.77	4.77	3.43	8.70	6.46	6.96	5.48	3.88
Δu_{max}	30.4	22.5	22.6	27.7	19.8	14.9	19.5	22.1	27.6

This phenomenon has already been briefly investigated in [Fleischer *et al.* 1991] and will become clearer when we analyze one model in detail in the next section.

Although there are significant differences between the models A – H and I, all models have in common the levitation of the atmosphere in comparison to an exponentially decreasing density structure of a hydrostatic model. This effect is due to the deposition of mechanical energy caused by the piston assumption at the inner boundary which simulates the interior pulsation. As already mentioned, all models are passed periodically by shock waves and develop an outflow or wind.

Table 4.2 shows some resulting global quantities of the fully evolved model calculations: the time averaged values for the mass loss rate $< \dot{M} >$, the time averaged final outflow velocity $< u_\infty >$, the averaged dust to gas ratio $< \rho_d/\rho_g >$, the maximum and minimum value of the optical depth τ at $\lambda = 1\mu m$, maximum and minimum stellar luminosity $L_{\star,\mathrm{max}}$, $L_{\star,\mathrm{min}}$ during a cycle (typical course shown in Fig. 2.4) and the maximum velocity jump at the shock front Δu_{max}.

A more detailed analysis of the dependence of the resultant quantities on the model parameters is subject of Sec. 4.4. Here, we only list some obvious results.

From the plot of the radial structures in Figs. 4.1 and 4.2 it can be seen, that both, the mass loss rates and the hydrodynamical velocities are strongly varying during a cycle. The mass loss rates vary by at least one order of magnitude. Therefore, instead of taking the actual local values of $\dot{M}$, u_∞, ρ_d/ρ_g we consider their corresponding mean values averaged over one pulsational period. For $r = 15R_*$ the averaged values are shown in Table 4.2.

The mass loss rates fit reasonably well into the observed range for Miras and LPVs, whereas the final outflow velocities of the models with consistent treatment of dust formation and growth exhibit relatively high values. Especially, those models with a value of the overabundance of oxygen to carbon exceeding 2.5 show the highest values of $< u_\infty >$. Although not unrealistic, they obviously belong to the upper half of the range of observed wind velocities.

In addition, one gets a first result concerning the relation between the overabundance of carbon to oxygen ϵ_C/ϵ_O and the averaged outflow velocity $< u_\infty >$. From Table 4.1 and Table 4.2 it can be seen immediately that a high excess of carbon results in a high outflow velocity, a tendency already known from stationary model calculations of CDS (e.g.[Gail and Sedlmayr 1985]). But obviously, this connection is also dependent on other parameters and again we refer to Sec. 4.4.

Model D does not look as "perfect" as the other models do. Some remarks at the end of Sec. 4.3.1 seem to be appropriate.

4.3 Exemplary analysis of a model with consistent treatment of dust formation

To study the process of dust formation, growth and evaporation under dynamical conditions our computational method allows two canonical ways to depict the results.

One way is, of course, to plot the global radial structure of the shell at various instants of time to get an overall picture of the CDS. The other way is, to follow selected mass elements during a certain time interval, by means of the Lagrangian formulation. Thereby, these elements serve as tracers for the varying physical conditions throughout the shell. Both descriptions are necessary for a complete understanding of the physical situation in the shell.

As an example, we present both descriptions in detail for model E. We omit this discussion for the other models with a detailed treatment of the dust complex, because their radial structure and temporal behaviour are qualitatively similar.

4.3.1 The radial structure

Figures 4.3,...,4.6 show a time sequence of the radial structure of the CDS during a little more than one cycle at several selected instants of time. Figures 4.3 and 4.4 comprise the first half of this cycle, Figs. 4.5 and 4.6 the second half and the

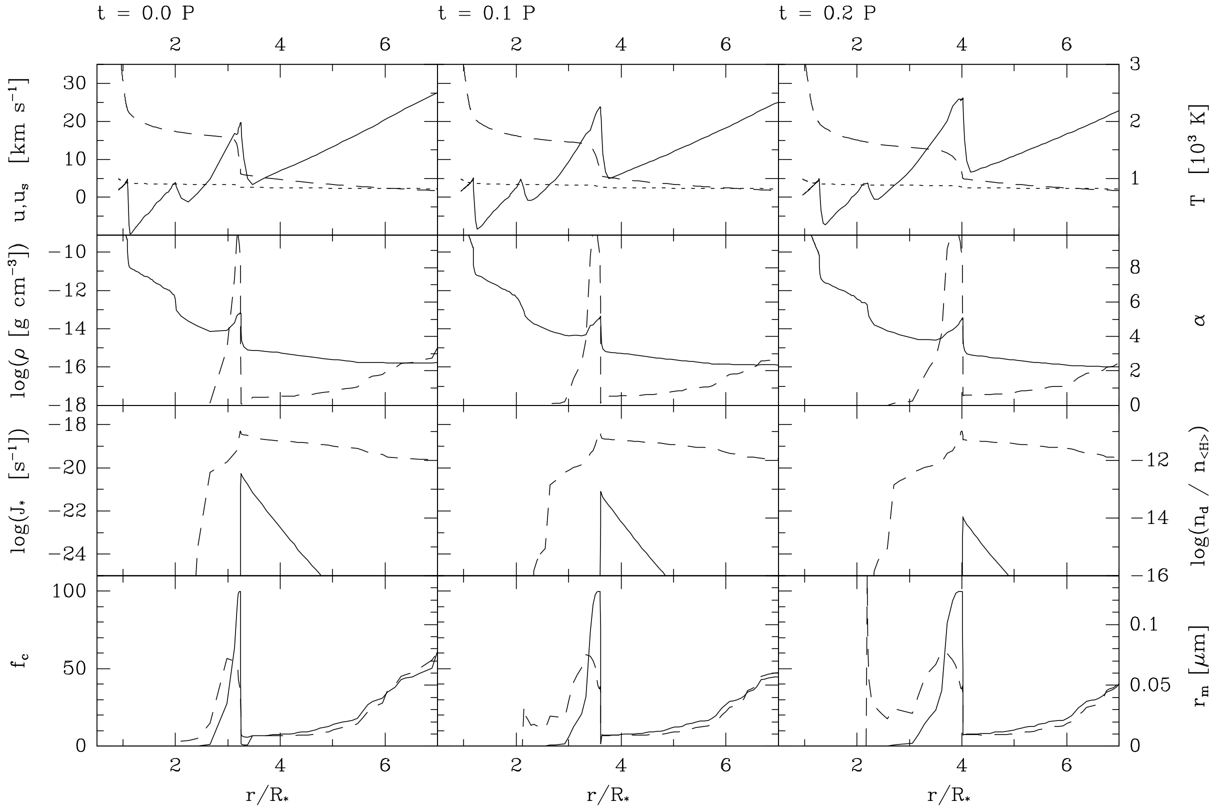

Figure 4.3: Radial structure of Model E at selected instants of time during the pulsational cycle

---

beginning of the next pulsational period. In each plot the time increases from left to right.

Figure 4.3 shows the time sequence of the radial profile of the *hydrodynamical and dust* quantities at three instants, beginning at the first half of the pulsational cycle:

upper row: the velocity u (solid line), the velocity of sound u_s (short–dashed line), both belong to the l.h.s. ordinate, and the temperature T (long–dashed line), r.h.s. ordinate,

2nd row: the logarithm of the density ρ (solid line, l.h.s. ordinate) and the radiative acceleration α in units of the gravitational acceleration (dashed line, r.h.s. ordinate),

3rd row: the logarithm of the nucleation rate $J_\star$, i.e. the number of dust grains formed per second and H-atom (solid line, l.h.s. ordinate), and the logarithm of the number of dust grains per H-atom $n_\mathrm{d}/n_{<\mathrm{H}>}$ (dashed line, r.h.s.ordinate). If relevant evaporation occurs also the logarithm of the

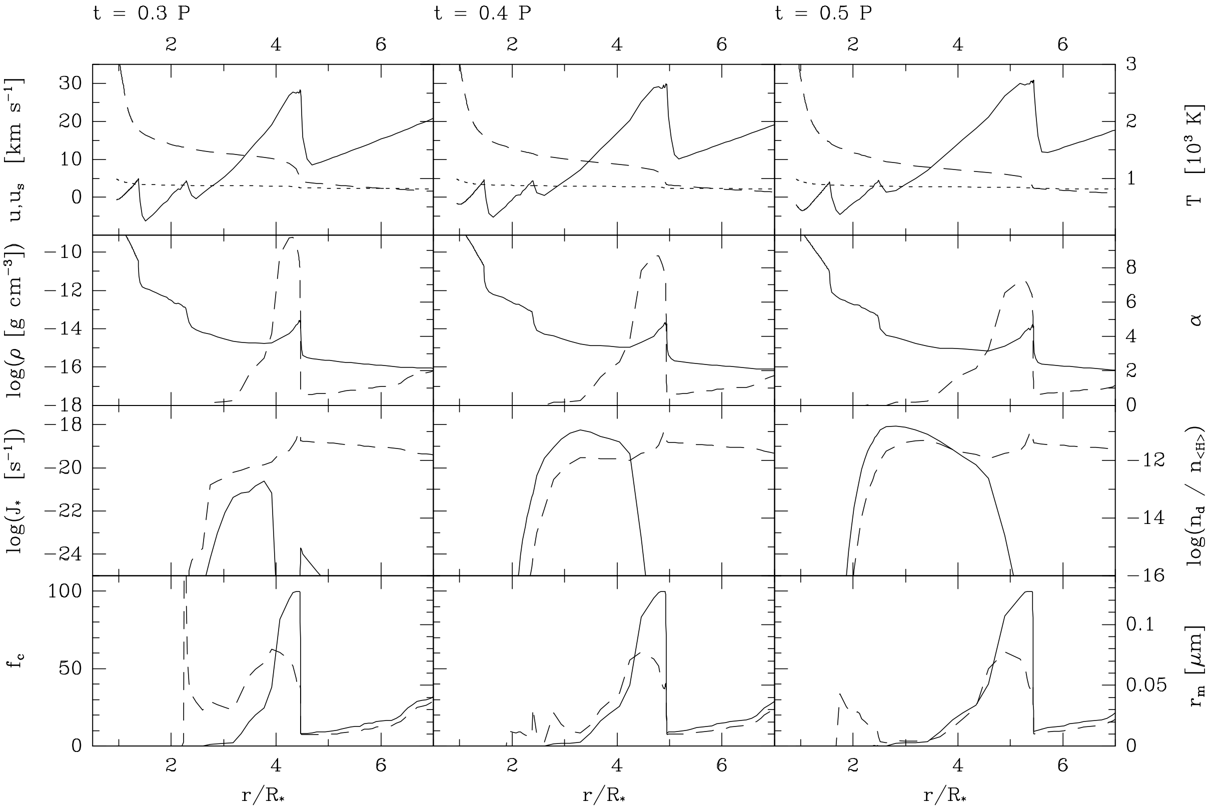

Figure 4.4: Fig. 4.3 continued

evaporation rate $J_{\rm ev}$ is shown (dashed-dotted line) and scaled as the nucleation rate,

lower row: the degree of condensation $f_{\rm c}$ (solid line, l.h.s. ordinate), and the mean particle radius r_m (dashed line, r.h.s. ordinate). The degree of condensation is given in % .

The radius is always plotted in units of the stellar radius of the initial hydrostatic model.

Figure 4.4 shows the time sequence of the radial profile of the *same* quantities at the following three instants of time.

Figures 4.5 and 4.6 continue the time sequence of the radial structure of the same quantities at six instants during the second half of the first pulsational cycle and the first half of the next pulsational cycle..

This sequence of plots can be conceived as a periodically repeating series since the situation at $t = \beta\, P$ equals the structure at $t = (\beta + 1)\, P$, where β is an arbitrary dimensionless time parameter.

It is natural to define the beginning of the cycle of dust formation as that instant of time where a new maximum in the number of dust particles per H-atom arises. Thus, we conclude that the cycle of dust formation starts between

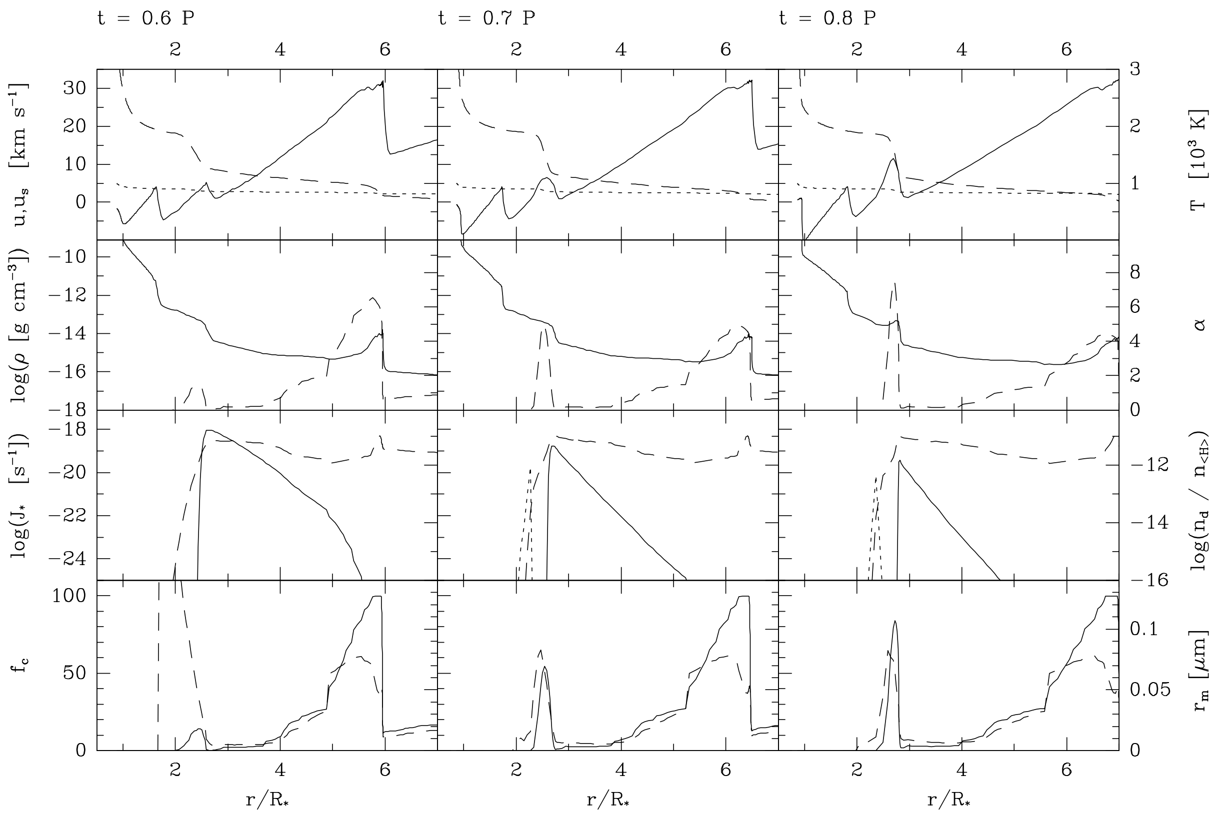

Figure 4.5: Fig. 4.4 continued

$t = 0.2P$ and $t = 0.3P$ of the hydrodynamical cycle. Nevertheless, we begin the time sequence shown in Figs. 4.3,..., 4.6, at $t = 0.0P$ of the hydrodynamical cycle. Dust formation and interior pulsation are phase-shifted. However, this is not an essential result, since the beginning of the hydrodynamical cycle has been chosen arbitrarily, see Sect. 2.3.

The discrete, shell like structure of the radial dust distribution can be understood by the following *discussion of the interaction of the dust formation and the hydrodynamics and thermodynamics.*

Between $t = 0.2P$ and $t = 0.3P$ a new peak in the nucleation rate develops in the radius interval between $3\,R_\star$ and $4\,R_\star$. Subsequently, the number of dust grains per H-atom steeply increases in this radius interval. There are two reasons for this nucleation phase.

First, the material that has been pushed outwards by the preceding shock front is now decelerated or almost at rest and remains in a region with fairly constant density in the radius interval under consideration (cf. time development of the density structure between $t = 0.2P$ and $t = 0.4P$). Second, the temperature is decreased substantially. For example, the temperature at $3.0R_\star$ which exceeds 1700 K at $t = 0.1P$, drops down to 1300 K at $t = 0.4P$. This happens on the one hand due to the inward movement of the inner boundary, which causes

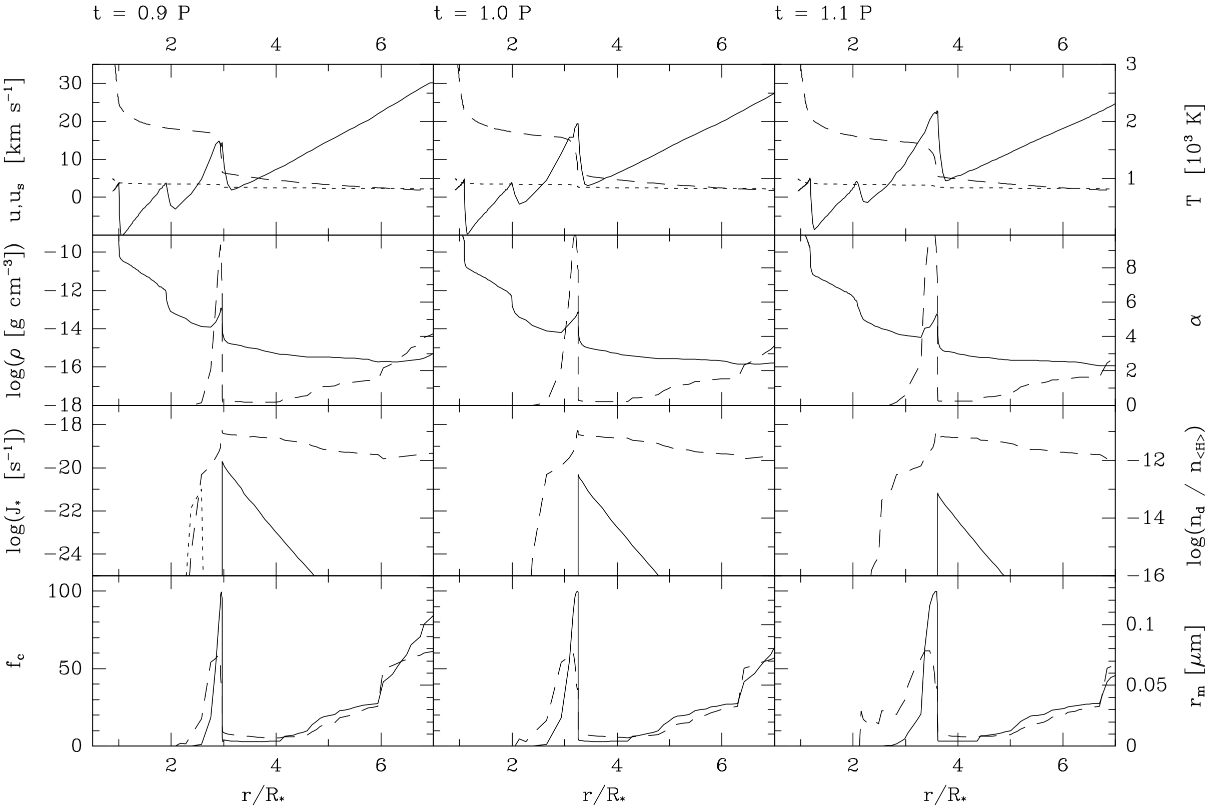

Figure 4.6: Fig. 4.4 continued

---

also an inward movement of the stellar radius between $t = 0.3P$ and $t = 0.75P$ and therefore a decrease of the temperature at a given radial distance from the star. On the other hand, and more important, this happens due to the vanishing influence of the back-warming of the preceding dust layer. We will discuss this effect in some more detail at the end of this section.

The decrease of the temperature is the most important process in this time interval. It provides conditions that are favourable especially for the nucleation of dust particles, as can be seen by the inward moving peak in the nucleation rate, the subsequent steep increase of the number of dust grains per H-atom up to $n_{\rm d}/n_{<\rm H>} = 4.0\,10^{-12}$ at $r = 3.0R_\star$ and at $t = 0.5P$, and the steep decrease of the mean particle radius r_m due to many small newly formed grains. Finally, the growth of the grains causes a tiny, but noticeable peak of the degree of condensation $f_{\rm c}$ of about 2% around $3R_\star$ at $t = 0.5P$.

At $t = 0.6P$ these dust particles at the inner edge, between $r = 2.5R_\star$ and $r = 3.0R_\star$, are overrun by the new shock wave which develops in the radius interval $r < 2.0R_\star$ in the first half of this hydrodynamical cycle. Although, it is already damped (cf. decreasing velocity amplitude of the innermost shock from $t = 0.1P$ to $t = 0.5P$), this shock wave suffices to compress the mass elements containing the newly formed dust particles, thereby providing favourable conditions for particle growth by increasing the density of at least two orders of magnitude. This causes a steep increase of the degree of condensation around $r \approx 2.8R_{\star}$ from $t = 0.7P$ to $t = 0.9P$, which amounts to values as high as 98%.

According to Eqs. (2.15) and (2.42) a steep increase of the radiative acceleration on dust grains follows (cf. the plot of α in Fig. 4.5), reaching a maximum value of $\alpha = 9.1$ at $r = 2.9R_{\star}$ and $t = 0.9P$. This acceleration reverses the infall of the dust particles, and moreover induces a perturbation into the velocity field which subsequently steepens to become a new strong shock wave. This shock is connected with an outgoing shell of material as can be seen in Fig. 4.4 by the outmoving peak of the degree of condensation, which reaches values as high as 100%.

During this process of forming the dust generated shock between $t = 0.7P$ and $t = 0.9P$, new particles are still formed in front of the peak of the degree of condensation, i.e. at larger radii (cf. plot of $n_{\rm d}/n_{<{\rm H}>}$ at $r \geq 3.0R_{\star}$ and $t = 0.9P$), where $n_{\rm d}/n_{<{\rm H}>}$ reaches its maximum value of $1.0\,10^{-11}$. However, these grains are overrun by the newly formed shock. It sweeps up and compresses the material ahead of it and thus produces an enhanced density where the grains find excellent conditions for growth. By this effect, the radiative acceleration on dust is monotonically increased (self-accelerated) till its maximum value, followed by a broadening of the peak of α (cf. plots of α between $t = 0.0P$ and $t = 0.3P$). The velocity jump of the outgoing shock front is increased by radiation pressure on dust up to $\Delta u_{\max} = 19.7 \mathrm{km\,s^{-1}}$.

Summarizing this discussion so far, we can say that *dust formation is triggered by the interior pulsation in such a sense that the pulsation defines the onset of a new dust formation cycle by providing an appropriate temperature in the first half of the cycle and an appropriate density in the second half. Subsequently, the development of the circumstellar structure is dominated by the dust complex, which produces by a self-accelerating mechanism the dominating shock waves that run through the dust shell.*

In the innermost peak of the degree of condensation a large amount of dust effectively absorbs radiation and by its opacity affects the temperature structure according to Eq. (2.39). As can be seen from the plots of the temperature (especially Fig. 4.3), the dust opacity has a significant influence on the temperature profile. The step in the temperature stratification of at least 600K around $r = 3.2R_{\star}$ at $t = 0.0P$ moves outward along with the newly formed peak in $f_{\rm c}$ but always slightly behind. The effect is caused by the newly formed dust layer which blocks the outgoing radiation and therefore heats the material behind, i.e. at smaller radii.

The temperature reaches values high enough to evaporate a considerable amount of particles at the inner edge of the newly formed shell, as can be seen from the plot of the evaporation rate between $r = 2.2R_{\star}$ and $r = 2.8R_{\star}$ in the time interval $t = 0.7 - 0.9P$, accompanied by a decrease of the number of dust grains per H-atom $n_d/n_{<{\rm H}>}$ in the region under consideration. Furthermore, this back-warming prevents of course the formation of new dust particles in the inner region.

The temperature values are temporarily substantially higher and the dust forming region is narrower compared to calculations where the dust opacity is not taken into account (cf. [Fleischer *et al.* 1991], i.e. the temperature was determined exactly as described in [Bowen 1988a]), and back-warming does not occur.

The preceding discussion shows, that *the dust complex does not only have important influence on the hydrodynamics of the system but due to the "back-warming" effect also on its thermodynamics, and thereby triggers the formation of new dust particles.*

Model D: We would like to finish this section with some remarks concerning Model D, cf. Fig. 4.1. As the preceding discussion has shown, dust formation and growth are rather sensitive processes due to the local temperature and density conditions, respectively. Small fluctuations in the temperature, either due to physical or numerical reasons, may cause a beginning of dust formation in one Lagrangian element but not in the neighbouring mass shell. This causes the spikes visible in the degree of condensation at the innermost developing dust shell. Numerically these fluctuations may be caused by an insufficient distribution of the grid points in the innermost region of the CDS.

Furthermore, dust growth in Model D is so effective that two dust shells are formed during one pulsational cycle. The first shell formed during the cycle induces the dust–accelerated shock front, as described above, whereas the second dust forming and growth process in the wake of the first front cannot influence the hydrodynamical structure. It sweeps up the material and causes a density inversion but cannot build up a real shock front. Instead it only causes a slight perturbation in the velocity structure. Nevertheless, this is a constantly repeating phenomenon, as is indicated from the two intermediate shells at 5 and 12 $R_\star$ the distance of which is the same as that of the "regular" shells.

If the mechanisms described so far really take place in Miras and LPVs, then it is very unlikely, that the overabundance is so fine–tuned, that a completely regular pattern of the radial structure will arise. Hence, if moderate irregularities in the models occur, and it is assured that they are not due to numerical bugs, then probably these models are more appropriate to describe the real behaviour of Miras and LPVs as the totally regular calculations. There is no obvious physical mechanism, that ensures, that only *the* amount of carbon is dredged up, that suffices to produce absolute periodic structures.

4.3.2 Selected Lagrangian elements

Figures 4.7 and 4.8 show the time development of the physical quantities of interest during two periods in four selected Lagrangian zones, i.e. in the comoving

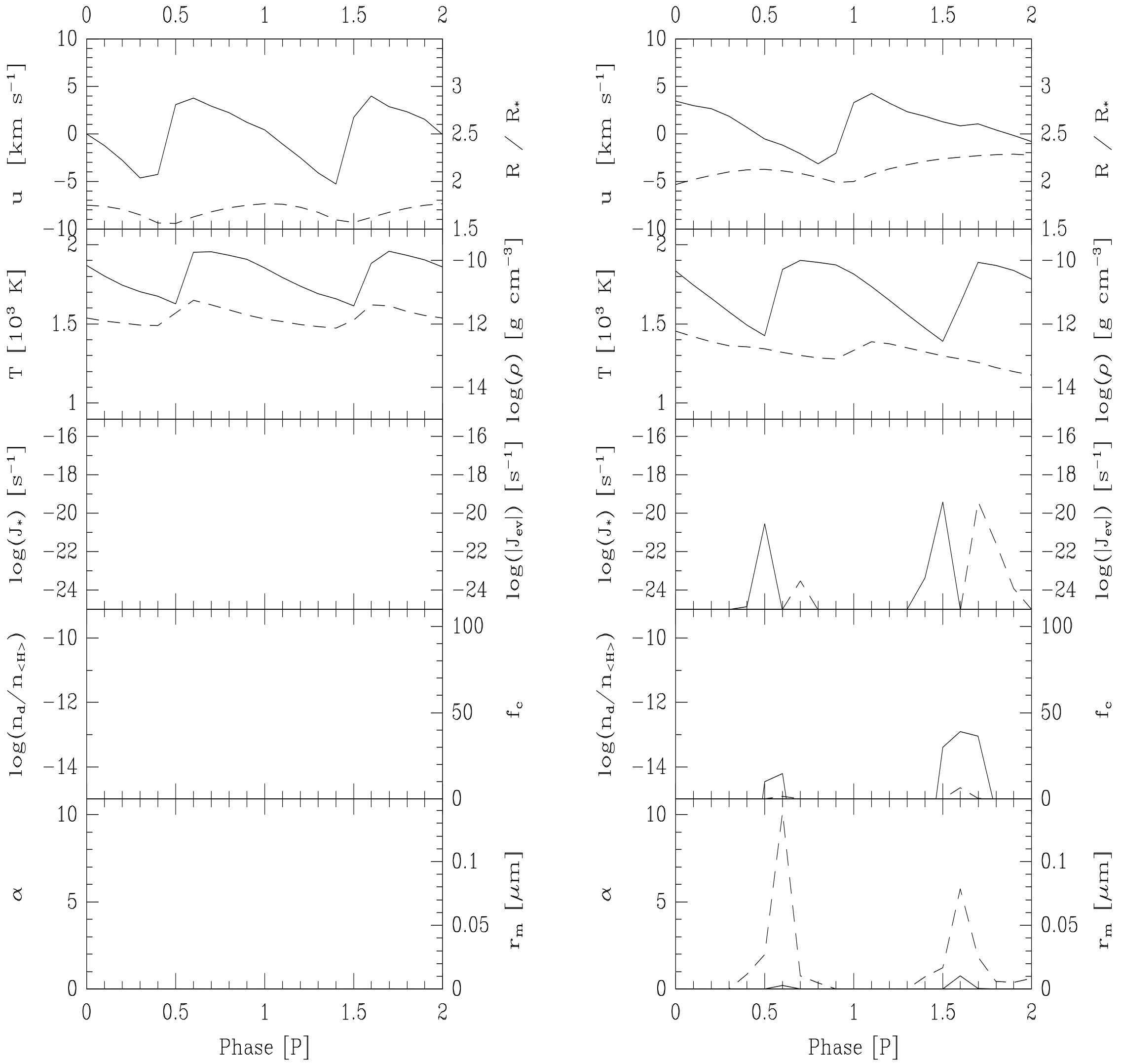

Figure 4.7: Time development of certain physical quantities, cf. text, during two periods in two selected Lagrangian zones of model E.

---

frame of the gas. From Fig. 4.7, left column, to Fig. 4.8, right column, the mass elements have an increasing initial position. The figures show from top to bottom

a. the velocity u of the mass shell (solid line) and the radial position R (dashed line) in units of the stellar radius of the initial hydrostatic model,

b. the temperature T (solid line) and the logarithm of the density ρ (dashed line) in these zones,

c. the logarithm of the nucleation rate $J_\star$ (solid line) and the logarithm of the evaporation rate $J_{\rm ev}$ (dashed line),

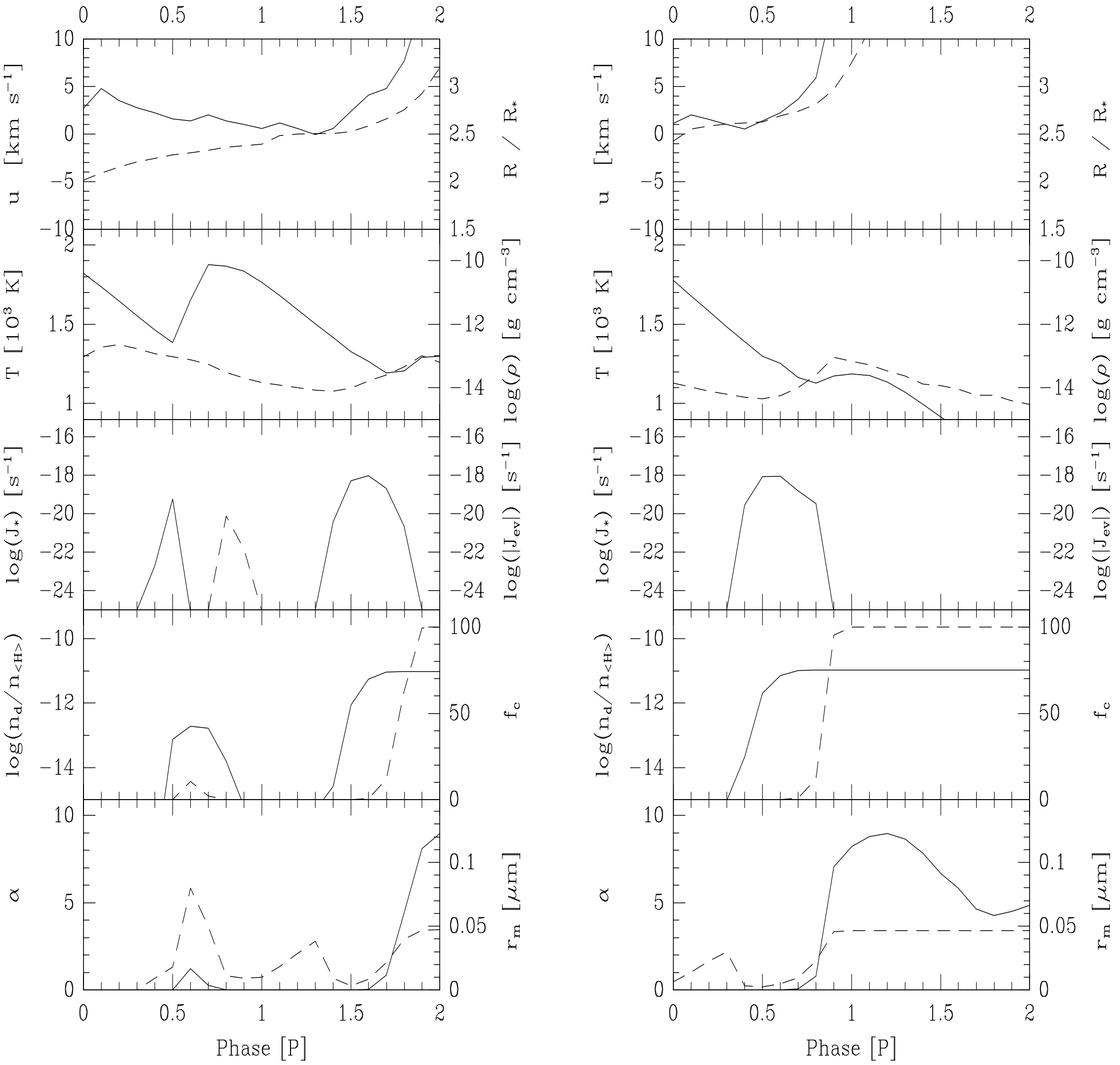

Figure 4.8: Fig. 4.7 continued. Time development of the same physical quantities of model E, cf. text, during the two periods in two selected Lagrangian zones located farther outwards.

---

d. the logarithm of the number of dust grains per H-atom $n_{\rm d}/n_{<\rm H>}$ (solid line) and the degree of condensation $f_{\rm c}$ (dashed line) and finally

e. the acceleration due to radiation pressure on dust α (solid line) and the mean particle radius $r_{\rm m}$ (dashed line) in these shells.

The *innermost* zone (cf. left column of Fig. 4.7), is passed periodically by strong shock waves created by the interior pulsation. This leads to a quasi-ballistic movement of this zone through the atmosphere as can be seen from the course of the radial position R.

The time development of the density and the temperature are determined by the compression of the element due to the periodic passage of shock waves. The compression leads to a density enhancement of almost one order of magnitude and a subsequent increase of the temperature of about 400 K. After the passage of the shock wave one would expect the temperature to decrease in a similar manner compared to the density. However, this is not the case. The temperature decreases less steeply than the density and remains fairly constant between $t = 0.6P$ and $t = 0.8P$. This is caused by the back-warming of the newly formed dust layer, which is located at a larger radial position at these instants and prevents a decrease of the temperature due to the expansion in the mass element under consideration until the new dust layer has moved further outwards. We return to this point in some more detail after the discussion of the fourth Lagrangian zone.

Since the temperature in this innermost zone always exceeds 1600 K, during the two cycles no formation of solid particles is possible and the zone remains completely dust-free.

The *second* zone (cf. right column of Fig. 4.7), although at the beginning of the phase ($t = 0.0P$) located only at a slightly larger radial position, is pushed outwards by the first shock wave to a maximum radial position of $\approx 2.3R_\star$, which is about $0.6R_\star$ farther outwards than the first zone just discussed.

Hence, in this first cycle, at maximum radial position and therefore at minimum temperature of about 1400K, formation of new particles becomes possible and a small peak of the nucleation rate develops between $t = 0.4P$ and $t = 0.6P$. However, as the number of newly formed particles remains very small, there is only a slight increase of the number of dust grains per H-atom $n_{\rm d}/n_{<\rm H>}$. These few, newly formed particles grow and finally have a rather high mean particle radius. Nevertheless, since the degree of condensation also remains small, this is an irrelevant amount of dust.

At $t = 0.5P$ a surprising effect occurs in this zone. The temperature is still expected to decrease due to the expansion after the preceding shock wave, similar to the time development of the density. However, at $t = 0.6P$ a temperature jump of at least 400 K occurs. This sudden increase is solely caused by the back-warming of a newly formed dust layer farther out. It heats the mass element up to $\approx$ 1900 K and causes complete evaporation of the dust particles, just newly formed.

The element is shocked again at $t = 1.0P$. It is pushed farther outwards and again formation of a few new particles occurs at temperature minimum at $t = 1.5P$. During this second cycle also a noticeable peak in the degree of condensation f_c, and subsequently in the radiative acceleration α occurs. This induces a slight perturbation in the velocity structure. However, due to the back-warming, again effective evaporation occurs during the second half of this cycle and at the end the mass element remains almost dust free.

During the first cycle the *third* Lagrangian zone (cf. Fig. 4.8 left column) behaves similar to the second one. Although located only slightly farther outwards than the second zone at $t = 0.0P$ the third zone carries out a small but constant outward directed movement, although one would conclude from the curvature of the trajectory of this element that it will fall back to an inner position. At minimum temperature during the first cycle, effective nucleation is possible, but due to the positive temporal temperature gradient, these newly formed grains do not find favourable conditions for growth, and moreover, they are immediately evaporated due to the dramatic increase of the temperature caused by the back-warming effect. Only a negligible amount of very small particle remains, as can be seen from the course of the mean particle radius r_m at $t = 1.0P$. Subsequently, at almost constant density and decreasing temperature these grains grow and the mean particle radius increases.

The situation changes quickly when the element reaches its maximal radial position in the second cycle at $t = 1.4P$. There, at a temperature of ≈ 1300 K effective nucleation becomes possible. The number of dust grains per H-atom $n_d/n_{<\mathrm{H}>}$ increases steeply and the mean particle radius r_m decreases due to the large amount of newly formed particles. However, as the density is too low to allow for growth of these particles there is no increase of the degree of condensation at $t = 1.5P$. Grain formation dominates growth in this phase.

At $t = 1.5P$ the element is overrun by a shock wave created by the interior pulsation. Now, due to this compression, the grains find good conditions for growth and the mean particle radius increases steeply to $0.05\mu m$. This growth phase causes also a steep increase in the degree of condensation f_c which reaches values as high as 100 % and consequently, also the radiative acceleration on dust α increases. The resulting high value at the end of the second cycle accelerates the material quickly to a supersonic velocity.

In contrast to the processes in the third zone, in the *fourth* zone effective formation of dust particles is possible already during the first cycle due to lower temperatures at $t = 0.4P$ (cf. Fig. 4.8 right column). This formation phase causes a steep increase of the number of dust particles per H-atom $n_d/n_{<\mathrm{H}>}$. However, as the density still decreases no growth is possible till $t = 0.6P$.

At $t = 0.7P$ this element is overrun by a shock wave which compresses the element and very effective growth of the newly formed dust particles takes place. Although also the temperature slightly increases, a degree of condensation of 100% is reached at the end of the first cycle.

The resulting acceleration due to radiation pressure on dust prevents the element from infalling (cf. dip in the velocity structure at $t = 0.8P$), and amplifies the outward movement of the element initiated by the preceding shock wave.

Obviously, the third and the fourth zone belong to the peak of a new dust shell formed in consecutive periods. We have discussed the periodic formation of these shells already in the previous section.

The periodic formation of an outmoving dust shell is responsible for the unusual time development of the temperature structure, especially in the second and third zone, which we mentioned when discussing the time development of these selected Lagrangian elements. The stellar radiation is blocked by the opacity of the suddenly formed shell, thereby heating the material behind it, i.e. located at smaller radii. This is the reason why this effect is absent in the third Lagrangian element during the second cycle but has been present in the first cycle. There, this particular mass element has been situated farther inwards and has been heated by the back-warming effect of the dust shell, which during this cycle has been formed in an outer region.

This back-warming effect demonstrates that formation and growth of solid particles also has considerable influence on the thermodynamical structure. Back-warming is responsible for the occurrence of evaporation at temperatures exceeding 1900 K. Although evaporation has not a decisive influence on the interaction between dust and hydrodynamics, it, nevertheless, restricts the radial interval where solid particles can be formed.

Summarizing the preceding discussion,*we find again that the intimate relation between dust formation and dynamical structure in CDS around LPVs may be conceived as a two-step process which consists of:*

1. *a temperature decrease which allows for an effective nucleation of dust grains and*

2. *an avalanche growth phase due to the compression by a subsequent shock wave.*

Since the description in the comoving frame of the gas clearly reveals that the mass elements are pushed outwards by radiation pressure on dust, we conclude with regard to the wind-mechanism that indeed the outflow is initiated by the pulsation but is accelerated by the dust.

4.3.3 The grain size spectrum

In the previous sections we have concentrated our discussion on the inner region of the CDS, where dust formation, growth and evaporation take place. Especially the above analysis of the Lagrangian elements shows, that the resulting grain size spectrum depends strongly on the history of the considered mass element. The grain size distribution function reflects the history of the fluid parcel on its trajectory through the atmosphere. Therefore, for the entire CDS no uniform grain size spectrum can be expected.

We have considered the formation of spherical, amorphous carbon grains. In Fig. 4.9 we present three size spectra of dust particles taken from different zones far out in the wind where grain growth is definitely stopped and the spectra have reached their final shape. Fig. 4.9 shows the logarithm of their particle size distribution function f as a function of the particle radius r given in μm.

The distinct peaks present in the spectra result from succeeding phases of dust formation and growth that have taken place in these three zones. The lower

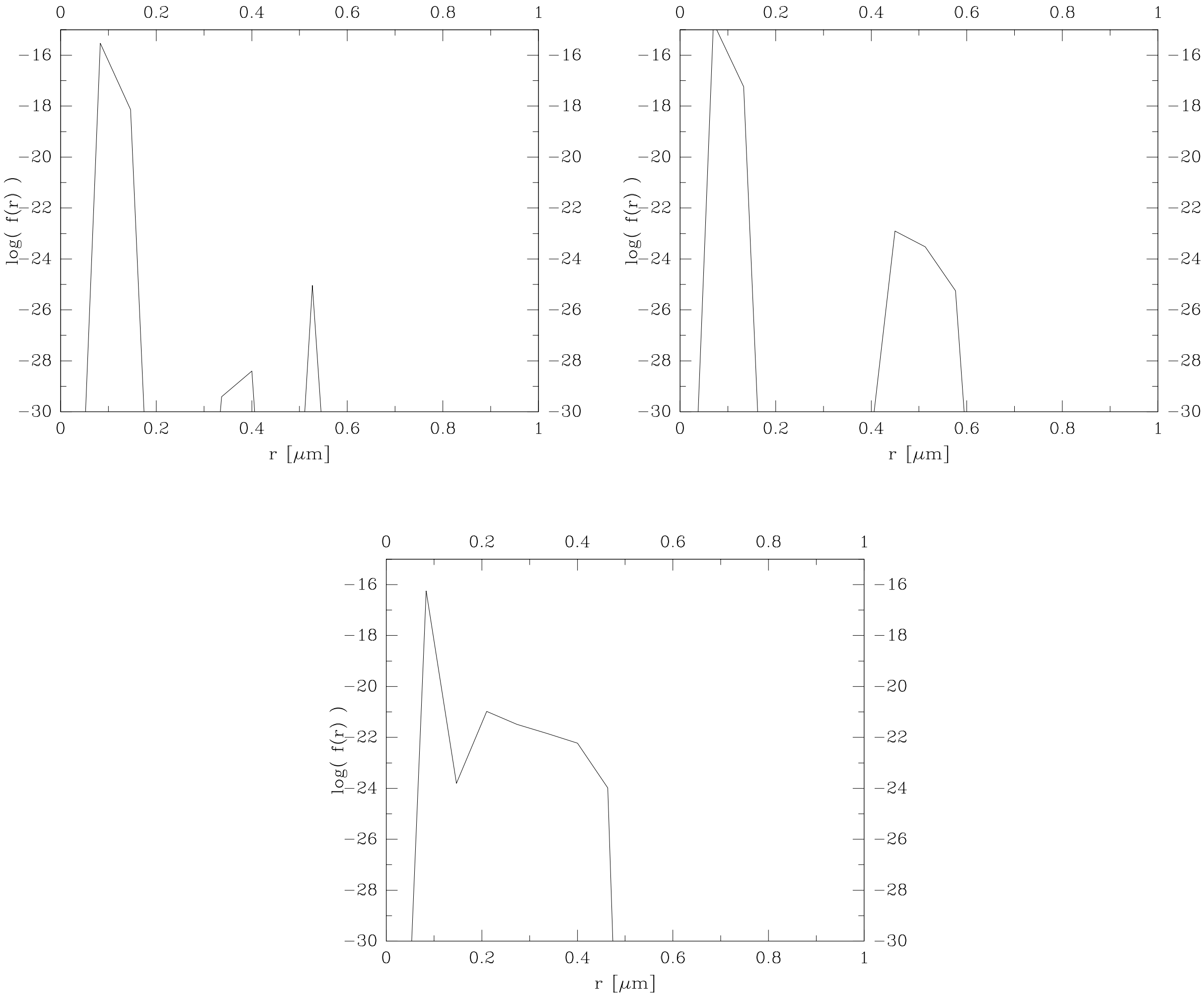

Figure 4.9: Selected grain size distribution functions taken from mass shells of a typical model calculation: $T_* = 2600$ K, $M_* = 1.0\ M_\odot$, $L_* = 1\ 10^4\ L_\odot$, $\epsilon_C/\epsilon_O = 1.8$, P = 325 d, $\Delta u_p = 2$ km s^{-1}.

---

spectrum in Fig. 4.9 belongs to a zone where dust formation has taken place as described for the element on the r.h.s. in Fig. 4.8: There has been a single phase with favourable conditions for dust formation and growth, where relatively large particles evolved. The spectra of the other two zones show, that these zones have undergone two, respectively three, cycles of dust formation and growth before being pushed to the outer regions.

The grain size distribution functions show that the assumption of the small particle limit is valid in our models, since the upper limits of the size spectra of the dust particles are small compared to the wavelengths of interest. The maximal particle size radius remains well below 1μm. This result is in contrast to the calculations of stationary dust driven winds [Dominik *et al.* 1989]. The presence of pulsation in the present calculations limits the time interval, which a fluid element stays in the innermost dense region under excellent growth conditions. In stationary dust driven winds this mechanism is absent and a considerable amount of particles reaches rather large sizes, up to a few μm.

Furthermore, each distinct peak of the size distribution function is rather narrow. The dust particles in each element are not distributed homogeneously over a large size interval but are concentrated in certain small grain size intervals. These intervals are determined according to the duration of the phase of formation and growth and according to the physical conditions under which the particles have evolved. Again this behaviour is caused by the limiting effect of pulsation, which also allows multiple phases of formation and growth in one fluid element.

Obviously, the size spectra have not such a smooth appearance as one would expect. Unfortunately, this has a purely numerical reason: During the phase of growth in the Lagrangian elements the size distribution function is saved over a given maximum–particle–radius grid such that in the case of evaporation it can be traced backwards to yield the evaporation rate. If a very effectively growing zone reaches an upper particle size limit, the prescribed particle size grid is extended for *all* zones by keeping the number of grid points constant and doubling their distance. Since this prescribed particle size grid is held the same for all elements, i.e. no matter how the growth process evolves in a special element (effective or less effective) the particle size distribution function is often saved with a rather coarse resolution. In principle, it is possible to prescribe individual particle size grids for the zones but one has to be careful, e.g. with the rezoning scheme. Therefore, with the present version of the code it is only possible to make qualitative statements concerning the spectra.

However, calculations performed with an improved version of the code which includes an individual particle size grid for each Lagrangian zone show in principle the same results as described above [Gauger 1993, private communication].

4.3.4 The optical depth

Fig. 4.10a (upper panel) shows the radial structure of the monochromatic optical depth τ_λ at $\lambda = 1\mu$ at two instants during the cycle, $t = 0.0P$ (solid line) and $t = 0.5P$ (dashed line), calculated for Model E. The lower diagram, Fig 4.10b, depicts the diluted optical depth τ_L at the same instants of time, also for model E. The minimum and maximum values of $\tau_{1\mu}$ for the models A – G are listed in Table 4.2.

The quantities $\tau_{1\mu}$ and τ_L are measured inwards adopting the boundary condition $\tau_{1\mu}(\infty) = \tau_L(\infty) = 0$. To calculate $\tau_{1\mu}$ we assume that the dust particles are small compared to the wavelength, and hence the absorption efficiency of amorphous carbon is represented approximately by a λ^{-1}–law. We use the expression given in [Lucy 1976], to calculate the complex index of refraction. Lucy fitted

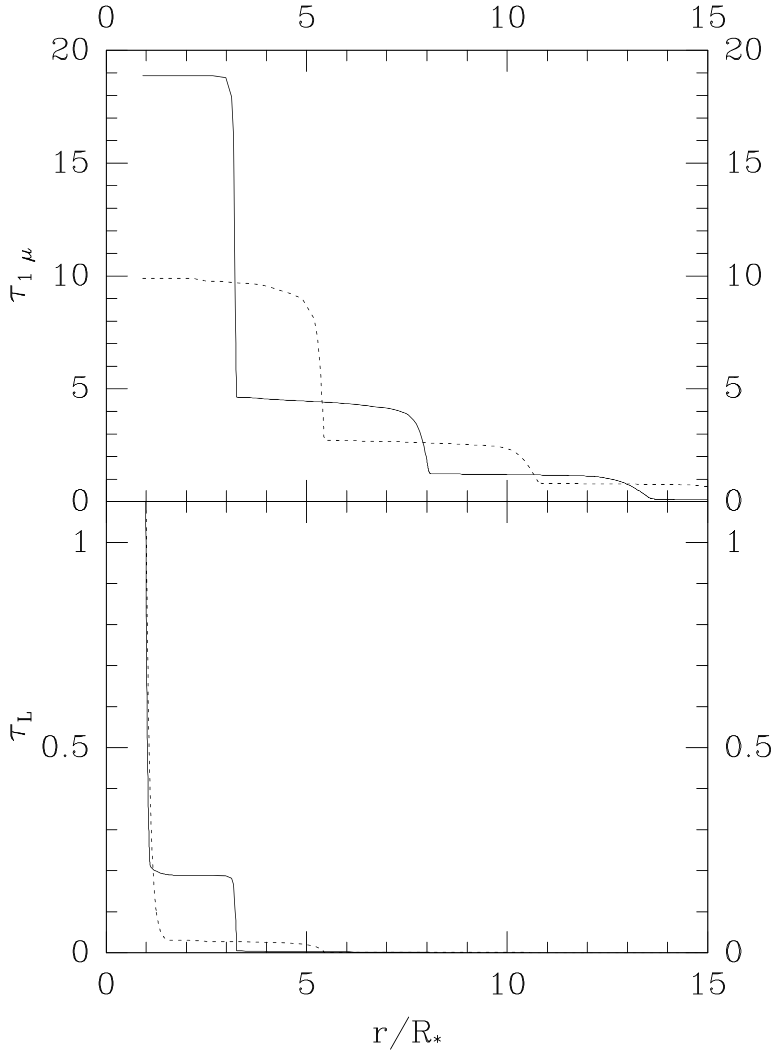

Figure 4.10: upper panel: Radial structure of the monochromatic optical depth $\tau_{1\mu}$ at $t = 0.0P$ (solid line) and $t = 0.5P$ (dashed line). lower panel b: Radial structure of the diluted optical depth τ_L at the same instants of time. Shown for Model E.

---

experimental data to get his Eq. 13 and states that it becomes a poor approximation for $\lambda \leq 3.5\mu m$. τ_L is determined by Eq. (2.41).

Fig. 4.10a indicates that $\tau_{1\mu}$ varies during the cycle, but the CDS remains optically thick for the whole pulsational period, except for models A and B. Table 4.2 shows the maximum and minimum values of $\tau_{1\mu}$ at the inner boundary of the CDS within a pulsational cycle for the models A – G.

The resultant monochromatic optical depth $\tau_{1\mu}$ for the shell is in good agreement with the observations of CDS around late type stars, e.g. for IRC +10216 ([Griffin 1990], [Ridgway and Keady 1988]).

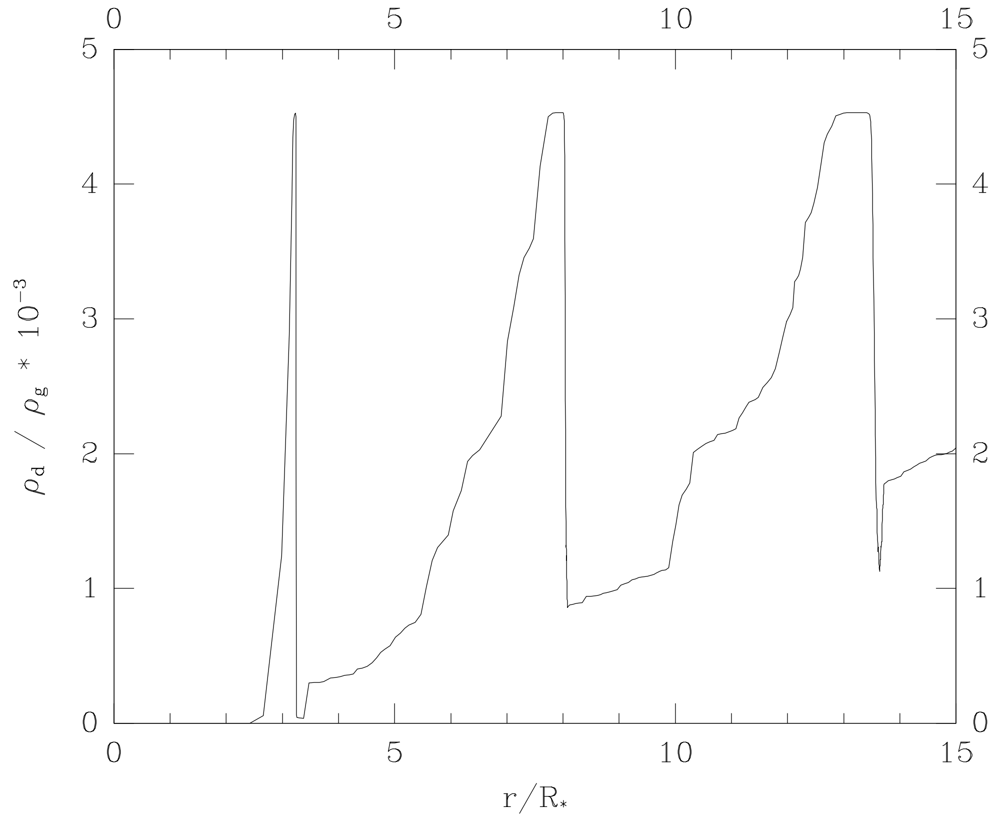

Figure 4.11: Radial structure of the dust to gas ratio ρ_d/ρ_g at $t = 0.0P$.

The diluted optical depth τ_L, which according to Eq. (2.39) determines the temperature structure of the dust shell, remains smaller than 0.25 everywhere within the dust shell. Thus, our semi-analytical approach to treat the radiative transfer, which requires $\tau_L < 1$ within the dust shell, is justified.

4.3.5 The dust to gas ratio ρ_d/ρ_g

Fig. 4.11 shows the radial course of the dust–gas ratio for model E at the instant $t = 0.0P$. The time averaged values for ρ_d/ρ_g for the models A – G are listed in Table 4.2, p.100.

According to the definitions in Chap. 2 the quantity ρ_d/ρ_g is simply given by

$$\frac{\rho_d}{\rho_g} = \frac{m_0\, K_3\, n_{<\mathrm{H}>}}{\sum_i m_i\, n_i} \quad , \tag{4.1}$$

where m_0 is the monomer mass and i labels the contributing species of the gas phase with mass m_i and density by number n_i. In case of C-stars the r.h.s. can be immediately expressed by the degree of condensation f_c and the overabundance of carbon to oxygen ϵ_C/ϵ_O:

$$\frac{\rho_d}{\rho_d} = \frac{12.0}{1.4}\, f_c\,(\frac{\epsilon_C}{\epsilon_O} - 1.0)\,\epsilon_O \quad , \tag{4.2}$$

where we have assumed only H and He to contribute to the gas density ρ_g.

The calculated dust to gas ratios lie well in the range from $\approx 10^{-3}$ up to 10^{-2} derived from observations (e.g. [Knapp 1985], [Sopka *et al.* 1985], [Jura 1986a], [Olofsson *et al.* 1987]).

Already from Tab. 4.2 it is surprisingly evident, that the gas to dust ratios are confined to a narrow range of values. A more detailed analysis of the dependence of the resulting dust to gas ratios on the model parameters can be found in the next section.

In connection with this result it is interesting to mention a remark in [Olofsson *et al.* 1987] who find dust to gas ratios being considerably higher than the values one would obtain if only the carbon excess relative to oxygen, as derived by [Lambert *et al.* 1986], has condensed into grains. This might be another hint that the overabundances of carbon to oxygen derived by [Lambert *et al.* 1986] are in fact too small since their sample is biased towards low ϵ_C/ϵ_O–ratios.

4.4 Influence of the model parameters

It is the aim of this chapter to present those models calculated so far which exhibit a cyclic behaviour from one period to the next period, i.e. the situation at $t = \beta\, P$ equals the structure at $t = (\beta + n_P)\, P$, where β is an arbitrary dimensionless time parameter and $n_P = 1$. Tab. 4.3, on p.97, contains the parameter of the initial hydrostatic models while Tab. 4.4, on p.100, contains the resultant quantities from the evolved models. The quantities $\dot{M}$, u_∞, and ρ_d/ρ_g again are averaged over at least one pulsational period.

Chapter 6 is devoted to models with $n_P \neq 1$.

Since the models presented here were "forced" to give $n_P = 1$, perhaps some parameters, e.g. the overabundance of carbon to oxygen ϵ_C/ϵ_O, were chosen to give the desired dynamical behaviour instead of yielding models of real Miras and LPVs. Because of the immense amount of computing time, most models were not checked whether $n_P = 1$ could also be achieved e.g. with a lower value of ϵ_C/ϵ_O. Therefore the dependencies presented here should be taken with some care and should not be compared too close with observational relations but, nevertheless, some clear principal trends are obvious. However, in connection with the models to be presented in Chap. 6, a broad and realistic range of parameters of real Miras and LPVs is covered, such that the relations derived in Chap. 6 are well worth to be compared with observations or even used as a prediction for observations to be done.

Table 4.3: Parameters of the initial hydrostatic models. Temperatures are given in K, luminosities in $L_\odot$, stellar radii in $R_\odot$, stellar masses in $M_\odot$, periods in d, Δu_P in kms^{-1} and R$_{inner}$ in $R_\star$

No.	$T_\star$	ϵ_C/ϵ_O	$L_\star$	$R_\star$	$M_\star$	P	Δu	R$_{inner}$
1	3000	2.80	4590	251	1.00	350	3.0	0.97
2	3000	2.75	4618	251	1.00	350	3.0	0.97
3	3000	2.50	5328	269	1.20	350	4.0	0.99
4	2900	3.00	4392	262	1.25	322	3.0	0.97
5	2800	2.50	7000	355	1.00	500	2.0	0.84
6	2800	2.40	4045	269	1.00	400	3.0	0.87
7	2800	2.20	4045	269	1.00	400	3.0	0.97
8	2800	2.00	8524	391	1.00	800	3.0	0.91
9	2800	2.00	6500	355	1.00	400	2.0	0.84
10	2800	2.00	4045	269	1.00	400	2.0	0.84
11	2600	2.00	2910	265	1.00	388	3.0	0.96
12	2600	1.90	8000	440	1.00	500	1.0	0.91
13	2600	1.85	8000	440	1.00	600	2.0	0.91
14	2600	1.80	10000	508	1.00	650	2.0	0.91
15	2600	1.80	7500	426	1.00	650	2.0	0.91
16	2600	1.80	2910	265	1.00	388	4.0	0.97
17	2600	1.70	7500	426	1.00	750	2.0	0.91
18	2600	1.55	7500	426	1.00	900	2.0	0.91
19	2500	1.95	7500	460	1.00	450	2.0	0.91
20	2500	1.75	9000	504	1.00	776	1.0	0.87
21	2450	1.25	30000	959	1.00	2988	1.0	0.82
22	3000	2.20	4618	251	1.00	700	7.0	0.97
23	3000	1.90	4618	251	1.00	700	7.0	0.97
24	3000	1.70	4618	251	1.00	700	7.0	0.97
25	3000	1.50	4618	251	1.00	700	7.0	0.97
26	3000	1.45	4618	251	1.00	700	7.0	0.97

4.4.1 Influence of the overabundance of carbon to oxygen

Fig. 4.12 shows the dependence of the outflow velocity u_∞, the mass loss rate $\dot{M}$ and the dust to gas ratio ρ_d/ρ_g on the overabundance of carbon to oxygen ϵ_C/ϵ_O for the sample of single periodic models, i.e. $n_P = 1$. Additionally, for this sample of models we have plotted the ratio of gas to dust as a function of the period of the dust shell models. The values were taken from Tabs. 4.3 and 4.4 on p.97 and p.100, respectively.

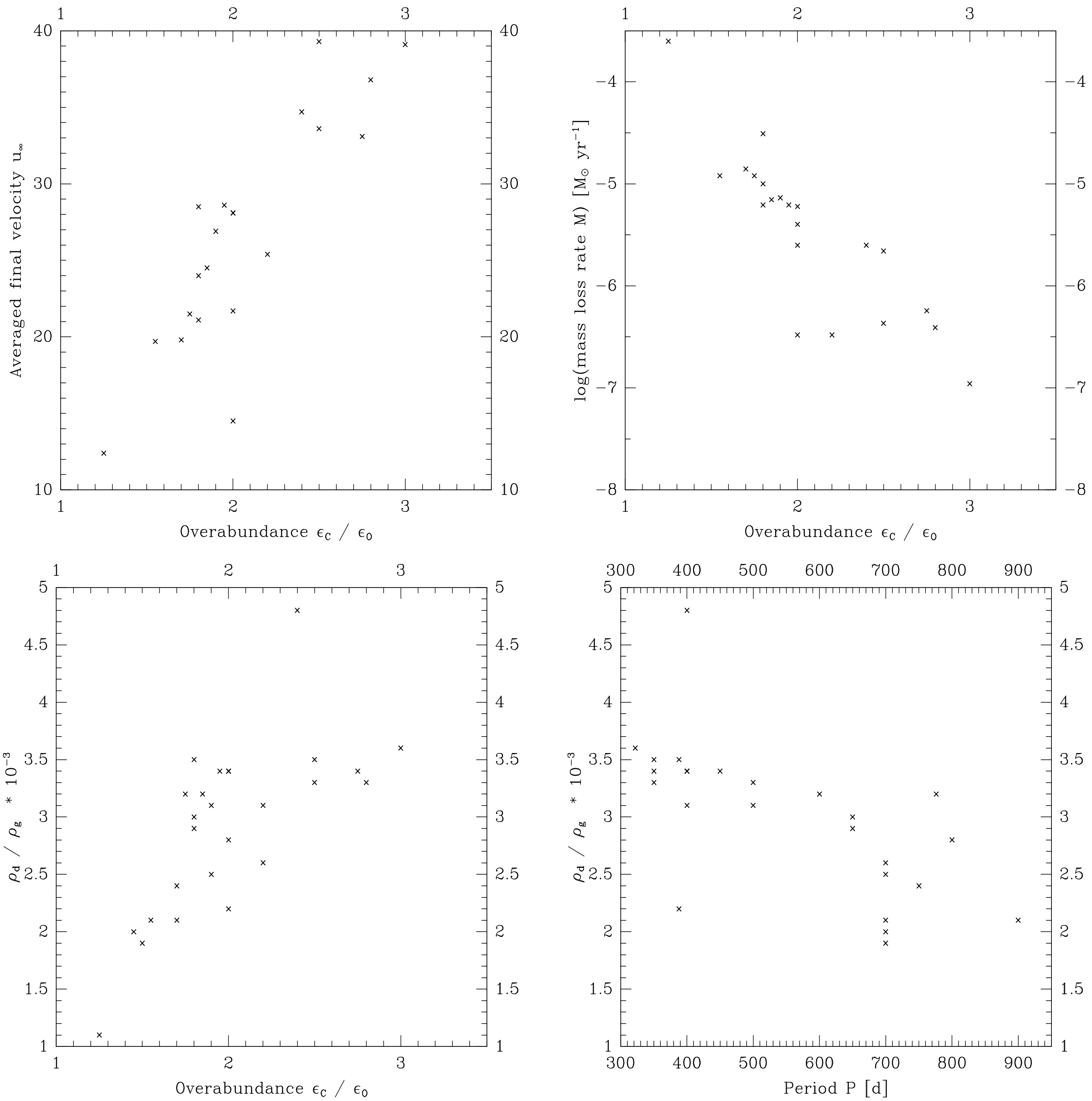

Figure 4.12: Dependence of the final outflow velocity, the logarithm of the mass loss rate and the ratio of dust density to gas density on the overabundance of carbon to oxygen. Additionally shown is the ratio of dust to gas as a function of the period of the models.

The plot on the upper left of Fig. 4.12 clearly indicates that there exists an almost linear correlation between u_∞ and ϵ_C/ϵ_O. Since the acceleration due to radiation pressure on dust is direct proportional to the amount of condensed material, the increase of the velocity with the increasing amount of condensable material, namely carbon, can easily be seen. For the case of stationary dust driven winds [Dominik *et al.* 1990, Winters 1994] found a similar correlation. The independence of this correlation from the influence of other quantities, however, is remarkable. This correlation becomes even more intriguing in Sec. 6.3.2, when combined with the multiperiodic models ($n_P \neq 1$).

The mass loss rate $<\dot{M}>=<4\pi r^2 u_\infty \rho>_{15R_\star,P}$ (this nomenclature means averaging at a fixed radial position of 15 $R_\star$ over a time interval of at least one pulsational period) shows a decrease with increasing ϵ_C/ϵ_O. This results mainly from the increase of the outflow velocity with increasing overabundance: From Figs. 4.1 and 4.2 it can be seen that the higher the outflow velocity the lower are the densities in the wind, i.e. at larger radii from the star. A higher outflow velocity yields a density of at least on order of magnitude smaller in the outflow and thus, prevents higher mass loss rates. This somewhat handwaving argument is not always true as a closer analysis of Tabs. 4.3 and 4.4 shows. Compare e.g. models No. 6, 7 and 10. Although model No.6 has a higher overabundance of carbon and thus a higher outflow velocity it also exhibits a higher mass loss rate than model No. 7. This demonstrates the decisive influence of the rest position of the piston and the corresponding levitation of the atmosphere.

The larger the distance of the piston from the photosphere, the higher is the input of mechanical energy, and thus, the higher is the mass loss rate. Although model 10 has a significant lower overabundance of carbon compared to model 6, its piston is located farther inside the atmosphere and causes the same mass loss rate as for model 6. Models, which are directly comparable, e.g. No.1 and 2, show the overall trend indicated by Fig.4.12.

Furthermore, one should keep in mind, that the *logarithm* of the mass loss rate is plotted. The quantities actually scatter by at least two orders of magnitude for a given carbon overabundance. Hence, the relation should be taken with care, and better be interpreted carefully, that there is no evident correlation between the mass loss rate and the overabundance of carbon to oxygen.

In contrast, Models No. 22 to 26 of Tabs. 4.3 and 4.4 clearly demonstrate the decisive influence of the overabundance of carbon to oxygen on the final outflow velocity. For this series of models all other parameters are held constant and only ϵ_C/ϵ_O is reduced, simultaneously the final outflow velocity decreases. The reduction of condensable material results in a less efficient transmission of radiative energy to the surrounding gas, and hence, the efficiency of the driving mechanism is reduced. Although, the overall behaviour of these four models is unchanged, i.e. basically they all show up to have $n_P = 1$.

Table 4.4: Calculated values of the evolved models with consistent treatment of dust formation and growth

No.	$\dot{M}$	u_∞	ρ_d/ρ_g	$L_{\star,min}$	$L_{\star,max}$	Remarks
1	3.9 10^{-7}	36.8	3.3 10^{-3}	3900	5460	
2	5.7 10^{-7}	33.1	3.4 10^{-3}	3896	5434	
3	4.3 10^{-7}	39.3	3.5 10^{-3}	–	–	$L_{*,min,max}$ not det.
4	1.1 10^{-7}	39.1	3.6 10^{-3}	3773	5116	
5	2.2 10^{-6}	33.6	3.3 10^{-3}	5483	8747	
6	2.5 10^{-6}	34.7	4.8 10^{-3}	4718	8576	
7	3.3 10^{-7}	25.4	3.1 10^{-3}	3351	4889	
8	6.0 10^{-6}	21.7	2.8 10^{-3}	5091	9662	
9	4.0 10^{-6}	28.1	3.4 10^{-3}	4770	7620	
10	2.5 10^{-6}	28.1	3.4 10^{-3}	4769	7622	
11	3.3 10^{-7}	14.5	2.2 10^{-3}	2425	3516	
12	7.3 10^{-6}	26.9	3.1 10^{-3}	7369	9495	
13	7.0 10^{-6}	24.5	3.2 10^{-3}	6308	9345	
14	1.0 10^{-5}	28.5	2.9 10^{-3}	8704	12060	
15	6.2 10^{-6}	24.0	3.0 10^{-3}	6430	9391	
16	3.1 10^{-5}	21.1	3.5 10^{-3}	2288	3589	without κ_D
17	1.4 10^{-5}	19.8	2.4 10^{-3}	6479	9465	
18	1.2 10^{-5}	19.7	2.1 10^{-3}	6467	9350	
19	6.2 10^{-6}	28.6	3.4 10^{-3}	6969	9435	
20	1.2 10^{-5}	21.5	3.2 10^{-3}	8485	10610	
21	2.5 10^{-4}	12.4	1.1 10^{-3}	23950	39410	
22	4.1 10^{-6}	26.4	2.6 10^{-3}	1821	8689	
23	3.8 10^{-6}	23.1	2.5 10^{-3}	1806	8757	
24	4.2 10^{-6}	21.0	2.1 10^{-3}	1808	8723	
25	3.2 10^{-6}	16.7	1.9 10^{-3}	1817	8743	
26	3.5 10^{-6}	13.2	2.0 10^{-3}	1820	8778	

Remarkably, a closer analysis of the models with the high overabundance of carbon shows, that in this case in fact *two* shocks occur per pulsational period which are induced due to a very efficient dust formation process. This phenomenon can be seen especially evident in the model with $\epsilon_C/\epsilon_O = 2.2$. These shocks finally merge to result in a single shock that travels through the atmosphere. If the overabundance is decreased this effect eventually vanishes, i.e. only one dust–induced shock per period develops, further reduction of ϵ_C/ϵ_O leads to multiperiodic models, cf. the corresponding models in Chap. 6, until due to very low overabundances effective dust formation is not possible any longer, and also the outflow vanishes.

It is interesting to note, that the resulting dust to gas ratios of almost all models are confined to a narrow interval, $2\,10^{-4} \leq \rho_d/\rho_g \leq 4\,10^{-3}$. This means, however, the overabundance is increased, the amount of dust is still small compared to the surrounding gas. The values of ρ_d/ρ_g found e.g. by [Jura 1986a] exhibit a similar confinement to a narrow interval around $4.5\,10^{-3}$.

A similar behaviour is found of the dust to gas ratio as function of the period, cf. Fig. 4.12 lower right plot. The quantity ρ_d/ρ_g is independent of the value of the period. There is a minor decrease with increasing period, however, one should again notice the scaling of the ordinate, which proves, that this is not a clear trend at all. Therefore, the dust to gas ratio should not be used e.g. as a tracer for certain evolutionary scenario, which, usually, include an increase of the period towards the Planetary nebulae stage. Nevertheless, this finding might be useful for a comparison with observations.

A rather trivial rule has proved to be effective during the stage of calculating this sample of models. To construct a model with $n_P = 1$ for a given set of parameters, it can be proposed from our numerical experience, to start with an overabundance as high as possible (numerically) and then successively to reduce ϵ_C/ϵ_O until the model is still single periodic. A more quantitative approach, although also from numerical experience, can be found in the next section.

4.4.2 Influence of the period, the temperature and the piston amplitude

The upper panel of Fig. 4.13 shows the dependence of the final outflow velocity and the mass loss rate on the period. Again the both quantities are time averaged.

Additionally, in the upper right plot is shown a mass–loss–period relation derived from observations by [Vassiliadis and Wood 1993]. These author state that this relation only holds for the pre–superwind phase, i.e. for periods less than 500 d. Our models show the same exponential increase of the mass loss rate as derived from observations. A quite reasonable agreement, although, there seems to be a tendency for the theoretical models to lie above the line proposed by [Vassiliadis and Wood 1993].

A similar equation proposed by [Vassiliadis and Wood 1993] for a u_∞ –P relation indicates an increase of the final outflow velocity with period, i.e. is in clear anti–correlation with our models. This contradiction has to be investigated again when we deal with the complete set of model calculations, i.e. also with the models with $n_P > 1$.

We want to look closer at individual models. Consider the series of models No. 19, 12, 13, 15, 17 and 18 of Tabs. 4.3 and 4.4. The models are ordered with decreasing overabundance of carbon. Except for the period the other model parameters are (almost) equal. Thus, we get the following remarkable rule of thumb or at least a proposition which should be confirmed by a more extensive

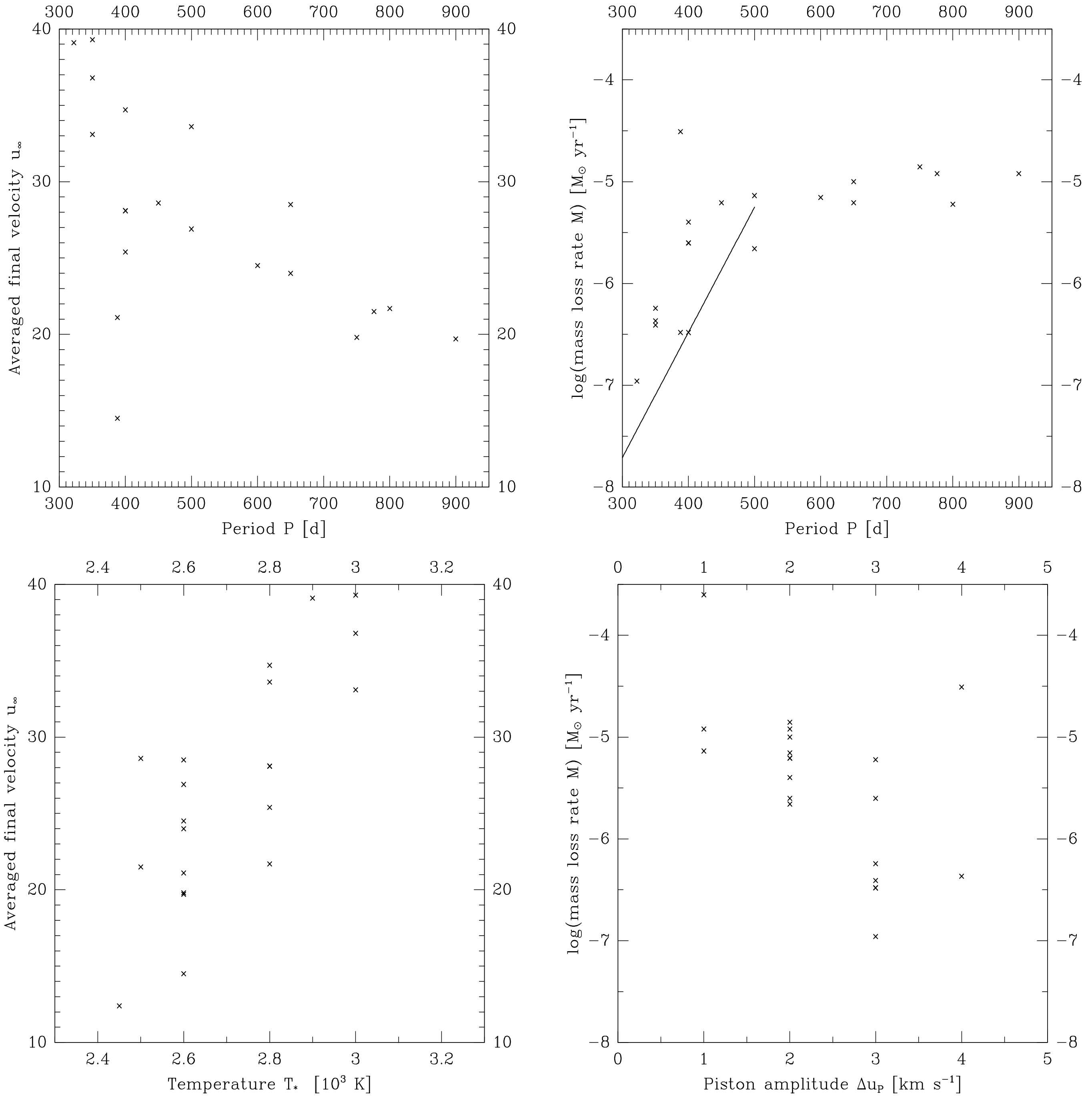

Figure 4.13: Dependence of the final outflow velocity and the logarithm of the mass loss rate on the period, dependence of the final outflow velocity on the effective temperature, and dependence of the logarithm of the mass loss rate on the piston amplitude. The solid line in the upper right plot represents the mass–loss–period relation derived from observations by [Vassiliadis and Wood 1993].

and systematic grid of models, where Tab. 4.3 can be used as guidance for calculating further single periodic models:

> *Let* A *be a model with* $n_P = 1$ *calculated in the limit case of isothermal shocks. If* ϵ_C/ϵ_O *of model* A *is reduced by* ≈ 0.05*, simultaneously the period is increased by* ≈ 50 *d and all other parameters are held constant, then the so calculated model* B *will also have* $n_P = 1$.

This proposition should hold for model parameters chosen not too "extreme", i.e. it should hold for luminosities $\leq 10^4 L_\odot$, for temperatures between 2400 and 3000 K and periods in a range typical for LPVs. Obviously, the reduction of condensable material, and hence the reduction of the transmission of radiative energy by the dust to accelerate the gas, has to be counterbalanced by an increase of mechanical energy input by the piston.

The left plot in the lower panel of Fig. 4.13 shows the dependence of the time averaged final outflow velocity on the effective temperature. The plot exhibits a direct correlation between u_∞ and $T_\star$. This behaviour is due to the dependence of the outflow velocity on the overabundance. Since lower effective temperatures yield lower temperatures at a given distance from the star where the density is high enough to start dust formation, the dust can already be dynamically determining at low overabundances. The higher $T_\star$ the farther outwards located is the point of the onset of dust formation and the overabundance of carbon to oxygen has to be high for the dust formation to be effective. "Effective" in this sense means, that dust is the dominant ingredient for the developing wind structure and the atmospheric stratification is produced by the mechanisms described in detail in one of the previous sections.

The right plot in the lower panel of Fig. 4.13 shows the dependence of the logarithm of the time averaged mass loss rate on the piston amplitude Δu_P. It turns out that Δu_P is one of the parameters which are of minor influence for the resultant structure of the CDS and no correlation between $\dot{M}$ and Δu_P can be found. For models with $n_P = 1$ each value of Δu_P yields a large scattering of possible mass loss rates. This is a further confirmation that the dust drives the wind, and gives a nice demonstration of the mass loss mechanism. Pulsation solely causes a levitation of the atmosphere, which supports the formation of dust. The increase of the piston amplitude only increases this support. According to [Holzer 1987] most of the mechanical energy input, however, goes into lifting the material out of the gravitational field than into accelerating the wind, and hence, producing a higher mass loss rate. Finally, once dust is present, it dominates the atmospheric structure, accelerates the outflow to its final velocity, and mainly accounts for the observed mass loss rates.

Furthermore, during the performance of the calculations we found, that it is impossible to turn a model with $n_P \approx 1$ into a model with $n_P = 1$ by changing the amplitude of the piston. Which is simply a confirmation of the minor influence of the piston amplitude. The determining parameter of the mechanical energy input is the period. With regard to model calculations for a real object this is a rather fortunate circumstance since the periods are well determined from observations. The piston amplitude can then be chosen somewhat reasonable, and, although less well determined from observations, should not hinder a reliable modelling of concrete objects.

The other parameter of minor dynamical influence is the stellar mass. As can be seen from Tabs. 4.3 and 4.4 a variation of the stellar mass of $\approx 25\%$ can easily be compensated by a slight variation of the overabundance of carbon or the stellar luminosity, i.e the dynamical structure is rather insensitive to a change of the stellar mass. Therefore, we have usually chosen a value of 1 $M_\odot$, which we found reasonable for an AGB–stars. Furthermore, the principle results presented in this chapter would also occur in model calculations with substantially higher or lower stellar mass. The investigation of the quantitative dependence could be a subject of future work, especially if self–gravitation is taken into account.

The stellar luminosity, as the source of the radiation energy, is definitely a parameter of major influence, which is essential for the development of distinct dynamical regimes and thus, will also be investigated separately in the next chapter. To demonstrate the influence on the models, consider models No. 14 and 15 of Tabs. 4.3 and 4.4. Both models are equal except for the luminosity, which reduced by 25% in Model 15 compared to Model 14. The increase of the radiation source results in an increase of the mass loss rate as well as an increase of the final outflow velocity.

4.5 Conclusions

In the following we want to summarize briefly the principle results of this chapter.

- The results reveal the key role of the dust for determining the atmospheric structure. In contrast to previous calculations (e.g. [Bowen 1988a]) there is an intimate relation between the dust complex, hydrodynamics and thermodynamics, which results in a complex dynamical behaviour.

- Under appropriate conditions, dust formation and growth can take place in an avalanche like process, which, due to radiation pressure on dust, finally induces a perturbation in the velocity structure, which steepens to become a shock wave. The dust induced shock wave may occur phase–shifted to the pulsational shock. Then it dominates the atmospheric structure, whether the pulsational shock front is damped.

- Given sufficient amounts of condensable material, the dust solely is able to produce these strong shock waves once or even multiple times each pulsational cycle, thereby also producing a discrete or onion–like structure of the shell.

- Dust formation takes place as a two step process: The temperature decrease in the wake of the innermost shock wave allows effective nucleation, subsequent compression by the next, pulsational shock waves produces favourable conditions for grain growth and causes an avalanche growth phase.

- By the "backwarming" effect the dust limits its own nucleation process and decisively influences the temperature structure, which also can cause thermal evaporation of dust grains. Otherwise, thermal evaporation does not show up as a decisive process for the circumstellar structure.

- The resulting particle size distribution functions of the individual Lagrangian zones reflect the history of the different dust formation processes through which the zones went, and usually consist of different distinct peaks.

- The overabundance of carbon to oxygen ϵ_C/ϵ_O decisively influences the final outflow velocity, an increase of ϵ_C/ϵ_O causes a linear increase of u_∞.

- The rest position of the piston at the inner boundary decisively influences the input of mechanical energy and has to be seen as an additional model parameter or has, at least, to be held constant when the influence of the physical parameters is investigated.

Chapter 5

The exterior κ–mechanism and the limit case of a stationary dust driven wind

5.1 Introduction

A common feature of stars evolving along the Asymptotic Giant Branch (AGB) is the occurrence of pulsation accompanied by a substantial mass loss. Especially the phase of large–amplitude, long–period pulsations seems to be characterized by the most rapid mass loss. These long–period variables (LPVs) and Miras have a period range which scatters around a maximum by number of $\approx$ 350d [HOFFMEISTER *et al.* 1990] and mass loss rates up 10^{-4} $M_{\odot}$ yr^{-1}, e.g. [KNAPP *et al.* 1993].

Time–dependent model calculations of circumstellar dust shells (CDS) around LPVs take the effects of pulsation into account by applying the so called *piston* approximation ([WOOD 1979], [BOWEN 1988A], [FLEISCHER *et al.* 1992] (henceforth called Paper I), [FEUCHTINGER *et al.* 1993]). Thereby, the pulsation is described by a sinusoidal moving inner boundary of the model grid, which is situated a few percent of the photospheric radius below the photosphere. For the desired frequency of the piston the period of the star is chosen and the amplitude is adjusted roughly to produce the observed luminosity variation.

In contrast to the other authors, we presented in Paper I dynamical models of CDS around LPVs, which include a detailed treatment of dust formation, growth and evaporation and demonstrated in detail the key role of the dust complex for the resultant physical structure of the CDS. We found that the dust is strongly correlated to the hydrodynamical quantities and that radiation pressure on dust is able to produce the dominant strong shock waves which run through the atmosphere. In [WINTERS *et al.* 1993] (henceforth called Paper II) we investigated the optical appearance of these dust shell models and found that the dust complex decisively influences the lightcurves of the objects under consideration.

The aforementioned investigations have in common, that pulsation together with radiation pressure on dust grains can account for the observed high mass loss rates of LPVs and Miras.

On the other hand, extensive work has been performed to construct *stationary* wind models of late type giants which include radiation pressure on dust, e.g. [LUCY 1976], [MENIETTI AND FIX 1978], [BERRUYER AND FRISCH 1983], [KOZASA *et al.* 1984], [GAIL AND SEDLMAYR 1985]. [GAIL AND SEDLMAYR 1987B], [DOMINIK *et al.* 1990], and [WINTERS *et al.* 1994A], demonstrated that stationary wind models are completely determined by the prescription of the four fundamental parameters: stellar mass M$\star$, stellar luminosity L$\star$, effective temperature $T_\star$ and the abundance ratio of carbon relative to oxygen ϵ_C/ϵ_O. They showed that the resultant mass loss rates and final outflow velocities of these self–consistent model calculations are in good agreement with the observed range of values. The theoretical spectra calculated with this model approach closely match e.g. that of the prominent infrared object IRC +10216. An important result of [DOMINIK *et al.* 1990] is, that purely dust driven winds are possible only in a certain region of the HR–diagram. Furthermore, [GAIL AND SEDLMAYR 1987C] deduced a minimum mass loss rate for the carbon–rich as well as for the case of an oxygen-rich atmosphere, above which radiation pressure on dust grains is able to drive a circumstellar wind. Below this mass loss rate the wind cannot be driven by this mechanism, i.e. not by this mechanism alone.

With regard to these two different modelling approaches, the time–dependent and the stationary, the questions arise, whether and under which conditions it is possible with our dynamical code to calculate models without a piston at the inner boundary, which means exactly to calculate models with a piston with an amplitude of $0 kms^{-1}$. Which mechanism initiates the outflow (Since we start the calculations from an initially hydrostatic model)? Is it possible to construct a "stationary wind" solution and which physical quantities limit the existence of such a solution? If such solution exists, is it stable?

It is the aim of this chapter to address these questions and to present exemplary model calculations in the limit case of isothermal shocks for a carbon–rich atmosphere.

5.2 Results

We want to deal with the problem in two steps. First we investigate the initial phase of a model run, i.e. the phase of the hydrostatic model. As a second step we describe the mechanism which provides a continuous force to drive a wind without additional mechanical energy input.

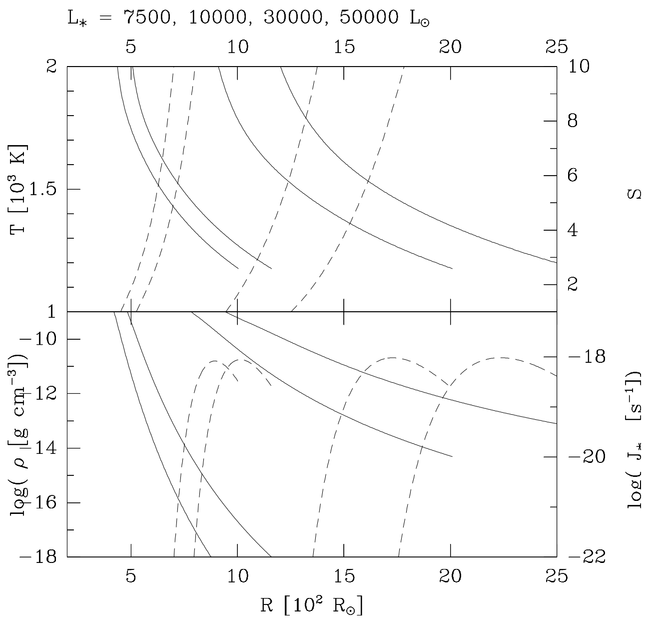

Figure 5.1: Initial hydrostatic models with $M_\star = 1.0\ M_\odot$, $T_\star = 2600$ K, and different luminosities $L_\star$ as indicated. The higher the luminosity, the more extended is the model The quantities, which are explained in the text, are shown as a function of the temperature. Note that the radius is given in units of the solar radius

---

5.2.1 The onset of the instability

Figure 5.1 shows the radial structure of different quantities for 4 hydrostatic models with different luminosities. The radius is given in units of $10^2 R_\odot$. The following quantities are plotted:

upper diagram: the temperature T (solid lines) and the supersaturation ratio S (dashed lines),

lower diagram: the logarithm of the density ρ (solid lines) and the logarithm of the nucleation rate $J_\star$ (dashed lines).

From the left to the right the curves belong to the models with $L_\star = 7500$, 10000, 30000, 50000 $L_\odot$, respectively.

Our modelling approach includes the description of the formation of small clusters from the gas phase by means of the classical nucleation theory, i.e. the formation of clusters of a critical size in a supersaturated vapor is described by means of thermodynamical quantities. The supersaturation ratio S is defined by , cf. [Gauger *et al.* 1990],

$$S = \frac{p(1)}{p_v(1)} \ , \tag{5.1}$$

where $p(1)$ denotes the partial pressure of monomers of the condensing species and $p_v(1)$ denotes the vapor saturation pressure with respect to the dust temperature, which in our case equals T_g. The quantity S decides whether dust formation starts: if S is below 1 no dust is present. However, the real onset of nucleation requires not only $S \geq 1$ but S has to exceed a minimum supersaturation ratio S_c. We adopt a value of $S_c = 3$, cf. [Draine and Salpeter 1977] to start the dust calculation in a certain Lagrangian zone.

From Fig 5.1 we infer that dust formation is possible in all four initial hydrostatic models, since the value of $S_c = 1$ is exceeded in all models. The nucleation rates reach equally high values, but the curves are rather narrow for the first two models, while a broad peak occurs for the high luminosity models. However, only in the latter two models nucleation occurs in a dense environment, while in the models with $L_\star = 7500$ and $10000\ L_\odot$ the density is almost four orders of magnitude smaller. This allows a subsequent effective growth phase in the high luminosity models and a subsequent development of an outflow driven by radiation pressure acting on the newly formed dust grains even without additional input of mechanical energy. In both of the low luminosity models the onset of this instability is prevented since almost no dust growth is possible and, apart from minor numerical fluctuations, the models remain in hydrostatic equilibrium.

Thus, the onset of the instability and the development of an outflow is determined by the density gradient of the initial hydrostatic model. The higher the luminosity, the more extended is the initial model and the less steeper is the density gradient. Hence, these high luminosity models show the development of an instability, solely caused by dust formation. However, for real stars of the type under consideration. hydrostatic equilibrium is a rather worse approximation. There will always be deviations from hydrostatic equilibrium due to the presence of waves and radiation pressure on molecules, which cause a levitation of the atmosphere . Hence, the assumption of a hydrostatic models is the worst case, and in real situations it is even more likely for the instability to take place.

Although, dust formation only takes part in the outer layers of these models and we have to follow the further development of these models to investigate whether dust formation in the initial phase is a single event or a continuous process which yields a permanent mechanism to drive the wind.

5.2.2 Instability due to an exterior κ–mechanism

Figure 5.2 shows a sequence of the radial structure of the CDS at four successive instants of time. As usually, the radius is now given in units of the stellar radius

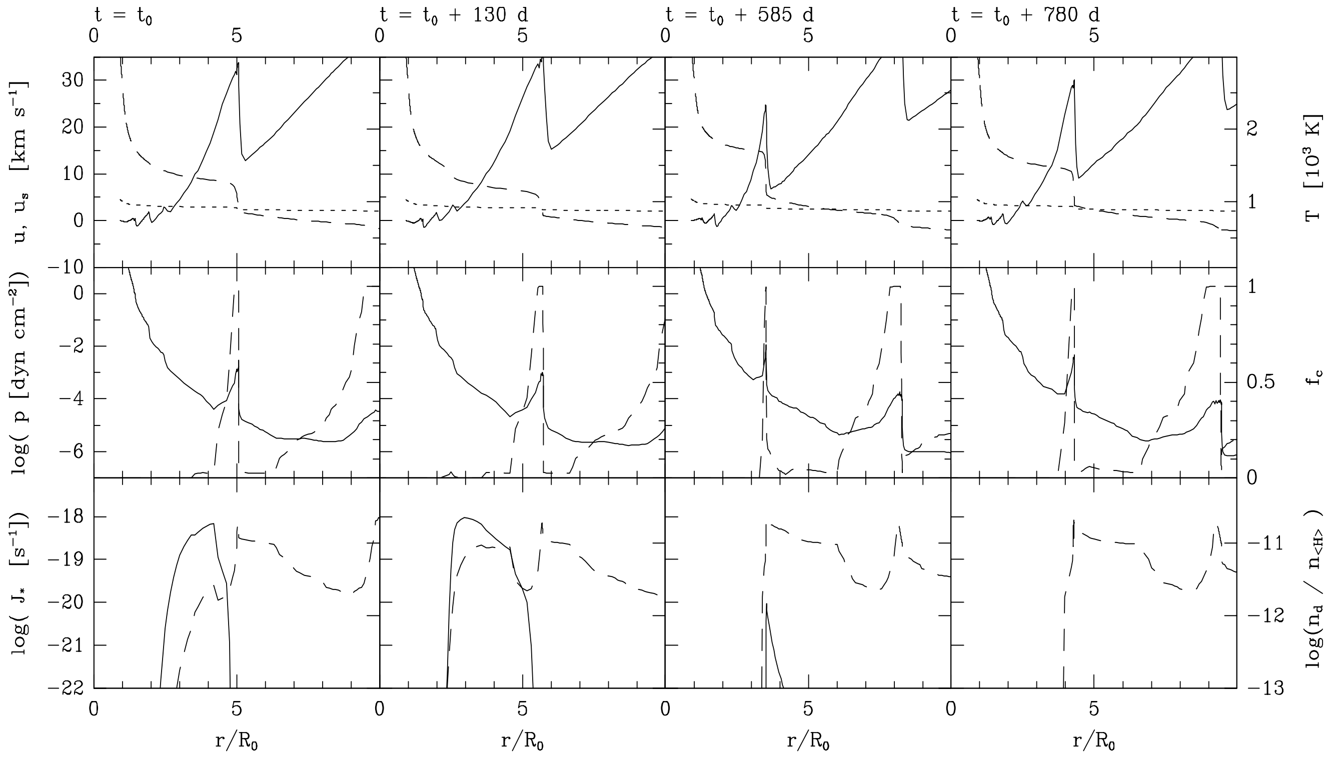

Figure 5.2: Radial structure of a model where the dust opacity *is* taken into account in the determination of the radiative equilibrium temperature. The quantities are explained in the text. The model parameters are: $M_\star = 1.0\ M_\odot$, $T_\star = 2600$ K, $L_\star = 3.0\ 10^4\ L_\odot$, $\epsilon_C/\epsilon_O = 1.80$, $\Delta u_P = 0.0$.

---

of the initial hydrostatic model.

In Fig. 5.2 the following quantities are plotted:

upper row: the velocity u (solid lines), the velocity of sound u_s (short dashed lines) and the temperature T (long dashed lines),

middle row: the logarithm of the pressure p (solid lines) and the degree of condensation f_c (dashed lines), i.e the fraction of condensable material actually condensed into grains,

lower row: the logarithm of the nucleation rate $J_\star$ (solid lines) and the logarithm of the number of dust grains per H–atom $n_d/n_{<H>}$ (dashed lines).

Although Fig. 5.2 shows a sequence taken from the evolved model with $L_\star = 30000\ L_\odot$, the instant of time t_0 could be conceived to be shortly after the initial phase in the following sense. The first dust shell has formed by the process described in the previous Chapter and due to the excellent growth conditions investigated in the previous section. The shell is now located at 4.5 $R_\star$. This dust layer has induced the corresponding shock wave, present at 4.5 $R_\star$ in Fig. 5.2, by the mechanism described in detail in the previous Chapter.

In the following, we want to investigate, how this newly formed dust shell develops and which processes it causes.

By the substantial backwarming effect of the innermost dust layer the temperature in the wake of the shock front is increased, and consequently the stellar radius in units of the initial radius increases a few percent. The increase of the temperature amounts to values of 100 K in the region around the stellar radius. Subsequently, cf. plots at $t = t_0 + 130d$, this leads to a slight increase of the pressure in the innermost region. More clearly, one should speak of a perturbation, that is induced in the region below 2 $R_\star$. The density so far is unaffected since no mechanical energy input is present. The material in the region of the stellar radius, which up to now has been falling inwards, since it is gravitationally bound and no really counterbalancing force has been present, reverses its direction of movement and flows outwards with a few m s^{-1} due to the increase of the pressure gradient.

Subsequently, this subsonic disturbance develops into a wave front with an amplitude of $\approx$ 1 km s^{-1}. This new small–amplitude wave runs outwards and finally compresses the material, thereby triggering dust growth. However, this implies, that in the region under consideration already dust formation has taken place. This is indeed true, as the plot of the number of dust grains per H–atom confirms. These grains have been formed in the wake of the previous fully developed shock wave, and dust nucleation is still going on, as the broad peak of nucleation rate at $t = t_0 + 130d$ shows. Due to this effective nucleation phase, the waves now provide favourable conditions to initiate dust growth. This can be seen from the tiny peak in the degree of condensation at $\approx 2.5 R_\star$ at $t = t_0 + 130$d. Again, dust condensation influences both, thermodynamics and hydrodynamics. Already at this instant of time it can also be seen that this peak already causes a tiny step in the temperature structure, thereby starting the next cycle of wave formation.

Subsequently, at radii around 3.5 $R_\star$, the grains grow very effectively and at $t = t_0 + 585$d a degree of condensation of almost 1 is reached.

Radiation pressure acts on the newly formed grains and via the close momentum coupling between grains and gas the whole two–component medium is accelerated to supersonic velocities. A new shock front forms which sweeps up the material and again enhances the conditions for dust growth. Nucleation of grains dies off in the wake of the newly formed shock front since the temperature becomes too high by the backwarming of the newly developing dust shell. Finally, at $t = t_0 + 780$d, nucleation completely stops since all condensable material in the shock front is actually condensed into grains and a broad new dust shell is formed.

During this phase the small–amplitude waves in the innermost region of the CDS run into a gas which is free of newly formed dust particles, and therefore without causing any effect on the dynamics these waves are rapidly damped. A reason for this damping could be the be ratio between the period of these small–amplitude waves and the respective cut–off period of the system. As investigated in Sec. 3.2.4, the propagation of small–amplitude waves is hindered if their period is larger than the cut–off period of the system.

When finally, the new dust layer has moved farther outwards and the temperature drops below $\approx$ 1300K a new nucleation phase starts and the whole process starts again. In this sense, the dust complex triggers its own formation, and, depending on the specific physical conditions, imprints a time scale on the system.

Summarizing, we find, that even in models without an applied exterior pulsation, the dust complex is able to build up a self-maintaining mechanism which produces an outflow which is periodically passed by strong shock waves. There are essentially two prerequisites necessary for this mechanism:

1. The density gradient of the initial hydrostatic model must be smooth enough, i.e. the density scale height must be high enough, to allow for dust formation already in this initial phase. However, as stated above, the development of the κ–instability is likely also to occur in models where the initial levitation and subsequent dust formation is achieved by other mechanisms apart from waves, e.g. by radiation pressure on molecules.

2. The interaction between the dust complex and the thermodynamics, i.e. the backwarming which rises the temperature, is necessary to initiate pressure–driven waves. Depending on the ratio of their period to the respective cut–off period of the system, these waves travel into the grain–containing region and start an avalanche growth phase.

Thus, in the models presented, the dust complex acts twofold. First, it initiates small–amplitude waves, which are necessary for effective growth in the succeeding cycle, and second, by the existence of the dust grains, they provide the possibility to transmit radiative momentum to the wind, and thereby driving the massive outflow.

Since the backwarming due to the dust opacity in the CDS plays the key role for this process we want to call this mechanism *exterior* κ*–mechanism*.

A similar mechanism of instability is known from the line–driven winds of hot luminous stars, e.g. [Rybicki 1987], [Owocki *et al.* 1988], [Owocki 1990]. In this context, small-scale fluctuations of the radial outflow velocity cause a Doppler-shift of the local line-frequency out of the shadow of the surrounding material, which results in an increased line–force which subsequently tends to increase the flow velocity. An instability analysis (for a review see e.g. [Rybicki

1987]) shows that these perturbations have rather large growth rates, such that they become quickly nonlinear, and small initial perturbations suffice to result in a wind which is passed by several shock waves.

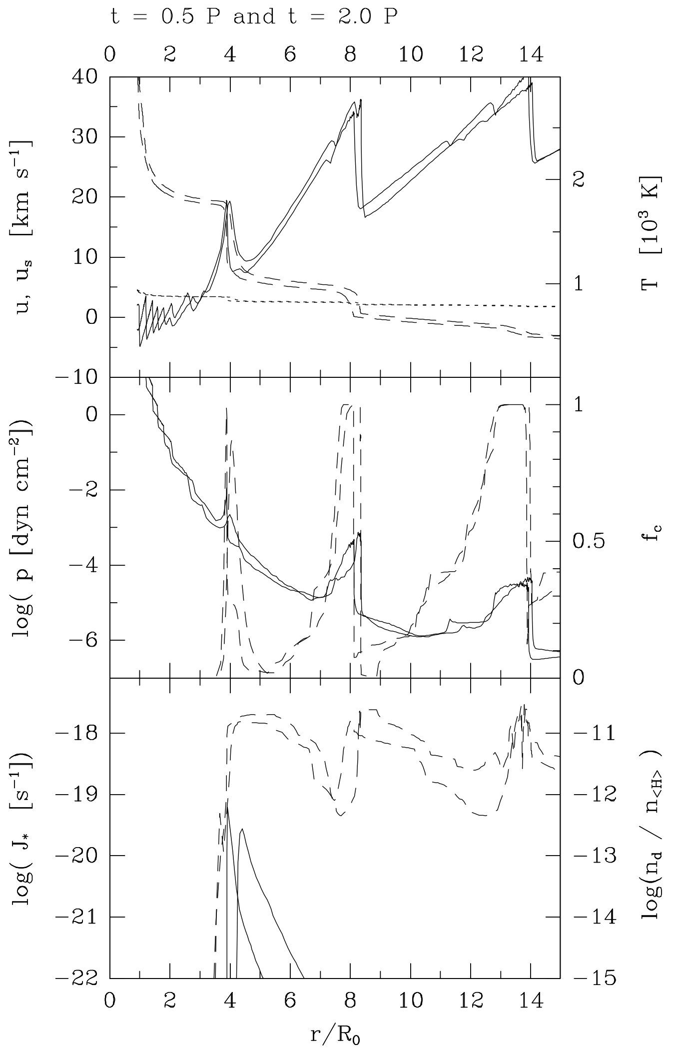

Figure 5.3: Radial structure of a model where the dust opacity *is* taken into account in the determination of the radiative equilibrium temperature at two different instants of time. The model is driven by a piston with period 650d and an amplitude of $\Delta u_P = 2$ km s^{-1}. The model parameters are the same as given for Fig 5.2.

5.2.3 The eigenperiod

We have shown in the previous section that the exterior κ–mechanism produces strong shock waves which run through the atmosphere by a self–regulated formation of dust particles. Following the development of the model presented in the last section a little bit further, as shown in Fig.5.2, reveals, that the exterior κ–mechanism is a strictly periodical phenomenon. Continuing the analysis of the model plotted in Fig. 5.2 would show, that the next shock is formed at $t = t_0 + 975d$, that, in fact, one shock is formed each 975 days. This time scale is the characteristic or *eigenperiod* of the atmosphere, which is inherent to the dust–forming system and is dependent on parameters such as the abundance ratio of carbon to oxygen or the stellar luminosity, cf. Sec. 5.3.

If the system obviously has an eigenperiod the question arises, how is the interplay with an exterior mechanical force, namely the piston at the inner boundary, which so far, of course, has been kept non–moving.

Fig. 5.3 depicts the radial structure of the same quantities as in Fig. 5.2, but for a model driven by a piston with a period of 650d and an amplitude of 2 km s^{-1}. The period is chosen exactly two third of the models eigenperiod. As indicated, two instants of time are plotted on top of each other.

Fig. 5.3 shows that, although a piston is applied at the inner boundary, the input of mechanical energy has no influence on the timescale of the circumstellar shell. The shell exhibits a cyclic pattern, apart from minor numerical fluctuations, on a scale of 1.5 times the period of the piston, i.e. exactly on its eigenperiod of 975d, whereas in the inner parts, i.e. below 3 $R_\star$, the pattern is completely dominated by influence of the piston, and characterized by the presence of low–amplitude shock waves. However, these waves do not suffice to change the characteristic time scale of the outer atmosphere, but do solely determine the time scale of the innermost region. At the instants of time shown in Fig. 5.3, when the outer structure is exactly periodic, the radial courses of e.g. the density structure in the innermost region are 180° phase-shifted, since these instants of time belong to the beginning and to the middle of the *pulsational* cycle, whose time scale determines the innermost structure.

Obviously, we find that the dynamical behaviour of the CDS is dominated by different "driving–regimes". These regimes represent different physical mechanisms or a combination of them, which account for the development of the outflow.

Among other calculations e.g. [Wood 1979] and [Bowen 1988a] also presented models which are purely driven by pulsation. Although these models were somewhat artificial, since they cannot account for the observed mass loss rates of Miras and LPVs, they represent one end of the scale of driving regimes. In Paper I we investigated the combined effect of pulsation and radiation pressure on dust. The model parameters of these calculations lie within the range were a dust driven outflow is only possible with additional energy support. The models presented here, although some include the effects of interior pulsation, are purely dominated by radiation pressure on dust. If the stellar luminosity of these models is reduced, the dominance of the dust diminishes. Further reduction eventually leads to a vanishing of the outflow, if no mechanical energy support is provided.

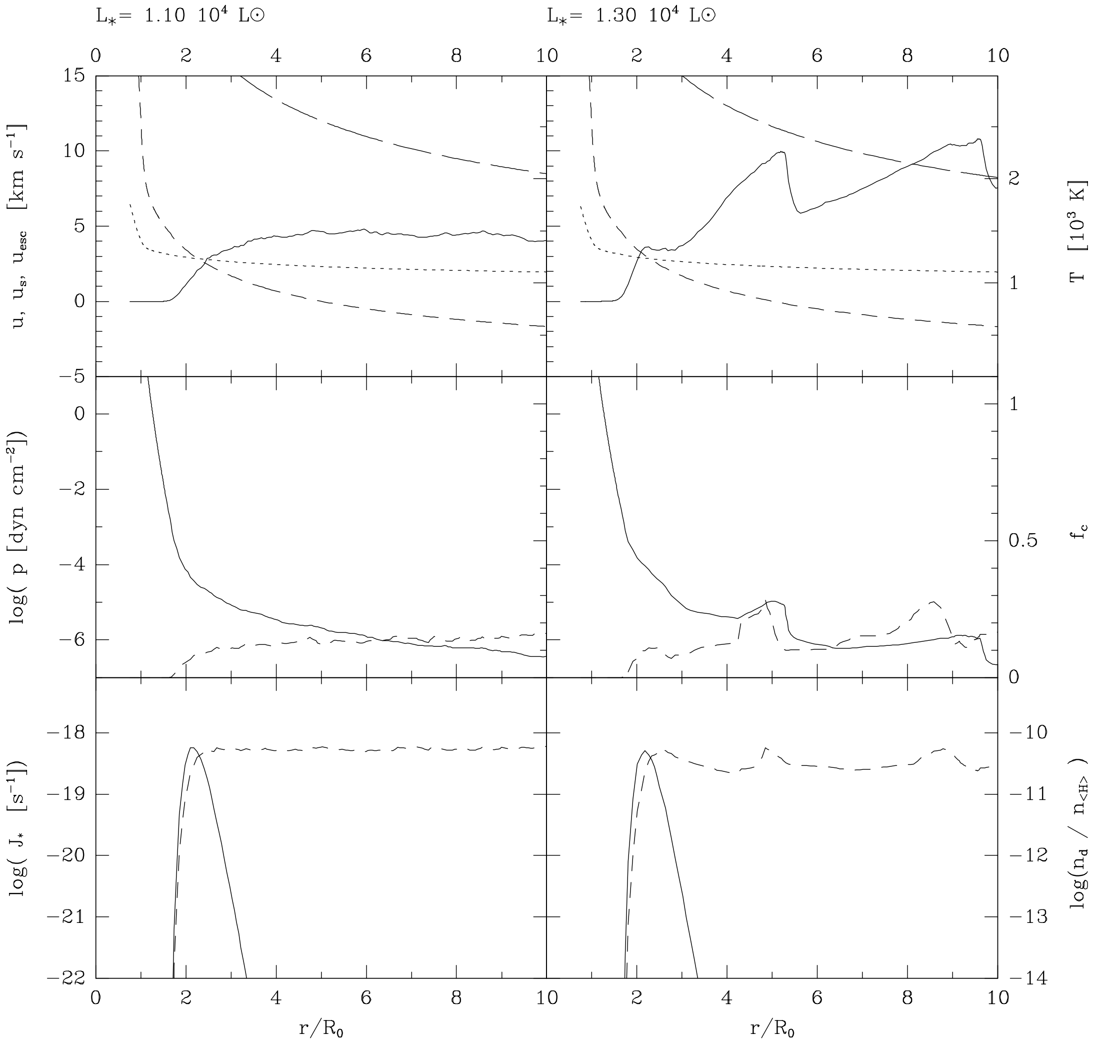

Figure 5.4: Radial structure of two models with different luminosities where the dust opacity *is* taken into account in the determination of the radiative equilibrium temperature. The parameters are equal to Model A of Fig. 5.2 except for the luminosities which are $L_\star = 1.10\ 10^4$ (l.h.s.), $1.30\ 10^4$ (r.h.s.), respectively.

5.2.4 The limit luminosity for the purely dust driven outflow

To determine the limit luminosity below which no dust driven outflow is possible and to investigate the behaviour of the models towards this limit luminosity, we have calculated a series of models with decreasing luminosity. The initial parameters as well as the resultant quantities are listed in Tabs 5.1 and 5.2, respectively.

A first evident and obvious result from these tables is that the decrease of the radiative force causes reduced mass loss rates and substantially decreased final outflow velocities. The reduction of the energy source for the outflow must reduce the rate of mass loss and the velocity of the outflowing matter. We will come back to a more detailed discussion of these tables later on, cf. Sec. 5.3.

Fig. 5.4 shows the radial structure of two models at the lower end of the luminosity scale. The same quantities as in Fig. 5.2 are plotted. To the upper row of the diagram we have added the course of the escape velocity u_{esc}, which is shown by the long-dashed line.

For the chosen set of model parameters the transition from the range, where the exterior κ–mechanism occurs to the range, where the dust opacity cannot influence the dynamics decisively, lies between $L_\star = 1.10\ 10^4$ and $1.30\ 10^4\ L_\odot$. Although dust nucleation in both models is almost identical, cf. plot of $J_\star$ in Fig. 5.4, which means that approximately the same amount of dust is formed and the position of the nucleation region are almost identical, however, the slightly less steeper density gradient of the r.h.s. model allows a somewhat more effective dust growth process, and hence, the onset of the exterior κ–mechanism. For the model on the l.h.s. the influence of the dust does not suffice to act as a valve, and thus, to modulate the resulting outflow.

This limit luminosity region also marks the dividing line, below which no purely dust driven outflow is possible. For the model with $L_\star = 1.10\ 10^4\ L_\odot$ (l.h.s.) radiation pressure on dust grains indeed is able to accelerate the flow to supersonic velocities but the radiative force does not succeed to lift the material out of the gravitational field. Below $1.10\ 10^4\ L_\odot$ a supersonic flow might develop for a certain time but will eventually collapse during the subsequent course of the model calculations. For the model on the r.h.s. of Fig. 5.4 radiation pressure on dust lifts the material out of the gravitational field at about 8 $R_\star$ and causes a "real" mass loss.

5.2.5 The limit case of a stationary dust driven wind

We have shown that the dust opacity plays a key role in determining the dynamics of the CDS. However, the l.h.s. model of Fig. 5.4 has already demonstrated what happens, if the interaction between the dust complex and the thermodynamics becomes negligible since dust formation has not been effective enough. In this

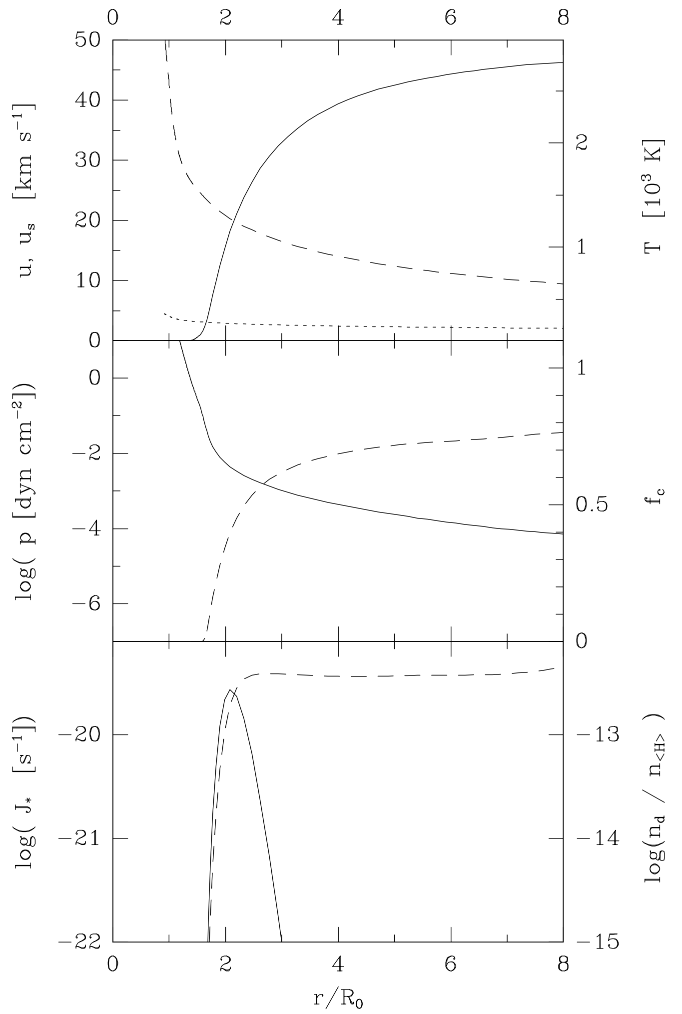

Figure 5.5: Radial structure of a model where the dust opacity *is not* taken into account in the determination of the radiative equilibrium temperature. The quantities are explained in the text. The model parameters are the same as in Fig. 5.2: $M_\star = 1.0\ M_\odot$, $T_\star = 2600$ K, $L_\star = 3.0\ 10^4\ L_\odot$, $\epsilon_C/\epsilon_O = 1.80$, $\Delta u_P = 0.0$.

---

section we would like to turn things around, and want to investigate the case were the coupling between the dust complex and the thermodynamics is a priori neglected, i.e. the case were in the determination of the temperature in radiative equilibrium only the constant gas opacity is taken into account.

Fig. 5.5 shows the same quantities as in Fig. 5.2 for a model calculation with exactly the same model parameters except that the temperature in radiative equilibrium is determined *without* taking into account the dust opacity.

The result is the typical structure of a stationary dust driven wind around a carbon star (cf. e.g. [Gail and Sedlmayr 1987b], [Winters *et al.* 1994a]). In the inner region, i.e. for radii below 1.5 $R_\star$, the dust driven wind solution starts with low velocities of only a few meters per second. Only a small amount of dust grains are present in this region, which stay rather long in this innermost dense region due to the low velocities. Therefore, they have excellent growth conditions and reach particle radii of a few μm. Since the nucleation rate is approximately 8 orders of magnitude smaller in this region than the range shown in Fig. 5.5, there is only a tiny amount of these large particles and they are dynamically irrelevant.

The temperature decreases with increasing distance from the star. Around 2 $R_\star$ the temperature is sufficiently low and effective nucleation of dust grains starts. Furthermore, these grains grow effectively and soon a dynamically relevant degree of condensation is reached. At $\approx$ 1.6 $R_\star$ radiation pressure on dust accelerates the flow to supersonic velocities.

In the outer region the nucleation rate rapidly decreases but the existing particles still grow, which leads to a continued incline of the degree of condensation. Finally in this model, 80% of the condensable material is condensed into dust grains and a final velocity of $\approx$ 48 km s^{-1} is reached. The high outflow velocity mainly results from the high final degree of condensation and from the high value of the stellar luminosity chosen for this model.

The main conclusion we draw from this surprising result is, that the exterior κ–mechanism really is based on a physical process whose central component is the dust opacity. If e.g. numerical artifacts were responsible for the occurrence of the exterior κ–mechanism, the neglect of a physical interaction would have led to anything but a known, well–studied solution. Furthermore, this result of "stationary" dust driven wind has been almost achieved already in the previous section, where we have investigated the limit luminosity. In the region near the limit luminosity, the model structure looked already rather similar to stationary dust driven wind, although all interaction between the physical ingredients were taken into account.

Again it is interesting to draw an analogy to the winds from hot, luminous stars. In his review [Owocki 1990] quotes several arguments from observations as well as from theory that give reasons to believe that the winds from hot stars are not stationary flows but have an internal structure and a time variability. Obviously, for the case of winds from cool star, there also exist stationary dust driven wind solutions which are not stable if all interactions are realized, since they develop instabilities as demonstrated in Sec. 5.2.2. An interesting question for future research would be to investigate whether this is the case for *all* stationary wind solutions. Clearly, this cannot be done with numerical methods but with a mathematical stability analysis which allows to analyse the manifold of solutions of the underlying system of basic equations and, therefore, this approach is beyond the scope of the present paper.

To summarize briefly, we get the result, that our code reproduces the stationary dust driven wind solution, if the coupling between the thermodynamics and the dust complex is neglected.

Table 5.1: Parameters of the initial hydrostatic models to demonstrate the exterior κ–mechanism

No.	$T_\star$	ϵ_C/ϵ_O	$L_\star$	$R_\star$	$M_\star$	P	Δu	R_{inner}
1	2600	1.80	50000	1100	1.0	–	0.0	0.76
2	2600	1.80	30000	852	1.0	–	0.0	0.91
3	2600	1.80	30000	852	1.0	–	0.0	0.76
4	2600	1.80	30000	852	1.0	–	0.0	0.91
5	2600	1.80	30000	852	1.0	–	0.0	0.91
6	2600	1.80	30000	852	1.0	–	0.0	0.91
7	2600	1.80	30000	852	1.0	650	2.0	0.91
8	2600	1.80	30000	852	1.0	650	2.0	0.91
9	2600	1.80	20000	696	1.0	–	0.0	0.76
10	2600	1.80	13500	571	1.0	–	0.0	0.76
11	2600	1.80	12700	555	1.0	–	0.0	0.76
12	2600	1.80	12500	550	1.0	–	0.0	0.76
13	2600	1.80	11500	528	1.0	–	0.0	0.76
14	2600	1.80	11000	516	1.0	–	0.0	0.76
15	2600	1.80	10000	492	1.0	–	0.0	0.76
16	2450	1.25	30000	959	1.0	–	0.0	0.82
17	2450	1.25	30000	959	1.0	–	0.0	0.82
18	2300	1.25	30000	1089	1.0	–	0.0	0.87
19	2300	1.25	30000	1089	1.0	–	0.0	0.87
20	2300	1.25	30000	1089	1.0	388	3.0	0.87

Table 5.2: Resultant quantities from the model calculations which show an exterior κ–mechanism

No.	$\dot{M}$	u_∞	ρ_D/ρ_G	$L_{\star,min}$	$L_{\star,max}$	Remarks
1	$4.0\ 10^{-4}$	32.5	$3.3\ 10^{-3}$	57660	61540	with κ_D
2	$5.8\ 10^{-5}$	37.2	$3.5\ 10^{-3}$	30380	33650	with κ_D, Eigenperiod $\approx$ 1.4
3	$6.5\ 10^{-5}$	37.5	$2.7\ 10^{-3}$	31220	33810	with κ_D
						continued on next page

continued from previous page						
No.	$\dot{M}$	u_∞	ρ_D/ρ_G	$L_{\star,min}$	$L_{\star,max}$	Remarks
4	3.7 10^{-4}	49.1	3.5 10^{-3}	29850	29870	withoutκ_D, stationary wind
5	7.4 10^{-5}	31.2	2.3 10^{-3}	30000	30000	with κ_D, $L_\star$ = const. $T_\star$ variabel
6	1.9 10^{-4}	27.7	2.0 10^{-3}	30000	30000	without κ_D, $L_\star$ = const. $T_\star$ variabel
7	6.9 10^{-5}	31.2	2.7 10^{-3}	27550	38740	with κ_D, $n_P = 1.5$
8	1.5 10^{-3}	56.0	3.9 10^{-3}	23320	26870	without κ_D, stat. wind with shocks
9	3.4 10^{-6}	30.2	1.6 10^{-3}	20480	22190	with κ_D
10	4.4 10^{-6}	24.4	1.6 10^{-3}	13630	14350	with κ_D
11	3.6 10^{-7}	8.6	6.8 10^{-4}	12720	12720	with κ_D
12	3.1 10^{-7}	7.9	6.0 10^{-4}	12520	12520	with κ_D
13	7.2 10^{-8}	5.7	6.8 10^{-4}	11510	11510	with κ_D
14	6.2 10^{-8}	3.2	6.5 10^{-4}	11010	11010	with κ_D
15	3.3 10^{-9}	2.9	1.8 10^{-4}	10010	10010	with κ_D, no wind
16	1.0 10^{-4}	13.5	1.1 10^{-3}	–	–	with κ_D, Eigenperiod = 7.7
17	9.1 10^{-5}	12.9	7.3 10^{-4}	–	–	without κ_D, stationary wind
18	2.4 10^{-4}	11.2	8.5 10^{-4}	30210	38780	with κ_D, Eigenperiod = 8
19	1.2 10^{-3}	18.6	1.1 10^{-3}	29630	29670	without κ_D, stationary wind
20	2.6 10^{-3}	20.6	1.2 10^{-3}	29020	31100	without κ_D, stat. wind with shocks

5.3 Discussion

In Tabs. 5.1 and 5.2 we have summarized the results of our model calculations.

In the last five models we reduced the overabundance of carbon to oxygen substantially to demonstrate that the exterior κ–mechanism also occurs in models with rather low ϵ_C/ϵ_O–ratios, and is not a result of presumably too high carbon overabundances.. Besides an outflow velocity, which is on the average substantially decreased in these models, the reduction of ϵ_C/ϵ_O also causes an extension of the eigen-period to 7.7 respectively 8 P, where P denotes the period of 388d of model No. 20. The eigenperiods of the models No. 1–15 are given in units of 650d.

Besides the models listed in Tab. 5.1, we have also calculated two series of models were the initial luminosity was held constant (2 10^4 or 3 10^4 $L_\odot$, respectively) and the ϵ_C/ϵ_O–ratio was varied. The luminosities were well above the limit luminosity for the exterior κ–mechanism. The result is an anti–correlation between ϵ_C/ϵ_O and the eigenperiod of the atmosphere. An increase of the condensable material, i.e. the ϵ_C/ϵ_O–ratio, results in a shortening of the eigenperiod. A result that is quite clear: since the initial conditions were equal for the models of one series, a large amount of condensable material ensures a high reoccurrence frequency of the exterior κ–mechanism, however, at low overabundances it takes a longer time interval until enough material is swept up to produce a subsequent shock.

In contrast, the eigenperiod is correlated nonlinearly with the luminosity. Longer eigenperiods are found for models with rather high luminosities and at the lower end of the luminosity scale. Around an initial luminosity of $L_\star = 2.0$ 10^4 $L_\odot$ there seems to be a minimum of the eigenperiod–luminosity correlation. In the high luminosity models a dramatic backwarming occurs with a temperature increase in the inner region up to a few hundred K due to the effective dust formation process. Therefore, it takes a longer time interval till the newly formed dust layer has moved outwards and the temperature in the dust nucleation region has appropriately decreased to allow for the next dust nucleation cycle. The length of the eigenperiod also increases towards the limit luminosity of the exterior κ–mechanism. These models are characterized by a less effective dust formation process. The resulting self–induced shock waves therefore have a smaller amplitude and travel through the atmosphere at a much lower velocity. Thus, it takes longer till the radial pattern repeats itself. Obviously, between these two limiting cases there exists a configuration where the effects of backwarming and dust formation are in an optimal state. One could also imagine this behaviour by a three–dimensional representation of the eigenperiod as a function of carbon overabundance and luminosity. The resulting graph would then closely resembles that of an atomic potential well.

As indicated in Tabs. 5.1 and 5.2, some of the models were also calculated with a piston applied at the inner boundary to simulate the interior pulsation. The piston had an amplitude of 2 km s^{-1} and a period of 650d for the models of the first series and an amplitude of 3 km s^{-1} and a period of 388d for the models of the second series. For the high luminosity models of the first series the piston only has minor influences on the resulting period of the CDS, cf. models No. 2 and 7. The atmosphere still changes on the scale of its eigenperiod. The minor influence of the piston stems from the density gradient of these models in the innermost region. There, the models still have the initial density structure of the hydrostatic model, i.e. a less steeper density gradient for the high–luminous models. Therefore, the steepening of the dust–induced waves is confined to smaller amplitudes and the compression of the material is limited. Nevertheless, the densities are high enough to allow very effective growth without additional compression. Going to lower luminosities the input of mechanical energy becomes more and more important. These models are determined by the interaction of the two driving forces: the dust complex and the piston. Since the characteristic periods of these forces are different the driving mechanisms can not interfere constructively. The whole system behaves like a forced pendulum, whose exterior force is not in resonance with the eigenperiod of the pendulum.

By the preceding discussion, we get a first brief idea how the effect *multiperiodicity* (already mentioned in Papers I and II) occurs. If the ratio of the period of the piston and the eigenperiod of the atmosphere does not have an integer value then the model behaves irregularily, if this ratio does have an integer value then we have a regular multiperiodic model, i.e. the radial structure of the model at a certain instant of time t_0 equals the radial structure at $t_1 = n_P P + t_0$, where P is the period of the piston and n_P is the integer–valued *multiperiodicity number*.

This gives a reasonable explanation for *multiperiodicity* for most of the models considered here. However, it remains to explain multiperiodicity for those models which do not possess an eigenperiod in the sense described here. In these models the multiperiodic outflow occurs via the combined interaction of pulsation and dust formation. A detailed analysis of these models will be the subject of a forthcoming paper of this series. A further aspect to be investigated in the near future, is the question, whether possibly the exterior κ–mechanism is likely to occur in *all* time dependent model calculations, which include the relevant interaction mechanism, without regard of the fundamental model parameters. This question arises by the following simple consideration. Given an arbitrary model calculated as described in Chap. 4, irrespective of its luminosity or overabundance of carbon to oxygen. What happens, if for the evolved model the piston suddenly is turned off or at least its amplitude is slowly decreased? Would it be possible, that the existing outflow is still maintained by the exterior κ–mechanism, despite the fact, that the support of mechanical energy is lacking? In principle, this problem could be easily answered by a demonstrative calculation with our developed code. Unfortunately, corresponding attempts failed so far due to numerical instabilities, such that the question has to remain still unanswered.

In Tab. 5.2 some models are labeled "stationary wind with shocks", a terminology that is perhaps somehow misleading. In fact, these models were calculated without taking into account the dust opacity into the determination of the temperature in radiative equilibrium but with a piston at the inner boundary. The overall radial structure is similar, as one would expect, to the models presented in Sec. 5.2.5 and Fig. 5.5, i.e. similar to the structure of a stationary dust driven wind. However, e.g. the radial structure of the velocity is modulated by a periodic pattern of small–amplitude waves. The reason why these waves, that result from the movement of the piston at the inner boundary, remain with a small amplitude is again the density gradient. The less steeper density gradient of these models with high luminosities prohibits a greater steepening of the waves. Dust formation starts at slightly larger radii, compared to Fig. 5.5, and is completely unaffected by the pulsation. Obviously, dust formation and pulsation behave independent in these models, since the important coupling by the backwarming caused by the dust opacity is neglected. For these models pulsation is an additional feature which is not necessary to drive the wind.

Tabs. 5.1 and 5.2 also contain two models whose luminosity was held constant during the entire model run. Since the luminosity is determined by the equation $L_\star = 4\pi R^2 \sigma T_\star^4$ we can use this equation vice versa to determine the stellar temperature if $L_\star$ is held constant. Thus, the luminosity is held constant in time and the stellar temperature varies periodically during the model run.

The resulting radial structure does only deviate quantitatively from the corresponding calculations in the previous sections. The overall dynamical structure is essentially the same. More important, this result demonstrates that the exterior κ–mechanism also occurs if the radiation source is held constant in time. This result gives a further confirmation of the finding that the exterior κ–mechanism really is caused by the valve property of the dust opacity. Major differences of these model calculations compared to the usual calculations were $T_\star$ is held constant, occur only in the final outflow velocities. Most probably this results from reduced growth conditions of the dust grains due to a more variable temperature structure. However, this gives a further hint about the influence of the approximation of isothermal shocks. If a varying stellar temperature does not prohibit the exterior κ–mechanism, then also cooling behind the shock front will not essentially affect this mechanism. Although, the temperature will show larger variations, this will only influence the exterior κ–effect quantitatively, e.g. by enlarging the eigenperiods.

5.4 Conclusions

We have presented dynamical models of circumstellar dust shells around carbon–rich long–period variables, which include time–dependent hydrodynamics and a detailed treatment of the processes of formation, growth and evaporation of dust grains.

We have demonstrated that for sufficiently luminous models an instability in the CDS occurs, which causes these models to develop shock waves, even if *no* piston is applied at the inner boundary. We found that the dust opacity in the shell plays a central role in this process and, therefore, called the effect *exterior κ–mechanism*. Basically, this mechanism consists of the interaction of self–induced small–amplitude waves and the dust complex.

It was demonstrated how the onset of this effect occurs in initially hydrostatic models. The stars under consideration, however, are most probably not in hydrostatic equilibrium. Small fluctuations are likely to be present in these objects, and could initiate the exterior κ–mechanism. Therefore, the effect is not an artificial computer experiment but a mechanism that should be realized in stars with the appropriate stellar parameters.

Furthermore, by the exterior κ–mechanism these luminous models are able to develop a massive slow outflow, typical for objects on the tip of the AGB *without* the support of mechanical energy by the pulsation. This finding supports the suggestion of e.g. [Dominik *et al.* 1990] that purely dust driven winds could provide a mechanism to account for the transition to the so called "superwind" phase. The superwind is thought to be a phase of increased extensive mass loss occuring at the very end of the AGB–evolution, immediately before the transition to the Planetary Nebulae stage. Since the dust driven wind models show an increased mass loss while the temperature decreases and the luminosity increases, which is similar to the final evolution on the AGB, dust driven wind represent a natural physical mechanism to account for the observed behaviour of the objects in this stage of stellar evolution.

The results demonstrate that dust driven wind solutions indeed exist. However, our exemplary calculations revealed that taking into account all interactions leads to the development of instabilities. Thus, stationary dust driven wind might only be a limit case, and the "standard" solution shows a complicated internal structure and is highly time variable as discussed above.

The dynamics of the models, which show the exterior κ–mechanism, reveal an eigenperiod, which is the characteristic time scale between two dust–induced shocks. This eigenperiod was found to depend nonlinearly on the luminosity and to be anti–correlated to the overabundance of carbon to oxygen. If the piston is turned on at the inner boundary of these models with a period different from the eigenperiod, the behaviour of the high–luminosity models remains unchanged since radiation pressure on dust grains completely dominates the dynamics of the shell.

Summarizing, the results again underline the importance of a detailed treatment of the formation of dust in *dynamical* models of Miras and LPVs. Taking into account the time–dependence of the mechanisms reveals the nonlinear behaviour of the physical processes and leads to similar results as already known from the line–driven winds from hot stars, which unifies our picture of mass loss mechanisms.

Chapter 6

Multiperiodicity

6.1 Introduction

Pulsation is an ubiquitous physical component of Miras and LPVs, some details of which have been discussed in Chap. 1.

From the observational point of view, pulsation seems to be closely related to a significant mass loss and the occurrence of a circumstellar dust shell. From the evaluation of observations of bright IRAS sources [Habing 1987] draws the following conclusion. If the value of the [2 μm] –[12 μm] color index of a source, which indicates substantial amounts of dust, has a value exceeding 1, then the object usually is a variable with a large pulsation amplitude. Those objects with no or small amplitudes are found to have no or small [2 μm] – [12 μm] excesses. For a large sample of objects from the Two Micron Sky Survey and the IRAS catalogue this result has been found also by [Jura 1986c] and has been presented in a very intuitive histogram.

It is the very aim of this chapter to investigate the general interplay between the pulsation and the dust complex. So far, the investigation has been focused on very special topics of dust formation in Miras and LPVs. In Chap. 4 we discussed in detail the role of pulsation for the development of a certain discrete structure of the CDS in connection with a consistent treatment of dust formation. An exemplary model calculation has been analyzed in great detail. The main emphasis has been given to explain the development of the dynamical structure of the atmosphere as well as to demonstrate the formation of dust under time-dependent conditions.

In Chap. 5, in contrast, we presented purely dust driven models. To account for an outflow without the support of mechanical energy, the model parameters had to be chosen somewhat extreme, i.e. the models had to have rather soft density gradients, i.e. a low density scale height, and therefore were rather extended which results in high luminosities. Under these conditions dust formation completely dominates the dynamical structure of the CDS.

In the present chapter we want to take a more general point of view. We want to allow for all values of the *multiperiodicity number* n_P (for a definition of n_P see below). The models in Chap. 4 were confined to $n_P = 1$. In most of the cases, this was done simply by increasing the overabundance of carbon to oxygen and to force the shell to adopt the period of the piston. In Chap. 5 we discovered that the shell indeed has an eigenperiod and is able to determine the dynamics by itself. The question we want to attack in more detail in this chapter is, whether there is a relation between the eigenperiod and multiperiodicity and if this relation can be put into any quantitative statements, such that predictions are possible how a certain model will behave.

Furthermore, this will shed some more light on a special "driving–regime": the pulsation–dust regime, an intermediate regime. On the one end of the "driving–scale" there is the pure dust regime, which seems to be applicable for the very late stages of the AGB evolution. The other end of the scale consists of the pure pulsation regime, which seems to be rather artificially and seems not to be applicable to any of the stages of stellar evolution of interest here.

As already mentioned some times, the interplay between pulsation and the dust forming system leads to *multiperiodicity*. First, how do *we* define multiperiodicity? If the radial structure of a certain model at an instant of time t_0 equals the radial structure at $t_1 = n_P P + t_0$, where P is the period of the piston and n_P is the integer–valued *multiperiodicity number*, we say the model is multiperiodic with the periodicity number n_P.

Usually, the velocity structure is taken as a tracer of multiperiodicity. Unfortunately, there is no practicable numerical algorithm to determine n_P. It is done "by hand" by placing plots on top of each other, and by comparing the respective data files. If the pattern repeats not only twice but over a suitable time interval, which, of course, has to be longer for larger n_P and the shocks present in the calculated radius interval lie satisfactorily atop of each other, we claim that the model is multiperiodic. A numerical algorithm would require to trace the shock front, which is a difficult task in Lagrangian codes, and to then define an ϵ–neighbourhood which the shocks are allowed to differ from one instant of time to the next. This would, of course, provide a more quantitative method to determine the multiperiodicity number.

In order to avoid confusion with the word *multiperiodicity* a few comments seem to be appropriate. The "standard" use of multiperiodicity means the occurrence of more than one pulsational mode, i.e. refers to processes far below the photosphere, e.g. [Wood 1976, Wood 1986], [Buchler 1990], [Buchler *et al.* 1991]. In the present context we refer to multiperiodicity also for circumstellar processes, i.e. we include the interaction between the CDS and the pulsation. Whether this has observable consequences which are usually attributed to "standard multiperiodicity", will be investigated in Chap. 7.

To make one thing explicitly: our *multiperiodicity* effect has nothing to do with a change of the movement of the piston. The piston is still assumed to perform pure sinusoidal variations, with *one* fixed frequency. No additional oscillation modes are taken into account. The resulting multiperiodicity is solely caused by effects in the circumstellar dust shell.

Before we come to some general results on multiperiodicity, we have to analyze two exemplary multiperiodic calculations in some detail in the next section.

6.2 Detailed analysis of multiperiodic models

A plot of the radial structure of a multiperiodic model at a certain instant of time differs in general, of course, only slightly from that of a model with $n_P = 1$ in Sec. 4. The models exhibit a levitated atmosphere compared to a hydrostatic density scale height, they are passed by strong shock waves, and the dust is distributed inhomogeneously in discrete layers. However differences occur, if we analyze the temporal behaviour of the physical quantities of interest.

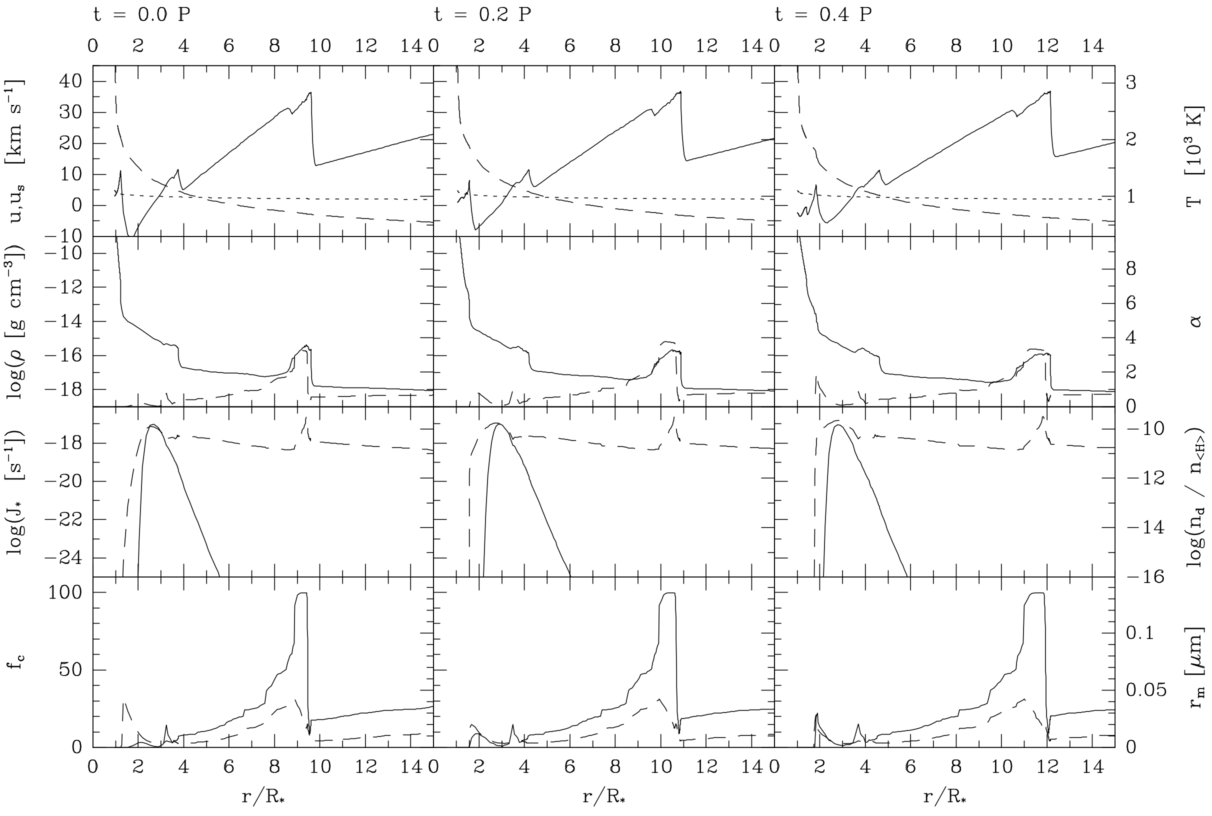

Figure 6.1: Radial structure of Model 23, cf. Tabs. 6.1, 6.2, at selected instants of time during the first pulsational cycle

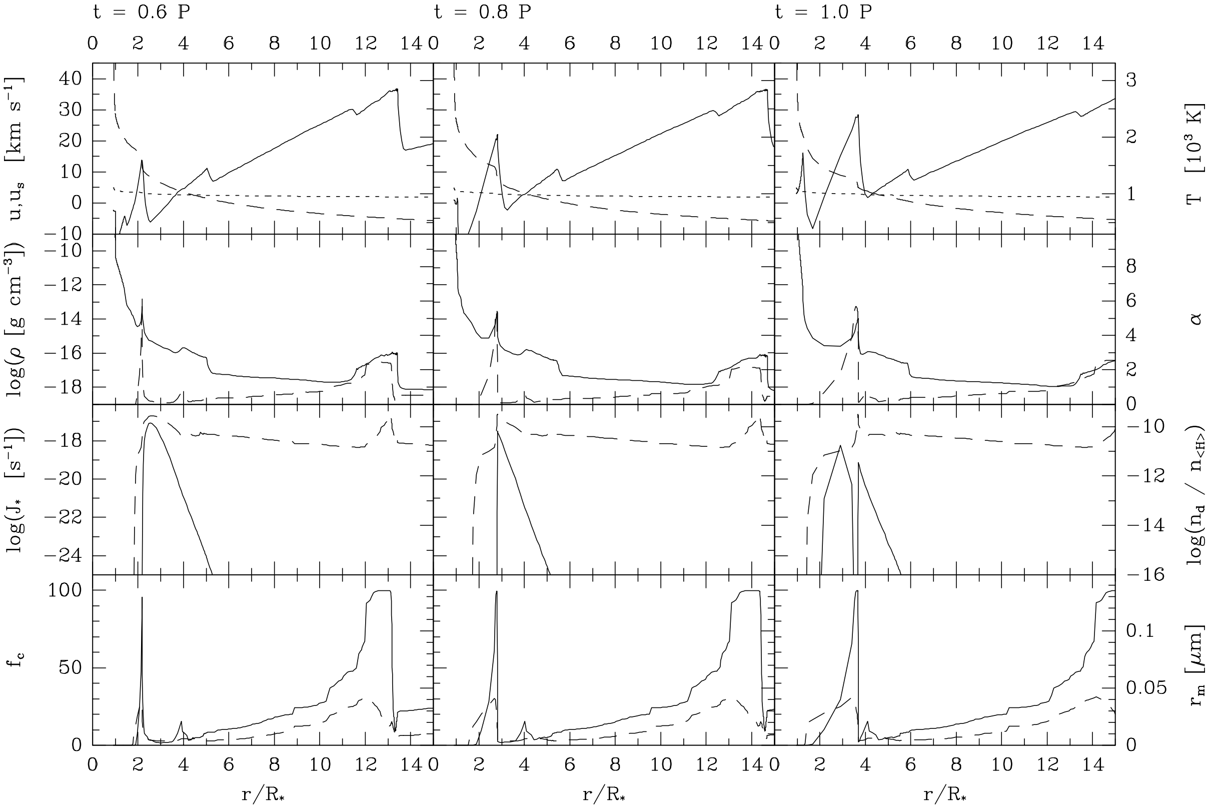

Figure 6.2: Fig. 6.1 continued

6.2.1 The radial structure

Figures 6.1, ..., 6.4 show a time sequence of the radial structure of CDS at twelve selected instants of time during **two** pulsational cycles. Figures 6.1 and 6.2 comprise the first pulsational period, Figs 6.3 and 6.4 the second. In the sequence of plots the time increases from the left to the right.

In detail, the Figs 6.1, ..., 6.4 show:

upper row: the velocity u (solid line), the velocity of sound u_s (short–dashed line), both belong to the l.h.s. ordinate, and the temperature T (long–dashed line, r.h.s. ordinate),

2nd row: the logarithm of the density ρ (solid line, l.h.s. ordinate) and the radiative acceleration α in units of the gravitational acceleration (dashed line, r.h.s. ordinate),

3rd row: the logarithm of the nucleation rate $J_\star$, i.e. the number of dust grains formed per second and H–atom (solid line, l.h.s. ordinate), and the logarithm of the number of dust grains per H–atom $n_d/n_{<H>}$ (dashed line, r.h.s. ordinate),

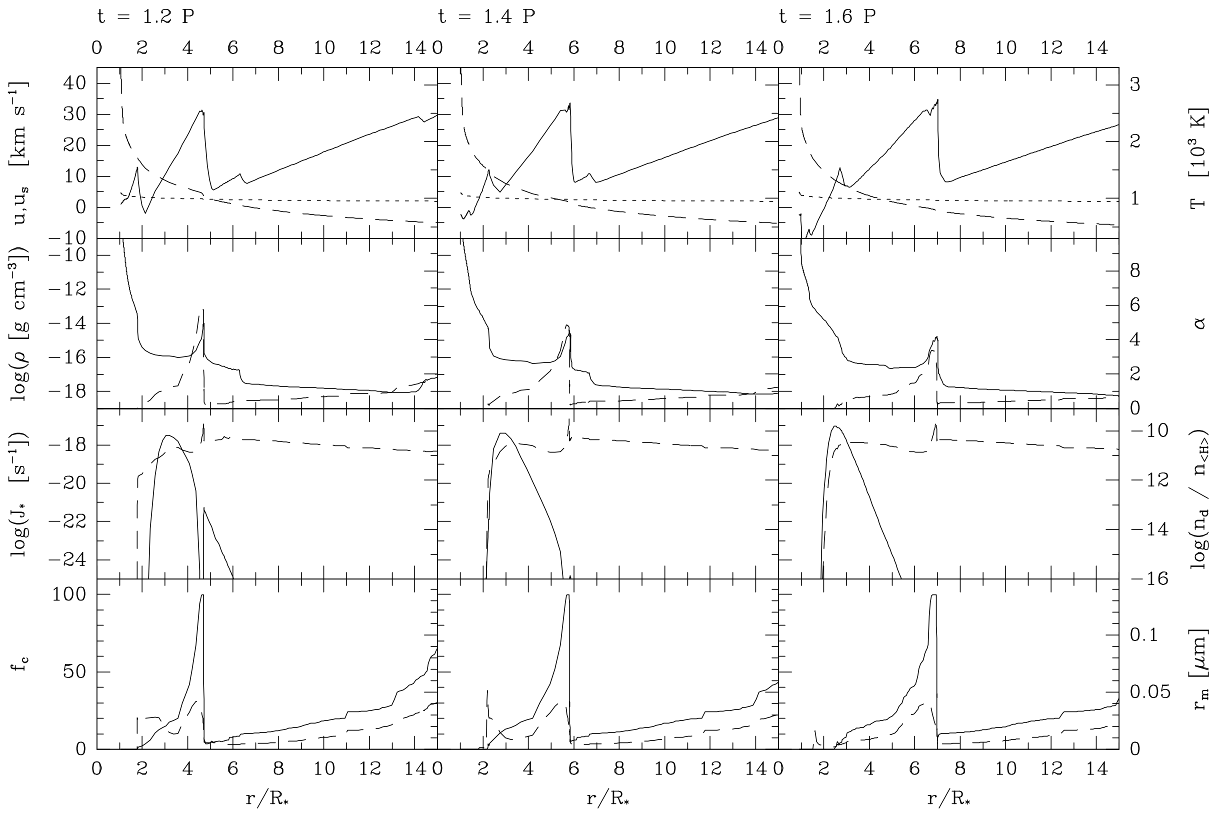

Figure 6.3: Radial structure of Model 23, at selected instants of time during the next pulsational period, continuation of Fig. 6.2

---

lower row: the degree of condensation f_c (solid line, l.h.s. ordinate) and the mean particle radius r_m (dashed line, r.h.s. ordinate). The degree of condensation is given in % .

Since evaporation turns out to have no significant influence on the global structure of the CDS, the evaporation rate J_{ev} is excluded from this plots. Evaporation is relevant only in certain zones, therefore we refer to the plots of selected Lagrangian elements, Sec. 6.2.2.

We begin the following discussion of the interaction between the dust formation and the hydrodynamics and thermodynamics at the beginning of the dust cycle, i.e. that instant of time when dust formation newly starts. This happens between $t = 0.8P$ and $t = 1.0P$, cf. Fig. 6.2. A new peak of the nucleation rate arises in the radius interval between 2 $R_\star$ and 3.5 $R_\star$. Subsequently, also the number of dust grains per H–atom steeply increase in the radius interval under consideration. The reason for this nucleation phase is twofold.

First, the density in the wake of the previous shock is still substantially in-

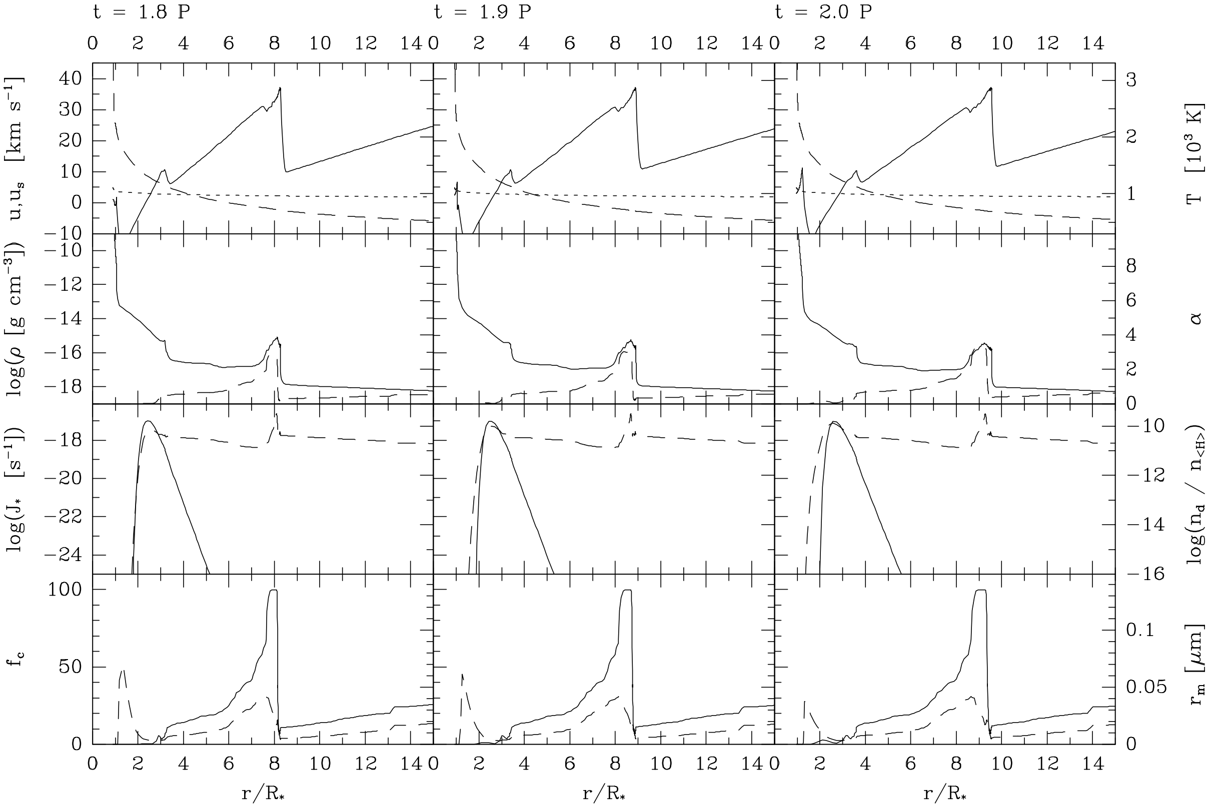

Figure 6.4: Fig. 6.3 continued

creased. Second, simultaneously the temperature decreases. The temperature, which at $t = 0.8P$ is well above 1600K at $\approx 2R_\star$ and drops down to 1300K at $t = 1.0P$. This happens due to the vanishing influence of the backwarming of the preceding dust layer. The dust opacity of this layer blocks the outgoing radiation and therefore heats the material behind, i.e. at smaller radii. The effectivity of the dust opacity vanishes with increasing radii, hence, the backwarming effect vanishes.

The temperature decrease is the most important process during this time interval. Since it continues during the following time intervals, it provides conditions that are steadily more favourable for the nucleation of dust particles, as can be seen from the broadening peak of the nucleation rate and the subsequent beginning rise of the number of dust particles per H–atom $n_d/n_{<H>}$. Finally, at $t = 1.2P$ the mean particle radius r_m in the innermost dust forming region starts the decline due to the huge amount of small newly formed particles.

During the time interval between $t = 1.2P$ and $t = 2.0P$ the newly formed dust particles are overrun by a shock wave initiated by the interior pulsation. In contrast to the model in Sec. 4.3.1, where this shock front causes an immediate growth phase, the shock wave in the present calculation has a smaller amplitude, and hence less impact to cause a sufficient compression of the material to start growth. The reason for the effective damping of the pulsational shock front is the strong shock of the preceding cycle.

In the wake of the preceding front the density gradient is almost zero, thus prohibiting a continued steeping of the succeeding wave, and thereby causing an early damping. In the wake of this smaller-amplitude shock front the particles that have been accelerated outwards start falling back to smaller radii, as can be seen from the inwards moving edge of the $n_d/n_{<H>}$–plot. Thereby, in the innermost region between 1 and 2 $R_\star$ a few particle grow effectively and cause a narrow increase of the mean particle radius in the radial interval. These are really a few particles, since this happens below the visible edge of the $n_d/n_{<H>}$ course, hence the number of particles present in this radius interval must be orders of magnitude smaller.

Remarkable for this time interval at the end of the second pulsational cycle is also the broad peak of the nucleation rate, which is now fully developed, and which causes the formation of a large amount of new particles between $r = 2R_\star$ and $r = 4R_\star$, cf. Fig. 6.4.

Fig. 6.1 shows that subsequently, the small–amplitude shock of the second cycle causes a tiny peak in the degree of condensation and thereby also in the acceleration of dust due to radiation pressure α. However, these tiny peaks again demonstrate the ineffectiveness of the small-amplitude shock: the material almost remains at the position were it was formed and does not follow the movement of the shock. The shock compresses the material, thereby causing a short growth phase, but moves farther outwards without affecting the material anymore. The small-amplitude shock front and the tiny new dust layer decouple very fast. The material is overrun by the shock without being affected anymore. At $t = 0.4P$ in Fig. 6.1 the position of the shock front is at almost 5 R$_\star$, whether the dust containing material is left at radii less than 4 R$_\star$.

The next phase starts with the development of a new pulsational shock wave, in the innermost region, between $t = 0.0P$ and $t = 0.4P$, cf. Fig. 6.1. At $t = 0.6P$ the dust particle at the inner edge of the dust shell, between $r = 2.0R_\star$ and $r = 2.5R_\star$ are overrun by this newly formed pulsational shock front. Although, it is already damped (cf. decreasing velocity amplitude of the innermost shock in Fig. 6.1 between $t = 0.0P$ and $t = 0.4P$). In contrast to the shock wave in the previous cycle, this shock front causes a sufficient compression of the material to initiate dust growth. The mass elements containing the newly formed dust particles are enhanced in density by almost two orders of magnitude, thereby receiving favourable conditions for dust growth. This causes a steep and rapid increase of the degree of condensation around $r \approx 2.5R_\star$ between $t = 0.4P$ and $t = 0.6P$, which amounts to values as high as 95%, cf. Fig. 6.2.

According to Eqs. (2.15) and (2.42) a steep increase of the radiative acceleration on dust grains follows (cf. plot of α in Fig. 6.2), reaching a maximum value of $\alpha = 6.2$ at $r = 2.4R_\star$ at $t = 0.6P$. This acceleration immediately stops the damping of the pulsational shock wave, and moreover amplifies the acceleration such that the shock wave is gaining in strength and increases in amplitude. Due to its effectivity of compression this shock front is connected with an outgoing new shell of material as can be seen in Fig. 6.2, e.g. by the outmoving peak of the degree of condensation which now reaches values as high as 100%.

During the process of shock–amplification between $t = 0.6P$ and $t = 1.0P$, new particles are still formed in front of the peak of the degree of condensation, i.e. at larger radii (cf. plot $n_d/n_{<H>}$ at $r \geq 2.8R_\star$ at $t = 0.8P$), were $n_d/n_{<H>}$ reaches its peak value of some 10^{-10}. However, these grains are soon overrun by the newly formed shock wave. It sweeps up and compresses the material ahead of it, thus enhancing the density where the grains find excellent conditions for growth. By this effect, the radiative acceleration on dust is kept on its maximum value and furthermore a broadening of the α–peak follows. The fact that α is kept at its peak value for a considerable time interval is remarkable, since according to Eqs. (2.15) and (2.42) one would expect a decrease of α due to the decrease of the temperature at larger radii.

Between $t = 1.0P$ and $t = 1.2P$ the newly formed shock front merges with the tiny peak in the degree of condensation, i.e. swallows up the material from the previous pulsational cycle. Some time later, between $t = 1.4P$ and $t = 1.6P$, the two hydrodynamical shock fronts merge, the small–amplitude shock front is overrun by the preceding front due to its larger expansion velocity.

We want to summarize the discussion so far. Obviously, we have to do with a model with multiperiodicity number $n_P = 2$. Comparing the plots at $t = 0.0, 1.0$ and $2.0P$, we conclude that the radial pattern repeats with a high accuracy, even in small details of the radial structure, after $t_1 = 2P + t_0$, i.e. $n_P = 2$. The dust complex is triggered by the interior pulsation in the sense that the hydrodynamics determine the onset of dust growth, by providing the appropriate density, which is only possible each *second* pulsational period. On the contrary, dust formation is rather independent of the hydrodynamics. Dust formation is possible almost during the whole of the two cycles and mostly is only dependent on the backwarming effect of the dust itself. If finally dust formation and subsequent growth becomes possible, it decisively influences the hydrodynamical structure and causes by a self–amplifying mechanism the dominating waves that run through the atmosphere. The shock fronts would soon be damped without dust and vice versa dust formation would be impossible without the shocks from the interior pulsation.

6.2.2 Selected Lagrangian elements

Figures 6.5 and 6.6 show the time development of the physical quantities of interest during two periods in four selected Lagrangian zones, i.e. in the comoving frame of the gas, for Model 23, cf. Tabs. 6.1 and 6.2. From Fig. 6.5, left column, to Fig. 6.6, right column, the mass elements are ordered by an increasing initial

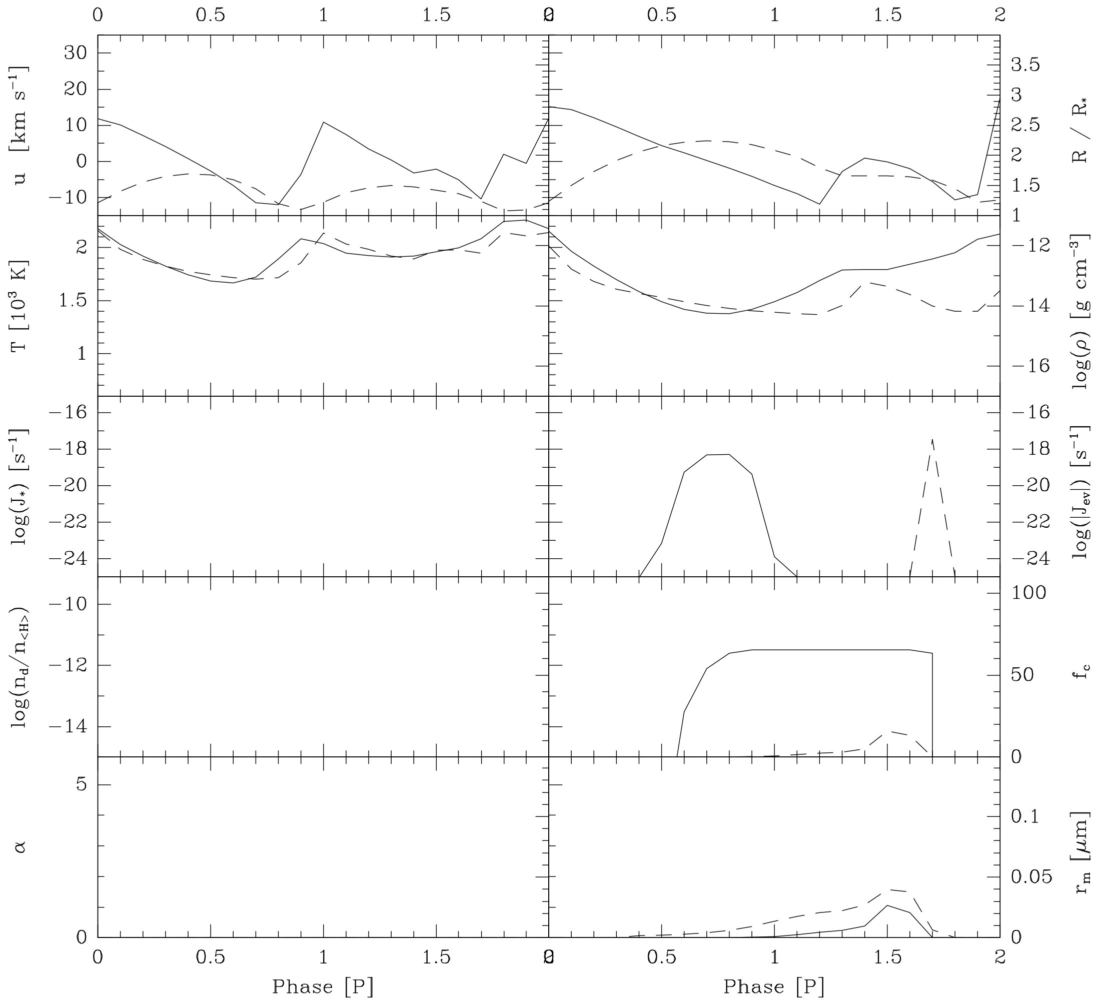

Figure 6.5: Time development of certain physical quantities during two pulsational periods in two selected Lagrangian elements of Model 23, cf. Tabs 6.1 and 6.2,. The quantities are explained in the text.

---

position.

Going from top to bottom the figures show

a. the velocity u of the mass element (solid line, l.h.s. ordinate) and the radial position R (dashed line, r.h.s. ordinate) in units of the initial hydrostatic model,

b. the temperature T (solid line. l.h.s. ordinate), and the logarithm of the density ρ (dashed line, r.h.s. ordinate),

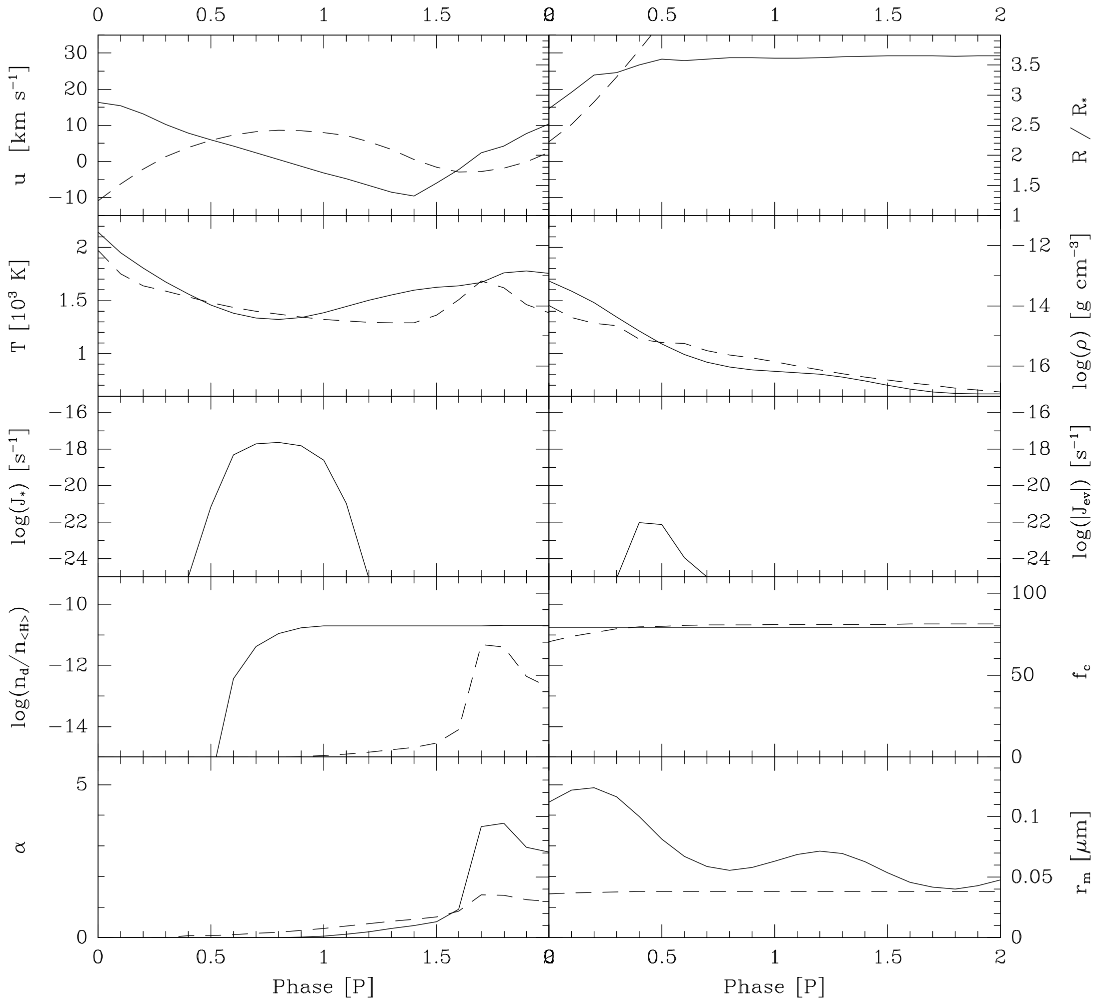

Figure 6.6: Fig. 6.5 continued. Time development of the same physical quantities of Model 23 during two pulsational periods of two selected Lagrangian elements which are located farther outwards.

---

c. the logarithm of the nucleation rate $J_\star$ (solid line), and the logarithm of the evaporation rate J_{ev} (dashed line),

d. the logarithm of the number of dust grains per H–atom $n_d/n_{<H>}$ (solid line, l.h.s. ordinate), and the degree of condensation f_c (dashed line, r.h.s. ordinate), and finally

e. the acceleration due to radiation pressure on dust α (solid line, l.h.s. ordinate) in units of the gravitational acceleration and the mean particle radius r_m

(dashed line, r.h.s. ordinate)

in these Lagrangian shells.

The *innermost* zone (cf. left column of Fig. 6.5) is passed periodically by strong shock waves created by the interior pulsation. This leads to a quasi–ballistic movement of this zone through the atmosphere as can be seen from the plot of the radial position R.

The time development of the density is determined by the hydrodynamical conditions, i.e. is determined by the compression of the element due to the periodic passage of shocks. The compression leads to a density enhancement of more than one order of magnitude and a subsequent increase of the temperature of almost 500 K. However, the temperature is a tracer, that the element is not exclusively determined by the hydrodynamics but already by the dust complex.

After the passage of the shock wave one would expect the temperature to decrease in a similar manner compared to the density, since the particle is moving outwards between $t = 1.0P$ and $t = 1.3P$. However, this is not the case. The temperature decreases less steeply than the density and remains fairly constant between $t = 1.1P$ and $t = 1.4P$. This effect is caused by the backwarming of the innermost dust layer, which is located at larger radii and prevents a decrease of the temperature due to the outward movement of the mass element under consideration.

Since the temperature in this innermost zone always exceeds 1650 K, during the shown cycles, no formation of solid particles is possible and the zone remains completely dust–free.

The *second* zone (cf, right column of Fig. 6.5), although at the beginning of the time sequence located only at a slightly larger radial position, experiences a completely different development. It is pushed outwards by the first shock wave to a maximum radial position of $r \approx 2.3R_\star$, which is only about 0.5 $R_\star$ farther outwards than the first zone.

Hence, in this first pulsational period, at maximum radial position and therefore at minimum temperature of about 1400K, the formation of new dust particles becomes possible and a broad peak of the nucleation rate occurs between $t = 0.5P$ and $t = 1.0P$. A steep increase of the number of dust grains per H–atom follows. However, as these particles are formed during a phase with decreasing density gradient, they do not find appropriate growth conditions and until $t = 1.2P$ they remain fairly small, as can be seen from the mean particle in Fig. 6.5. Furthermore, due to the same reasons also the degree of condensation and α remain with very low values.

This changes, when at $t = 1.3P$ the element is reached by the preceding pulsational shock front. The density is substantially enhanced and a growth phase starts, the mean particle radius as well as the degree of condensation increase, which reaches values as high as 20%. Since this causes a dynamically relevant amount of the radiative acceleration on dust, the element under consideration remains at its present position. The value of α is ≈ 1, thus balances the gravitational deceleration and keeps the element almost in rest at $r = 1.5R_\star$.

However at $t = 1.5P$ a surprising effect occurs in this zone. The temperature suddenly increases although the Lagrangian zone is still at rest. This sudden increase is solely caused by the backwarming of the previously formed dust layer located farther out. It heats the mass element up to more than 1900 K and causes *complete evaporation* of the dust particles. The value of the evaporation rate reaches values as high as the nucleation rate over a considerable time interval. Consequently, the number of dust grains per H–atom, the mean particle radius, the degree of condensation, and the radiative acceleration all drop to zero. The element ends up completely dust–free at the end of the second pulsational cycle.

The most remarkable fact of the *third* Lagrangian zone (cf. left column of Fig. 6.6) is, that during the two pulsational cycles shown, this zone is only shocked once. Although located only slightly farther outwards at $t = 0.0P$ than the zones discussed previously, this zone carries out an almost ballistic movement during two thirds of the time interval shown. At minimum temperature around $t = 0.8P$ effective nucleation takes place. However due to the positive temperature gradient and due to the decreasing density effective growth is prohibited. Nevertheless, the number of dust grains per H–atom increases steeply and already reaches its final value, but the values of f_c and α remain small.

Backwarming occurs during the first half of the second cycle. However, the rise of the temperature does not suffice to evaporate any dust particles. The zone is located at such large radii that backwarming cannot increase the temperature above the evaporation limit of $\approx$ 1900K.

At $t = 1.4P$ the element is overrun by the shock wave created by the interior pulsation. Now, due to this compression, the grains finds good conditions for growth and the mean particle radius increases to a maximum value of almost 0.05 μm for this element. This growth phase causes also a steep increase in the course of the degree of condensation, which reaches values as high as 70% and consequently, also the radiative acceleration on dust increases. The resulting high value of α at the end of the second cycle suffices to lift the mass element out of the gravitational field.

The *fourth* zone (cf. right column of Fig. 6.6) represents a zone in the transition region from the dust formation region to the wind region.

This zone exhibits a continuous outward directed movement, as indicated by the time development of the radius. The velocity increases slightly during the first half of the first cycle and then remains fairly constant. The velocity increase occurs due to a continued growth phase in the first half, which brings the degree of condensation to its value of $\approx$ 70%, and subsequently also the radiative acceleration reaches its final value. During the following time evolution, the temperature as well as the density decrease monotonically, due to the outward directed movement. Around $t = 0.5P$ this allows a last dust formation phase. However, this phase is not very effective, as can inferred from the course of $n_d/n_{<H>}$, which is completely unaffected. This is quite reasonable, since the peak value of $J_\star$ is at least four orders of magnitude smaller than in the growth phases of the elements previously discussed. Due to the considerable low densities no further growth is possible and the mean particle radius as well the degree of condensation remain constant. The following modulation of the radiative acceleration is caused by the sinusoidal change of the stellar luminosity.

The preceding discussion demonstrates the intimate relation between dust formation and the dynamical structure of the CDS. From the independence of certain elements, e.g. the mass element on the l.h.s. of Fig. 6.6, one concludes that under the conditions of the models presented here, multiperiodicity is a consequence of the hydrodynamics rather than of the dust complex. It seems that the lacking of each second shock wave, due to the early damping, leads to multiperiodicity with $n_P = 2$. Since the triggering mechanism is missing no dust formation occurs and the shells becomes multiperiodic. In this sense, the shell is forced by the pulsation to oscillate with a certain period, defined by the hydrodynamical conditions in the circumstellar shell, which in turn are, of course, also a consequence of the dust formation process .

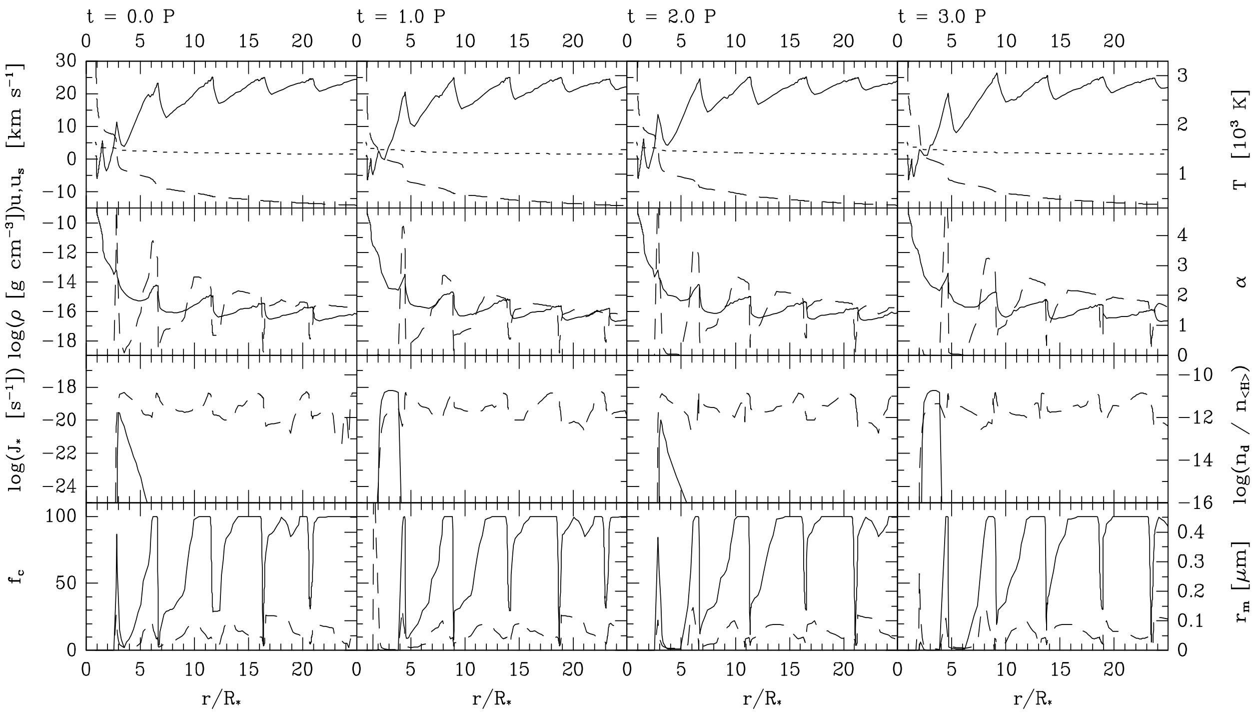

Figure 6.7: Radial structure of Model 14, cf. Tabs. 6.1, 6.2, at the beginning of four pulsational cycles

A further multiperiodic model

From the preceding discussion, especially of the radial structure of Model 23 it turned out, that a key mechanism to multiperiodicity is the periodic damping of shock waves according to the physical conditions of the ambient medium. We would like to investigate further results of this damping in some more detail.

Figure 6.7 shows a sequence of plots of the radial structure of Model 14, cf. Tabs 6.1, 6.2, at the beginning of four successive pulsational cycles. The same quantities as in the sequence of Figs. 6.1–6.4 in Sec. 6.2 are depicted.

The main difference between the radial structure of Model 23, cf. Sec. 6.2, and Model 14 is, that in the present model a dominant shock is created *each* period, although the model is multiperiodic with $n_P = 2$. In this sense "dominant" means, that the shock actually runs through the outer atmosphere and is not damped already in the inner dust forming region. In Model 14 the shocks which develop each period are located at different radii for a fixed instant of time. Fig. 6.7 shows, that at the beginning of the "even" periods, i.e. at $t = 0.0P$ and $t = 2.0P$, the shocks are located around 3 $R_\star$, whether for the "odd" periods, i.e. for $t = 1.0P$ and $t = 3.0P$ they are located farther outwards around 4.5 $R_\star$. A further hint, that Model 14 is in fact multiperiodic, gives the nucleation rate $J_\star$, cf. 3^{rd} row, solid line. The radial course of $J_\star$ very clearly reveals that there are indeed even and odd periods.

The reason for this behaviour is rather simple. In contrast to Model 23, the damping of each second pulsational shock front in the present model is not so strong such that it still suffices to trigger dust formation. The damping is not so strong, because the shock amplitude remains smaller in Model 14 due to the less steeper density gradient in the subphotospheric region. The density gradient is less steeper since the model is more luminous and, hence, more extended. Therefore, in the wake of the first shock front there still exists a density gradient which allows further steepening of the preceding wave. Thus, damping of the interior pulsational waves may not always be complete and may still influence the dynamical behaviour of the CDS.

Besides the slightly different dynamical behaviour of Model 14, interesting is also the regularity of the radial structure of the shell. In Fig. 6.7 we have plotted the radial interval up to 25 $R_\star$. The accuracy how the radial pattern repeats is remarkable. The even or odd periods, respectively, equal even in details such as the width of the innermost dust layer, as can be seen from the plot of the degree of condensation. Unfortunately, such a high accuracy is not always achievable, since it would require several model runs with slightly modified parameters and thereby would consume a large amount of computer time.

6.2.3 Time development of the optical depth

Figures 6.8 and 6.9 show the time development of the radial structure of the monochromatic optical depth τ_λ at $\lambda = 1\mu m$ (upper panel) and the time develop-

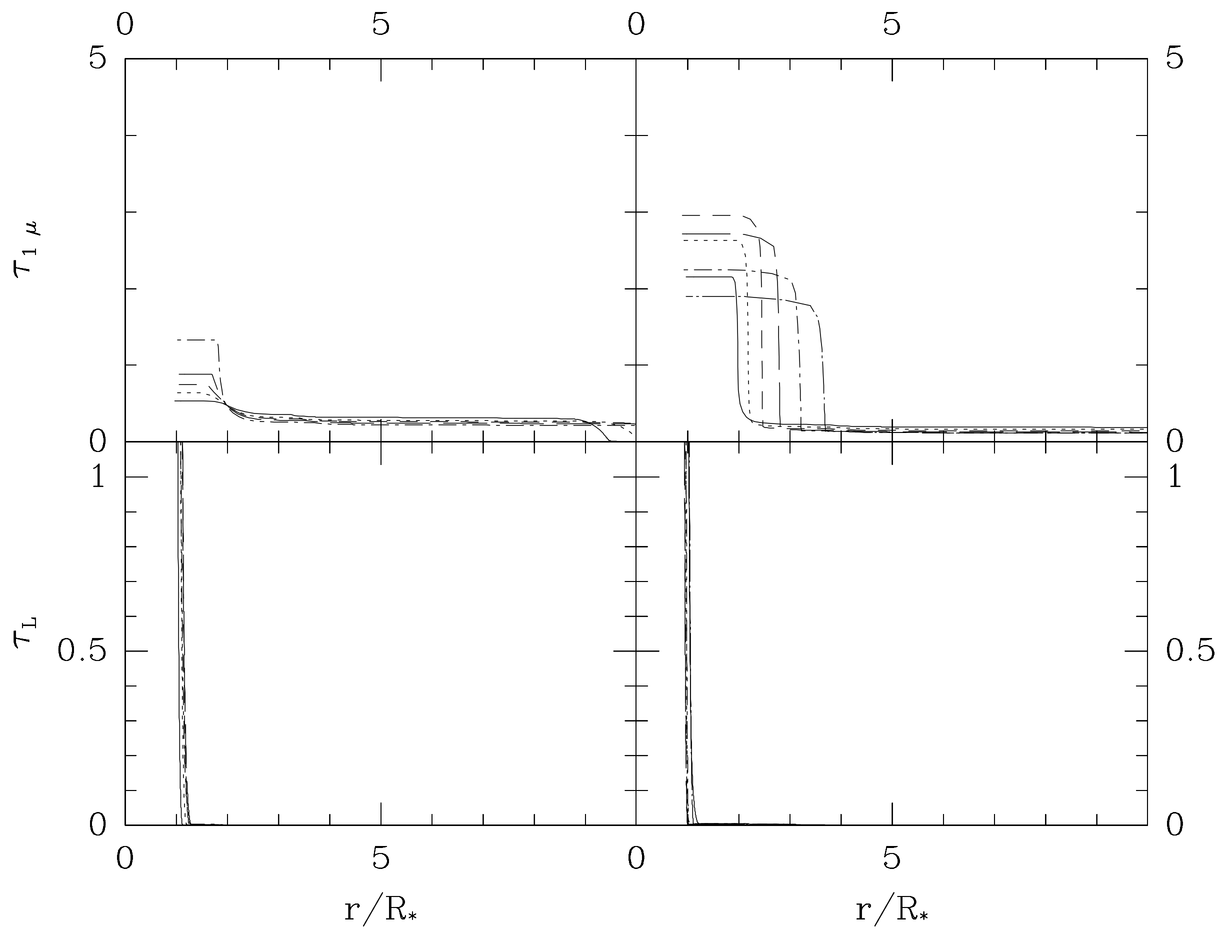

Figure 6.8: Time development of the radial structure of the monochromatic optical depth $\tau_{1\mu}$ and the diluted optical depth τ_L for Model 23 during the first pulsational cycle

---

ment of the radial structure of the diluted optical depth τ_L (lower panel). Both optical depths are given for Model 23, cf. Tabs. 6.1 and 6.2.

The l.h.s of Fig. 6.8 shows the following instants of time: $t = 0.0P$ (solid line), $t = 0.1P$ (dotted line), $t = 0.2P$ (short–dashed line), $t = 0.3P$ (long–dashed line), and $t = 0.4P$ (dashed–dotted line). The r.h.s. of Fig. 6.8 shows the *second* half of the first pulsational cycle. Beginning with $t = 0.5P$ with the same order of linetypes and additionally plotted is $t = 1.0P$ (long dashed–dotted line). The l.h.s. of Fig. 6.9 shows the following instants of time, $t = 1.1P, \ldots, t = 1.5P$, the r.h.s. $t = 1.6P, \ldots, t = 2.0P$ with the same order of linetypes.

The quantities $\tau_{1\mu}$ and τ_L are measured inwards adopting the boundary con-

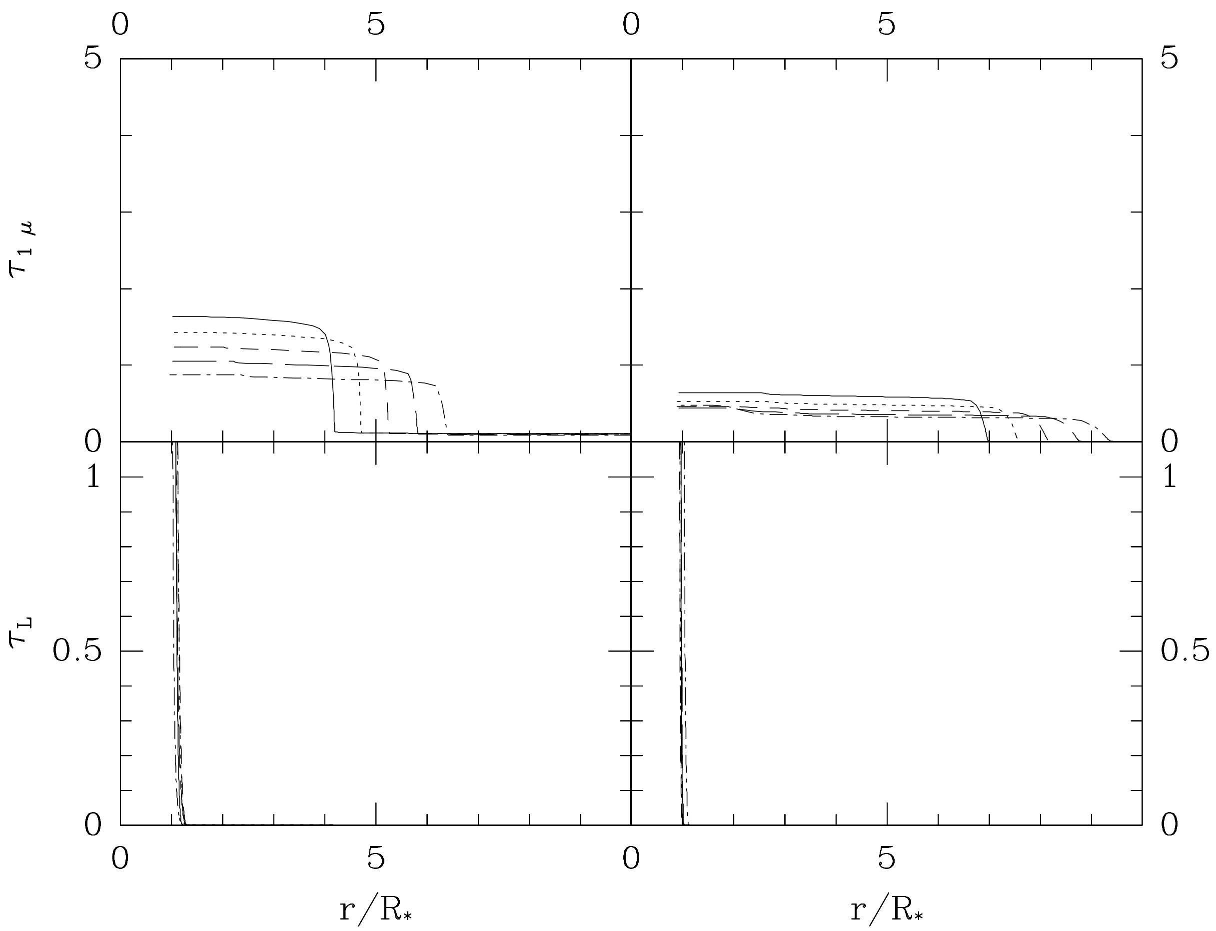

Figure 6.9: Fig. 6.8 continued, optical depth during the second pulsational cycle

---

ditions $\tau_{1\mu}(\infty) = \tau_L(\infty) = 0$. To calculate $\tau_{1\mu}$ we assume that the dust particles are small compared to the wavelength, and hence the absorption efficiency of amorphous carbon is represented approximately by a λ^{-1}–law. With regard to the plots of the mean particle radius in Sec. 6.2.1 this assumption seems to be clearly justified. We use the expression given in [Lucy 1976] to calculate the complex index of refraction.

The time development of the monochromatic optical depth $\tau_{1\mu}$ is a very intuitive tracer of the time scales which reign the evolution of the discrete dust layers.

During the first half of the first pulsational cycle, when the grains are overrun by the small–amplitude shock front, the thickness of the new dust layer slowly increases but the layer remains at rest around $R = 2R_\star$. During the second half of the first pulsational cycle, cf. r.h.s of Fig. 6.8, the layer becomes dynamical relevant, reaches its maximum thickness at $t = 0.7P$, and subsequently moves outwards rather fast. Due to the geometrical dilution the outward moving step of $\tau_{1\mu}$ decreases, until finally at $t = 2.0P$, the same radial structure as at $t = 0.0P$ is reestablished. This result thereby confirms that Model 23 is in fact multiperiodic with $n_P = 2$.

The diluted optical depth τ_L, which according to Eq. (2.39) determines the temperature structure of the dust shell, remains smaller than 0.05 everywhere within the dust shell. Thus, our semi–analytical approach to treat the radiative transfer problem, which requires $\tau_L < 1$ within the dust shell is especially justified for the multiperiodic models.

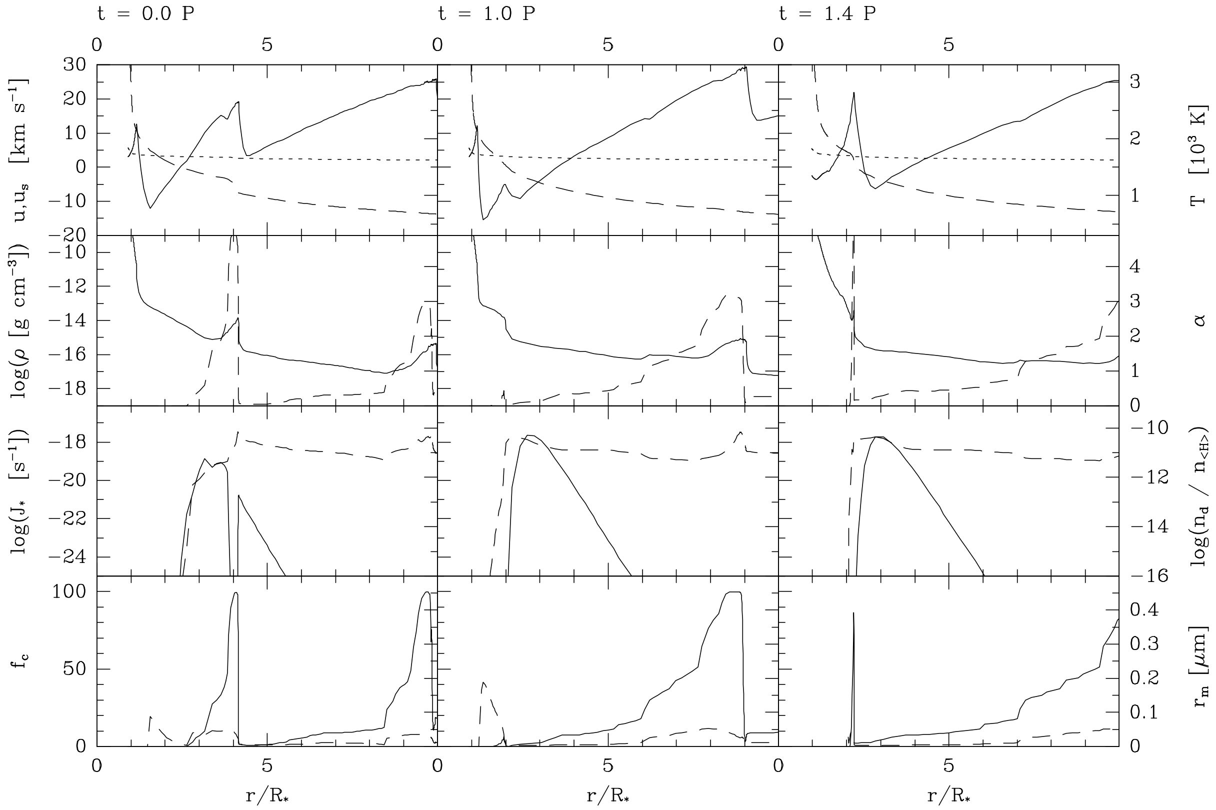

Figure 6.10: Radial structure of Model 24, cf. Tabs. 6.1, 6.2, at selected instants of time during three pulsational cycles

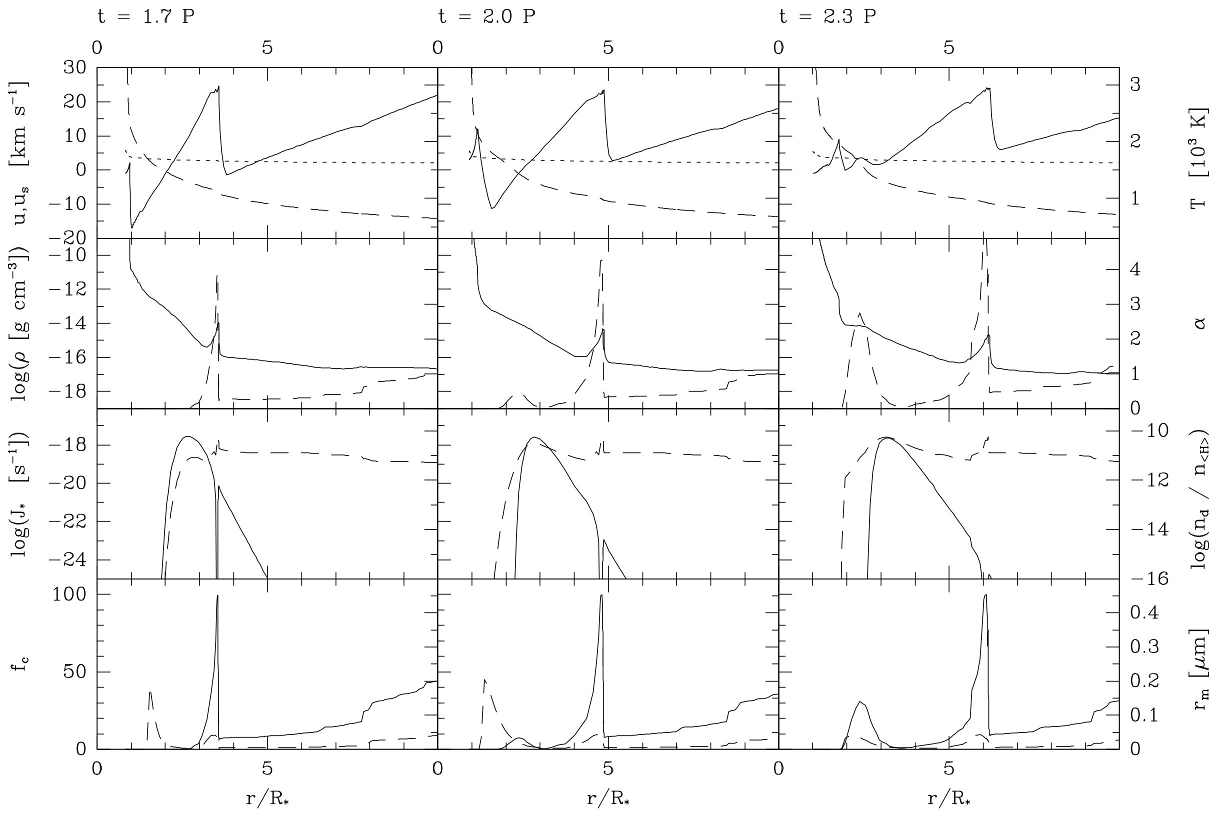

Figure 6.11: Fig. 6.10 continued

6.2.4 A different mechanism of multiperiodicity

Figures 6.10, …, 6.12 show a time sequence of the radial structure of CDS at nine selected instants of time during **three** pulsational cycles of Model 24, cf. Tabs 6.1, 6.2 and pages 148,149. Figures 6.10 and 6.11 comprise the first two and a half pulsational periods, Fig. 6.12 the second half of the third pulsational period. In the sequence of plots the time increases from the left to the right.

In detail, the same quantities are depicted as in Figs 6.1, …, 6.4 of Sec. 6.2.1.

If we take a look at $t = 0.0P$, cf. Fig. 6.10 l.h.s., and at $t = 3.0P$, cf. Fig. 6.12 r.h.s, we readily see that Model 24 is multiperiodic with $n_P = 3$. However, the processes that lead to this kind of dynamical behaviour are different and more intricate than those in Model 23 in Sec. 6.2.1.

The first pulsational period between $t = 0.0P$ and $t = 1.0P$ is characterized by continuous dust formation in the wake of the outmoving shock front. During this period the dust forming region moves inwards and at $t = 1.0P$ a large number of dust particles are present around 2 $R_\star$. This effect is amplified by the reverse shock front, which is located at $\approx 2R_\star$ at $t = 1.0P$, and which sweeps the particles to smaller radii and increases the region where dust is present inwards.

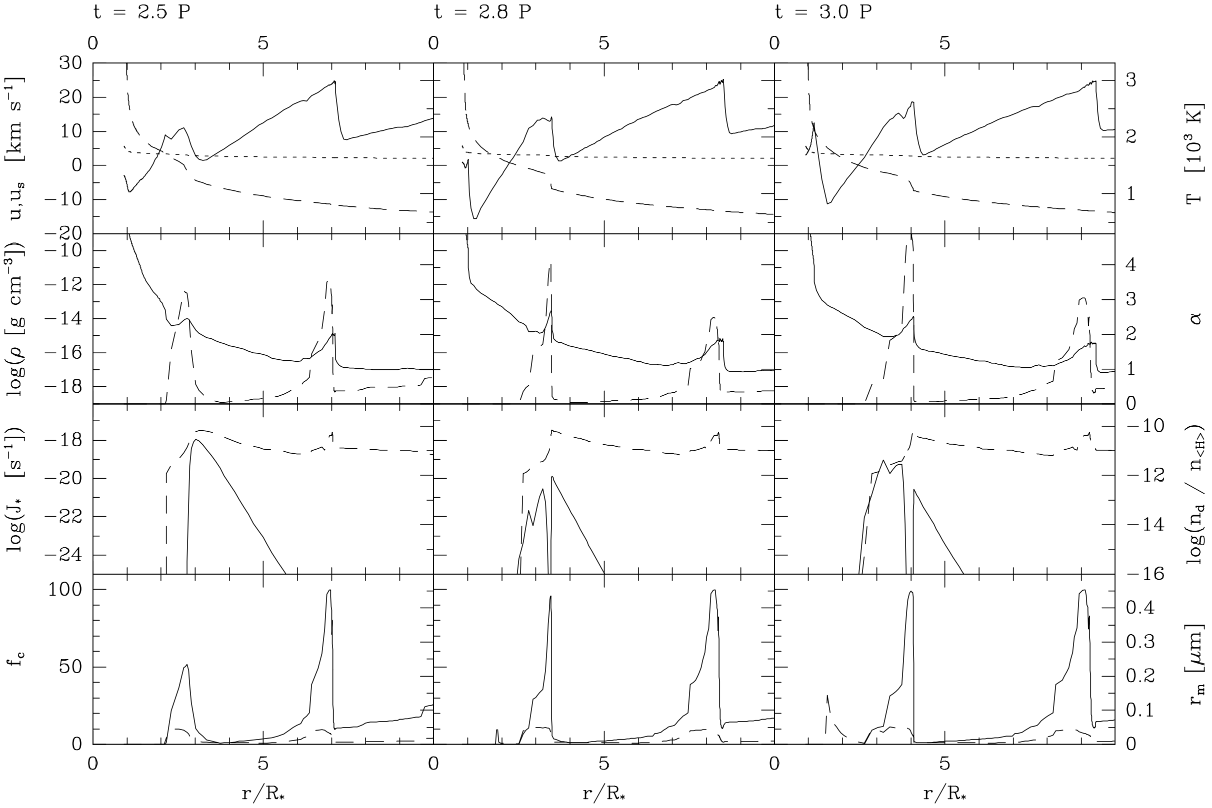

Figure 6.12: Fig. 6.10 continued

Thereby, the mean particle radius at the innermost edge of the dust shell rises to comparatively high values, but as usual, these are only very few large particles.

The next phase, till $t \approx 2.0P$ is characterized by the formation of a dust–amplified shock as described in detail in Sec. 4. Around $t = 1.4P$ the particles at the inner edge of the dust shell are overrun by a pulsational shock front. A thin, needle–like dust layer forms and amplifies the shock front by radiation pressure on dust. In the following, at $t = 1.7P$, the dust layer has only broadened a bit, but has increased its maximum value of the degree of condensation to values as high as 100%, by subsequent growth right behind the shock front. In the wake of this shock front, in the density–enhanced region around $R \approx 2.5R_\star$, effective nucleation takes place. The growth region broadens in the following, when the shock front moves outwards.

This effective growth phase is the most important prerequisite for the third phase, which begins at $t = 2.0P$. At this instant of time the physical conditions in the region with $R < 5R_\star$ is similar to that at $t = 0.0P$. However, due to the thinness of the outmoving dust layer the occuring backwarming effect is less pronounced. This results in a temperature stratification which at $t = 2.0P$ is $\approx 150K$ lower in the innermost region than at $t = 0.0P$. As a consequence dust *growth* starts in the dense and sufficiently cool region around 2.5 $R_\star$, as can be seen from the tiny peak in the degree of condensation in the middle column of Fig. 6.11. As this process is accompanied by a rise of the acceleration of dust due to radiation pressure a perturbation is induced in the velocity field which can clearly be seen at $t = 2.3P$ (cf. Fig. 6.11 r.h.s).

This perturbation occurs asynchronous to the interior pulsation. Subsequently, it steepens, accompanied by an avalanche growth phase and a self-acceleration, which finally leads to a new purely dust–induced shock front.

This is one of the most interesting results. The mechanism described above is the same as described in [Fleischer *et al.* 1991]: the generation of shocks by radiation presure on newly formed dust grains. The process occurs without *direct* support of the interior pulsation, as e.g. in the previous cycle where the pulsational shock front is "only" amplified by radiation pressure on dust. In the third phase the generation of the shock front is independent from or asynchronous to the interior pulsation.

The second half of the third phase is characterized by a merging of pulsational and dust–induced shock and the development of a reverse shock. The merging of the shocks occurs at $t = 2.5P$. According to [Courant and Friedrichs 1948] the overtaking of shock waves moving in the same direction in gases with adiabatic exponent $\gamma \leq 5/3$ results in a transmitted shock, a reflected rarefraction wave, which generally is weak, and a contact discontinuity between transmitted shock and rarefraction wave.

At $t = 3.0P$ at least the weak, inwards moving rarefraction wave and the transmitted shock are clearly developed, the contact discontinuity, indicated by a characteristic density structure, is not yet clearly visible.

To summarize, we find that the multiperiodic Model 24 is characterized by three totally different phases of dynamical processes taking place. At the beginning of the first and third phase the backwarming effect serves as a switch which decides whether a purely dust–induced shock front is generated or not. Although all processes described were already known, the interaction is more complicated than e.g. in Model 23 and the characterisation of this discussion as a different mechanism of multiperiodicity is justified.

6.3 Discussion

It is the aim of this section to present some general results about multiperiodicity. The last section has demonstrated that multiperiodicity is in detail a quite complicated process, such that a general description is a rather difficult task. However, our calculations reveal some unique rules that describe multiperiodicity and allow the prediction of the behaviour of a model for a certain set of parameters. To call these rules "laws" would overestimate their validity, since they were purely found by exemplary numerical calculations and thus, a general proof can hardly be given, at least with numerical methods.

6.3.1 Preselecting multiperiodicity

We have summarized the results of our model calculations in Tabs. 6.1 and 6.2. Table 6.1 shows the input parameter of the calculations, the parameter of the initial hydrostatic models: $T_\star$ in $[K]$, ϵ_C/ϵ_O, $L_\star$ in $[L_\odot]$, $R_\star$ in $[R_\odot]$, $M_\star$ in $[M_\odot]$, P in $[d]$, Δu_P in $[kms^{-1}]$, and R_{inner} in $[R_\star]$. Strictly speaking, only $T_\star$, $M_\star$ and $L_\star$ are parameters of the initial hydrostatic model. The overabundance, the period, and the amplitude of the piston are additional parameters of the dynamical model. The value of the rest position of the piston at the inner boundary is also listed, since it has some influence, e.g. on how far the pulsational waves can steepen before they run into the dust shell and how much mechanical energy is delivered to the atmosphere. Strictly speaking, it has to be considered as a seventh model parameter.

Table 6.1: Parameters of the initial hydrostatic models which turn out to be multiperiodic models

No.	$T_\star$	ϵ_C/ϵ_O	$L_\star$	$R_\star$	$M_\star$	P	Δu	R$_{inner}$
1	2450	1.25	30000	959	1.30	388	3.0	0.82
2	2450	1.25	30000	959	0.70	388	3.0	0.82
3	2450	1.25	30000	959	1.00	388	3.0	0.82
4	2450	1.25	30000	959	1.00	388	5.0	0.82
5	2450	1.25	30000	959	1.00	388	7.0	0.82
6	2450	1.25	30000	959	1.00	388	9.0	0.82
7	2700	1.25	30000	790	1.00	388	3.0	0.82
8	2450	1.25	30000	959	1.00	388	2.0	0.82
9	2450	1.25	30000	959	1.00	388	1.0	0.82
10	2450	1.25	30000	959	1.00	388	0.0	0.82
11	2450	1.25	30000	959	1.00	776	3.0	0.82
12	2450	1.25	30000	959	1.00	776	1.0	0.82
13	2450	1.25	30000	959	1.00	621	3.0	0.82
14	2500	1.75	9000	504	1.00	388	1.0	0.87
15	2500	1.75	9000	504	1.00	259	4.0	0.87
16	2500	1.75	9000	504	1.00	194	5.0	0.87
17	2800	2.00	7000	355	1.00	750	2.0	0.91
18	2800	2.20	7000	355	1.00	400	2.0	0.84
19	2800	1.75	7000	355	1.00	400	2.0	0.91

continued on next page

continued from previous page								
No.	$T_\star$	ϵ_C/ϵ_O	$L_\star$	$R_\star$	$M_\star$	P	Δu	R_{inner}
20	2800	2.00	7000	355	1.00	600	2.0	0.91
21	3000	2.00	5328	269	1.20	350	4.0	0.99
22	3000	2.00	5328	269	1.20	350	4.0	0.99
23	3000	2.20	4618	251	1.00	350	3.0	0.97
24	3000	1.96	5331	269	1.00	400	3.0	0.92
25	3000	1.96	4618	251	1.00	350	3.0	0.97
26	3000	1.96	6777	304	1.00	500	3.0	0.92
27	3000	1.96	3912	231	1.00	300	3.0	0.92
28	2600	1.40	12000	539	1.00	400	3.0	0.84
29	2800	1.50	8500	391	1.00	400	1.0	0.84
30	2800	1.50	8500	391	1.00	400	5.0	0.84
31	3000	1.40	4618	251	1.00	700	7.0	0.97
32	3000	1.38	4618	251	1.00	700	7.0	0.97
33	3000	1.35	4618	251	1.00	700	7.0	0.97
34	3000	1.30	4618	251	1.00	700	7.0	0.97

Table 6.2: Calculated values of the evolved models with consistent treatment of dust formation and growth and $n_P > 1$

No.	$\dot{M}$	u_∞	ρ_D/ρ_G	$L_{\star,min}$	$L_{\star,max}$	Remarks
1	$6.7\ 10^{-5}$	11.5	$7.3\ 10^{-4}$	–	–	$n_P \approx 8$, $L_{*,min,max}$ not det.
2	$8.8\ 10^{-4}$	13.5	$1.1\ 10^{-3}$	31730	37860	$n_P = 9$
3	$1.9\ 10^{-4}$	13.1	$9.4\ 10^{-4}$	33740	38430	$n_P = 8$
4	$2.1\ 10^{-4}$	12.6	$8.6\ 10^{-4}$	35460	40070	$n_P = 8$
5	$2.8\ 10^{-4}$	13.0	$9.2\ 10^{-4}$	37020	41740	$n_P = 8$
6	$3.0\ 10^{-4}$	12.8	$6.9\ 10^{-4}$	38180	43940	$n_P = 8$
7	$6.3\ 10^{-5}$	10.9	$6.0\ 10^{-4}$	34930	37920	$n_P = 10$
8	$1.5\ 10^{-4}$	13.1	$9.1\ 10^{-4}$	32550	37040	$n_P >\approx 7$
9	$1.9\ 10^{-4}$	13.7	$1.0\ 10^{-3}$	31340	35530	$n_P >\approx 7$
10	$1.0\ 10^{-4}$	13.5	$1.1\ 10^{-3}$	30020	35030	EP = 7.7
11	$2.5\ 10^{-4}$	13.5	$9.7\ 10^{-4}$	30650	44030	$n_P = 4$
12	$1.2\ 10^{-4}$	12.9	$1.0\ 10^{-3}$	28870	33750	$n_P \approx 4$
13	$2.3\ 10^{-4}$	12.8	$9.9\ 10^{-4}$	33850	43220	$n_P = 5$
14	$2.2\ 10^{-5}$	21.5	$3.7\ 10^{-3}$	8332	11680	$n_P = 2$
15	$2.0\ 10^{-5}$	20.5	$3.0\ 10^{-3}$	11010	12430	$n_P = 3$
16	$2.1\ 10^{-5}$	20.7	$3.2\ 10^{-3}$	10990	12550	$n_P = 4$
						continued on next page

continued from previous page

No.	$\dot{M}$	u_∞	ρ_D/ρ_G	$L_{\star,min}$	$L_{\star,max}$	Remarks
17	3.1 10^{-6}	18.7	2.9 10^{-3}	5859	8738	$n_P = 2$
18	1.0 10^{-6}	27.5	2.8 10^{-3}	6310	7474	$n_P = 2$
19	6.1 10^{-6}	21.0	2.6 10^{-3}	6077	8312	$n_P = 2$
20	8.8 10^{-6}	25.0	3.5 10^{-3}	6088	8526	$n_P = 2$
21	3.1 10^{-7}	27.1	2.7 10^{-3}	4305	6423	$n_P = 2$, without κ_D
22	1.9 10^{-7}	22.9	2.5 10^{-3}	5329	5352	$n_P = 2$, with κ_D
23	3.1 10^{-7}	24.9	2.8 10^{-3}	3896	5440	$n_P = 2$
24	1.1 10^{-6}	23.0	2.9 10^{-3}	4341	6811	$n_P = 3$
25	2.9 10^{-7}	22.0	2.1 10^{-3}	3896	5432	$n_P = 2$
26	1.2 10^{-6}	27.9	2.7 10^{-3}	5394	8793	$n_P = 2$
27	8.5 10^{-7}	19.7	3.5 10^{-3}	–	–	$n_P \approx 2$, $L_{*,min,max}$ not det.
28	1.9 10^{-5}	14.5	1.3 10^{-3}	–	–	$n_P \approx 4$, $L_{*,min,max}$ not det.
29	2.9 10^{-6}	15.5	1.5 10^{-3}	–	–	$n_P = 3$, $L_{*,min,max}$ not det.
30	8.9 10^{-6}	17.3	1.6 10^{-3}	–	–	$n_P >\approx 3$, $L_{*,min,max}$ not det.
31	2.5 10^{-6}	11.2	1.8 10^{-3}	1810	8770	$n_P = 2$
32	1.6 10^{-6}	9.4	1.5 10^{-3}	1811	8770	$n_P = 2$
33	1.6 10^{-6}	5.3	9.8 10^{-4}	1810	8722	$n_P \approx 2$
34	5.0 10^{-7}	0.7	1.4 10^{-3}	1810	8702	no regular outflow

First, we discuss some special series of model calculations according to Tabs. 6.1 and 6.2.

Models No.1, ..., No. 13 are calculated with the same initial stellar luminosity. The first three models have different stellar masses. The result is only a minor influence of the stellar mass on the multiperiodicity number. Besides this result another is of interest. This little series of three models demonstrates that the available driving energy of the low–gravity, late–type star winds mostly goes into lifting the material out of the stellar gravitational field than into accelerating the outflow to its final velocity [Holzer and MacGregor 1985]: The available energy input is the same for all three models, however, the mass loss rate is anti–correlated with the stellar mass, and the final outflow velocity is nearly unaffected.

The models No. 4,..., 6 and 8, ..., 10 are calculated with different amplitudes of the piston at the inner boundary. Model No. 10 is calculated without interior pulsation. The eigenperiod of this model is $7.7 \cdot 388$d= 2987d. For low amplitudes of the piston, i.e. for the Models No. 8 and 9, the multiperiodicity number of the models have not been determined very exactly but the values of n_P certainly are larger than 7 and lower than 8. For the models with higher amplitudes of the piston the input of mechanical energy gains some more influence and the multiperiodicity number is increased to $n_P = 8$, and remains unchanged even for the models with a very high value of the amplitude of the piston at the inner boundary. Thereby, the mass loss rate changes only from a minimum value of 1.0 10^{-4} $M_{\odot} yr^{-1}$ to a maximum value of 3.0 10^{-4} $M_{\odot} yr^{-1}$ for the model with a piston amplitude of 9 kms^{-1}, the final outflow velocity can be regarded as independent of the increasing piston amplitude. The important reason for the considerably increasing influence of the mechanical energy is that the piston is located very deep below the photosphere and only a slight increase of the amplitude results in a substantially higher energy input.

That the substantial input of mechanical energy really has a minor influence on the multiperiodicity number, i.e. shifts it to larger values, has also been confirmed by a calculation that is not listed in Tabs. 6.1 and 6.2. We have calculated a model with the parameters equal to the models under consideration except for the period and the amplitude of the piston: P was chosen 1164d, and $\Delta u_P = 1$ km s^{-1}. The somewhat strange value of the period is easily explained: it was chosen $3 \cdot 388$d. Up to then, the working hypothesis was, that if the multiperiodicity number of the models mostly is 8, i.e. the basic time scale is $8 \cdot 388$d, then to get a model oscillating in resonance, we have to divide 8 by e.g. 3 and the model with $P = 3 \cdot 388$d would have a multiperiodicity number of $8/3 = 2.67$, i.e. we expected to get a model with $n_P \approx 2.7$. In fact, what we got was a model with $n_P > 2.5$ but n_P definitely < 2.6. If we take $n_P = 2.56$ and multiply it with 1164d we arrive at 2980d, i.e. exactly the eigenperiod of the basic model No. 10.

Furthermore, Tabs. 4.3 and 4.4 in Chap. 4 contain the corresponding model with $n_P = 1$, calculated with an amplitude of the piston of 1km s^{-1}, i.e. low mechanical energy input.

We summarize the discussion so far, that the mechanical energy has an influence on the multiperiodicity number of these high luminous models, but it is marginal and the determining basic time scale is indeed the eigenperiod of the model.

The result of the minor influence of the mechanical energy input confirms a remark made in Chap. 4. There, we stated, that it has been impossible during the performance of the model grid, to change a model with a multiperiodicity number of ≈ 1 to a model with $n_P = 1$ simply by increasing the amplitude of the piston. In the light of the previous discussion this is an obvious result.

Model No. 7 has been calculated with a higher effective temperature than e.g. model 3. The calculation reveals a multiperiodicity number of $n_P = 10$. This result is not too surprising, since changing the stellar temperature changes the stellar radius of the model, and hence the density scale height, which was identified in the previous chapter as a sensitive parameter for the eigenperiod of a model. Since there is only a small amount of condensable material available in Model 7 and the temperature is comparatively high, the formation and growth of dust is not very effective and the mass loss rate as well as the dust–to–gas ratio remain rather small.

The Models No. 11, . . . 13 are calculated with increased periods of the piston, i.e. with an overall much higher input of mechanical driving energy. The calculations reveal a multiperiodicity of $n_P = 4$ and $n_P = 5$, respectively. Multiplying the multiperiodicity numbers with the respective periods yields 3104 d. *This* is exactly the result one would get if one multiplies the period of the models with $P = 388$d with their respective multiperiodicity number of $n_P = 8$. However as discussed above, the product of *period* and *multiperiodicity number* is not exactly the eigenperiod of the system, but differs slightly from it, in the present case 117d, due to the input of mechanical energy.

We come back to this nevertheless general rule later, after we also discussed models which do not have an eigenperiod.

Although the input of mechanical energy is substantially increased in Models No. 11 – 13, this has not a profound influence on the mass loss rate or the final outflow velocity.

The next little series of models (No. 14, 15, 16) belongs to the range of model parameters where an eigenperiod of the system cannot immediately be found since the system shows no self–induced shocks by the exterior κ–mechanism. The models have a substantially decreased initial stellar luminosity compared to the previous sample of calculations. The models were calculated with a period of the piston of 388d, 259d, and 194d and reveal multiperiodicity numbers of $n_P = 2$, 3, 4, respectively. Again, multiplying P and the respective n_P we get a constant for this set of models: 776d. Again, in Chap. 4, Tabs. 4.3 and 4.4 we find the corresponding model with $n_P = 1$. Model 20 of Tab. 4.3 has a period of 776 days!

It is remarkable how independent the mass loss rates and final outflow velocities are from the variation of the period. We conclude from this result, that these quantities are completely determined by the dust complex, whether the action of the dust complex under the influence of an exterior force governs the dynamical behaviour of these models. The content of condensable material is equal for all of the four models and the models react on a typical basic time scale of 776d, which however cannot be identified as the eigenperiod of the system in the sense of Chap. 5, since without support of mechanical energy input the models would not develop a continuous outflow. These models do not exhibit an exteriorκ–mechanism. The time scale is engraved on the system by the exterior pulsation and yields regular results only if the ratio between basic time scale and piston time scale is integer–valued. Nevertheless, we call this basic time scale the (generalized) eigenperiod of the system, which gives the rather special definition in Chap. 5 a more appropriate and enlarged range of validity.

To finish this section we summarize the rule that enables us to preselect a certain multiperiodicity number, and thereby to predict how this special model will behave, if it is fully evolved:

Models with eigenperiod. For a given set of model parameters the calculation without piston at the inner boundary exhibits an eigenperiod P_e. To obtain a model with a multiperiodicity number n_1 divide $P_e/x = P_1$ and calculate a model with P_1 as the period of the piston and an amplitude not chosen too extreme. Actually, this means that the system *always* oscillates with its eigenperiod, and each chosen input period leads to a cyclic behaviour on the scale of the eigenperiod.

Models without eigenperiod. As a starting point we need a model that is within the desired range of model parameters and shows a regularly repeating radial pattern, say with a multiperiodicity number n_1. Let us further assume that the model has a period P_1. If we want the next model to have a multiperiodicity number n_2, then it should have a period of $(n_1 \cdot P_1)/n_2$. The model is forced to oscillate on a time scale which is prescribed by the piston.

The possible question arises, whether this distinction is perhaps artificial. Indeed, if we could prove, that for each given set of model parameters, which allows efficient dust formation, an eigenperiod exists, then the second rule would be obsolete. However, we mentioned already in Chap. 5 the numerical difficulties which occured while investigating this question in models with no apparent eigenperiod. A possible unification in the near future of these two cases would lead to a more comprehensive picture of CDS around LPVs.

6.3.2 The influence of the carbon overabundance on multiperiodicity

A very sensitive parameter for the occurrence of multiperiodicity is the overabundance of carbon to oxygen.

Model No. 21 of Tab. 6.1 and 6.2 has been calculated with a ϵ_C/ϵ_O–ratio of 2.0. The model reveals a multiperiodicity number of $n_P = 2$. The occurrence of multiperiodicity is caused by the same mechanism as discussed in detail for Model 23 in Sec. 6.2. Each second pulsational shock front is damped due to the hydrodynamical conditions in the wake of the preceding shock front. The strength of the damped front does not suffice to initiate dust growth, such that the shock front overruns the newly formed dust grains without impact. It is interesting to note, that the corresponding model calculated without taking into account the dust opacity in the determination of the temperature in radiative equilibrium also shows up to have $n_P = 2$. Obviously, thermodynamics, i.e. the back–warming effect, are not responsible for the multiperiodicity phenomenon, but hydrodynamics as described briefly above.

The corresponding model with $n_P = 1$ is No.3 listed in Tabs. 4.3 and 4.4 in Chap. 4. It has been calculated with an overabundance of carbon to oxygen of 2.5. Due to the substantially increased amount of condensable material, dust

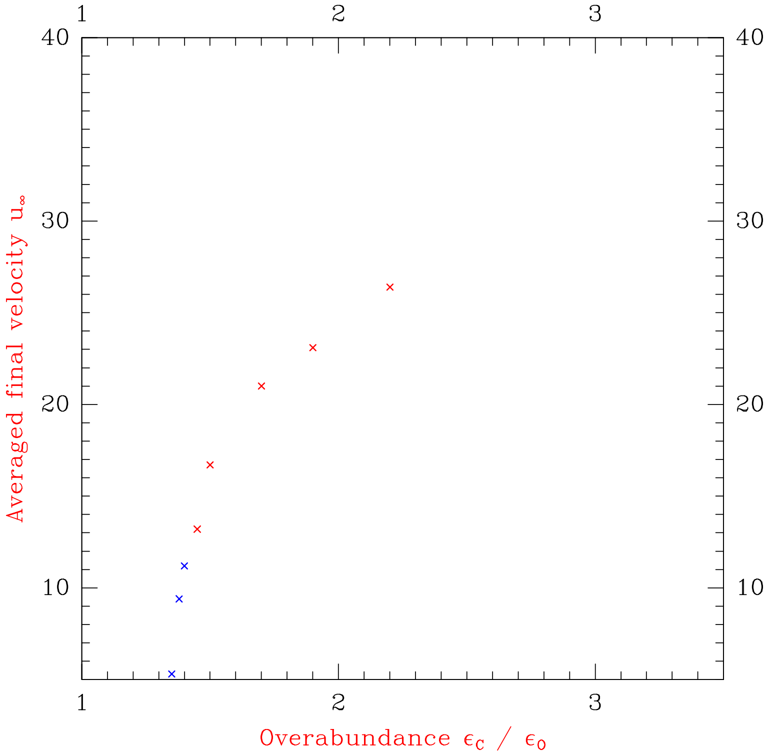

Figure 6.13: Dependence of the averaged final outflow velocity on the overabundance of carbon to oxygen for a series of models where all other parameters except ϵ_C/ϵ_O are held constant: $M_\star = M_\odot$, $T_\star = 3000K$, $L_\star = 4.6\,10^3 L_\odot$, $P = 700d$, $\Delta u_P = 1 km\, s^{-1}$, refer Tabs. 6.1, 6.2 and also 4.3, 4.4

---

formation and growth takes place effectively every period and thus the model has $n_P = 1$. Although, the hydrodynamical conditions in Model No.3 are similar to Model No. 21, the pulsational shock front each period suffices to trigger dust formation and to form a new dust layer which amplifies the pulsational shock front by radiation pressure on dust.

In Tabs. 6.1 and 6.2 Models No. 23 and 25 are calculated with different overabundances of carbon to oxygen. Both models are multiperiodic with $n_P = 2$. This demonstrates that the domains, where a certain value of the multiperiodicity number predominates, are not sharply defined but are smeared out over a considerable interval. Between these domains with a multiperiodicity number also ranges of ϵ_C/ϵ_O–values exist, where no regular behaviour of the model can be found, cf. Fig. 6.13 and below. Irregular here means, that at least no integer–numbered multiperiodicity number could be found. It does not necessarily mean, that the model in between are in fact somewhat chaotic. A more detailed discussion of Fig. 6.13 follows below in Sec. 6.3.3.

For this case, the corresponding model with $n_P = 1$ can again be found in Tabs. 4.3 and 4.4. The model has been calculated with the high carbon overabundance of 2.75.

The overabundance of carbon to oxygen can be used to "tune" a model to a certain multiperiodicity number. The ϵ_C/ϵ_O–value adjusts the generalized eigenperiod of the system, such that pulsation and dust growth time scales constructively interfere and a certain multiperiodicity can develop. In fact, most of the models in Tabs. 6.1 and 6.2 were found in this way. Unfortunately, the models cannot develop an outflow anymore if the overabundance is further decreased, such that it is not possible to present three or more multiperiodicity numbers for one series of models.

This result confirms the picture of those multiperiodic models which do not possess an eigenperiod generated by an exterior κ–mechanism as a pendulum subject to an exterior force. If the eigenfrequency and the frequency of the exterior force have an integer–valued ratio, we get constructive interference, otherwise both mechanisms interfere destructively and the oscillating system behaves irregularly or perhaps even chaotic. Besides the models included in Tabs. 6.1 and 6.2 we have calculated a lot more models which showed an irregular behaviour. At first these models were regarded as artificial, or even faulty due to possible numerical difficulties. Now, it has become clear that these models in fact constitute the vast amount of models, and those with regular behaviour, i.e. with a multiperiodicity number are an exception. Those models with $n_P = 1$ are even more rare in this context.

To gain more insight into the manifold of solutions of this complex, nonlinear system one should proceed as in the usual theory of dynamical systems, e.g. [Thompson and Stewart 1986], [Devaney 1986]. Thus, the next step would be to construct an appropriate phase space of the system under consideration. The resulting phase portrait would reveal which domains of attraction are inherent to the system, and whether the attractor is periodic or indeed a strange one, which would indicate chaotic behaviour. However, it is not quite clear whether these tools, which were developed for systems described by ordinary differential equations, are already worked out for partial differential equations.

6.3.3 Dependence of observable quantities on the parameters in multiperiodic models

The most important question whether the effect of multiperiodicity actually has observable consequences, e.g. on the lightcurves of Miras and LPVs is investigated in the next Chapter 7.

In this section we investigate the dependence of observable quantities such as the final outflow velocity u_∞, the mass loss rate $\dot{M}$ and the dust-to–gas ratio ρ_d/ρ_g on the overabundance of carbon to oxygen ϵ_C/ϵ_O and on the period P.

Fig. 6.13 shows a series of models where all model parameters except the overabundance of carbon to oxygen were held constant. The figure demonstrates that

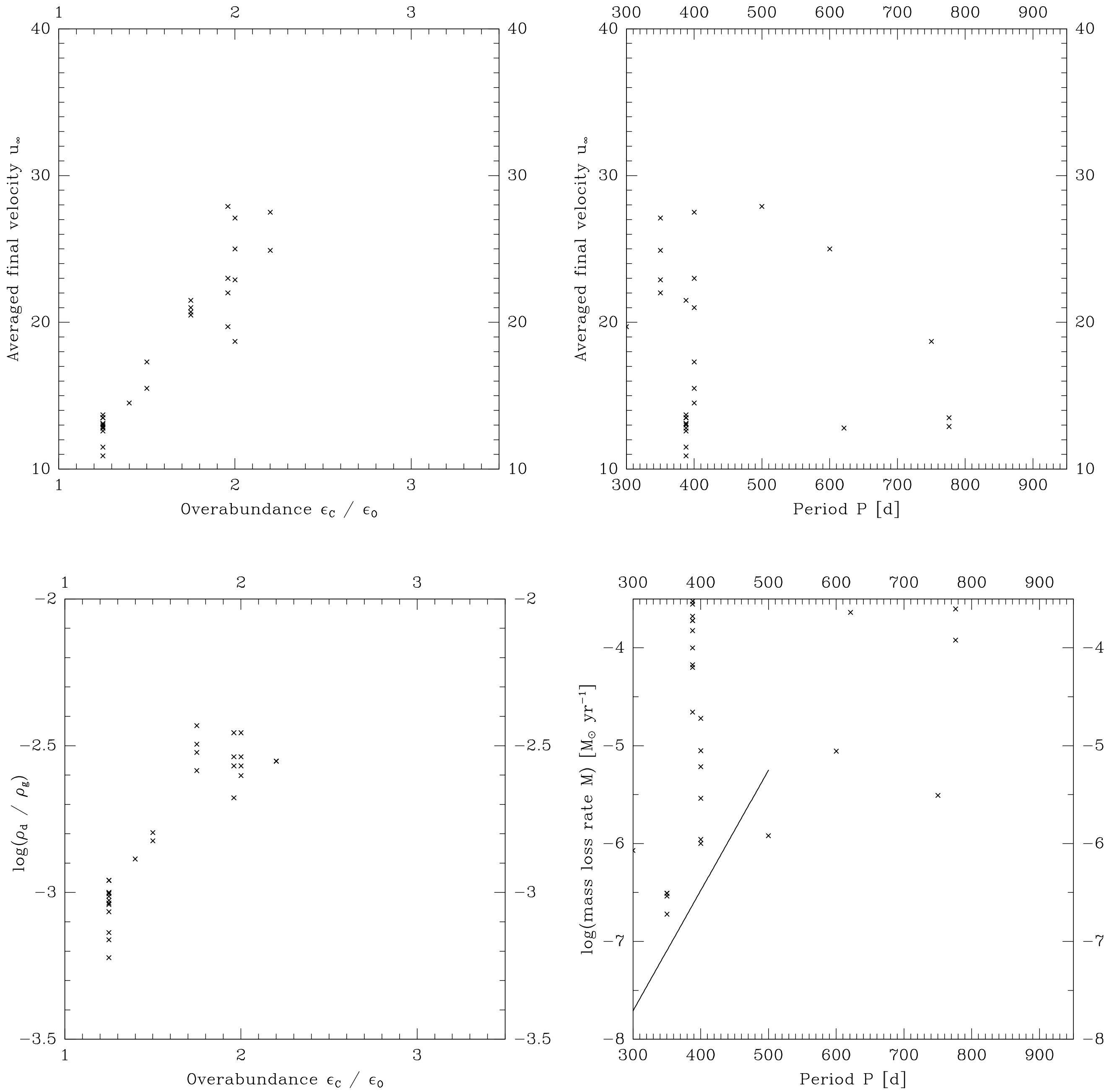

Figure 6.14: Dependence of the final outflow velocity and the logarithm of the dust– to– gas ratio on the overabundance of carbon to oxygen, and the dependence of the final outflow velocity and the logarithm of the mass loss rate on the period according to Tabs. 6.1, 6.2

the overabundance decisively influences the final outflow velocity and determines when multiperiodicity occurs. In fact the three models with the lowest overabundances are multiperiodic with $n_P = 2$, the others have $n_P = 1$. Besides, these models with $n_P = 1$ were found by applying the multiperiodicity rules stated above. The corresponding models, which served as a basis, were Models No. 23 and 25, which had a period of 350d!

Below a certain sharply defined edge no outflow is possible. A model calculated with $\epsilon_C/\epsilon_O = 1.30$ shows no regular outflow and a “final velocity” of ≈ 0.5 km s^{-1}. The sequence also shows that the overabundance parameter must be very fine–tuned to get a regular model: the $< u_\infty >$–ϵ_C/ϵ_O–relation decreases very steeply towards low overabundances. Fig. 6.13 also demonstrates that multiperiodicity or the behaviour with $n_P = 1$ is possible over a broader range of the overabundance, as already mentioned in the previous section. In the shape of this correlation between final outflow velocity and the overabundance of carbon to oxygen seems to be more or less the same for each series of models. This allows to determine “graphically” the edge of the carbon overabundance, below which no outflow is possible, i.e. the end of the pulsation–dust regime.

With regard to the whole sample of models, we find that in the case of $n_P = 1$ in Chap. 4, the Fig. 6.14 clearly indicates that there exists an almost linear correlation between u_∞ and ϵ_C/ϵ_O. Note, that the $u_\infty - \epsilon_C/\epsilon_O$ plots in Figs 4.12 and 6.14 are scaled equally. Obviously, the multiperiodic models constitute the lower end of the u_∞–ϵ_C/ϵ_O correlation. Preferably, multiperiodicity is found in models with low overabundance ratios of carbon to oxygen, see also below and Fig. 6.15.

This finding has profound consequences with regard to observations. From the observational point of view there is no correlation between u_∞ and ϵ_C/ϵ_O reported. This is mainly due to the fact that thick dust shells, i.e. with high carbon overabundance, do not allow the determination of photospheric abundances. In turn, since the final outflow velocities deduced from observations, e.g. [Knapp *et al.* 1982, Knapp and Morris 1985, Zuckerman and Dyck 1986a, Zuckerman *et al.* 1986], show values typically below ≈ 30 km s^{-1}, Fig. 6.14 would suggest that the overabundance of carbon to oxygen could not exceed the value 2.0 too much. Since there is a considerable scattering of the values in the very low overabundance region, it is rather clear that no correlation between u_∞ and ϵ_C/ϵ_O can be derived from observations.

Furthermore, these results lead to the suggestion, that most real LPVs and Miras are in fact multiperiodic, since the multiperiodic models gather in the lower overabundance region.

See Chap. 7 for the manifestation of multiperiodicity in the optical appearance of these models.

Independently, with a different approach, [Winters 1994] found nearly the same correlation for the case of stationary purely dust driven winds. This is really quite remarkable, since it is a completely different modelling approach.

This gives a further strong argument that the correlation is real and could be used to determine a possible (narrow) range of the carbon overabundance of a certain object once its final outflow velocity is known. Thereby, also for very thick dust shells, a determination of the carbon overabundance becomes possible.

In the following we consider the whole sample of multiperiodic models to investigate the dependence of observable quantities on the overabundance of carbon to oxygen. The plots on the left of Fig. 6.14 show the dependence of u_∞ and ρ_d/ρ_g on ϵ_C/ϵ_O, cf. also Fig. 6.13. The values are taken from Tabs. 6.1 and 6.2.

The plot of the gas–to–dust ratio shows a confinement to values around 10^{-3} as for the models in Chap. 4. This is not a very surprising result. If the amount of condensable material is increased or lowered by a factor of two or three, and we even assume that all available material actually condenses into grains, the amount of dust is still small compared to the amount of gas present in the CDS.

The right panel of Fig. 6.14 shows the dependence of the averaged final outflow velocity and the mass loss rate on the period. In the $\dot{M}$–P plot we have additionally plotted the mass–loss–period relation derived from observations by [Vassiliadis and Wood 1993]. A similar relation for the u_∞–P correlation proposed by [Vassiliadis and Wood 1993] indicates an increase of the final outflow velocity with period. As for the models in Chap. 4 we find a clear contradiction to the results of our calculations with regard to the $u_\infty - P$ relation. However, the main reason for this contradiction is a selection effect of our calculations. Most of the parameter sets of the models in Chap. 4 and the present Chapter were not varied in a systematic way over a large parameter range. The parameter were chosen with the intention to demonstrate certain nonlinear processes and mechanisms. However, a principle failure of our models to explain these relation cannot be a priori excluded. If even a systematic variation of the model parameter would not lead to a closer matching with the observed relation, then one has to look e.g. for a possible neglect of a physical interaction in the model calculation.

Further calculations, which yield a systematic grid of models, should answer that question if the models presented here are able to reproduce these observed relations if the parameters are chosen in the suitable range for Miras and LPVs.

In Fig. 6.15 we have plotted the two most easily accessible quantities to observations, u_∞ and $\dot{M}$, as a function of ϵ_C/ϵ_O. This time, for convenience, we have plotted the multiperiodic models, indicated by crosses, as well as the non–multiperiodic models ($n_P = 1$), which are indicated by dots. The left hand side of Fig. 6.15 shows the already discussed linear correlation between the final outflow velocity and the overabundance, shown here for a slightly larger velocity interval. It can be clearly seen that the models with $n_P = 1$ are situated in the region with "large" carbon overabundance. However, "large" means, that objects with these overabundances, if they exist, have extremely thick dust shells, which prevent an observational determination of photospheric abundances. Nowadays accessible to observations are only sources with rather thin dust shells, e.g. the

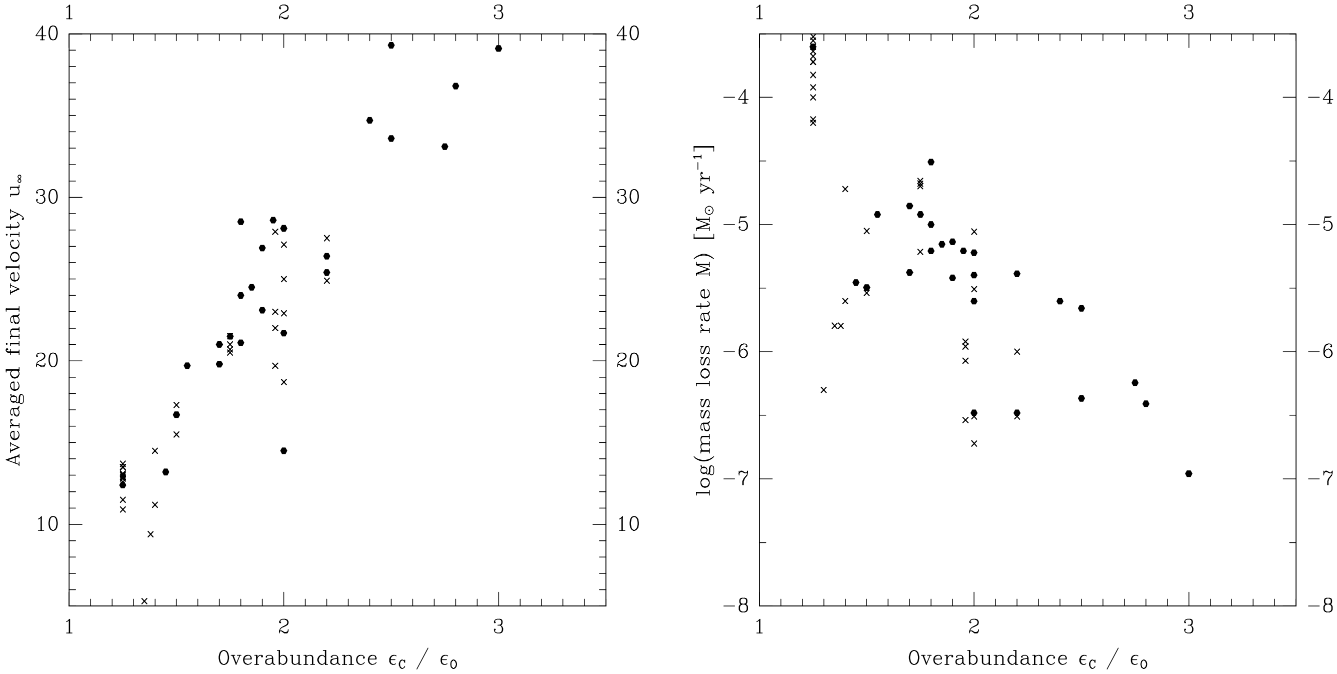

Figure 6.15: Dependence of the final outflow velocity and the logarithm of the mass loss rate on the overabundance of carbon to oxygen for the whole sample of multiperiodic and non–multiperiodic models

---

objects recently observed by [Olofsson *et al.* 1993a, Olofsson *et al.* 1993b] range in the lower left corner of this diagram. Planetary nebulae in contrast, as the next stage of stellar evolution for Miras and LPVs, are known to have carbon overabundances larger than the scale of Fig. 6.15, e.g. > 4 [Beichman *et al.* 1983]. So, models with "large" carbon overabundances cannot a priori be considered as unrealistic as is argued sometimes. In this sense, the linear correlation between u_∞ and ϵ_C/ϵ_O is a prediction from our models calculations with profound consequences for observations.

In the next chapter we demonstrate, that even for the case of very thick dust shells, there should be a phase where photospheric light reaches the observer. Although this phase is rather short, at most 10% of the pulsational period, theoretical calculations could predict that instant of time, when observations should be made, to determine the photospheric abundances of these objects, supposed, of course, that the mechanism described in the next chapter turns out to be real.

In contrast to the u_∞–ϵ_C/ϵ_O relation there seems to be *no* correlation between mass loss rate and carbon overabundance. The right hand side plot of Fig. 6.15 seems to suggest an anti–correlation, however, one should keep in mind that we have plotted the *logarithm* of the mass loss rate. At a fixed value of the overabundance the values of the resultant mass loss rates vary up to 3 orders of magnitude. A similar behaviour is found in the model calculations performed by the Vienna group [DORFI 1993, private communication]. The reason for this behaviour is the "non–unique" behaviour of the models, i.e. there exists no correlation between overabundance, final outflow velocity, *and* resulting density structure. The density structure, i.e. the levitation of the atmosphere, depends for example sensitively on the strength of the piston, i.e. on the input of mechanical energy by the interior pulsation, a quantity, which only marginally affects the final outflow velocity. The development of a certain density structure is intimately related to the velocity field, and both are nonlinearly coupled to the other processes, such that a straightforward prediction of the development of the mass loss rates can hardly be done. A hint from observations, that in fact the processes are strongly coupled can be inferred from Fig. 18 of [OLOFSSON *et al.* 1993A]. It shows the observed mass loss rates as a function of the outflow velocities of the stars of their sample. For a fixed value of the outflow velocity, there also exists a large scattering of the values of the mass loss rates, up to two orders of magnitude, which suggests the strong influence of other physical processes.

The independence of the mass loss rate from the overabundance of carbon to oxygen is also known in the case of stationary dust driven winds [DOMINIK 1992], such that in the mass loss formula derived from these self–consistent calculations by [DOMINIK *et al.* 1990], the ϵ_C/ϵ_O ratio does not enter as a parameter. The derivation of a similar formula for the time–dependent case could be a nice result from further systematic grid calculations.

6.4 Conclusions

We have demonstrated that the complex interaction between the processes of dust formation and growth and the interior pulsation leads to a complicated and non–unique dynamical behaviour of the CDS around Miras and LPVs. It turns out that the mass loss mechanism, which simply may described as the combined interaction between pulsation and radiation pressure on dust, in fact consists of at least two distinguishable mechanisms.

For the first mechanism pulsation triggers dust formation by providing appropriate densities that allow effective nucleation. In turn radiation pressure on the newly formed dust amplifies the pulsational shock front and accelerates the material to supersonic velocities. The second mechanism occurs without direct impact of the pulsation. At a certain instant during the period the density as well as the temperature are in the sufficient range of values to allow both, nucleation and also subsequent growth of dust particles. This results in a purely dust–induced instability, which causes a perturbation in the velocity structure, which steepens and becomes a shock wave. This shock wave sweeps up the material and causes an avalanche growth effect. Radiation pressure on dust finally accelerates the material and drives the massive outflow.

It is interesting to note that both mechanisms can be realized in a single model calculation, as demonstrated in Sec. 6.2.4. As a conjecture we would suggest, that if multiperiodicity with an odd multiperiodicity number n_P is realized, then the mechanism of dust–induced shocks must be involved, since it induces a time scale different from the pulsational one and can produce intermediate structures.

For the high luminous models we have confirmed the result of the chapter that the dynamics of these models are completely governed by their eigenperiod. Applying a mechanical energy input to those models yields a different multiperiodicity number, depending on the period of the exterior force. However, the basic time scale of these models is still the eigenperiod. The applicability of these models for real objects is given for the upper top of the AGB, right before the transition to the planetary nebulae phase. In this stage of stellar evolution we find very luminous objects, with a few $10^4 L_\odot$, which are heavily obscured by dust. Since the carbon–rich planetary nebulae are known to have rather high overabundances of carbon to oxygen, which range up to values of 12, e.g. [Zuckerman and Aller 1986], also these transient stars should already have high ϵ_C/ϵ_O–ratios. It is then possible to imagine that there exists a short intermediate evolutionary phase, where the interior pulsation has ceased but the outer atmosphere is still passed by strong shock waves which are produced by the exterior κ–mechanism. Unfortunately, we are not aware of any hints from observations that such a phase really exists.

The models with typical AGB–luminosities of Miras and LPVs, e.g. $\approx 10^4 L_\odot$, we have demonstrated that they are governed by the interior pulsation. The input of mechanical energy introduces a new time scale to the system, that forces it to oscillate with a period that can be derived from the period of the applied piston at the inner boundary. If the piston is not in proper resonance with the system, irregular or even chaotic dynamics develop. These findings suggest to conceive the CDS as a dynamical system subject to an exterior force and to apply the respective mathematical tools to determine the nature of these dynamics in a quantitative way. Investigations pointing in this direction have been carried out already, e.g. [Icke *et al.* 1992], although with rather simplified dynamical systems. We come back to this point after we have investigated the influence of multiperiodicity on the optical appearance of Miras and LPVs in the next Chap. 7.

A further result follows from the statistical analysis of the whole sample of multiperiodic models. The multiperiodic models constitute the lower end of the u_∞–ϵ_C/ϵ_O relation. From the dynamical point of view this means that multiperiodicity should be a common phenomenon in real Miras and LPVs, since they are supposed to have "low" ϵ_C/ϵ_O values.

The detailed treatment of dust formation, growth and evaporation in connection with a time–dependent description of Miras and LPVs reveals a wealth of non–linear phenomena, which possibly could not be discovered all in the present work, and which could be revealed by investigations in greater detail in future research. In any case, the time–dependent models already reveal some interesting correlations between model parameters and observable quantities. If these correlations turn out to be indeed true, they will have significant impact on observations. Current theoretical models are on a hitherto unreached level, that allows for a direct comparison with observations, see the following chapter.

Chapter 7

The optical appearance of the dynamical dust shell models

7.1 Introduction

Long–period variables (LPVs) are intrinsically cool objects many of which are surrounded by large amounts of dust. These dust particles are effective absorbers of radiative energy which they reradiate at longer wavelengths after an internal relaxation process [Woolf and Ney 1969]; [Gehrz and Woolf 1971]. Therefore, most LPVs are primarily infrared sources.

Improved instrumental capabilities in this spectral range and in the millimeter range have led to an increased interest in observations of late–type giants in the last years and produced a vast amount of observational data. This provided an extensive basis for a more thorough understanding of these objects. Based on this material e.g. [Sopka *et al.* 1985], [Claussen *et al.* 1987], [Thronson *et al.* 1987], [Willems and deJong 1988], [Jura *et al.* 1989], [Jura and Kleinmann 1989], [Groenewegen *et al.* 1992] were able to derive e.g. mass–loss rates, gas–to–dust ratios, distances, luminosities or final outflow velocities for various large samples of objects.

All of these quantities are not directly accessible to observations. In order to interpret the observations simple models are constructed to determine the desired quantities. E.g. [Sopka *et al.* 1985], who focus their attention to derive mass–loss rates from submillimeter observations at 400μ, have to know, among other quantities, the distance of the source as well as a value for the cross section of the grain material, in order to derive the mass–loss rates from their observed fluxes. Besides the rather uncertain values of the distances, which introduces errors into the interpretation, they also assume a uniform value for the cross section of the material for both oxygen–rich as well as carbon–rich circumstellar shells. Hence, the resulting values for the mass–loss rates are contaminated with considerable errors. Based on IRAS low resolution spectra [Willems and deJong 1988] try to construct a simple silicate dust shell which should explain the evolution of carbon stars. Because of many oversimplifying assumptions, e.g. an optically thin dust shell of uniform temperature with uniform grain size and a constant gas–to–dust ratio of 100, it seems at least questionable whether such an investigation can yield the desired result.

Compared to this kind of investigations relatively little attention was drawn to a systematic photometric monitoring of LPVs in the infrared range. The up–to–date most complete set of observations was published recently by [LeBertre 1992], [LeBertre 1993]. His monitoring of C–stars [LeBertre 1992] covered observations of 23 objects in the $1 - 20\mu$m range during a period of ≈ 6 years. The stars of his sample were especially selected to contain optically bright and dust enshrouded carbon stars.

He is perhaps the first to note that the usual interpretation of lightcurves to be sinusoidal should be taken with care. The lightcurves of a large fraction of his sample of C–stars show "irregularities", i.e. some lightcurves exhibit a plateau on their ascending branches or even intermediate extrema, especially at short wavelengths. Since these "irregularities" are reproducible from cycle to cycle, they have to be considered as real features of the lightcurves. In addition he notes that some lightcurves show a drift in time either of the average magnitude or of the amplitude. Similar behaviour with "bumps" and secondary maxima on the rising as well as on the declining branch is reported for visual lightcurves by [Mattei *et al.* 1990].

Other authors, e.g. [Lockwood and Wing 1971], [Celis 1977], [Werner *et al.* 1980], [Feast *et al.* 1984], or [Jones *et al.* 1990] presented photometric observations either for a more restricted time interval, for only one object or only at one wavelength, or with a less continuous coverage of the observed time interval. Only interested in the determination of pulsational periods and mean photometric properties [Jones *et al.* 1990] accumulated a considerable amount of photometric data of 63 AFGL sources over a period of 9 years but do not comment on temporal changes in the lightcurves, which are definitely present in their plots with normalized phase.

Parallel to the advances on the observational part also the theoretical dynamical modelling of CDS around Miras and LPVs achieved fundamental improvements in the last years. Based on the pioneering papers of [Willson and Hill 1979] and [Wood 1979], [Bowen 1988a] and [Bowen and Willson 1991] improved this modelling approach by an inclusion of parametrized cooling laws which yield a more realistic modelling of the post–shock relaxation of the gas in the atmosphere. Very recently [Feuchtinger *et al.* 1993] have formally overcome the problem of parametrized cooling laws by solving the complete set of equations of radiation hydrodynamics.

Nevertheless, all these models severely lack a detailed treatment of dust formation, growth and destruction. Instead, only a simple formula, first introduced by [Wood 1979], is assumed to simulate the acceleration by radiation pressure on dust.

This approach was shown to be insufficient to reveal the key role of the solid particles in determining the structure of the CDS [Fleischer *et al.* 1991] and [Fleischer *et al.* 1992], henceforth called Paper I.

In Paper I we presented dynamical models of CDS around LPVs which include time–dependent hydrodynamics and a detailed treatment of the processes of formation, growth and evaporation of carbon grains. The models were calculated in the limit case of isothermal shocks, which, nevertheless, yield a realistic picture of the dynamical interactions which determine the internal structure of the CDS. In these calculations the radiative transfer problem is solved using the semi–analytical method of [Lucy 1971], [Lucy 1976] in grey approximation which yields a radiative equilibrium temperature structure at every instant of time but neither a spectrum nor a lightcurve of the model.

For the present investigation we have coupled the hydro–code of Paper I with the frequency–dependent radiative transfer code of [Winters *et al.* 1994a] and [Winters 1994] to study the optical appearance of our dust shell models.

We present theoretical lightcurves in the range of $0.5 - 25\mu$m for demonstrative model calculations of carbon–rich LPVs and draw a comparison to observed lightcurves.

We start with a short description of the modelling method in Sect. 7.2. In Sect. 7.2.1 we summarize our approach to calculate the dynamical structure of the shell. Section 7.2.2 comprises a brief description of the radiative transfer code and the coupling to the hydro–code. In Sect. 7.3 we present the results of our calculations. Since the details of the radial structure of the dust shell models have been discussed in Paper I, in Sect. 7.3.1 only the main features of these results are summarized. The lightcurves are presented in Sect. 7.3.2 and Sect. 7.3.3. As an example, we analyze in Sect. 7.3.2 for one typical model calculation in some detail how the shape of the lightcurve is influenced or even produced by the discrete structure of the CDS. In Sect. 7.3.3 we discuss the lightcurves of three different model calculations with respect to their long–term behaviour. The results are followed by a discussion in Section 7.4 where we compare our exemplary calculations with results from observations. We finish this paper with the conclusions in Sect. 7.5.

7.2 The modelling method

Since the details of the modelling method and the basic equations solved with both codes have been discussed elsewhere (Paper I, [Winters *et al.* 1994a]), here we only give a brief summary of the main ingredients.

7.2.1 Hydrodynamical model calculation

We consider a spherically symmetric shell around a pulsating red giant with mass $M_\star$, effective temperature $T_\star$, luminosity $L_\star$ and pulsation period P.

The time–dependent hydrodynamical equations are written in Lagrangian coordinates and solved by explicit integration according to the difference scheme given in [Richtmyer and Morton 1967]. Cooling of the gas behind the shock fronts is assumed to take place instantaneously, i.e. we treat the shocks in the isothermal limit case as in the calculations presented in Paper I.

The set of moment equations describing dust formation, growth and dust destruction due to thermal evaporation developed by [Gail and Sedlmayr 1988] and [Gauger *et al.* 1990]) is solved simultaneously. For the calculation of the dust complex it is essential to know the chemical composition of the gas phase. We use the same set of hydrocarbons (H, H_2, C, C_2, C_2H, C_2H_2) in chemical equilibrium as in Paper I to calculate the particle densities of the species contributing to the growth of carbon grains. Solar abundances [Allen 1973]) are assumed for all elements except for the abundance of carbon ϵ_C which we consider as a free model parameter in order to account for a carbon–rich element composition.

For the calculation of the dynamical structure of the circumstellar shell the radiative transfer problem is treated by the semi–analytical method of Lucy [Lucy 1971], [Lucy 1976] which yields the local equilibrium temperature T_{eq} at every instant of time. Since we assume isothermal shocks the gas temperature T_g equals T_{eq} throughout the atmosphere at every instant of time.

At the inner boundary of the model a sinusoidal variation of the velocity with amplitude Δu and period P, the piston, is applied to simulate the interior pulsation of the star.

Thus, our models are defined by the prescription of the 4 fundamental stellar parameters ($T_\star$, $L_\star$, $M_\star$, ϵ_i) and of (P, Δu) to describe the interior pulsation. To start the calculation an initial hydrostatic model with the selected number of grid points (here 1024) and the desired values of $T_\star$, $L_\star$ and $M_\star$ is constructed. The velocity amplitude of the piston is increased slowly until the maximum value is reached and the calculation of the dust complex is started simultaneously. The development of the model is followed until a cyclic pattern of the radial structure is reached.

7.2.2 Radiative transfer calculation

Since the details of the radiative transfer code are discussed elsewhere [Winters 1994], we only summarize the basic equations and give a brief description of the solution method. Further details can also be found in [Mihalas 1978].

For a given radial hydrodynamical structure of the dust shell model, i.e. at a fixed instant of time, the frequency–dependent stationary radiative transfer equation in spherical geometry for a two component medium consisting of molecular gas and solid dust particles is solved. Assuming that the material absorbs and scatters isotropically, the equation reads

$$\begin{aligned}\frac{\partial I_\nu}{\partial r} + \frac{1-\mu^2}{r}\frac{\partial I_\nu}{\partial \mu} &= -\left(\kappa_\nu^{a,g} + \kappa_\nu^{a,d} + \kappa_\nu^{s,g} + \kappa_\nu^{s,d}\right) I_\nu \\ &\quad + \left(\kappa_\nu^{s,g} + \kappa_\nu^{s,d}\right) J_\nu \\ &\quad + \kappa_\nu^{a,g} B_\nu(T_g) + \kappa_\nu^{a,d} B_\nu(T_d) \end{aligned} \tag{7.1}$$

The absorption and scattering coefficients are denoted by κ_ν^a and κ_ν^s, respectively. The additional superscript g and d refer to the gas and the dust component. The other symbols have the usual meaning in the context of radiative transfer.

The radiation field is calculated by an iteration between the monochromatic moment equations and the formal solution for the monochromatic specific intensity.

The moments of the specific intensity are defined by

$$M_i := \int_{-1}^{+1} \mu^i I(\mu) d\mu \quad i = 0, 1, \dots \; . \tag{7.2}$$

According to [Mihalas and Hummer 1974] the first two moment equations can be combined to a second order differential equation for the first moment

$$\frac{\partial^2}{\partial X_\nu^2}\left(f_\nu q_\nu r^2 J_\nu\right) = \frac{r^2}{q_\nu}\left(J_\nu - S_\nu\right) \quad . \tag{7.3}$$

Thereby, the variable Eddington factor $f_\nu = K_\nu / J_\nu$, the sphericality function q_ν, the monochromatic source function S_ν and a suitable chosen depth scale X_ν are introduced. At the inner boundary the diffusion approximation in a form that provides a total flux of $L_\star/16\pi^2$ entering the atmosphere is applied. The outer boundary condition is given by the assumption that no inward flowing radiation exists at $r = R_{\max}$.

The formal solution of the radiative transfer equation is gained by integrating along the characteristic lines of the Eq. 7.1 in (p,z)–coordinates, i.e. for p = const, the equation

$$\left.\frac{\partial^2 j_\nu}{\partial \tau_\nu^2}\right|_{p=const} = \left.(j_\nu - S_\nu)\right|_{p=const} \quad , \tag{7.4}$$

where

$$j_\nu = \frac{1}{2}\left(I_\nu^+ + I_\nu^-\right) \quad , \tag{7.5}$$

$$d\tau_\nu = -\chi_\nu dz, \quad \tau(z \longrightarrow \infty) = 0 \quad . \tag{7.6}$$

The total extinction coefficient χ_ν is defined by

$$\chi_\nu = \kappa_\nu^{a,g} + \kappa_\nu^{a,d} + \kappa_\nu^{s,g} + \kappa_\nu^{s,d} \quad . \tag{7.7}$$

The quantities I_ν^+ and I_ν^- denote the intensities propagating in the direction of $+z$ or $-z$, respectively.

The radiative transfer processes considered here are grey absorption and thermal emission of the gas and frequency–dependent absorption and thermal emission of the dust component. In order to keep consistency with the hydrodynamical model, the transport coefficients of the gas are replaced by an average absorption coefficient $\kappa^{\rm g}$ which gives a gas opacity of $\kappa^{\rm g}/\rho = 2 \cdot 10^{-4}{\rm cm}^2{\rm g}^{-1}$ (ρ: mass density) (cf. [Bowen 1988a], Paper I). This value roughly represents the Rosseland mean gas opacity in the relevant temperature and density range.

For calculating the dust opacity the dust particles are assumed to be spherical and small compared to the relevant wavelength of the radiation field. The assumption of the *small particle limit* is approximately justified for the time–dependent models considered here, since the mean particle radius remains smaller than 0.1μm throughout the circumstellar shell (cf. Paper I). With these assumptions the absorption coefficient of the dust component $\kappa_\nu^{\rm d}$ can be expressed as cf. [Gail *et al.* 1984]

$$\kappa_\nu^{\rm d}(r) = \frac{8\pi^2 a_0^3}{\lambda} {\rm Im}\left\{\frac{m(\nu)^2-1}{m(\nu)^2+2}\right\} K_3(r) = \chi_\nu^{\rm d}(r)\,, \tag{7.8}$$

and equals the extinction coefficient of the dust component $\chi_\nu^{\rm d}$. For all calculations presented here, the complex refractive index $m(\nu)$ of the grain material is taken from [Maron 1990] which is appropriate for pure amorphous carbon grains. The quantity $K_3(r)$ is the third moment of the size distribution function $f(a,r)$ of the dust particles. It is defined by

$$a_0^3 K_3 = \int_{a_\ell}^{\infty} a^3 f(a,r) da\,, \tag{7.9}$$

where a is the radius of the dust grain, a_0 denotes the hypothetical radius of a monomer contained in a dust grain, and a_ℓ is a lower limit size of the dust particles. Since we assume the dust particles to be small compared to the wavelength, we neglect the contribution of light scattering by the grains. Thus, the emissivity ϵ_ν is given by thermal emission of gas and dust:

$$\epsilon_\nu(r) = \epsilon_\nu^{\rm g}(r) + \epsilon_\nu^{\rm d}(r) = \kappa^{\rm g} B_\nu(T(r)) + \kappa_\nu^{\rm d} B_\nu(T(r))\,, \tag{7.10}$$

where B_ν is the Kirchhoff–Planck function and the superscripts $^{\rm g}$ and $^{\rm d}$ denote the gas and the dust component, respectively.

By definition, K_3 equals the number of monomers condensed into grains per cm^3 and, therefore, is related to the degree of condensation f_c, i.e. the fraction of condensable material actually condensed into grains. In the case of pure carbon grains, which is considered here, the degree of condensation is given by

$$f_c = \frac{K_3}{(\epsilon_{\rm C} - \epsilon_{\rm O}) n_{<\rm H>}}\,, \tag{7.11}$$

where we have assumed that all oxygen is locked up in the CO–molecule ($n_{<\rm H>}$: total density of hydrogen atoms). Thus, the radiative acceleration in units of the local gravitational deceleration

$$\alpha = \frac{\chi_H}{\rho} \frac{L_\star}{4\pi c G M_\star} \tag{7.12}$$

is directly proportional to the degree of condensation in the small particle approximation (χ_H: flux–mean extinction coefficient, c: speed of light, G: gravitational constant).

Table 7.1: Parameters of the initial hydrostatic models. Also given are the time averaged mass loss rates and final outflow velocities of the evolved models

	Model A*	Model B	Model C
$T_\star$ [K]	2600	2500	2450
$\epsilon_{\rm C}/\epsilon_{\rm O}$	1.8	1.34	1.25
$L_\star$ [$10^4\, L_\odot$]	1.0	1.0	3.0
$M_\star$ [$M_\odot$]	1.0	1.0	1.0
P [d]	650	370	621
Δu [km s^{-1}]	2.0	6.0	3.0
$< \dot{M} >$ [$M_\odot$ yr^{-1}]	1.0 10^{-5}	3.0 10^{-5}	2.9 10^{-4}
$< u_\infty >$ [km s^{-1}]	28.5	12.8	14.7

* Model A is equal to Model E of Chapter 4

7.3 Results

Table 4.1 shows the parameters of the initial hydrostatic models. Additionally given are the time averaged values of the mass loss rate and the final outflow velocity of the evolved models. Since there are few, if any, real objects for which all of these parameters are determined by observations, we have chosen the model parameters to represent prototypes of cool, dust–enshrouded carbon giants. For this kind of objects, e.g. [Claussen *et al.* 1987] find typical values of the luminosity of the order of $10^4 L_\odot$, irrespective of the pulsational period. The investigations of [Lambert *et al.* 1986] and [Olofsson *et al.* 1993a, Olofsson *et al.* 1993b] confirm, that the objects under consideration are in fact rather cool with effective temperatures well below or approximately 3000 K. [Lambert *et al.* 1986] find e.g. for R Scl an overabundance of carbon to oxygen of 1.34 and an effective temperature of 2550 K. [Olofsson *et al.* 1993a] quote a period of R Scl of 370 d, cf. Model B. IRC +10216, for instance, is known to be a highly evolved luminous source with a period exceeding 600 d, cf. [Witteborn *et al.* 1980] and [Ridgway and Keady 1988].

Since the model parameters inevitably had to be chosen following different observational investigations, one cannot expect that the sets of parameters satisfy the various fit–formulae obtained from the results of certain evolutionary calculations (e.g. core mass–luminosity relations (cf. [Boothroyd and Sackmann 1988a]), or the radius–mass–luminosity relation [Iben 1984], a detailed discussion can also be found in a recent paper explicitly devoted to the problems with the core mass–luminosity relations [Boothroyd and Sackman 1992]). Furthermore, our sets of model parameters do not fit to the well known period–mass–radius relations of [Ostlie and Cox 1986], which were derived from linear, nonadiabatic pulsation analysis calculations for oxygen–rich, less luminous ($L_\star \leq 7000\,L_\odot$) models with stellar temperatures between 2700 K and 3400 K.

7.3.1 Radial structure of the dust shell models

Figure 7.1 depicts a typical radial structure of the CDS at the beginning of the hydrodynamical cycle shown for Model A, cf. Table 7.1. The following quantities are plotted:

upper diagram: the velocity u (solid line), velocity of sound u_s (dotted line) and the temperature T (dashed line),

middle diagram: the logarithm of the density ρ (solid line) and the degree of condensation f_c, i.e. the fraction of condensable material actually condensed into grains (dashed line) (cf. Eq. 7.11),

lower diagram: the logarithm of the nucleation rate $J_\star$, i.e. the number of dust grains formed per second and H–atom (solid line) and the logarithm of the number of dust grains per H–atom $n_{\rm d}/n_{<\rm H>}$ (dashed line).

Radii are always given in units of the stellar radius R_0 of the initial hydrostatic model.

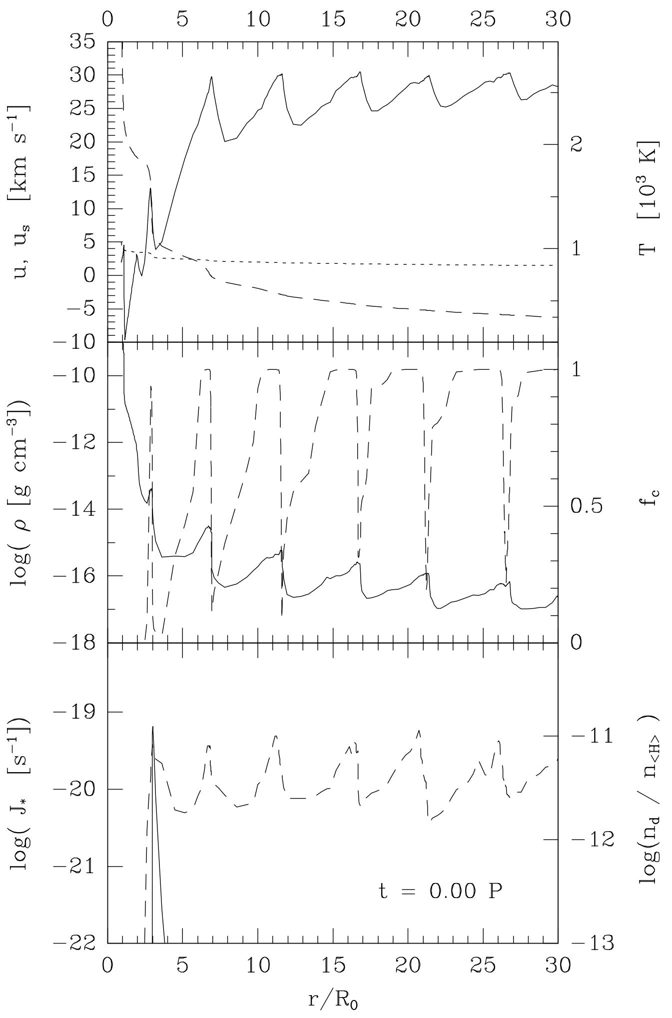

Figure 7.1: Radial structure of Model A at $t = 0.00P$

The consistent calculation of dust formation and grain growth and destruction shows up to have significant influence on the resulting dynamical structure of the CDS. As the degree of condensation and the number of dust grains per H–atom in Fig. 7.1 show, the dust is distributed inhomogeneously across the shell. The dust grains are concentrated in distinct layers, equidistant for each model, and exhibit a shell or onion like structure which is closely related to the hydrodynamical structure of the CDS.

Fig. 7.1 also shows the determining influence of the dust on the thermodynamical structure of the CDS. There are several steps in the course of the temperature which coincide with spikes in the degree of condensation.

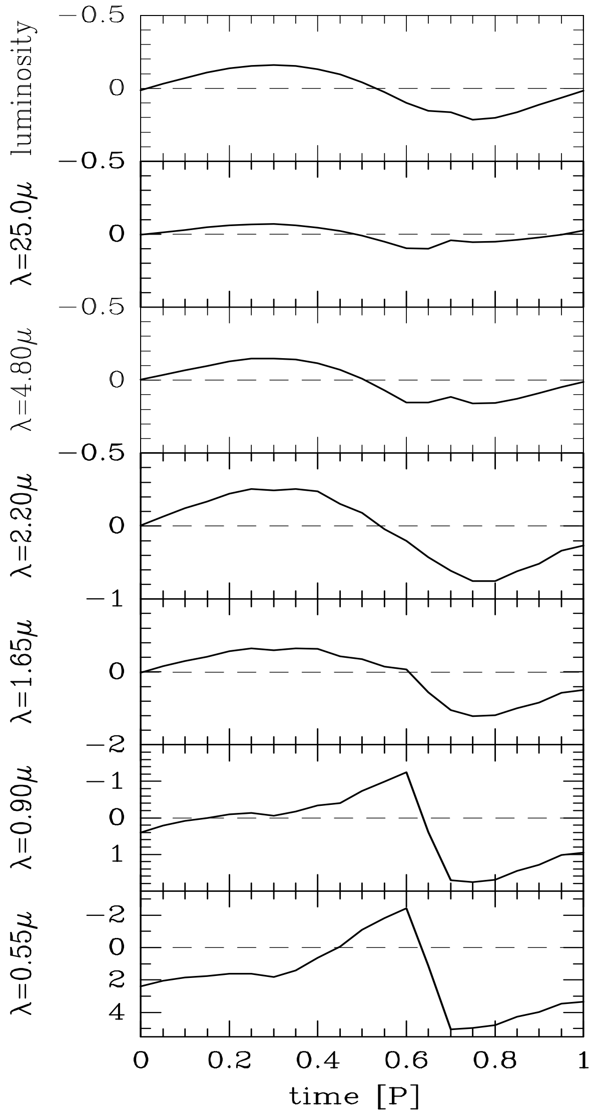

Figure 7.2: Theoretical lightcurves (in magnitudes, relative to the mean magnitude) of Model A at different wavelengths over a time interval of one pulsational period. Note the different scaling of the ordinate at different wavelengths

---

These interactions are investigated in detail in Paper I and, therefore, are only briefly summarized here.

The discrete structure of the atmosphere is not produced solely by the shock waves caused by the interior pulsation of the star, but is a very product of the process of dust formation. In a first step the interior pulsation defines the onset of dust *formation* by providing appropriate low temperatures in the region between 3 and $4R_0$. In a second step pulsation triggers grain *growth* by a compression of the material in this radius interval and, thus, provides densities favourable for the growth process. In a short time interval values of f_c as high as 1 are reached, i.e. all condensable material is actually condensed into grains. The quantity f_c is proportional to the radiative acceleration of the dust grains (cf. Paper I and Eqs. 7.8, 7.11, 7.12). Since the grains are closely momentum coupled to the gas, the sudden increase of the radiative acceleration causes a perturbation in the velocity field which steepens to become a shock wave, thereby compresses the material and, in turn, accelerates dust growth. Thus, the prominent shock waves which propagate through the atmosphere (cf. Fig. 7.1) are produced by a self–accelerating mechanism caused by dust formation.

Furthermore, the newly formed dust in the inner shells, due to its opacity, effectively blocks the outgoing radiation and heats the material closer to the star. This back–warming, seen as steps in the temperature structure in Fig. 7.1, also influences the formation of new dust particles.

Due to pulsation and back–warming, dust formation and growth is only possible in a small radius range and during a limited time interval. This results in the discrete structure of the CDS. The complex interplay among the processes of dust formation and growth, hydrodynamics and thermodynamics shows that the dust particles play the key role in determining the atmospheric structure of LPVs and Miras. The influence of periodic dust formation on the lightcurves of these objects is discussed in detail for Model A in the next section.

7.3.2 The lightcurves of Model A, detailed analysis

The theoretical lightcurves of Model A are displayed in Fig. 7.2 for several wavelengths between 0.55μm and 25μm during a time interval of one hydrodynamical period P. The sinusoidal variation of the inner boundary (cf. Sect. 7.2.1) is reflected by the temporal variation of the stellar luminosity, shown in the upper panel of Fig. 7.2. Apart from the smooth temporal variation of the flux which is caused by this luminosity variation, the long wavelength lightcurves ($\lambda > 2.2\mu$m) additionally exhibit pronounced narrow secondary maxima which occur periodically within the third quarter of the pulsational cycle (cf. Fig. 7.5). In the short wavelength lightcurves ($\lambda < 2.2\mu$m), the variation due to the luminosity is almost completely concealed by strong features occuring periodically around $t = 0.60P$. The maximum value of these peaks decreases towards longer wavelengths until the pronounced structure eventually disappears at $\lambda = 2.2\mu$m. The flux minimum seen at $t = 0.70$P in the short wavelength lightcurves exactly corresponds to the intermediate maximum in the long wavelength lightcurves.

The occurrence of these striking features in the lightcurves is an immediate consequence of the dynamical behaviour of the discrete dust layers.

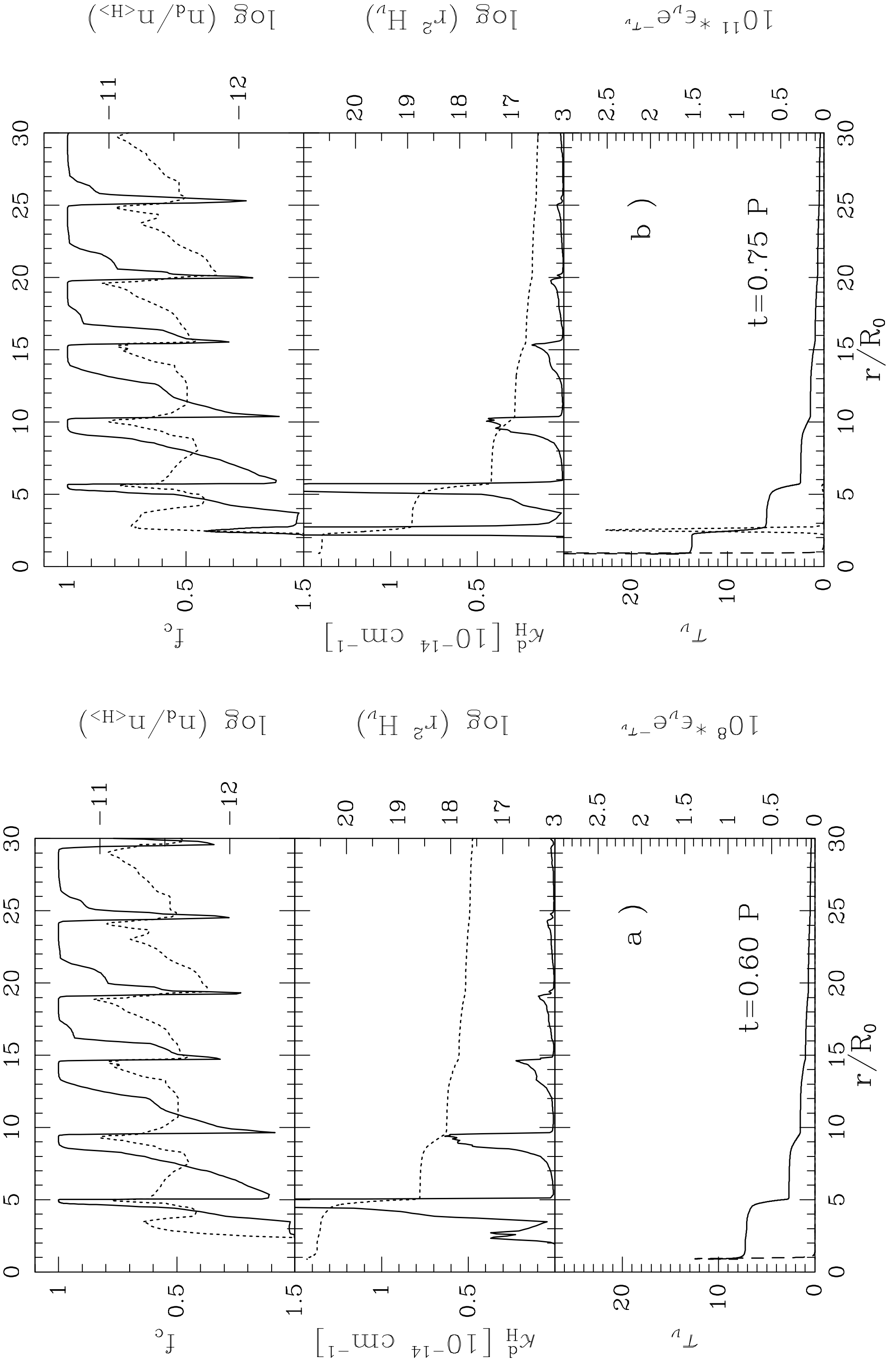

Figure 7.3: Radial structure of Model A at **a)** the beginning of the dust formation cycle at $t = 0.60P$ and **b)** at $t = 0.75P$. The quantities shown are explained in the text. r^2H_ν is given in [ergs^{-1}Hz^{-1}] and $\epsilon_\nu e^{-\tau_\nu}$ in [ergs^{-1}cm^{-3}sr^{-1}Hz^{-1}]. Frequency–dependent quantities refer to a corresponding wavelength of $\lambda = 0.90\mu$m

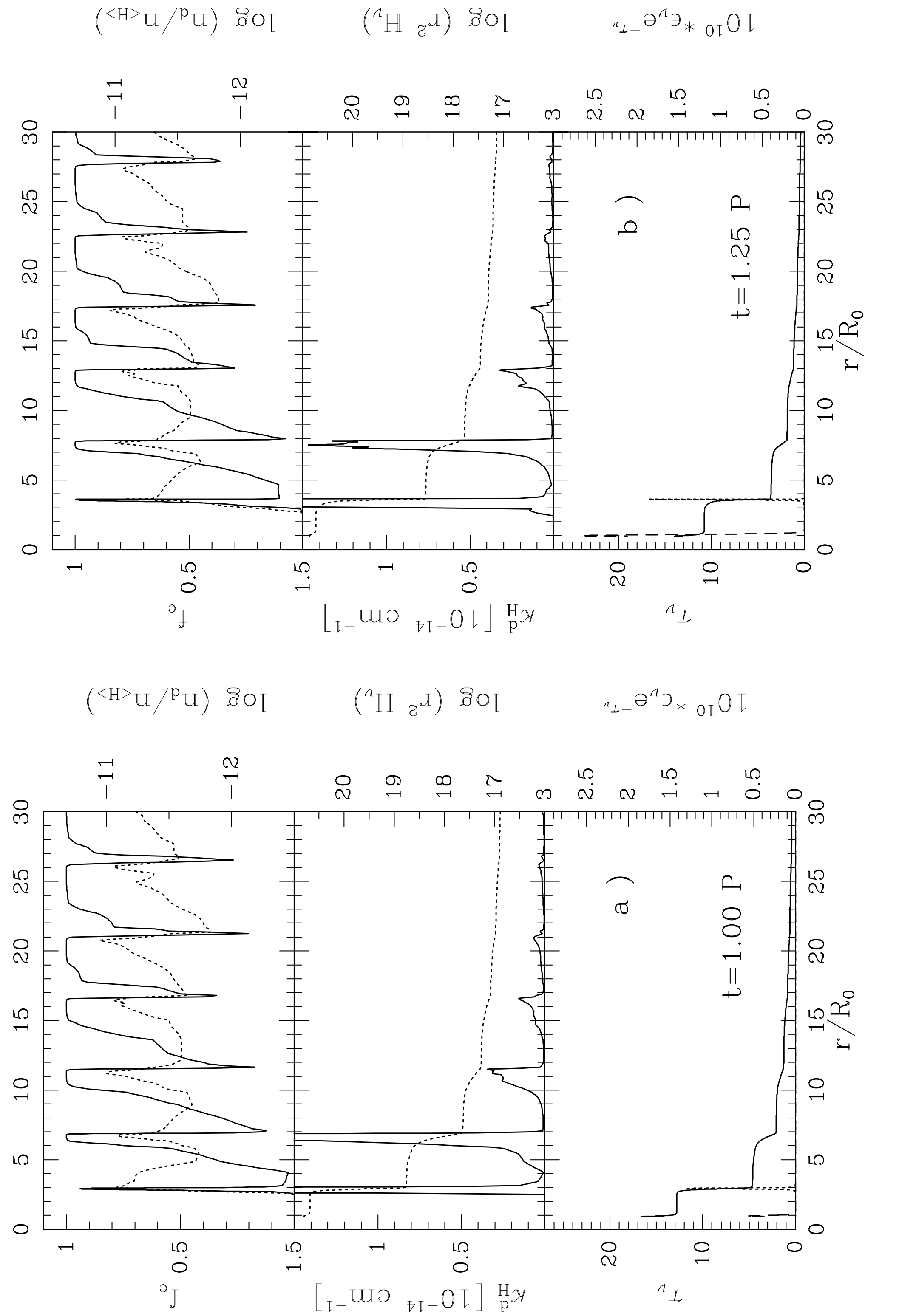

Figure 7.4: Same as Fig. 7.3 at **a)** $t = 1.00P$ and **b)** at $t = 1.25P$, again at $\lambda = 0.90\mu\text{m}$

In Figs. 7.3 and 7.4 the radial course of several quantities which are of interest for the following discussion of the lightcurves are shown at four selected instants during the pulsational cycle. The quantities shown in these figures are:

upper diagram: the degree of condensation f_c (solid line) and the logarithm of the particle density of dust grains n_{d} normalized to the total hydrogen particle density $n_{<\mathrm{H}>}$ (dashed line),

middle diagram: the flux mean absorption coefficient of the dust component κ_H^d (solid line) and the logarithm of the Eddington flux H_ν at $\lambda = 0.90\mu$m passing through the spherical surface at radius r, multiplied by r^2 to eliminate the pure geometrical dilution (dashed line),

lower diagram: the total (gas and dust) optical depth τ_ν at $\lambda = 0.90\mu$m (solid line), the local contribution of dust emission to the 0.90μm *intensity* reaching the outer shell boundary in radial direction $\epsilon_\nu^d \mathrm{e}^{-\tau_\nu}$ (short–dashed line) and the respective contribution due to gas emission $\epsilon_\nu^g \mathrm{e}^{-\tau_\nu}$ (long–dashed line).

We start the discussion of the lightcurves at time $t = 0.60P$ shortly after the beginning of a new dust formation cycle (cf. Fig. 7.3a)). At this instant, all dust layers present in the circumstellar shell are fully developed, i.e. the degree of condensation within these layers has reached its maximum value of 1 and the layers are moving outwards. At $t = 0.60P$ the total dust optical depth has reached its minimum value during the cycle, the dust optical depth at $\lambda = 0.90\mu$m is $\tau_{0.90\mu} = 7.23$. Simultaneously the short wavelength lightcurves reach their peak value (cf. Fig. 7.2). Due to the relatively small optical depth, the dominant contribution to the short wavelength radiation that escapes from the shell is produced by photospheric gas emission (cf. Fig. 7.3a)). Between $t = 0.60P$ and $t = 0.70P$ a new dust layer begins to form as indicated by the enhanced particle density of dust grains already at $t = 0.60P$ seen in Fig. 7.3a) around $3R_0$. At this instant new dust particles condense from the gas phase, but these particles are still too small to produce a relevant degree of condensation. Although the nuclei already show up in the flux mean absorption coefficient κ_H^{d}, they still do not influence the optical depth at this time. The newly formed dust particles subsequently grow very effectively and, thereby, increase the optical depth of the new dust layer. From $t = 0.70P$ on, the short wavelength photospheric radiation is already effectively blocked by the new layer (cf. the radial variation of the Eddington flux in Figs. 7.3a) and b)). At the same time the minimum value of the short wavelength lightcurves is reached, whereas in the long wavelength lightcurves a shallow intermediate maximum occurs. The main contribution to the short wavelength flux is now provided by thermal dust emission, originating from the front of the innermost dust shell (note the different scaling of the source contribution $\epsilon_\nu \mathrm{e}^{-\tau_\nu}$ in Figs. 7.3a) and b). Note also that the *flux* is given by an angle integration of $\epsilon_\nu \mathrm{e}^{-\tau_\nu}$ and, thus, the respective source contribution is weighted by the radiating surface). At longer wavelengths, absorption of the stellar radiation field is less effective, and thermal dust emission from the newly formed layer contributes a significant fraction to the emergent flux and produces the retarded intermediate structure in the long wavelength lightcurves. At $t = 0.75P$ the degree of condensation in the newly formed dust layer has reached a value of $f_c = 0.41$ (cf. Fig. 7.3b)), the optical depth of the new layer alone has increased to $\Delta\tau_{0.90\mu} = 7.75$ and, thus, produces the innermost step of the τ–structure displayed in Fig. 7.3b) (the optical depth of the new layer at 25μm is $\Delta\tau_{25\mu} = 0.21$ at this instant). During the following time interval until $t = 1.00P$ the optical depth of the new dust layer increases up to its maximum value of $\Delta\tau_{0.90\mu} = 8.40$ due to growth of the dust grains, whereas the degree of condensation reaches the maximum possible value of $f_c = 1$ not until $t = 1.25P$ (cf. the sequence of Figs. 7.3b), 7.4 a), b)). Obviously, there are two competing processes during this phase: Between $t = 0.75P$ and $t = 1.00P$ dust formation and growth exceeds the dilution of the material due to expansion, whereas between $t = 1.00P$ and $t = 1.25P$ expansion predominates. Simultaneously, the outer layers merely expand and due to geometrical dilution of the material the optical depth in front of the newly formed layer decreases. Within this time interval the short wavelength radiation which escapes from the dust envelope is predominantly produced by thermal emission of dust located in the outer part of the new layer. This changes at $t = 1.35P$, when the total optical depth has reached a value of $\tau_{0.90\mu} = 9.70$. Due to expansion, caused by radiation pressure on the new dust shell, the innermost layer has become increasingly transparent ($\Delta\tau_{0.90\mu} = 6.50$ at $t = 1.35P$) and cooler. At this time the contribution of photospheric gas emission again exceeds the contribution emerging from the radiating dust layer. Simultaneously, the short wavelength lightcurves start to rise steeply until $t = 1.60P$, when the total optical depth of the shell has again reached its minimum value of $\tau_{0.90\mu} \approx 7$, with the innermost dust layer contributing $\Delta\tau_{0.90\mu} = 4.37$ to this value.

Thus, in the case of Model A discussed here, we can clearly distinguish two different phases within one hydrodynamical period which are essentially characterized i) by effective dust formation and growth (between $t = 0.60P$ and $t \approx 1.00P$) and ii) by expansion of the dust layers (between $t \approx 1.20P$ and $t = 1.60P$). During the relatively short first part of phase i), where very effective dust formation and growth takes place, the optical depth of the circumstellar shell increases from almost zero at $t = 0.60P$ to $\Delta\tau_{0.90\mu} = 7.75$ at $t = 0.75P$ and, thus, leads to the steep decline of the short wavelength lightcurves. Due to expansion of the dust layers during phase ii), the optical depth decreases, which results in the increase of the short wavelength lightcurves. In the long wavelength lightcurves the formation of a new dust layer between $t = 0.60P$ and $t = 0.75P$ leads to the intermediate maxima seen in Figs. 7.2 and 7.5, which are caused by thermal dust emission originating from the new layer.

A necessary condition for the strong features in the lightcurves to occur, produced by the mechanism of dust formation, is the existence of distinct phases, during which the respective competing processes (dust formation and expansion) are subject to very different time scales. For Model A this is the case in the interval between $t = 0.60P$ and $t = 0.75P$ where the time scale of grain growth τ_{gr} is considerably shorter than the expansion time scale τ_{exp} and between $t = 1.25P$ and $t = 1.60P$, where expansion predominates due to radiative acceleration of the new layer. For Models B and C these distinct phases are multiple times longer, cf. the discussion in the next section.

Summarizing the preceding discussion, we state:

– The occurrence of the intermediate structures in the lightcurves critically depends on the temporal evolution of the optical depth of the innermost dust layer.

– The short wavelength radiation seen during the peak of the lightcurves of Model A (between $t = 0.35P$ and $t = 0.70P$, cf. Fig. 7.2) is mainly produced by photospheric gas emission.

7.3.3 The lightcurves of Models A – C, long-term analysis

Figs. 7.5, 7.6 and 7.7 show the lightcurves of Models A – C for three representative wavelengths.

Fig. 7.5 shows the long–term behaviour of the lightcurves of Model A which has been discussed in detail in the previous section. From the periodic occurrence of the intermediate structures at $\lambda = 1.25\mu$m and $\lambda = 25\mu$m it can be inferred that the formation of a new dust layer periodically takes place during every second half of the hydrodynamical cycle. The lightcurve at 25μm shows a slightly asymmetric shape and exhibits an internal structure on the rising branch which regularly occurs and is even more pronounced at longer wavelengths.

All curves are characterized by a periodic re–occurrence of all features at the same phase during the sequence of hydrodynamical pulsation cycles.

In contrast to Model A, Models B and C exhibit a different behaviour. These models (cf. Fig. 7.6 and 7.7) show alternating high maxima at all wavelengths. Models B and C show a quasi–sinusoidal behaviour on the scale of one pulsational period which is superposed by a long–scale oscillation. To get an idea how these surprising finding could be explained we have to go back to the results of the hydrodynamical calculations.

In Paper I it was mentioned that, depending on the carbon abundance ϵ_C, the formation of a new dust shell can take place *every* hydrodynamical period, as is the case for Model A, but also every second, third ... pulsational period, i.e. the radial structure of the CDS at a certain instant of time $t = \beta P$ equals the structure at $t = (\beta + n_P)P$, where β is an arbitrary dimensionless time parameter and $n_P = 1, 2, \ldots$ is the *multiperiodicity* number. A detailed analysis

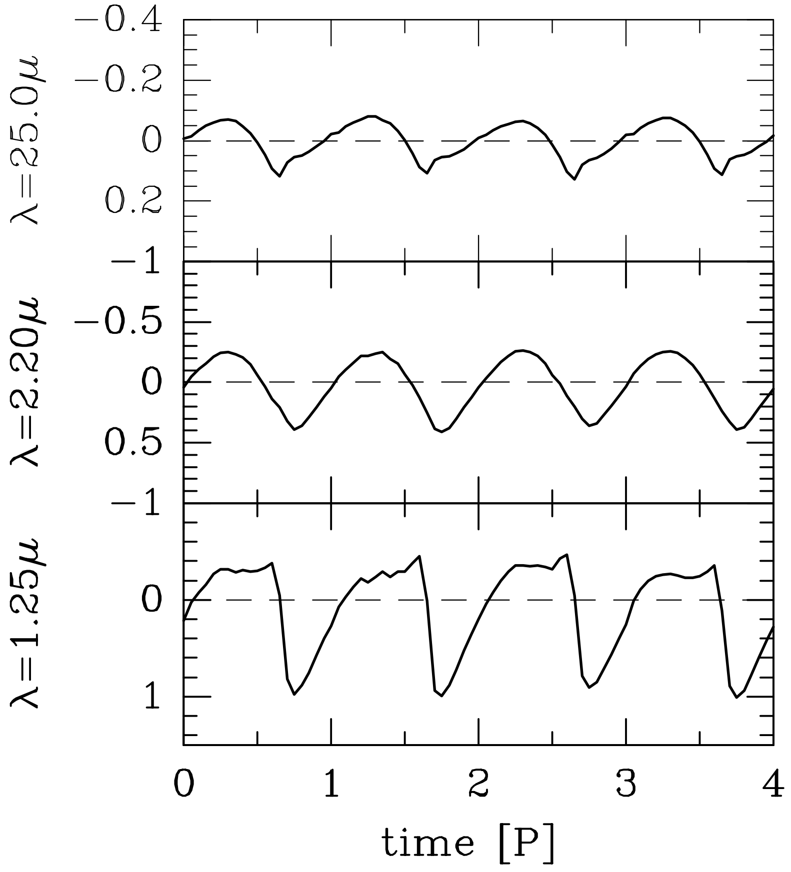

Figure 7.5: Theoretical lightcurves (in magnitudes, relative to the mean magnitude) of Model A at different wavelengths. Note the different scaling of the ordinate at different wavelengths

---

of the occurrence of multiperiodicity is beyond the scope of the present paper. We just state that for Model B $n_P = 4$, for Model C $n_P = 5$ whereas for Model A $n_P = 1$. In principle, the process of the formation of a new dust shell is the same in Models B and C as described in detail for Model A. The difference is the timescale: The formation of a fully evolved new dust layer takes a time interval of four pulsational cycles in Model B compared to one pulsational cycle for Model A.

Obviously, the course of the lightcurves at longer wavelengths, e.g. at 25.0μm reflects the global dynamical behaviour of the dust shell model. A new dust layer is formed at each of the deep minima at $t \approx 2.5, 6.5, 10.5\ldots$ P, respectively (cf. Fig. 7.6). The newly formed layers move outwards and reach their maximum degree of condensation just before the next layer is formed, i.e. at

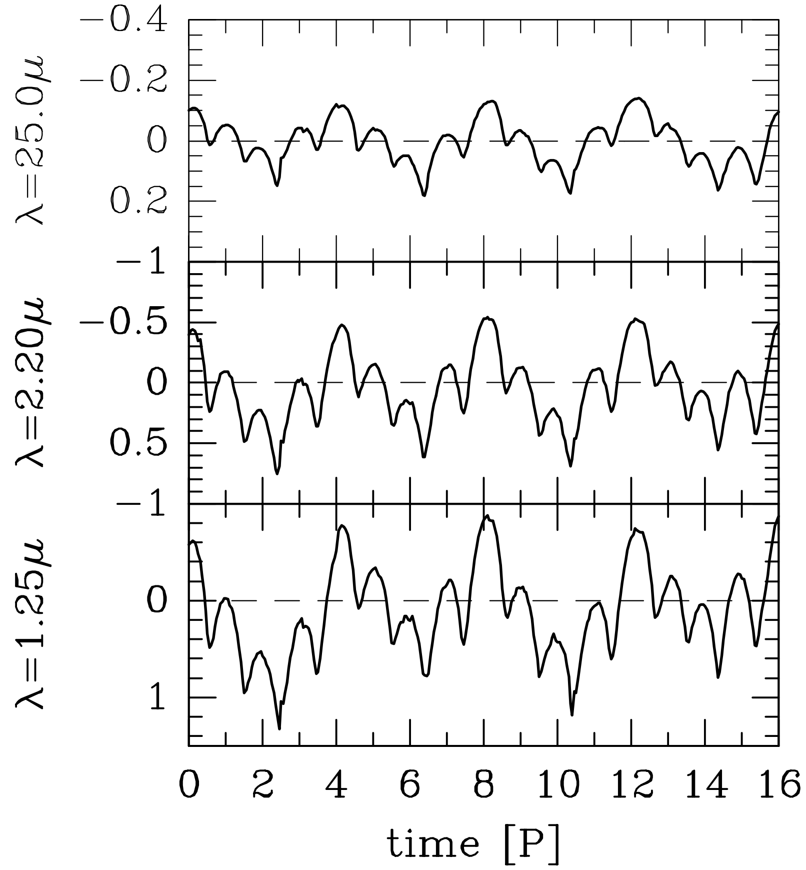

Figure 7.6: Theoretical lightcurves (in magnitudes, relative to the mean magnitude) of Model B at different wavelengths. Note the different scaling of the ordinate at different wavelengths

---

$t \approx 6.0, 10.0, 14.0\ldots$ P, respectively.

The minima at $t \approx 2.5, 6.5, 10.5\ldots$ P (cf. Fig. 7.6) have an alternating depth at shorter wavelengths. This is due to a slight variation of approximately 0.5 R_0 of the exact radial location where the new dust layer is formed. Caused by the local hydrodynamical conditions at $t \approx 2.5, 10.5, \ldots$ P dust formation already starts at slightly smaller radii and, therefore at higher densities which leads to a larger optical depth of the newly formed layer. Thus, the course of the short wavelength lightcurves sensitively probes the physical conditions in the innermost region of the dust shell.

Model C behaves similar to Model B, therefore a detailed description is omitted here.

A detailed analysis of the effect of *multiperiodicity* will be the subject of a

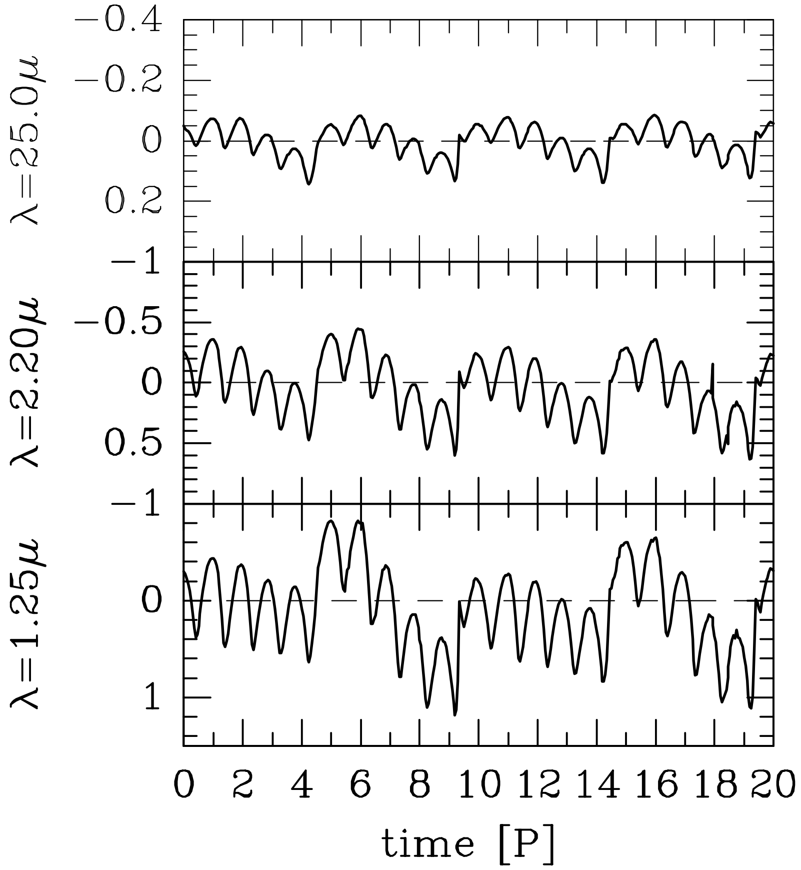

Figure 7.7: Theoretical lightcurves (in magnitudes, relative to the mean magnitude) of Model C at different wavelengths. Note the different scaling of the ordinate at different wavelengths

---

forthcoming paper.

7.4 Discussion

We do not intend to model a special object but to present results of a theoretical investigation, which is devoted to the principle physical mechanisms, and reveals an important influence of the dynamical structure on the optical appearance of LPVs and Miras. Thus, we cannot expect a quantitative agreement between our model calculations and the observations but at most a qualitative agreement of certain characteristic features.

To draw this comparison we choose the measured lightcurves of two objects

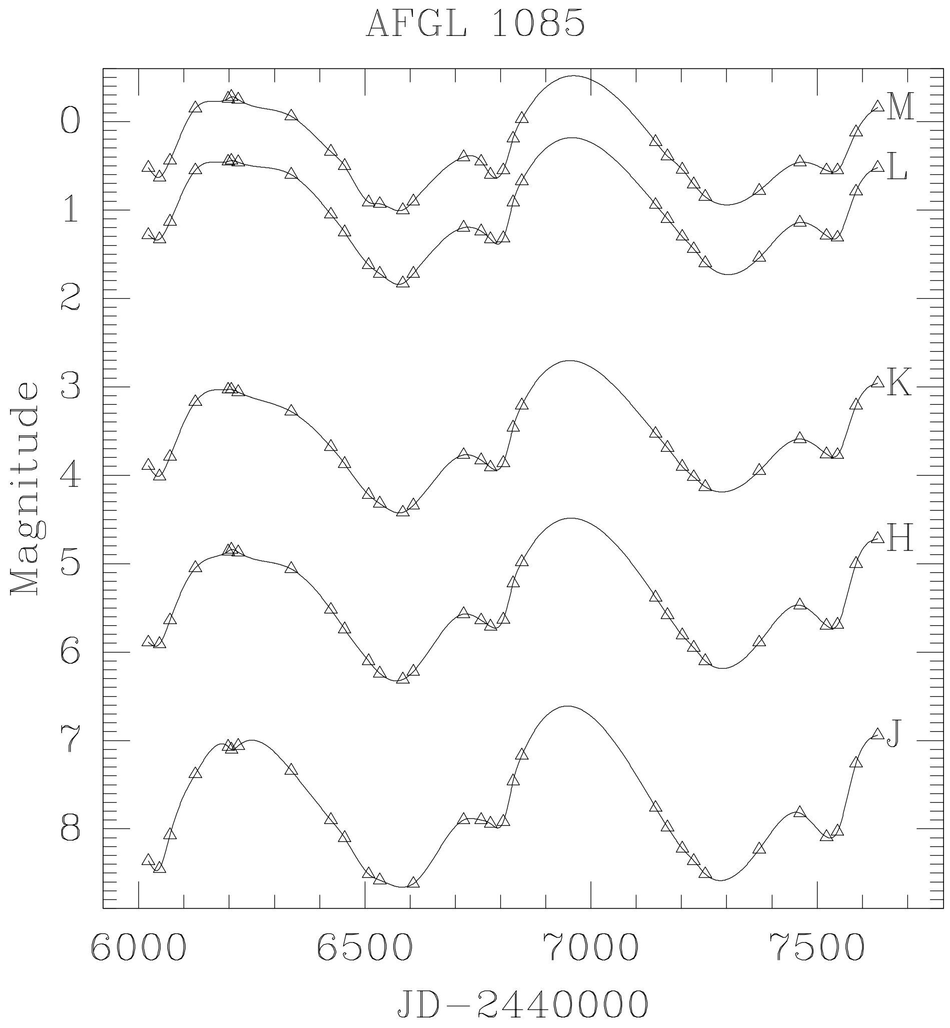

Figure 7.8: Observed lightcurves of AFGL 1085, data are taken from [LeBertre 1992]

---

of the sample of [LeBertre 1992], AFGL 1085 and the carbon–rich Mira R Fornacis (cf. Figs. 7.8, 7.9). For R For it is possible to combine the data of Le Bertre with those of [Feast *et al.* 1984], except for a slight disagreement of the L photometric fluxes. Therefore, we omitted these data when we connected the measured points of R For and AFGL 1085 by a cubic spline interpolation (the M fluxes were not measured by [Feast *et al.* 1984]).

The characteristic features of the AFGL 1085 lightcurves (cf. Fig. 7.8) are the intermediate extrema, already noted by [LeBertre 1992]. With respect to our model calculations, these intermediate structures could be caused by the sudden formation of a new dust layer similar to Model A.

In the short wavelength lightcurves ($\lambda < 2.2\mu$m) of Model A the dynamical

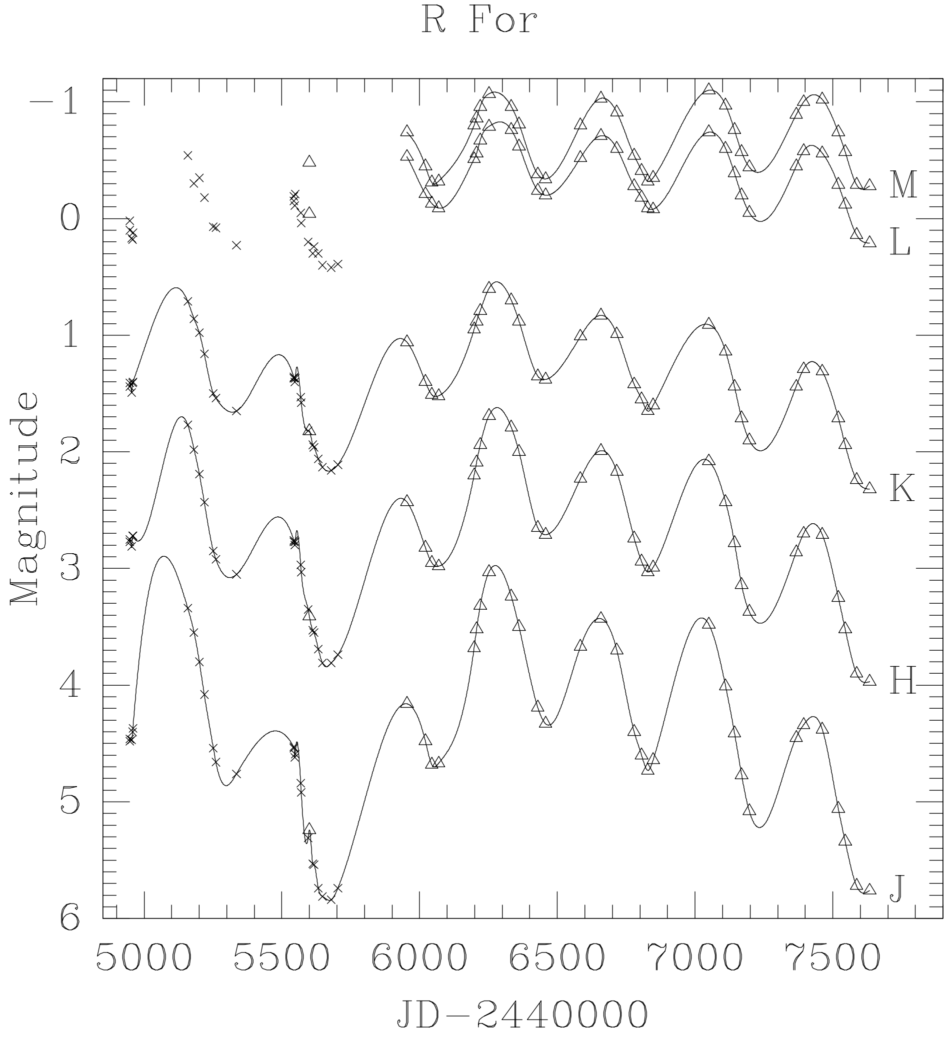

Figure 7.9: Observed lightcurves of R For. Observational data are taken from (△): [LeBertre 1992] and (×) [Feast *et al.* 1984]

---

behaviour of the discrete dust layers causes rather narrow, additional maxima, which are steeply decreasing in time due to the rapid increase of the dust optical depth. These additional maxima follow the broad, plateau–like maxima produced by the varying luminosity (cf. Figs. 7.2 and 7.5). At longer wavelengths ($\lambda > 2.2\mu$m), on the other hand, the periodic formation of new dust layers leads to shallow intermediate maxima on the ascending branches of the lightcurves, which are produced by thermal dust emission originating mainly from these new layers. Due to the wavelength dependence of the dust opacity, the features in the synthetic lightcurves, which are produced by absorption of photospheric radiation at shorter wavelengths and by dust emission at longer wavelengths, accordingly depend on the wavelength.

However, the intermediate structures present in the observed lightcurves (e.g. AFGL 1085) could also be caused by different mechanisms, e.g. by the dissipation of shock wave energy in the inner parts of the atmosphere (cf. [FEUCHTINGER *et al.* 1993]) which is transferred to the radiation field. Furthermore, the formation of secondary shocks in the innermost dust–free region (the occurrence of which has been thoroughly investigated by [BOWEN 1990] and [WILLSON *et al.* 1993]) could also lead to such intermediate structures in the lightcurves. In both cases, the *strength* of the secondary maxima might also depend on the wavelength, but we do not expect that this mechanism could produce minima at shorter wavelengths and simultaneously maxima at longer wavelengths. To decide, whether dust formation is responsible for the occurrence of the observed intermediate maxima, the promising objects (e.g. AFGL 1085, R Lep, ...(see [LEBERTRE 1992]) should be simultaneously monitored with a sufficient temporal resolution during the phases of interest in a wide spectral regime (e.g. between 0.90μm and 100μm).

The presence of discrete dust layers in our models also causes rippled or even step–like structures in the radial brightness profiles as well as in the theoretical visibilities, which result from these calculations [WINTERS 1994]. Similar structures have been observed e.g. for IRC +10216 [RIDGWAY AND KEADY 1988]. A detailed discussion of these results can be found in [WINTERS 1994] and will be subject of a forthcoming paper [WINTERS *et al.* 1994B].

Since the discrete structure of the dust shell may provide an explanation for both, the occurrence of intermediate structures in the lightcurves as well as the pronounced structures in observed brightness distributions, from a theoretical point of view, we would favour the dust mechanism described in this section to be responsible for the bumps in the lightcurves.

The lightcurves of R For (cf. Fig. 7.9) show a systematic drift in magnitude very similar to the multiperiodic Model B. [FEAST *et al.* 1984] found R For to exhibit an "anomalously" deep minimum in 1983. A similar deep minimum has been observed in 1990 by [LEBERTRE 1992]. Secondary variations with characteristic time scales multiple times longer than the main period have also been found in the lightcurves of several other objects by [ALKSNIS 1990].

In terms of our model calculations we could explain this behaviour by the interplay of two distinct processes with different time scales: The regular pulsation of the star, which provides the "short" hydrodynamical time scale, and the process of dust formation and growth, which, under the conditions of Models B and C has a time scale of four respectively five times longer. Thus, the CDS can be conceived as a dynamical system under the influence of an external exciting mechanism, or, to use a simple analogy from classical mechanics, the CDS behaves similar to a pendulum, which is subject to a periodic external force.

We expect from our model calculations that observations of R For continuing the monitoring of [LEBERTRE 1992] would again reveal a long–term increase of the lightcurves.

We finish this section with a remark concerning our general assumption of isothermal shocks. If cooling of the post–shock gas is taken into account, the interaction processes become even more complicated but the discrete structure of the CDS is conserved [Gauger *et al.* 1994a]. However, since a main cause for the behaviour of the synthetic lightcurves is the periodic formation of dust, we expect that the features presented here, will also appear in models where time–dependent post–shock cooling of the gas is taken into account.

7.4.1 The driven Keplerian oscillator

In order to explain irregularities which are superposed to the regular variations of Mira variables or to explain the regular component of the lightcurves of Semi–regular variables [Icke *et al.* 1992] have constructed the model of the so called driven Keplerian oscillator.

[Icke *et al.* 1992] assume that the pulsations of AGB stars are caused by processes well below the photosphere, which they call the *interior* and that this *driving* oscillator can be described by the following equation

$$R_i = R_0 + B\sin(\omega_i t) \ , \tag{7.13}$$

where R_i denotes the radius of the spherically symmetric interior, R_0 is the rest position of this oscillator, B its amplitude and ω_i its frequency.

Separated by a transition zone from the interior lies the *mantle*, i.e. the *driven* oscillator. Pressure waves from the interior propagate through the transition zone until they hit the mantle, where they are dissipated. The mantle is represented by a spherical shell of radius R_m and mass m.

With these assumptions they derive the equation of motion for the mantle

$$\frac{\partial^2 R}{\partial \tau^2} = -\frac{1}{R^2}\left(1-\frac{1}{R}\right) + Qw^2 b \sin\left[w\left(\tau - R + r_0 + b\sin(w\tau)\right)\right] \tag{7.14}$$

in dimensionless variables. Essentially, the problem is now described by three parameters: the compactness $w = \omega_i/\omega_m$, the interior amplitude $b = B/R_\star$, and the coupling strength Q, which describes the absorption of sound waves in the mantle.

The Eq. 7.14 is solved numerically for some simpler limit cases and the Poincaré map of the solution exhibits some remarkable features. Even though the unperturbed (undriven) system is linear and has a phase portrait without singular points the appearance of *weak chaos* can clearly be seen. The basic mechanism of weak chaos is, that the driving oscillator detunes the eigenfrequency of the driven oscillator. This mechanism depends, of course, on the amplitude as well as on the strength of the oscillation. The shifted frequency can be a rational multiple of the driving frequency, and rational tori, called Kolmogorov–Arnol'd–Moser tori, are created by the perturbation, and furthermore, chaotic orbits occur.

The application of this driven one–zone stellar oscillator to the problem of irregularities of AGB-star lightcurves gives rise to a family of equations which are fascinating by their own right, however, the connection with real lightcurves seems to be doubtful. The considerations of [Icke *et al.* 1992] demonstrate that the motion of the gas elements around the photosphere can be very complicated. However, as the preceding chapters have shown, dust plays an essential role in the dynamics of the CDS. A description of the dynamics in the sense of [Icke *et al.* 1992] must include the effects of dust, therefore, the dynamical behaviour will be even more complicated but also more realistic. The effects of dust could be implemented with a respective acceleration term in the equation of motion, at least as a 0^{th} order approximation. The driven one–zone stellar oscillator including dust is certainly a model that can account for a more thorough understanding of the dynamical phenomena in CDS and will be subject of future research.

7.5 Conclusions

Theoretical lightcurves of carbon–rich long–period and Mira variables are presented.

Based on dynamical models of CDS, which include time–dependent hydrodynamics and a detailed treatment of the processes of formation, growth and evaporation of carbon grains (cf. Paper I), frequency–dependent radiative transfer calculations have been carried out which yield the synthetic lightcurves of these dust shell models.

It is demonstrated how the complex interplay among the processes of dust formation and growth, hydrodynamics and thermodynamics decisively influences the short–scale behaviour as well as the long–term course of the lightcurves. The dust component plays the key role in producing features, such as intermediate extrema and secondary periods, which similarly occur in observed lightcurves. Thus, *multiperiodicity*, in principle, is a mechanism that could explain the observed shift in the amplitude of the lightcurves. This mechanism provides a rather natural explanation for the observed behaviour.

In turn, if the multiperiodicity number is determined from observations it provides a very restrictive additional constraint for theoretical model calculations. From the model calculations we also know that the final outflow velocity is linearly correlated with the overabundance of carbon to oxygen, cf. Figs. 4.12 and 6.14 and [Winters 1994] for the case of stationary dust driven winds. Most of the values of the final outflow velocities derived from observations lie in the range between 10 and 30 km s^{-1}. With respect to the theoretical calculations this result limits the carbon overabundance of AGB stars to values of ≤ 2.0, cf. Fig. 6.14. Given a certain value of the outflow velocity the overabundance of carbon to oxygen is fixed within a range of $\pm$ 0.2. Since the fundamental pulsational period of an object can be very accurately determined by observations, hence, the parameter most sensitive to the model calculations, can be provided by observations of the object which is intended to be modeled. Comparing the resulting spectra or visibilities of theoretical calculations should then allow to determine stellar parameters, such as luminosities and temperatures, which are not directly accessible to observations.

The comparison between our theoretical lightcurves and the observations shows that our simple coupling of the dynamical dust shell calculations and the radiative transfer calculations is a promising approach to understand the optical appearance of LPVs and Miras. Thus, although the models presented here are still preliminary, theoretical modelling has been improved to reduce the gap between theory and observation. A first step has been taken towards the construction of consistent models which give a reliable physical interpretation of observations.

On the observational part a simultaneous monitoring of LPVs and Miras in a wide spectral region with an appropriate temporal resolution is desirable to improve the observational data base and to allow a detailed comparison with improved theoretical model calculations in the near future.

Chapter 8

Further applications of the dynamical models

In this chapter we want to treat some side aspects of the present work which are either test cases for the numerical calculations or could serve as germs for future research, e.g. the application of the present code to another type of objects.

8.1 Model calculations in the adiabatic limit case

The model calculations including a consistent treatment of dust formation growth and evaporation so far were exclusively calculated in the limit case of *isothermal* shocks. The present section is devoted to calculations in the other limiting case: the limit case of *adiabatic* shocks. This will serve us either as a test for the accuracy of our numerical scheme and also as an interesting example for the separation of dust formation and pulsation. Calculations in the limit case of adiabatic shocks have been presented and discussed by other authors, e.g. [Wood 1979], [Willson and Hill 1979], however, these models were calculated without the influence of dust or at least they lack the detailed treatment of dust formation and growth, and therefore the decisive influence of the dust complex on the dynamics is neglected.

Before we present the results we want to recall some equations from elementary shock wave theory, e.g. [Landau and Lifshitz 1987].

8.1.1 Some results from elementary shock wave theory

Discontinuities can move with velocities different from the gas flow velocity. Here, we consider a fixed coordinate system and define v_n as the gas velocity normal to the surface of discontinuity and v_s as the velocity of the surface itself. Then,

$u = v_n - v_s$ will be the velocity of the gas relative to the discontinuity. If we have the case that the discontinuity propagates along the direction of the gas flow we have $v_n = 0$ and hence, $u = -v_s$.

A subscript 1 denotes quantities describing the unperturbed gas, i.e. the gas into which the discontinuity moves (upstream, preshock). Correspondingly, a subscript 2 refers to the post–shock gas behind the discontinuity.

Across the surface of discontinuity the laws of mass, momentum and energy conservation can be applied, e.g. [Zel'dovich and Raizer 1966], which yield

$$\begin{aligned} \rho_1 u_1 &= \rho_2 u_2 && (8.1)\\ p_1 + \rho_1 u_1^2 &= p_2 + \rho_2 u_2^2 && (8.2)\\ \epsilon_1 + \frac{p_1}{\rho_1} + \frac{u_1^2}{2} &= \epsilon_2 + \frac{p_2}{\rho_2} + \frac{u_2^2}{2} \ , && (8.3) \end{aligned}$$

where p, ρ, and ϵ denote pressure, density, and internal energy of the gas, respectively. The Eq. (8.1) describes the existence of a continuous mass flux across the shock front. The equality of the forces exerted on the gas on both sides of the discontinuity is expressed by Eq. (8.2), i.e. a continuous momentum flux crossing the shock front. In the absence of external energy sources, the internal energy ϵ is the result of the compressive work done on a certain fluid element, which is expressed by Eq. (8.3).

If we introduce the mass flux density j and the specific volume $V = 1/\rho$, we get from Eq. (8.1)

$$\rho_1 u_1 = \rho_2 u_2 = j \ , \tag{8.4}$$

and hence, $u_1 = jV_1$ and $u_2 = jV_2$. Substituting this into Eq. (8.2) we obtain

$$j^2 = \frac{p_2 - p_1}{V_1 - V_2} \ . \tag{8.5}$$

Since j^2 is always positive, two possibilities arise: $p_2 > p_1$, $V_1 > V_2$, or $p_2 < p_1$, $V_1 < V_2$. The first case corresponds to stable compression waves that result from an increase of entropy. This is the case that actually occurs in realistic shocks [Landau and Lifshitz 1987]. Rewriting Eq. (8.3) in the form

$$\epsilon_1 + p_1 V_1 + \frac{1}{2} j^2 V_1^2 = \epsilon_2 + p_2 V_2 + \frac{1}{2} j^2 V_2^2 \ , \tag{8.6}$$

and replacing j^2 by Eq. (8.5) we get

$$\epsilon_2 - \epsilon_1 = \frac{1}{2}(p_1 + p_2)(V_1 - V_2) \ . \tag{8.7}$$

This equation is called *shock adiabatic* or *Hugoniot relation*. If we now turn to the case of shock waves in a perfect gas with a constant value of the specific heat γ, which is the case valid for the present work, we can write the internal energy as

$$\epsilon = \frac{pV}{\gamma - 1} \ , \tag{8.8}$$

and insert this equation into Eq. (8.7). We obtain

$$\frac{V_2}{V_1} = \frac{(\gamma+1)p_1 + (\gamma-1)p_2}{(\gamma-1)p_1 + (\gamma+1)p_2} \ . \tag{8.9}$$

Using the equation of state for an ideal gas we can rewrite Eq. (8.9) in terms of the ratio of the temperatures across the shock front

$$\frac{T_2}{T_1} = \frac{p_2(\gamma+1)p_1 + p_2(\gamma-1)p_2}{p_1(\gamma-1)p_1 + p_1(\gamma+1)p_2} \ . \tag{8.10}$$

For the case of very strong shock waves for which $p_2 \gg p_1$ and $p_2 \gg (\gamma + 1)p_1/(\gamma-1)$ the preceding equations can be simplified to give

$$\begin{aligned} \frac{T_2}{T_1} &= \frac{p_2(\gamma-1)p_2}{p_2 p_1 \left[\frac{(\gamma-1)}{p_2}p_1 + (\gamma+1)\right]} \\ &= \frac{(\gamma-1)}{(\gamma+1)}\frac{p_2}{p_1} \ , && (8.11) \\ \frac{V_2}{V_1} = \frac{\rho_2}{\rho_1} &= \frac{(\gamma-1)}{(\gamma+1)} \ . && (8.12) \end{aligned}$$

This means that the value of the temperature behind the shock can have large values and is only bounded by the ratio of the densities. In contrast, the densities attain a constant value, for the case of a monoatomic gas with $\gamma = 5/3$ this value is $\rho_2/\rho_1 = S = 4$.

In the next section we want to compare these theoretical results with the results of our numerical calculations.

8.1.2 Results

Figure 8.1 shows the radial structure of Model No. 2, cf. Tabs. 8.1 and 8.2 at the beginning of the pulsational cycle. In detail, the Fig. 8.1 shows

upper panel: the hydrodynamical velocity u (solid line), and the velocity of sound u_s (dotted line, both l.h.s. ordinate), and the temperature in radiative equilibrium or dust temperature T_d (dashed line, r.h.s. ordinate),

2nd panel: the logarithm of the density ρ (solid line, l.h.s. ordinate), and the acceleration due to radiation pressure on dust α in units of the gravitational acceleration (dashed line, r.h.s. ordinate),

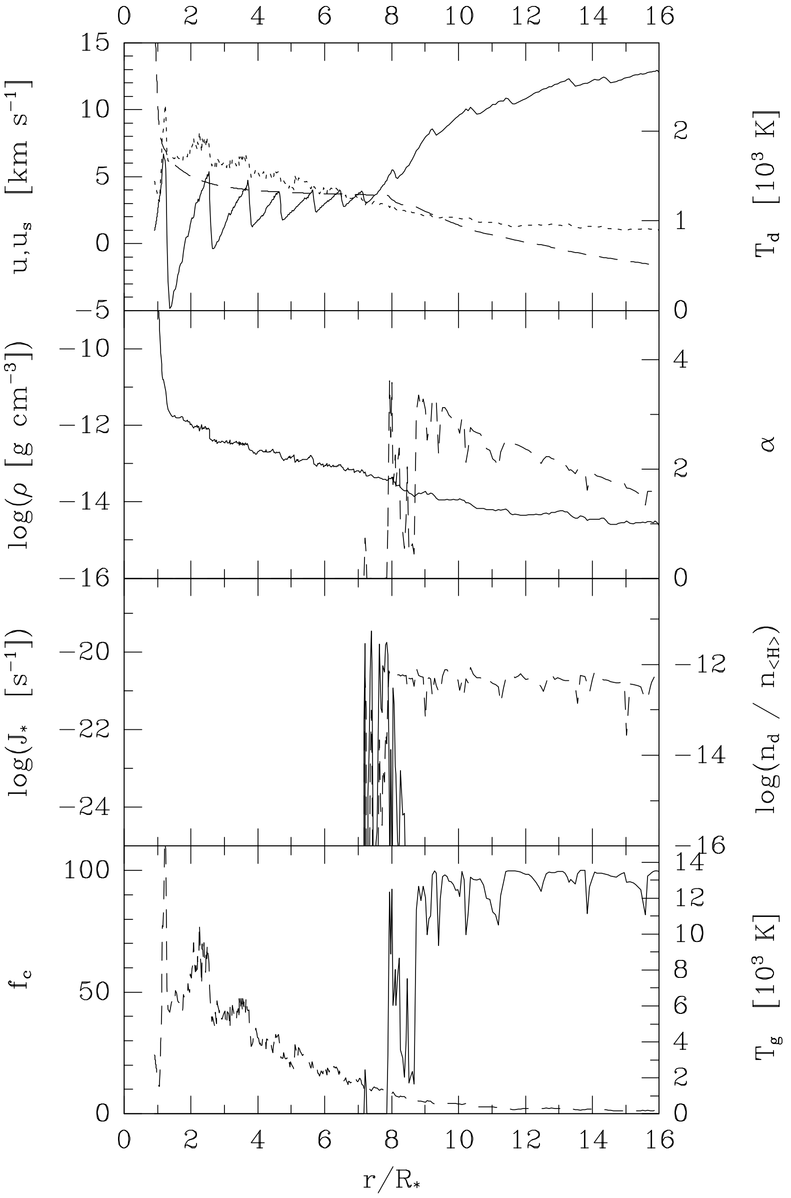

Figure 8.1: Radial structure of a model calculated in the limit case of adiabatic shocks, shown for Model No. 2 of Tabs. 8.1 and 8.2

3rd **panel:** the logarithm of the nucleation rate $J_\star$ (solid line, l.h.s. ordinate), and the logarithm of the number of dust grains per H–atom $n_d/n_{<H>}$ (dashed line, r.h.s. ordinate),

lower panel: the degree of condensation f_c (solid line, l.h.s. ordinate), and the gas temperature (dashed line, r.h.s. ordinate). The degree of condensation is given in % .

For these calculations we do not have a unique temperature structure but have to decide between the temperature of the dust, which is assumed to be in equilibrium with the radiation field, and the temperature of the gas which is strongly influenced by the compression of the shock waves. Due to the strong shock waves the gas temperature reaches values as high as 1.5 10^4K.

Nucleation of dust grains starts as far as $r \approx 7R_\star$, when the temperature T_g is sufficiently low. Due to the extreme sensitivity of the nucleation rate on temperature fluctuations the nucleation rate appears as a conglomerate of several spikes rather than one broad peak as in the models in the limit case of isothermal shocks. Dust growth also starts in the region around $\approx 7R_\star$, as can be seen from the rising peak in the degree of condensation.

Subsequently, radiation pressure acting on the newly formed dust grains drives the material through the sonic point, which is located at $\approx 8R_\star$. In turn, by the occurrence of dust formation, the dust complex determines the position of the sonic point. In these calculations pulsation alone is incapable to lift the material out of the gravitational field or even to accelerate the material to supersonic velocities. Until the pulsational shock fronts reach the dust forming region, they are already strongly damped and, therefore do not have a significant dynamical impact or a triggering function in the dust formation cycle. However in general, pulsation is needed to provide the overall conditions which allow dust formation. Pulsation provides the levitated atmospheric structure, i.e. a decreased density scale height, which is a necessary prerequisite for dust formation. To summarize, we find a spatial separation between the pulsation and the dust complex, i.e. they are dynamically decoupled. The decoupling also reflects in the structure of the outer shell where we find a vanishing discrete, onion–like structure, and the CDS appears to have more or less the structure of a purely dust–driven stationary wind, cf. Sec. 5.2.5.

Table 8.1: Parameters of the initial hydrostatic models for the calculations in the adiabatic limit case

No.	$T_\star$	ϵ_C/ϵ_O	$L_\star$	$R_\star$	$M_\star$	P	Δu	R_{inner}
1	2600	1.80	10000	492	1.0	650	2.0	0.91
2	2450	1.50	7500	479	1.00	388	1.0	0.91

To compare our numerical results with the results from the shock wave theory, cf. Sec. 8.1.1, we have extracted the following values from our data file, which belong to the innermost strong shock front: $T_1 = 6728$K, $\rho_1 = 1.5810^{-12}$g cm^{-3}, $p_1 = 0.69$ dyn cm^{-2}, $T_2 = 11520$K, $\rho_2 = 5.8610^{-12}$g cm^{-3}, $p_2 = 4.42$dyn cm^{-2}.

Inserting these values into Eq. (8.11), we get for the ratio of the temperature a value of 1.71, for the r.h.s, i.e. basically the ratio of the pressure values, 1.58. The ratio of $\rho_2/\rho_1 = 3.69$, compared to a theoretical value of 4. Thus, we find a good agreement between the theory and our numerical results, and have further confirmation that the code functions correctly.

Table 8.2: Resultant quantities of the model calculations in the adiabatic limit case

No.	$\dot{M}$	u_∞	ρ_D/ρ_G	$L_{\star,min}$	$L_{\star,max}$	Remarks
1	2.0 10^{-4}	16.7	4.5 10^{-3}	8773	11430	$n_P = 1$
2	1.5 10^{-4}	15.7	2.7 10^{-3}	7158	8503	$n_P = 1$

Comparing the results of the calculations in the adiabatic limit with the corresponding calculations in the isothermal limit, cf. Tabs. 4.4 and 6.2, we find that the mass loss rates are considerably increased due to the lack of radiative losses. Since in the adiabatic limit case no cooling occurs in the post–shock region the whole shock energy is used to levitate the atmosphere, hence, models calculated in the limit case of adiabatic shocks have a smaller density scale height than the corresponding models in the isothermal limit, and hence, the adiabatic models have a higher mass loss rate. Due to the radial structure of the gas temperature dust formation is not so effective compared to the isothermal models, and thus, the outflow is accelerated only to considerably lower velocities. However, the increased density structure surmounts this effect, and the mass loss rates are nevertheless increased. The difference of our calculations to the calculations of [Wood 1979], who presented models in the limit case of adiabatic shocks without dust, is mainly the input of mechanical energy. In Wood's calculations the rest position of the piston has been rather far below the photosphere compared to the present calculations, which result in the disastrous mass loss rates of up to $10^{-2} M_\odot yr^{-1}$ of his models.

The range of application for models in the limit case of adiabatic shock seems to be mostly in theoretical considerations. The densities in the innermost region of the CDS are high enough to allow for effective cooling, such that the adiabatic shock approximation should be a rather poor assumption for the inner region. We will come back to this point in some more detail in the next chapter, when we discuss the basic assumption of our modelling approach. The models calculated in the adiabatic limit show an extended chromospheric region, which definitely should have observable consequences. Unfortunately, there seems to be no evidence from observations for chromospheric activity of evolved late–type stars, e.g. [Pasquini *et al.* 1990]. Indeed, [Jura 1986c] reports that there exists an anti–correlation between the existence of a dust shell and the occurrence of a chromosphere. However it seems to be not quite clear, whether this anti–correlation does not stem from the simple fact, that a chromosphere is in principle not observable in the presence of a thick dust shell.

8.2 Models for RV Tauri star–like objects

The motivation for these calculations is twofold. First, it is interesting to consider the calculation of models with rather high effective temperatures and short pulsational periods from a purely "numerical" point of view, and to find out, whether under these unfavourable conditions dust formation and growth is actually possible. Second, there is a long lasting discussion in the literature about the cause for the shape of the lightcurves of RV Tauri stars, cf Sec. 8.2.1. Since these objects are also known to have carbon– as well as oxygen–rich dust shells, the question arises whether we could make any contributions to solve the problem with our approach to model circumstellar shells.

8.2.1 Introduction

RV Tauri stars are pulsating variables of population II–type with periods between 30 and 150d, e.g. [Raveendran 1989]. Their spectral type is F, G or K. The luminosities of these objects range from a few $10^3 L_\odot$ up to $10^4 L_\odot$ [Gillet *et al.* 1990]. Infrared broad–band photometric observations of the prominent RV Tauri star R Scuti and other RV Tauri stars, e.g. [Gehrz 1972], show a mid–infrared excess due to thermal emission by dust located in a cool shell surrounding the star. As pointed out by [Goldsmith *et al.* 1987] it is likely that RV Tauri stars may have multiple dust shells and they suggest that mass loss and grain formation may be a sporadic rather than a continuous phenomenon. By fitting blackbody functions to their optical and near–infrared data [Goldsmith *et al.* 1987] derived effective temperatures, and furthermore, inner dust shell radii. The stellar temperatures range from $\approx$ 4200K up to $\approx$ 6800K, the inner dust shell radii from 2.1 up to 30 $R_\star$. In most cases the inner radius of the shell was found to be equal to the condensation radius of the assumed grain material, which implies that the object is undergoing current mass loss. In certain cases a larger inner radius suggested that the mass loss events are sporadic. [Baird 1981] fits model atmospheres to high resolution optical spectra in order to derive effective temperatures at different lightcurve phases. The temperature range he determines is in agreement with [Goldsmith *et al.* 1987]. An abundance analysis for the prominent object AC Her performed by [Baird 1981] yields a metallicity (excluding CNO) of $Z = 0.06 Z_\odot$. The carbon abundance was found to be enhanced relative to the other metals with $\epsilon_C = 0.2\epsilon_{C,\odot}$.

Although, many details are known, a consistent general picture has not yet been established and also the evolutionary status of RV Tauri objects seems not completely certain. It has been first postulated by [Baird 1981, Baird 1982] that RV Tauri objects are post–AGB stars.

This is supported by an investigation of [Jura 1986b] who finds that it is likely that RV Tauri stars initially had a mass of 1 $M_{\odot}$ and lose mass at a rate of $\approx 10^{-5} M_{\odot} yr^{-1}$. However, based on IRAS 60 μm flux measurements, he concludes that the current mass loss rate at $\approx 10^{14} cm$ is about a factor of 100 smaller than the value of $10^{-5} M_{\odot} yr^{-1}$ that is derived for the cold material at $\approx 10^{16} cm$. Assuming an outflow velocity of 10 km s^{-1} the time for the dust to travel to the radius where it emits at 60 μm is 500 yrs, which he defines as the typical duration of the RV Tauri phase. Finally, [Jura 1986b] concludes that RV Tauri stars are the low mass, and at least for some cases the low metallicity portion of those stars that make the transition from the AGB phase to the white dwarfs. Due to their previously rather high mass loss rates it is likely that many of them will become planetary nebulae.

The main common characteristic feature of RV Tauri stars is the occurrence of alternating deep and shallow minima in the lightcurves. This behaviour is mostly derived from optical lightcurves, e.g. [Gillet 1992], the observational material for longer wavelengths seems to be too incomplete to reveal a similar shape, e.g. [Shenton *et al.* 1992]. On the basis of their lightcurves RV Tauri stars are subdivided into two classes, RVa and RVb. The former show a constant mean brightness, whereas RVb appear to have cyclically varying brightnesses.

Several theoretical attempts have been made to explain this characteristic behaviour of the lightcurves, cf. [Tuchman *et al.* 1993] and references therein. A frequently used explanation is based on the resonance between the first overtone and the fundamental mode of the stellar pulsation. Another hypothesis suggests that the alternation is caused by a coupling between the radial oscillation and large amplitude convective motions. If a certain convective mode has twice the period of the pulsational driving mode, the first subharmonic of the pulsation mode may be enhanced, as observed in the spectra of e.g. R Sct and AC Her. It has also been suggested that the pulsation of RV Tauri stars could be in a doubling bifurcation or even in a chaotic regime [Kovács and Buchler 1988, Buchler *et al.* 1991, Kovács and Buchler 1993]. The recent calculations of [Tuchman *et al.* 1993] support the pulsational resonance hypothesis. They have performed linear nonadiabatic pulsation calculations for an extensive range of input parameters. Thereby, they find that the observed periods and temperatures of RV Tauri stars can be reproduced by models of masses less than 0.8 $M_{\odot}$ with thin envelopes ($< 0.01 M_{\odot}$) and luminosities of a few thousand $L_{\odot}$. In most of their models the value of the fundamental mode is twice that of the first overtone, which leads them to conclude that a possible resonance between the modes is responsible for the alternating minima.

High dispersion IUE observations of Mg II reveal that the atmospheres of RV Tauri stars are passed by decelerating shocks [Shenton *et al.* 1992]. Emission stimulated by strong shock waves has long been postulated, e.g. [Baird 1982, Baird 1984, Gillet *et al.* 1989, Gillet *et al.* 1990]. High resolution spectroscopic observations of sodium lines presented by [Lèbre and Gillet 1991b] show that the blueshifted component has an unchanged profile for at least one luminosity period, whether the other sodium component shows a complex profile which varies strongly during the period. They attribute this spectroscopic behaviour to the propagation of two shock waves per luminosity period within the so called sodium layer. Thereby, they confirm an earlier work [Lèbre and Gillet 1991a] where they show that the outer atmospheric layers do not pulsate in phase, but that the pulsation mechanism seems to produce running waves which travel through the atmosphere.

However, due to the lack of a consistent modelling of the pulsational zones as well as of the circumstellar shell the interpretation of these observational findings are sometimes rather vague.

8.2.2 Results

Figure 8.2 shows the radial structure of the model which is calculated in the isothermal limit case at the beginning of the pulsational cycle. Although decisive parameters such as the luminosity have been varied extremely the overall global structure of all models is fairly good represented by Fig. 8.2.

In detail, Fig. 8.2 depicts

upper panel: the hydrodynamical velocity u (solid line), and the velocity of sound u_s (dotted line, both l.h.s. ordinate), and the temperature T (dashed line, r.h.s. ordinate),

2nd **panel:** the logarithm of the density ρ (solid line, l.h.s. ordinate), and the acceleration due to radiation pressure on dust α in units of the gravitational acceleration (dashed line, r.h.s. ordinate),

3rd **panel:** the logarithm of the nucleation rate $J_\star$ (solid line, l.h.s. ordinate), and the logarithm of the number of dust grains per H–atom $n_d/n_{<H>}$ (dashed line, r.h.s. ordinate),

lower panel: the degree of condensation f_c (solid line, l.h.s. ordinate), and the mean particle radius r_m (dashed line, r.h.s. ordinate).

It has to be pointed out that the models presented here are calculated with solar abundances except for the carbon abundance, whose ratio to the oxygen abundance is chosen as a free parameter. A reduced metallicity, as suggested by the example of AC Her, cf. [Baird 1981], would result in a less effective dust formation process and thus, in a less effective acceleration of the outflow, and possibly in a vanishing of the outflow. However, from observations little is known about the actual outflow velocities of objects that show current grain formation.

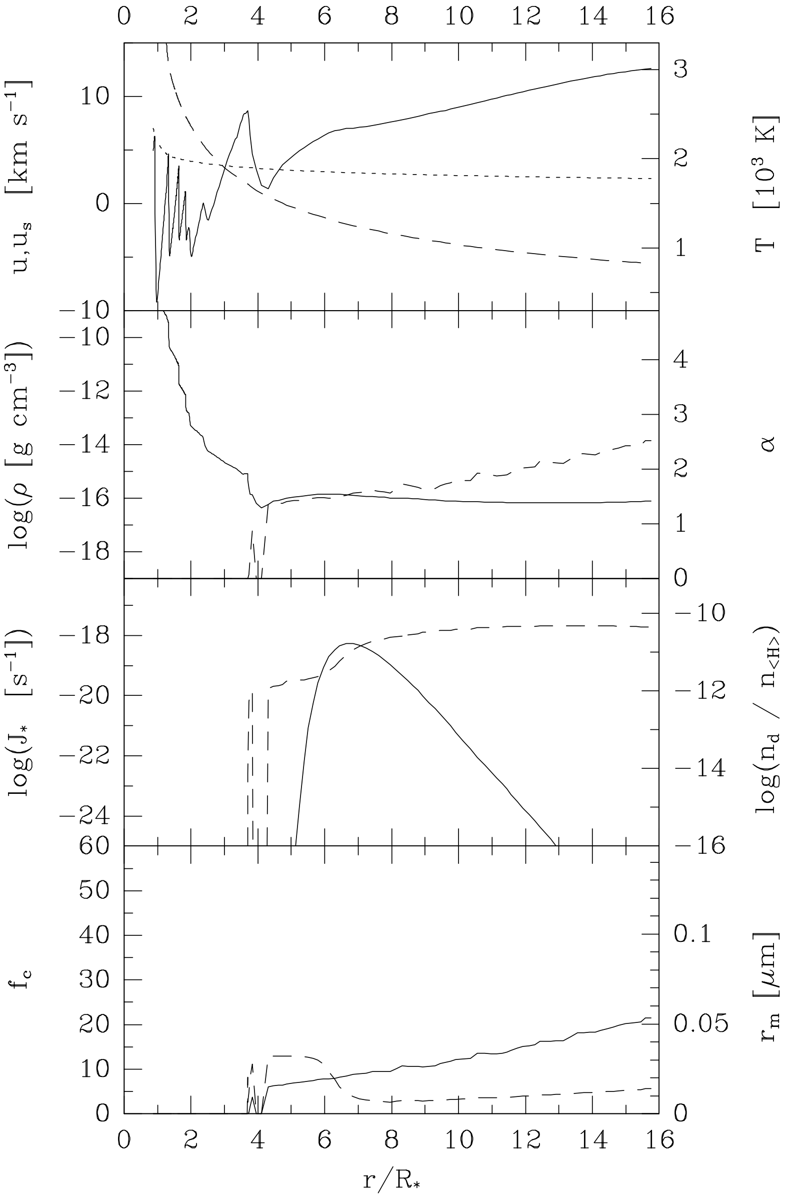

Figure 8.2: Radial structure of Model no. 1, cf. Tab. 8.3 and 8.4, which has parameters typical for RV Tauri stars

---

The radial structure of the models can be characterised by an inner zone with strong shock waves and an outer region, which contains a broad radial interval of dust formation, as can be seen from the broad peak of the nucleation rate in Fig. 8.2.

Table 8.3: Parameters of the initial hydrostatic models for the calculation of the RV–Tauri–like objects

No.	$T_\star$	ϵ_C/ϵ_O	$L_\star$	$R_\star$	$M_\star$	P	Δu	R_{inner}
1	4500	1.80	20000	232	0.8	100	5.0	0.91
2	3500	1.80	8000	242	0.7	75	5.0	0.87
3	3500	3.00	8000	242	0.7	75	7.0	0.91

The broad peak of the nucleation rate is due the comparatively high densities and low temperatures at radii around $8R_\star$. This hydrodynamical structure is an immediate consequence of the shock propagation in these atmospheres. Effective dust formation is a rather sporadic phenomenon in these models, i.e. n_P is large. Then, a strong shock is formed which travels outwards and considerably levitates the atmosphere. In the wake of the shock front dust formation and *growth* is possible, and radiation pressure on dust becomes high enough to accelerate the outflow. Dust growth is even possible at radii larger than 12 $R_\star$, which can be seen at the increase of the degree of condensation. For a long period of time, till the next shock propagates through the atmosphere, no back–warming is present that could hinder dust formation. Thus, the temperatures remain low between the passing of two shock fronts, which favours dust growth.

Table 8.4: Resultant time averaged quantities of the RV–Tauri-like model calculations

No.	$\dot{M}$	u_∞	ρ_D/ρ_G	$L_{\star,min}$	$L_{\star,max}$	Remarks
1	$7.5\ 10^{-7}$	12.0	$8.2\ 10^{-4}$	20410	25130	
2	$8.5\ 10^{-7}$	11.0	$7.5\ 10^{-4}$	8137	9177	
3	$3.3\ 10^{-9}$	7.0	$4.9\ 10^{-4}$	–	–	

There are two conclusions that we can draw from these calculations:

- Although dust is present in the circumstellar shells of RV Tauri stars it is very unlikely that a similar mechanism as presented in Chapter 7 is responsible for the characteristic shape of the lightcurves as one could have suspected before. The hydrodynamical and thermodynamical conditions prevailing in RV Tauri stars are not favouring effective dust formation. Thus, dust cannot account for a periodic influence of the lightcurves. One has also to keep in mind that we have performed the calculations assuming solar abundances. Reducing these abundances would yield even less dust.
- The calculations serve as a test case for similar calculations to be done

for oxygen–rich Miras and LPVs. We have shown that even in the case, where nucleation is less effective and occurs at large radii, dust is able to drive the stellar outflow. Thus we would suspect for oxygen–rich Miras and LPVs, that the non–linear phenomena described in the previous chapters are difficult to detect since dust formation is not as effective as in the respective C–stars, supposed only homogeneous dust growth is taken into account [Dominik *et al.* 1993].

Despite the fact, that no positive results could be achieved, the investigation of RV Tauri stars could be a promising side aspect of future research, especially with improved dust formation, i.e. taking into account the formation of core–mantle grains. Up to now, for these objects no consistent model calculations exist.

8.3 Model calculations with a general non-homogeneous nucleation rate – The formation of PAHs

8.3.1 PAHs in astrophysical environments

As early as in 1983 [Keller and Sedlmayr 1983] mentioned problems with the classical nucleation theory to describe the formation of circumstellar dust and proposed that a chemical pathway description via the formation of polyaromatic hydrocarbons (PAHs) would lead to a more realistic description of the formation of solids in astrophysical environments.

In 1984 [Léger and Puget 1984] proposed an explanation for the so far "unidentified IR emission features" of interstellar dust. They considered the heating of small grains by UV–photon absorption and estimated the IR emission. Under these conditions they found graphite to be one of the only solids that would not sublimate. Due to the large abundance of hydrogen, H–atoms are expected to be bound to the rim of the graphitic planes. Analyzing the whole grain emission spectrum they conclude that those small grains of carbon should be considered as large polycyclic aromatic molecules rather than as amorphous graphite.

The first theoretical approach to the problem of PAH formation can be found in [Keller 1987], where a general nonhomogeneous nucleation theory is proposed. Thereby, the formation of a carbon grain is described by a chain of chemical reactions, which starts at the most abundant molecule acetylene, C_2H_2, passes through the nucleation barrier and ends up with a grain, a macroscopic particle. The nucleation barrier is defined by the first reaction, the so called *critical reaction*, with a negligible destruction rate, and hence is the first reaction far from chemical equilibrium. However, for large cluster sizes the structural differences become more and more unimportant and also the reaction rates become more and more independent of the cluster size. Thus, for large clusters the situation is sufficiently described by kinetical equilibrium. For small clusters, in contrast, the destruction rates dominate and the reactions can be approximately described by chemical equilibrium. Hence, it is possible to determine the pathway up to the critical reaction only by calculating the reactions in chemical equilibrium.

[Keller 1987] considers the reaction

$$A_i + B_i \longrightarrow A_{i+1} + C_i \quad , \tag{8.13}$$

where A_i denotes a carbon–molecule (A_1 is acetylene, A_N the macroscopic grain), B_i denotes the growth substance and C_i is a byproduct. He shows that the quantity

$$J = k_i \; \overset{\circ}{n}_{A_i} \; n_{B_i} \left(\frac{n_{A_i}}{\overset{\circ}{n}_{A_i}} - \frac{n_{A_{i+1}}}{\overset{\circ}{n}_{A_{i+1}}} \right) \tag{8.14}$$

can be conceived as the rate of consumption of A_1 and formation of A_N, and hence as the grain formation rate. The quantity k_i denotes the reaction rate, n is the particle density and $\overset{\circ}{n}$ the density in chemical equilibrium.

Based on these considerations a numerical scheme has been developed [Keller and Dominik, private communication], which calculates the grain nucleation rate via the formation of such small PAHs, cf. next section for the application of this routine in dynamical calculations.

[Frenklach and Feigelson 1989] presented the solution of reaction network under the conditions prevailing in circumstellar carbon–rich shells to account for the formation of PAHs and for the first and second ring closure. They found that PAH production occurs at temperatures within the interval between 1100K and 900K and that the formation of a relevant amount of PAHs requires particularly dense and slow stellar winds.

Recently, in a series of papers [Cherchneff *et al.* 1991], [Cherchneff and Barker 1992], [Cherchneff *et al.* 1992], and [Cherchneff *et al.* 1993] extended and modified the work of [Frenklach and Feigelson 1989]. Thereby most important is the application of a more realistic underlying hydrodynamical model, where they claim to include the effects of shock waves based on calculations by [Bowen 1988a]. These investigations confirm that PAH formation yields are extremely sensitive to the gas density and temperature, and furthermore, are found to be less abundant than inferred from observations of late–type stars. They conclude that PAH formation is unlikely in the wind itself but should be initiated already in the region of the photosphere.

8.3.2 Results

As a test calculation with a nucleation rate constructed according to Eq. (8.14) we present a model with $M_\star = 1.0 M_\odot$, $T_\star = 2450$K, $L_\star = 3.010^4 L_\odot$, $\epsilon_C/\epsilon_O = 1.25$,

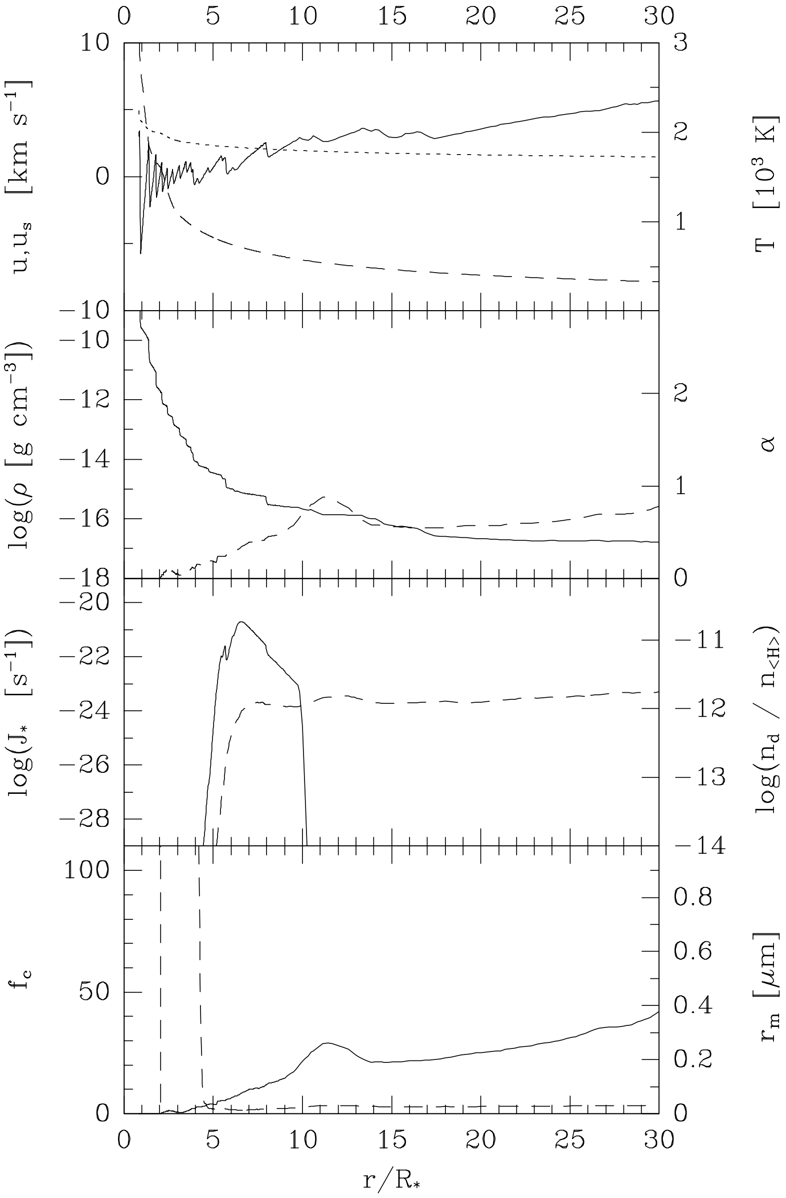

Figure 8.3: Radial structure of a model calculated with a nucleation rate according to [Keller 1987]

P = 776d, and $\Delta u_P = 3kms^{-1}$. It has to be mentioned that we only treat the *formation* of small PAHs, for the calculation of the growth rate it is still assumed that we have amorphous material as in all the previous calculations. This is done due to the fact that we have no treatable reaction network at hand, but nevertheless allows to study dust formation and growth, starting at considerably lower temperatures. Furthermore, it is rather likely that larger dust grains do not consist of pure PAHs but that PAHs serve as seeds for the condensation of further structures.

In order to obtain meaningful values of the nucleation rate the density of hydrogen has to be arbitrarily fixed to be $n_H = 2n_{H_2}$, cf. [Gail and Sedlmayr 1987a], since downstream from a point of $\approx$ 1500K the thermal equilibrium value of n_H/n_{H_2} drops rapidly to values of 10^{-8} in the condensation zone with no effective reactions to increase the value again. However, since atomic hydrogen is most important for the nucleation rate, the abundance of H has to be suitably chosen.

Figure 8.3 shows the radial structure of the model which is calculated in the isothermal limit case at the beginning of the pulsational cycle. In detail, Fig. 8.3 depicts

upper panel: the hydrodynamical velocity u (solid line), and the velocity of sound u_s (dotted line, both l.h.s. ordinate), and the temperature T (dashed line, r.h.s. ordinate),

2nd panel: the logarithm of the density ρ (solid line, l.h.s. ordinate), and the acceleration due to radiation pressure on dust α in units of the gravitational acceleration (dashed line, r.h.s. ordinate),

3rd panel: the logarithm of the nucleation rate $J_\star$ (solid line, l.h.s. ordinate) according to [Keller 1987], and the logarithm of the number of dust grains per H–atom $n_d/n_{<H>}$ (dashed line, r.h.s. ordinate),

lower panel: the degree of condensation f_c (solid line, l.h.s. ordinate), and the mean particle radius r_m (dashed line, r.h.s. ordinate).

The calculation shows that dust formation can start effectively around 800K or between 6 and 8 $R_\star$, where a considerably broad peak of the nucleation rates develops. Again, dust formation and pulsation are separated in the sense that pulsation has no direct impact on dust formation but prepares the surrounding physical conditions by e.g. levitating the atmosphere. Due to the low densities dust growth is not so effective compared to calculations with the classical nucleation rate, and hence the mean particle radius as well as the degree of condensation remain small. Nevertheless, the resultant acceleration due to radiation on dust suffices to drive the wind through the sonic point to supersonic velocities.

Although chemically inconsistent, the calculation is valuable with respect to the planned models of oxygen–rich shells. There, condensation is expected to occur at similar low temperatures as in the calculations presented here. Thus, one should expect that also in the case of oxygen–rich circumstellar wind the interplay between pulsation and the dust complex is able to drive the stellar outflow. In the models we have calculated so far with the nucleation rate according to [Keller 1987] dust formation is a sporadic phenomenon due to a reduced effectivity of the formation of dust grains, i.e. the models have large multiperiodicity numbers $n_P > 5$ or even behave irregularly, i.e. even for a long model run no apparent integer–valued multiperiodicity number could be found. Thus, the dynamical effects presented for C–rich environments, e.g. dust–induced shocks or exterior κ–mechanism, will be smoothed and not be so clearly detectable if they indeed occur, due to a less "violent" process of dust formation.

Chapter 9

Discussion of the approximations

The main part of this section is devoted to a discussion of some approximations inherent in our modelling approach, in order to clarify which further improvements are necessary and whether it is possible to incorporate them.

9.1 The limit case of isothermal shocks

In order not to complicate the situation too much we have considered isothermal shocks in this first approach. This fundamental approximation of the models presented here means, that the postshock temperature of the gas equals its preshock value.

The strong simplification is mainly motivated by the aim of this paper devoted to investigate the complex interplay between the dynamical structure of the shell and the dust component which best is revealed on the basis of a simple model where the important coupling mechanisms are not obscured by other effects.

Thus, to justify that our approach already yields a reliable description of the principle interaction mechanisms, a key question is, whether cooling in the postshock region in the inner parts of the CDS is fast enough to be approximated in the isothermal limit case and if it is effective enough to allow for substantial dust formation. Once the dust is formed, it decouples from the gas and the grain temperature equals the radiative equilibrium temperature. Then the grains are unaffected by sudden changes of the gas temperature, since the energy exchange between the dust and the radiation field dominates the exchange between the dust and the gas, cf. [Gauger *et al.* 1990].

However, first calculations with a consistent treatment of the dust complex including either the parametrized cooling laws given by [Bowen 1988a] or modified cooling laws, cf. below, indicate that under the specific physical conditions prevailing in the circumstellar dust shell

i) the cooling functions yield the rates necessary to reach the isothermal postshock temperature values and,

ii) especially in the inner dustforming region of the CDS, cooling occurs indeed fast enough to allow for a dust formation process in a similar manner as described in the previous Chapters.

In fact, the model calculations presented in [Gauger *et al.* 1993, Gauger *et al.* 1994b, Gauger *et al.* 1994a] which also include calculations with a Rosseland mean absorption coefficient for the gas according to [Scholz and Tsuji 1984], show that

i) the discrete structure of the CDS is conserved,

ii) the prominent shocks still result from the strong coupling of the dust complex to the hydrodynamics,

iii) the backwarming effect still determines when and where new dust particles are formed,

iv) the post–shock cooling region occurs only as a rather narrow peak, a spike, behind the shock front, if modified cooling laws compared to [Bowen 1988a] are applied. In fact, these calculations very closely resemble the case where isothermal shock fronts are assumed.

The very efficient cooling of these modified cooling laws can be understood by the following consideration. [Bowen 1988a] assumed that the cooling function Q is proportional to $\rho(T_g - T_{eq})$. However considering the complete system of radiation hydrodynamics, the respective energy exchange terms in the thermal energy equation for the gas and the radiative energy equation are proportinal to $\kappa_g\, \rho(J - S_g)$, where J is the zeroth moment of the radiation field ($4\pi J/c$ is the radiation energy density) and S_g is the source function of the gas. Assuming LTE, the source function term is given by the Kirchhoff–Planck law, applying the Stefan–Boltzmann law yields and exchange term proportional $\kappa_g\, \rho(T_{eq}^4 - T_g^4)$.

Thus, cooling appears to be much more effective as in the approach of [Bowen 1988a] even if a constant gas opacity is taken into account. Using a variable gas opacity yields larger values of κ_g in the innermost region compared to the previously assumed constant value, which results in an effective acceleration of the material already at smaller radii. Thus, the photospheric density is reduced and in total a decreased mass loss rate results [Gauger *et al.* 1993]. However, the overall radial structure of such a model differs only slightly from a model calculated in the limit case of isothermal shocks.

Summarizing we can state, that the assumption of isothermal shocks does not affect the principle dynamical effects in the inner part of the CDS, and it is justified to use this limit case to reduce the computational time, if the investigation is aimed to study the principal dynamical phenomena.

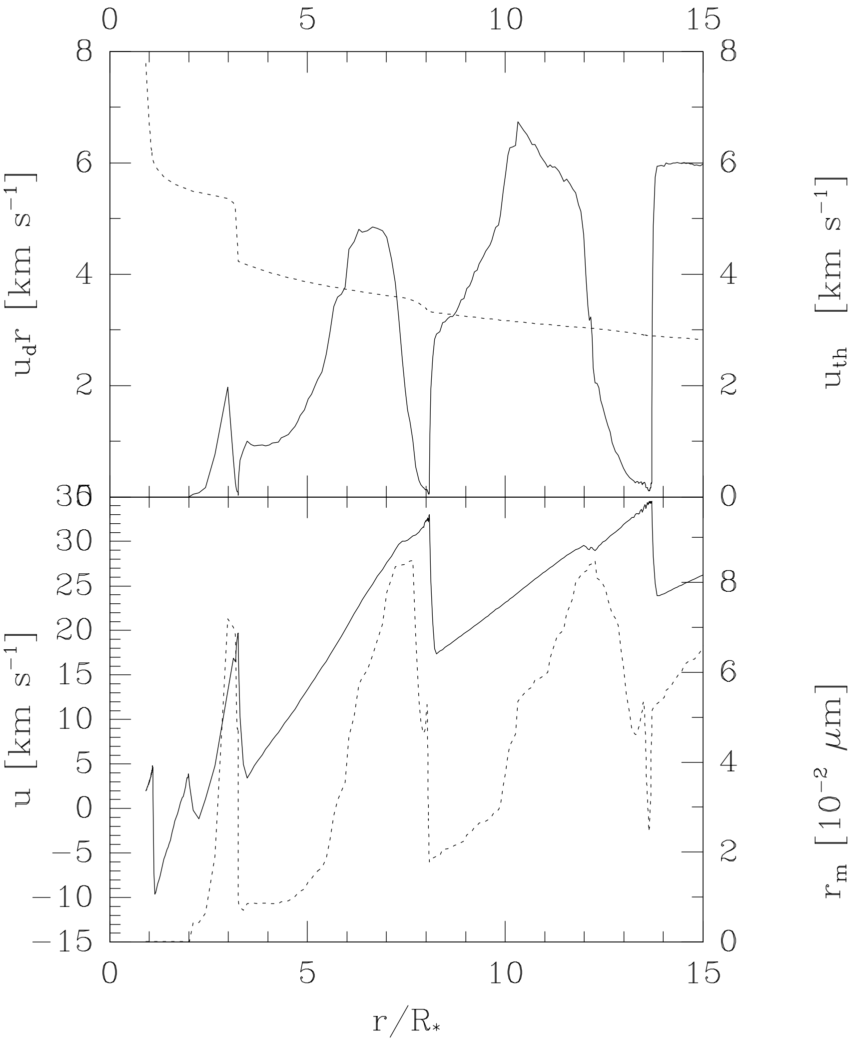

Figure 9.1: upper panel: Radial structure of the equilibrium drift velocity u_d (solid line) and the thermal velocity u_{th} (dashed line). Lower panel: for comparison, radial structure of the gas velocity u (solid line) and the mean particle radius r_m (dashed line)

9.2 The neglect of drift

To calculate the quantity α, the ratio of the radiative to the gravitational acceleration, cf. Eq. (2.15), we assume the grains to be completely momentum coupled to the gas. However, one cannot expect the dust grains in the CDS would also be position coupled to the gas. To get an estimate of the error introduced by treating the gas-dust mixture as a single component fluid, it is necessary to consider the equilibrium drift velocity u_d which is the limit value for the drift velocity if the net acceleration of the particle is zero, i.e. the sum of the frictional acceleration g_{fric}, the gravitational acceleration g and the radiative acceleration g_{rad} equals zero.

By using Eq. (2.43) for the temperature dependence of the Rosseland mean of the extinction coefficient of spherical amorphous carbon grains the radiative acceleration can be written as

$$g_{rad} = 5.9\,\frac{L_\star}{4cr^2}\,\frac{a_0^3}{m_0}\,T_D \quad , \tag{9.1}$$

where a_0, m_0 and T_D are the monomer radius, the monomer mass and the dust temperature, respectively.

According to the expression, which is given by [Yorke 1988], the deceleration due to friction can be written as

$$g_{fric} = -\frac{\pi a_0^2}{m_0}\frac{1}{N^{1/3}}\rho u_d \sqrt{u_d^2 + (\frac{4}{3}\,u_{th})^2} \quad , \tag{9.2}$$

where N is the number of monomers contained in a dust grain and

$$u_{th} = \sqrt{\frac{8kT}{\pi m_H \mu}}$$

is the thermal velocity.

Inserting these expressions into the equation

$$g_{fric} = \frac{GM_\star}{r^2} - g_{rad} \tag{9.3}$$

one gets a quadratic equation for u_d^2, which can be solved analytically for a given hydrodynamical structure and a specified particle radius. For an estimate we use the mean particle radius.

A typical radial course of u_d (solid line) is shown in the upper diagram of Fig. 9.1 for model E at phase $t = 0.0P$. For comparison, also the thermal velocity u_{th} (dashed line) is depicted. The lower diagram, Fig. 9.1b, shows the gas velocity u (solid line) and the mean particle radius r_m (dashed line).

As a consequence of the small mean particle size, for all models u_d is at most of the order of the thermal velocity u_{th} within the dustforming region (cf. Fig 9.1b).

Thus, our result justifies the neglect of drift and, furthermore, is in good agreement with the results of e.g. [Sopka *et al.* 1985] and [Dominik *et al.* 1989]. Based on self–consistent stationary models [Dominik *et al.* 1989] furthermore investigate the effect of drift on the growth rate which on the one hand causes a reduction of the growth rate since the drifting dust particles move faster than the gas. On the other hand the collisional rates for drifting particles are higher which increases the growth rate. They demonstrate the effect of drift on the resulting particle size distribution function in the wind. It results in a considerable narrowing of the distribution function, a reduction of the amount of rather large and very small particles.

[SOPKA *et al.* 1985] performed drift broad–band submillimeter observations to derive mass loss rates from evolved stars, by using an expression for the drift velocity derived by [GOLDREICH AND SCOVILLE 1976, KWAN AND LINKE 1982]

$$u_{drift} = \left(\frac{L_\star \, u_{gas} \, Q_r}{\dot{M}_{gas} \, c} \right)^{1/2} \quad , \tag{9.4}$$

where Q_r denotes the radiation pressure efficiency. Inserting values taken from other observations for u_{gas} and $\dot{M}_{gas}$ and using a value of 0.05 for Q_r (twice as much as the value in [KWAN AND LINKE 1982]) they derive drift velocities for their sample of objects which are only of the order of a few km s^{-1}.

9.3 The chemistry of the gas phase in circumstellar dust shells

In contrast to the chemistry of the interstellar medium the chemistry of circumstellar dust shells is characterized by a wealth of peculiarities: with respect to chemistry considerations the physical conditions, e.g. temperature and density, range over a large interval. The time evolution preceeds on comparatively short time scales, and the influence of the interstellar UV–field favours the presence of photochemistry in the transition region to the ISM, i.e. in the outer layers of the CDS. Due to sufficiently high densities at sufficiently low temperatures carbon–rich CDS offer the advantage to synthesize complex organic molecules. Furthermore, due to these physical conditions CDS are well known to be the site of greatest importance for cosmic grain formation, which we discussed in detail in the previous chapters. CDS are the major source of element enrichment and dust grains for the ISM, returning enriched material at a rate of $\approx 1 M_\odot yr^{-1}$, thus, playing a key role in the galactic chemical evolution.

For recent reviews on astrochemistry see [GUSTAFSSON 1989, TURNER 1989, OMONT 1991].

For the present calculations we have assumed all species of the gas phase to be in chemical equilibrium. Thus, only the local temperature and thermal pressure, the thermochemical data and the elemental abundances are needed as input parameters, and complications by the unknown specifica of certain reaction mechanisms are avoided.

However, it is well–known, that strong departures from chemical equilibrium could be induced by

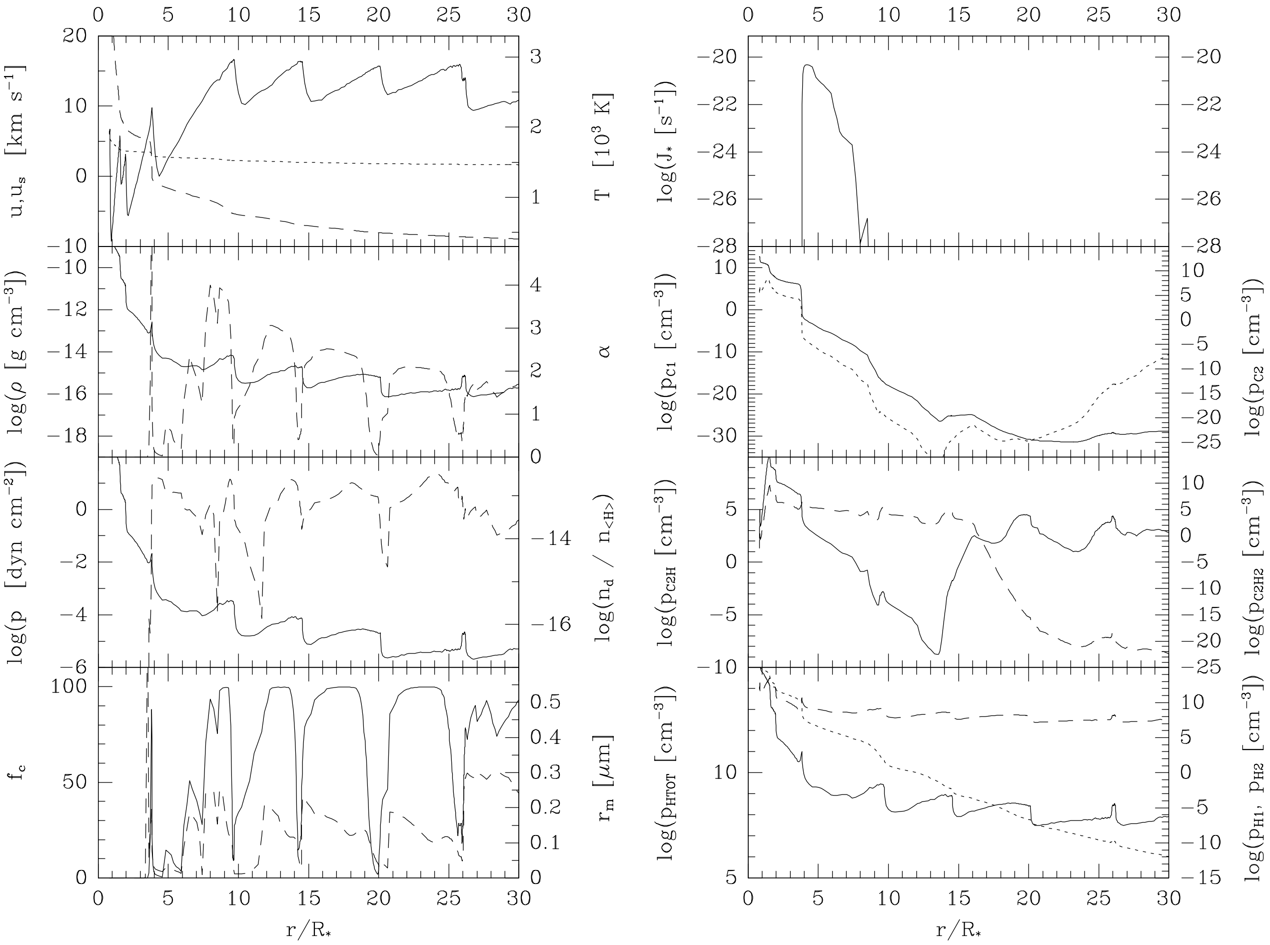

Figure 9.2: Radial structure of the hydrodynamical and chemical quantities of a typical model calculation: $T_* = 2500$ K, $L_* = 1\ 10^4\ L_{sun}$, C/O = 1.34, $M_* = 1.0\ M_{sun}$, P = 370 d, $\Delta u_p = 6$ km s^{-1}

---

i) the periodic passage of strong shock waves which cause the dissociation of molecules. E.g. calculations of interstellar shocks have shown [Hollenbach and McKee 1979] that electron impact completely dissociates H_2 for shock velocities as large as 50 km s^{-1} at densities not exceeding $1\,10^2 cm^{-3}$, and for densities larger than $1\,10^4 m^{-3}$ already at shock velocities around 25 km s^{-1}. On the other hand shocks are able to initiate reactions in the heated post–shock gas, which would not occur otherwise.

ii) the expansion velocity u of the CDS of typical 10 – 20 km s^{-1}, which leads to a dilution of the atmosphere on a time scale $\tau_{dil} = r/u$ and, hence, reduces the rates of the kinetical reactions, resulting in a chemical time scale τ_{chem}, which is possibly longer than τ_{dil}, thereby causing a freeze–out of certain species in the outer regions.

iii) the presence of strong UV-fields which cause photo–ionization and –dissociation of atoms and molecules.

Strong UV-fields are caused by chromospheric activity, mainly observed in M-giants of early spectral-type. However, there exists an anticorrelation between the observed infrared-excesses and the presence of a chromosphere [Jura 1986c]. By analyzing $CaII$ emission of a sample of 65 evolved late–type giants and supergiants [Pasquini *et al.* 1990] deduced a correlation between chromosperic surface activity and stellar mass. They found 5 –10 $M_{\odot}$ stars in their He–burning phase to show the highest level of activity whether low–mass stars (up to $\approx 2M_{\odot}$) appear to be rather quiet. Hence, we conclude that in CDS around stars showing effective dust formation no strong UV-fields are present and, thus a departure from chemical equilibrium by UV-fields can be regarded as an effect of minor importance for the present investigation.

Calculations of a non-equilibrium chemistry around M-stars [Goeres *et al.* 1988, Beck *et al.* 1992] show that for this kind of neutral-radical chemistry the abundances of the nucleating species do not deviate severely from their equilibrium values. [Beck *et al.* 1992] have investigated in detail the influence of UV–fields on the chemistry in the dust–forming region. They demonstrate that if the flux of the UV photons drops below a certain limit value the chemistry approaches chemical equilibrium if the velocity is assumed constant (1 km s^{-1}) throughout the atmosphere. However in general, these calculations confirm that due to UV radiation most chemical reactions are far from chemical equilibrium, i.e. in principle non–equilibrium has to be regarded as the standard situation in circumstellar shells. Furthermore, non-equilibrium calculations for the oxygen–rich circumstellar shell of α Ori show that despite the presence of a chromospheric UV field the supersaturation ratios of SiO and Fe become high enough to allow the condensation of these species. Taking into account these results, the anti–correlation between the presence of a CDS and the occurrence of a chromosphere derived from observations by [Jura 1986c] could be interpreted in the following simple way: the presence of a dust shell hinders the detection of chromospheric activity.

Corresponding calculations for C-stars based on hydrodynamical structures derived from stationary wind calculations are currently under investigation [Patzer *et al.* 1993], and show that the most abundant species contributing to the nucleation can be roughly regarded to be in chemical equilibrium under negligible UV field conditions.

The comparison between the abundances derived from observations of IRC +10216 and those calculated from an equilibrium chemistry [Glassgold and Huggins 1986] (and references therein) give a first hint that this is indeed the case. Chemical equilibrium calculation for IRC +10216 performed by [Lafont *et al.* 1982] are in reasonable agreement with the few most abundant molecules.

However, these calculations have to be regared with skepticism since they omitted dust formation!

We conclude, that the adoption of chemical equilibrium for calculating the densities of the nucleating species is an approximation which yields a reliable basis for treating the problems we are interested in our context. Taking into account that the CPU-time required to produce *solely* one consistent dust shell model as described above, is typically 25 to 30 hours on a CRAY X-MP already demonstrates the difficulty if a non–equilibrium chemistry has to be included. In fact it shows, that at this stage, the consistent incorporation of a non-equilibrium chemistry into the model calculations is beyond today's computing facilities.

However, reasonable results of preliminary calculations on a level similar to Chap. 7 could be expected. Namely, the performance of non–equilibrium chemistry calculations *on* a hydrodynamical structure given by the path of selected Lagrangian elements through the atmosphere. Respective calculation are currently performed and the results will shed more light on the chemical structure of Miras and LPVs.

To get an idea of the radial chemical structure occuring from the present models we have plotted in Fig. 9.2 the course of the partial densities of the contributing species as well as the hydrodynamical structure. Note the different scaling of the ordinate of the "chemistry plots" in the right column. Basically, two things are worth to be mentioned. First, the strong extraction of carbon from the gas phase due to dust formation up to $\approx 15R_*$, and second, that C_2H_2 is indeed the most abundant molecule in the dust–forming region.

9.4 The radiative transfer problem

Usually, the radiative transfer problem is solved using the semi-analytical method of [Lucy 1971], [Lucy 1976] which yields a reliable radiative equilibrium temperature structure at every instant but does not provide a spectrum, which would be necessary for a more detailed comparison with the observations.

Already the model calculations in Chap. 7, which were based on the calculations with the detailed frequency–dependent radiative transfer of [Winters *et al.* 1994a] on a given hydrodynamical structure, and which therefore, can be conceived as a first level of improvement have led to results in considerable agreement with observations. However, a closer coupling would be desirable.

In principle, a closer coupling between time–dependent dynamics and frequency–dependent radiative transfer could be achieved by performing an iteration scheme similar to that described in [Winters *et al.* 1994a] for the iteration between radiative transfer and stationary hydrodynamics. Simple CPU–time requirements however suggest that such a procedure certainly is not applicable from the beginning with the hydrostatic model. Assuming not too great a change in the temperature structures (T_g, T_d) resulting from the radiative transfer calculations the procedure at most could be performed approximately each 500 steps during one period (assuming typically 10^4 time steps per period) of the evolved hydrodynamical model.

To account for the correct contribution of cold dust to the spectral energy distribution the model has to be sufficiently extended. In the stationary case this extension usually is of the order of 10^4 stellar radii.

Extending the dynamical models could be done by increasing the number of grid points. This is the simplest method. However, it is limited on the one hand by the available computer memory and on the other hand by the time it takes for the material to reach the chosen outer boundary, i.e. a model run can be performed only for a finite interval of pulsational periods, typically $\approx$ 200 P, until the model disintegrates. Thus, the extension performed by inserting new grid points yields circumstellar shells of only a few 10^2 stellar radii.

A more elegant method would be to extend the model by analytic expressions, i.e. if for instance at a certain radius the velocity jump at the shock front has become sufficiently small, the radial velocity course is continued by a *constant* velocity. The continuation of other quantities could be somewhat more difficult. Therby, extensions of 10^4 $R_\star$ could be easily achieved.

A combination of both methods is planned to be used for the calculation of spectra of Miras and LPVs in the near future.

9.5 The piston approximation

We have simulated the pulsation of the star by a sinusodial moving inner boundary. From our experience, we would suspect that the shape of the variation of the innermost radius point, e.g. a saw-toothed shape, would not alter the results too much, similar results are reported by [Bowen 1988a].

Considerable progress could be achieved if the course of the radial movement of the piston could be deduced from consistent calculations of the pulsation driving region. By solving the nonlinear system of radiation hydrodynamics for the case of Cepheids [Dorfi and Feuchtinger 1991] have performed such kind of calculations. Unfortunately, due to the lack of an appropriate treatment of time–dependent convection, corresponding calculations for the case of Miras are not yet available.

Chapter 10

Summary of results

In this chapter we give a concise summary of the results and "theses" of this work. It allows a quick access to the major topics of this dissertation. The intention of this chapter is really to summarize the key points of this work than to serve as an extended abstract. The **number in brackets** after each item indicates the section, where detailed information can be found.

- Dust plays the key role in the determination of the structure of the circumstellar dust shell. The numerical model calculations reveal the intimate relation between the dust complex, hydrodynamics, thermodynamics, and chemistry (4.2).

- Due to the comprehensive modelling approach, which includes a detailed treatment of dust formation, growth, and evaporation at least three properties arise, concerning the radial structure of the dust shell, which are inherent in almost all model calculations (4.2):

  i) the interior pulsation causes a levitation of the atmosphere due to the deposition of mechanical energy by the dissipation of strong shock waves, which travel periodically through the atmosphere.

  ii) the dust particles are concentrated in distinct layers, and the CDS exhibits a shell or onion like structure. Hence, the dust grains are inhomogeneously distributed, which is a major difference to all previous calculations by other authors, who assumed a homogeneous distribution of the dust.

  iii) the influence of the dust opacity on the thermodynamical structure results in a substantial back–warming effect. This yields an increase of the temperature up to some hundred K behind the shock front, which causes a limitation of the time interval where dust formation is possible, and in some cases even causes an evaporation of dust particles at the inner edge of the dust shell.

- Dust formation is revealed to take place as a two–step process (4.3,4.3.2):

  i) in a first step, the interior pulsation triggers dust formation, i.e. it defines the onset of nucleation of new dust particles by providing appropriate low temperatures.

  ii) in a second step, the newly formed grains are overrun by a pulsational shock wave, which compresses the material and provides enhanced densities. Hence, the grains find excellent conditions for growth.

- Once the dust is formed, it completely determines the atmospheric structure. The compression by the pulsational shock causes an avalanche growth phase, which in turn by a self–accelerated mechanism produces a new strong shock wave which runs through the atmosphere. Depending on the actual model, the pulsational shock front remains as a strongly damped remnant between the dominating dust–induced shock fronts (4.3.1).

- The resulting grain size spectra show, that the dust grains remain rather small ($< 1\mu$m) compared to calculations for stationary dust driven winds. This is caused by the interior pulsation, which limits the time interval of a certain element of matter in a region with favourable growth conditions. The shape of the spectra also show some peculiarities, since they reflect the history of the fluid parcel on its trajectory through the atmosphere. Thus, the spectra could consist of distinct peaks, which refer to multiple phases of growth in this element (4.3.3).

- The ratios of dust to gas in the resulting outflow of the model calculations are in good agreement with observations. They show a confinement to a narrow range of values, i.e. are almost independent of the basic input parameters, a result that is also known from observations (4.3.5).

- The analysis of the influence of the model parameter shows, that the overabundance of carbon to oxygen ϵ_C/ϵ_O is the most sensitive parameter. For sufficiently high values of ϵ_C/ϵ_O the development of a dust–induced shock *each* pulsational period follows, these models are called single–periodic and are referred to with a multiperiodicity number of $n_P = 1$. The overabundance does not only influence the dynamical behaviour of the models, as summarized below, but has also decisive influence on observable quantities, such as outflow velocity and mass loss rate. A more detailed correlation is given below (4.4.1).

- From the calculation of a larger grid of single periodic models a convenient correlation between carbon overabundance and pulsational period for the calculation of further single periodic models is derived. This rule is quite handsome, because it allows the prediction of the general behaviour of the model to be calculated (4.4.2).

- The finding of the aforementioned rule demonstrates, that the other model parameters are only of minor influence, if a reasonable range of values is assumed (4.4.2).

- For sufficiently luminous models it is shown in detail, that an instability in the CDS arises, which causes the development of strong shock waves, and a massive, slow wind occurs even without the support of mechanical energy by the piston. The occurrence of this effect is demonstrated to rely on the following two prerequisites

  i) the density scale height of the initial hydrostatic model must be sufficiently low, such that dust formation and growth may occur already in this initial phase.

  ii) the interaction between a substantial amount of dust and the thermodynamics by the backwarming due to the dust opacity leads to the development of pressure driven waves, which initiate an avalanche growth process.

  Due to key role of the dust opacity, we call this effect *exterior* κ*–mechanism* (5.2.2).

- Due to the self–regulated dust formation process, the exterior κ–mechanism provides a self–maintaining process which drives a stellar outflow. The formation of shocks turns out to be a strictly periodic phenomenon, which defines a characteristic time scale or *eigenperiod* of the dust forming stellar atmosphere (5.2.3).

- In the case of less effective dust formation or in the case of a priori neglected interaction between the dust complex and thermodynamics, the well known solution of a "stationary" dust driven wind is found. This fact gives rise to the proposition that stationary dust driven winds in general are dynamical unstable, similar to the case of winds from hot luminous stars, where these instabilities are already well established (5.2.5).

- An anti–correlation between the overabundance of carbon to oxygen and the eigenperiod of the dust forming system is found. An increase of condensable material causes a shortening of the eigenperiod (5.3).

- The luminosity is correlated nonlinearly with the eigenperiod. Long eigenperiods are found for models with either very high luminosities or with luminosities just above the critical limit luminosity, below which no outflow develop without additional support by e.g. mechanical energy (5.3).

- A further non–linear effect arises due to the consistent treatment of the whole system of hydrodynamics, thermodynamics, and dust formation. For suitable chosen model parameter, the radial structure of the circumstellar dust shell repeats after a time $t_1 = n_P P + t_0$, where P is the period of the piston, n_P is an integer–valued number. The piston itself performs a pure sinusoidal movement without any overtone modes taken into account.

We call this effect *multiperiodicity*, the number n_P is called the multiperiodicity number (6.2).

- At least two different mechanisms were revealed to account for multiperiodicity:

  i) The first mechanism is based on the periodic damping of the pulsational shock waves, which then do not suffice to trigger dust formation anymore. The damping, in turn, occurs due to the physical conditions of the ambient medium, which are mainly determined by the dust formed in a previous cycle (6.2.1).

  ii) The second mechanism occurred in a demonstrative model calculation, which exhibits three different phases of dynamical processes taking place. The first and the third phase are characterized by substantial backwarming which serves as a switch to decide whether dust formation is taking place or not. The second phase is characterized by a pure dust–induced shock, without direct support from the interior pulsation and phase–shifted to it (6.2.4).

- The variation of mechanical energy input was to found to have only a marginal influence on the multiperiodicity number (6.3.1).

- For models with and even for model without apparent eigenperiod, rules were established, that allow to preselect or to predict the behaviour of a further model to be calculated, once one model of the respective series showed a regular behaviour (6.3.1).

- The overabundance of carbon to oxygen was found to be the most sensitive parameter influencing multiperiodicity. It was shown, that it can be used to "tune" a model to a desired multiperiodicity number or even to remove multiperiodicity and to produce a "regular" model with $n_P = 1$ (6.3.2).

- A clear linear correlation was found between the final outflow velocity and the overabundance of carbon to oxygen. In fact, by analyzing the whole sample of theoretical models, with $n_P = 1$ and > 1, it was found that the multiperiodic models were confined to the region of low outflow velocities and respective low overabundances. This correlation can be used to derive carbon overabundances, from observational determination of the final outflow velocity, even for objects with rather thick dust shells.

Assuming 30 km s^{-1} as an upper boundary for the final outflow velocity of typical carbon stars, then these objects have carbon overabundances not exceeding the value of 2.0 (6.3.3).

- The ratio of dust to gas, plotted as a function of the carbon overabundance for the whole sample of theoretical models, was found to be confined to the same narrow range of values as suggested by observations (6.3.3).
- Theoretical lightcurves of the dynamical dust shell models are presented (7.3).
- The lightcurve of an exemplary model calculation with $n_P = 1$ shows up to have intermediate structures, "bumps", similar to those observed in real LPVs. The occurrence of these intermediate structures critically depends on the temporal evolution of the optical depth of the innermost dust layer. It is shown that the phase, where the intermediate structure shows up, can be associated with the formation of a new dust shell. Thereby, a rather natural explanation for these features occuring in real lightcurves is provided (7.3.2).
- Furthermore, it is shown, that the short wavelength radiation, which is seen in the phase, where the intermediate structure occurs, is mainly produced by the emission of photospheric gas. This result opens new perspectives for specific observations of the objects under consideration (7.3.2).
- Multiperiodicity also has a specific manifestation in the theoretical lightcurves. It shows up as a drift in the amplitude of the lightcurves, i.e. as a superposition of a longer period to an oscillation whose fundamental mode is provided by the period of the piston. A similar behaviour is observed in the lightcurves of real objects, e.g. R For (7.4).
- Preliminary calculations for RV Tauri–like objects have been performed. From the parameters known, these atmospheres of these objects are rather unfavourable for dust formation. It is shown, that, nevertheless, dust formation takes place and is able to drive a stellar outflow. However, since dust formation does not occur as massive as in respective LPVs, it is very unlikely, that the characteristic shape of the RV Tauri star lightcurves is significantly influenced by dust, as for instance in the calculations in Chapter 7 (8.2.2).
- Test calculations with a general non–homogeneous nucleation rate, which simulates the formation of small Polyaromatic Hydrocarbons (PAHs), have been performed, and show, that dust formation starts effectively around 800 K. The spatial intervals, where either pulsation or dust formation dominate, are well separated. The resultant acceleration of the material due to radiation pressure on dust suffices to maintain a stable outflow (8.3.2).

- Models with assumed radiation pressure on dust, which can be calculated with the code developed during this work as a simple limit case, are not appropriate to describe the circumstellar dust shells of Miras and LPVs. As a detailed treatment of dust formation is neglected in these models, they are contaminated with free parameters, which hinder a quantitative comparison with observations (3.3).

- The formation of pre–shocks in the innermost dust–free region of the CDS can be sufficiently explained within the framework of linearized fluid equations. Depending on the ratio between the period of the interior pulsation and the cut–off period one, or more, or even none pre–shock develops (3.2.4).

Chapter 11

Outlook

Consistent dynamical models of circumstellar dust shells around Miras and Long-period variables including the formation, growth and evaporation of amorphous carbon grains have been presented. The necessity of taking into account *all* relevant physical interactions to understand these fascinating objects has been stressed more than once. Although a lot of promising results have been achieved, still more remains to be done to arrive at a thorough understanding of this late stage of stellar evolution.

Most of the models presented here were calculated in the limit case of isothermal shocks. Post–shock cooling can be taken into account, and first demonstrative calculations show, that the circumstellar dynamics are very similar to the case described in the present work. However, a representative grid of models with post–shock cooling has to be calculated, to investigate how e.g. the correlation between the final outflow velocity and the carbon overabundance is influenced quantitatively. It will also very interesting and important to calculate the optical appearance of these dust shell models.

To investigate further the optical appearance, besides lightcurves, also spectra and visibilities should be calculated to compare the theoretical models with different kinds of observations. This will also imply to achieve a closer coupling of the present code to the detailed radiative transfer program, to take into account the back–reaction of the radiative transfer on the thermodynamical structure.

As stated above we have considered the formation of amorphous carbon grains. Although very likely, amorphous carbon grains will not form exclusively and moreover not purely, such that other components, e.g. PAHs, should be taken into account. However, this brings us to the point of the chemistry calculations. Until the consistent incorporation of a non–equilibrium chemistry becomes possible due to the increase of computer power, at least an extended equilibrium chemistry should be used to improve the determination of the gas phase.

In fact, most Miras and LPVs are oxygen–rich. The investigations, so far devoted exclusively to carbon–rich objects, have to be extended to oxygen–rich objects as well. A crucial question will be the investigation about the nature of the grains formed in these atmospheres. Preliminary calculations show, that pure SiO or Fe–grains are not able to maintain a continuous outflow. For the case of M–stars the consideration of heterogeneous growth is of decisive importance. The formation of dirty or core–mantle grains presumably will suffice to drive the winds from these type of objects. These investigations will yield the first results from consistent time–dependent calculations about the internal structure and chemical composition of the grains injected into the interstellar medium. In this case, however other driving mechanisms, apart from pulsation, could be of great influence to support the outflow, e.g. radiation pressure on molecules.

Since dust is not expected to have that dominant role in M–stars as it plays for C–stars, the question has to be addressed, whether effects like multiperiodicity or the exterior κ–mechanism also occur in the oxygen–rich situation. Due to the experiences made with carbon–rich atmospheres, it is very likely, that in fact multiperiodicity is the standard situation of oxygen–rich Miras and LPVs.

A great improvement for the models, carbon–rich as well as oxygen–rich, will be the coupling of the code to a program for the stellar interior to achieve a more reliable description of mechanical energy input by pulsation.

However, if these more or less “academical” investigations are completed we arrive at the crucial, ultimate test: the modelling of a concrete object. This is a great challenge, since, due to the consistent approach, there are only a few free model parameters to vary. They must account for an extensive variety of observational facts that exist for some fairly good observed objects, e.g. mass loss rate, final outflow velocity, spectral energy distribution, brightness distribution, gas to dust ratio, etc.

If this test should fail, it will, nevertheless, yield some good estimates which input components still have to be improved, or which additional processes possibly should be taken into account. However, being optimistic, this test will be positive, and the theoretical model calculations could serve as a powerful tool to derive stellar parameters that are not directly accessible to observations. Furthermore, these calculations could be use to plan more specific observations of certain objects to improve even the observational material.

Apart from the points mentioned above, one should not forget, that numerical calculations still reveal just a small region of the possible set of solutions for a given dynamical system. Suitable mathematical methods to investigate the manifold of solutions should shed some more light on the complex dynamics of Miras and LPVs, and will help at a deeper and somewhat more general understanding of these systems. Furthermore, these methods should allow a final decision about the possible chaotic phenomena suspected to take place in these objects.

Though in this field of research, the future development and in particular the significance of certain problems are hardly predictable, however, the points listed above at least should describe the obvious and badly needed content of future theoretical research on Miras and LPVs.

Epilogue

Mechanisms of mass loss from late type stars have been the topic of this work. Circumstellar dust, revealed as the crucial ingredient to drive the mass loss, is copiously formed in the stellar outflow. Hence, we have investigated the origin interstellar dust. In fact, late type stars are the most important sources of fresh interstellar material. According to [Gehrz 1989], the input of dust to the interstellar medium (ISM) relative to all stars is achieved to about 35% by M–stars, to 32% by RLOH/IR–stars (radio luminous OH/IR–stars), and to 20% by Carbon stars. Only 8% is contributed by Supernovae, and only 0.02% by RV Tauri stars. [Gehrz 1989] estimates for galactic objects, that the total amount of mass lost e.g. by all M–stars sums up to 1.3–2.8 $M_\odot\ yr^{-1}$, and for C–stars 0.34–0.96 $M_\odot\ yr^{-1}$.

Surviving successfully the transition from the wind to the interstellar medium [Woitke *et al.* 1993], the dust, however, is subject to various physical processes and chemical reactions, once being in the ISM [McCray and Snow 1979].

The evolutionary picture of interstellar dust, which is now emerging, is again a cyclic one. Before being destroyed by interstellar shocks or being incorporated in solar system bodies, the particles are cycled back and forth through molecular clouds and diffuse clouds several times. Thereby, they undergo a variety of structuring processes: they are subject to grain–grain collisions, they are exposed to shocks from Supernovae, their surface is sputtered by the hot phase of the ISM, and they accrete atoms and molecules from the gas phase. [Mathis 1990] estimates that a typical parcel of dust and gas has been in and out of a molecular cloud due to the rotation of the galaxis at least every $3\,10^8$yr, or more than 10 times during its mean lifetime. A small silicate core captured within a molecular cloud accretes various ices and gradually builds up an inner mantle of organic refractory material, which has been produced by photoprocessing of the volatile ices. Because of their vivid evolution, the organic refractory mantle of the grains cannot be considered as a homogeneous substance but more or less as the layers of a tree trunk, where the innermost layers have been most irradiated and the outer parts contain rather fresh material.

Eventually, the grains are trapped in a collapsing cloud, which forms a presolar nebula. Again, the particles undergo a substantial metamorphosis during the aggregation, finally ending up, if not incorporated into a new sun or a planet, in asteroids, in comets, or as interplanetary dust particles (IDP). Nowadays, we are convinced, that the comet dust, the meteorites, and the IDPs we observe, originate from larger bodies in the interstellar dust 4.5 billion years ago, however, the details of this development are still not completely certain [GREENBERG 1989A].

The importance of this sample of interplanetary material can at least be demonstrated by two reasons. First, for the modern scientists meteorites and comets serve as witnesses of the initial cosmogonic, star forming process. It is now known, that meteorites contain a wealth of carbonaceous, and organic matter up to amino acids [CHYBA 1990], but also heavier elements such as Si, Mg, or Fe [GREENBERG 1989B]. Second, the Earth is still undergoing a bombardment by interplanetary material. Thereby, the current infall rate e.g. of intact organic carbon is estimated to $3.2\,10^8$g yr^{-1}, or 0.006 g cm^{-2} in 10^8 yrs [ANDERS 1989]. There have been serious efforts to suggest, that this organic matter played a vital role for the origin of life on Earth. In fact, if this infall rate has been partially increased to 10^{10}g yr^{-1} in the very early epoch of Earths development, then, the total current biomass of $\approx 6\;\,10^{\,17}$ g could be accreted in $\approx 6\;\,10^7$ yrs [WHITTET AND CHIAR 1993]. This strongly supports the idea about the extraterrestrial origin of life.

However, meteorites supply only a negligible fraction, $\approx\; 10^{-5}$, of the total carbon infall on Earth. By far most of the material is provided by interplanetary dust particles with diameters between 1 and 100 μm [ANDERS 1989]! These results follow from simple considerations about the behaviour of particles of different size in the terrestrial atmosphere. For instance, for very small particles, are known to be destroyed by photolysis. Particles, with masses more than 10^{-6}g, are eroded by ablation before the remainders are strongly heated by conduction and the organic material is destroyed; see Fig. 1 of [ANDERS 1989] for the intervals where matter can survive the infall.

There is another interesting point. We mentioned already that amino acids are found in meteorites, e.g. the Murchison meteorite, which fell down in Australia in 1969, contained at least 74 amino acids, i.e an excess of non–biological amino acids, which are not found on Earth [CHYBA 1990]. The atoms of individual amino acid molecule may be structurally arranged in two ways, such that both configurations are mirror images of each other. The resulting L– or D–isomers are called enantiomers[1]. Unequal mixtures of enantiomers cause an optically active substance since they rotate the plane of polarization of light in opposite directions. An equal mixture of enantiomers is called *racemic*. Terrestrial life is based almost exclusively on L–amino–acid isomers [CHYBA 1990]. Yet, no convincing explanation exists for this fact. However, very recently, [ENGEL *et al.* 1990] reported to have measured an excess of L–type alanine, an amino acid, in Murchison.

[1]from the Greek *enantios*: opposite

The finding of a meteoritic preference of L–amino acids would provide an explanation for terrestrial biology's choice. Furthermore, non–racemic mixtures of amino acids have been used as an indicator of biologically derived molecules. Does the excess of L–enantiomers in Murchison mean, that there are yet undiscovered mechanisms of abiotic synthesis of amino acids, or does it even arise evidence for extraterrestrial life ...

Again, this demonstrates, that dust and prerequisites of life are indeed closely connected. Apart, from the bombardment with dust in our everyday life, which nobody really notices, there is yet another beautiful manifestation of interplanetary dust. Consider yourself on the terrace of a charming cottage somewhere in the middle of nowhere with a large glass of cold german beer. Soon after evening twilight or shortly before dawn (if you did not drink too much), on a dark, moonless night a faint luminosity may be seen just above the horizon: the *zodiacal light*. This phenomenon is caused by the scattering of the sunlight by interplanetary dust particles concentrated in the ecliptic. Probably, the next morning after you have recovered from drinking, you may also want to read about the zodiacal light. Numerous publications appeared, which are concerned with this topic, e.g. [Dollfus 1989] and references therein, and also, the possibly most popular british astronomer B.H. May has devoted his studies to this phenomenon.[2] During this period, he wrote

No star can light our way
in this cloud of dark and fear.
But some day one day ...[3]

[2][Hicks, May & Reay 1972, 1974] He is perhaps better known as guitarist and vocalist of the british rock group QUEEN. It seems that he quitted astronomical research shortly before he finished his PhD ...

[3]Brian Harold May: Some day one day. From the album "Queen II", 1974, EMI Rec. Ltd.

Bibliography

[Alexander *et al.* 1983] Alexander, D. R., Johnson, H. R., and Rypma, R. L., 1983. Effect of molecules and grains on Rosseland mean opacities. *ApJ*, **272**, 773–780.

[Alksnis 1990] Alksnis, A., 1990. Variability of carbon stars. In Mennessier, M. and Omont, A., editors, *From Miras to Planetary Nebulae: Which Path for Stellar Evolution?*, pages 279–285, Editions Frontières, Gif sur Yvette Cedex.

[Allen 1973] Allen, C. W., 1973. *Astrophysical Quantities*. The Athlone Press, London.

[Anders 1989] Anders, E., 1989. Pre–biotic organic matter from comets and asteroids. *Nature*, **342**, 255–257.

[Baird 1981] Baird, S. R., 1981. AC Herculis, a metal–poor, carbon–enhanced RV Tauri star. *ApJ*, **245**, 208–218.

[Baird 1982] Baird, S. R., 1982. Kinematic and shock phenomena in the atmosphere of AC Herculis. *PASP*, **94**, 850–859.

[Baird 1984] Baird, S. R., 1984. Causes of anomalous line-splitting in RV Tauri stars. *PASP*, **96**, 72–77.

[Barnbaum *et al.* 1991] Barnbaum, C., Kastner, J. H., and Zuckerman, B., 1991. The mass range of carbon stars. *AJ*, **102**, 289–294.

[Beck *et al.* 1992] Beck, H. K. B., Gail, H.-P., Henkel, R., and Sedlmayr, E., 1992. Chemistry in circumstellar shells. I. Chromospheric radiation fields and dust formation in optically thin shells of M-giants. *A&A*, **265**, 626–642.

[Beichman *et al.* 1983] Beichman, C. A., Keene, J., Phillips, T. G., Huggins, P. J., and Wooten, H. A., 1983. Neutral carbon in the egg nebula (AFGL 2688). *ApJ*, **273**, 633–638.

[Berruyer and Frisch 1983] Berruyer, N. and Frisch, H., 1983. Dust-driven winds. I. A two-fluid model and its numerical solution. *A&A*, **126**, 269–277.

[Berthold 1894] Berthold, G., 1894. *Der Magister Johann Fabricius und die Sonnenflecken nebst einem Excurse über David Fabricus* . Verlag von Veit & Comp., Leipzig.

[Bertschinger 1986] Bertschinger, E., 1986. On the structure and stability of radiative shock waves. *ApJ*, **304**, 154–177.

[Bertschinger 1989] Bertschinger, E., 1989. The evolution of cooling flows: self-similar cooling waves. *ApJ*, **340**, 666–678.

[Bertschinger and Chevalier 1985] Bertschinger, E. and Chevalier, R. A., 1985. A periodic shock wave model for Mira variable atmospheres . *ApJ*, **299**, 167–190.

[Blackwell *et al.* 1980] Blackwell, D. E., Petford, A. D., and Shallis, M. J., 1980. Use of the Infra-red Flux Method for determining Stellar Effective Temperatures and Angular diameters; the Stellar Temperatue Scale. *A&A*, **82**, 249–252.

[Blanco 1989] Blanco, V. M., 1989. Carbon stars. *Rev.Mex.astr.Astrofis.*, **19**, 25–27.

[Boothroyd and Sackman 1992] Boothroyd, A. I. and Sackman, I.-J., 1992. Breakdown of the core mass-luminosity relation at high luminosities on the asymptotic giant branch. *ApJ*, **393**, L21–L24.

[Boothroyd and Sackmann 1988a] Boothroyd, A. I. and Sackmann, I.-J., 1988. Low–mass stars. II. The core mass–luminosity relations. *ApJ*, **328**, 641–652.

[Boothroyd and Sackmann 1988b] Boothroyd, A. I. and Sackmann, I.-J., 1988. The production of low–mass stars. IV. Carbon stars. *ApJ*, **328**, 671–679.

[Bottlinger 1919] Bottlinger, K. F., 1919. Über das δ Cephei–Problem . *Astron. Nachr.*, **210**, 33–44.

[Bowen 1988a] Bowen, G. H., 1988. Dynamical modelling of long-period variable star atmospheres. *ApJ*, **329**, 299–317.

[Bowen 1988b] Bowen, G. H., 1988. The mechanism of mass loss from pulsating cool stars. In Stalio, R. and Willson, L. A., editors, *Pulsation and mass loss in stars*, pages 3–25. Kluwer Academic Publisher.

[Bowen 1990] Bowen, G. H., 1990. Dynamical phenomena in pulsating star atmospheres. In Buchler, J. R., editor, *The Numerical Modelling of Nonlinear Stellar Pulsations*, pages 155–171. Kluwer Academic Publishers.

[Bowen and Willson 1991] Bowen, G. H. and Willson, L. A., 1991. From wind to superwind: The evolution of mass-loss rates for Mira models. *ApJ*, **375**, L53 – L56.

[Buchler 1990] Buchler, J. R., 1990. The modelling of nonlinear stellar pulsations. In Buchler, J. R., editor, *The numerical modelling of nonlinear stellar pulsations*, pages 1–26. Kluwer Academic Publishers.

[Buchler *et al.* 1991] Buchler, J. R., Moskalik, P., and Kovács, G., 1991. Periodic stellar pulsations: stability analysis and amplitude equations. *ApJ*, **380**, 185–199.

[Celis 1977] Celis, L., 1977. Light and colour variation of the Mira stars. *A&AS*, **29**, 15–30.

[Chengalur *et al.* 1993] Chengalur, J. N., Lewis, B. M., Eder, J., and Terzian, Y., 1993. New OH/IR stars from color–selected IRAS sources. III. A complete survey. *ApJS*, **89**, 189–210.

[Cherchneff and Barker 1992] Cherchneff, I. and Barker, J. R., 1992. Polycyclic Aromatic Hydrocarbons and Molecular Equilibria in Carbon-Rich Stars. *ApJ*, **394**, 703–716.

[Cherchneff *et al.* 1991] Cherchneff, I., Barker, J. R., and Tielens, A. G. G. M., 1991. Polycyclic aromatic hydrocarbon optical properties and contribution to the acceleration of stellar outflows. *ApJ*, **377**, 541–552.

[Cherchneff *et al.* 1992] Cherchneff, I., Barker, J. R., and Tielens, A. G. G. M., 1992. Polycyclic Aromatic Hydrocarbon formation in carbon-rich stellar envelopes. *ApJ*, **401**, 269–287.

[Cherchneff *et al.* 1993] Cherchneff, I., Glassgold, A. E., and Mamon, G. A., 1993. The formation of cyanopolyyne in IRC+10216. *ApJ*, **410**, 188–201.

[Chorin and Marsden 1979] Chorin, A. J. and Marsden, J. E., 1979. *A Mathematical Introduction to Fluid Mechanics.* Universitext. Springer.

[Chyba 1990] Chyba, C. F., 1990. Extraterrestrial amino acids and terrestrial life. *Nature*, **348**, 113–114.

[Claussen *et al.* 1987] Claussen, M. J., Kleinmann, S. G., Joyce, R. R., and Jura, M., 1987. A flux-limited sample of galactic carbon stars. *ApJS*, **65**, 385–404.

[Clayton and Feast 1969] Clayton, M. L. and Feast, M. W., 1969. Absolute magnitudes of Mira variables from Statistical parallaxes. *MNRAS*, **146**, 411–421.

[Cohen *et al.* 1981] Cohen, J. G., Frogel, J. A., Persson, S. E., and Elias, J. H., 1981. Bolometric luminosities and infrared properties of carbon stars in the Magellanic Clouds and the Galaxy. *ApJ*, **249**, 481–503.

[Courant and Friedrichs 1948] Courant, R. and Friedrichs, K. O., 1948. *Supersonic flow and shock waves*, volume Vol. I of *Pure and applied Mathematics*. Interscience Publisher, Inc., New York, 5^{th} printing 1967 edition.

[DeGioia-Eastwood *et al.* 1981] DeGioia-Eastwood, K., Hackwell, J. A., Grasdalen, G. L., and Gehrz, R. D., 1981. A correlation between infrared excess and period for Mira variables. *ApJ*, **245**, L75 – L78.

[Devaney 1986] Devaney, R. L., 1986. *An Introduction to Chaotic Dynamical Systems*. Benjamin / Cummings Publishing.

[Dollfus 1989] Dollfus, A., 1989. *Cometary Dust and Zodiacal Light Connection*, volume 8 of *Highlights of Astronomy*, pages 295–304. Kluwer Academic Publ.

[Dominik 1992] Dominik, C., 1992. *Formation of dust grains in the winds of cool giants*. PhD thesis, Technische Universität, Berlin, FRG.

[Dominik *et al.* 1989] Dominik, C., Gail, H.-P., and Sedlmayr, E., 1989. The size distribution of dust particles in a dust-driven wind. *A&A*, **223**, 227–236.

[Dominik *et al.* 1990] Dominik, C., Gail, H.-P., Sedlmayr, E., and Winters, J. M., 1990. HR diagrams for dust driven winds around C-stars. *A&A*, **240**, 365–375.

[Dominik *et al.* 1993] Dominik, C., Sedlmayr, E., and Gail, H.-P., 1993. Dust formation in stellar winds. VI. Moment equations for the formation of heterogeneous and core-mantle grains. *A&A*, **277**, 578–594.

[Dorfi and Drury 1987] Dorfi, E. A. and Drury, L. O., 1987. Simple adaptive grids for 1-d initial value problems. *J.Comp.Phys.*, **69**, 175–195.

[Dorfi and Feuchtinger 1991] Dorfi, E. A. and Feuchtinger, M. U., 1991. Nonlinear stellar pulsations. I. Numerical methods, basic physics, initial models and first results . *A&A*, **249**, 417–427.

[Dorfi and Höfner 1991] Dorfi, E. A. and Höfner, S., 1991. Dust formation in winds of long-period variables. I. Equations, method of solution, simple examples . *A&A*, **248**, 105–114.

[Draine 1979] Draine, B. T., 1979. Time-dependent nucleation Theory and the formation of interstellar grains. *Ap&SS*, **65**, 313–335.

[Draine and Salpeter 1977] Draine, B. T. and Salpeter, E. E., 1977. Time dependent nucleation theory. *J.Chem.Phys.*, **67**, 2230–2235.

[Drinkwater and Wood 1985] Drinkwater, M. J. and Wood, P. R., 1985. Pulsation, mass loss and grain formation in cool giants. In Morris, M. and Zuckerman, B., editors, *Mass Loss from Red Giants*, pages 257–260. Reidel Publ. Comp.

[Eglitis 1993] Eglitis, I., 1993. Abundance ratio C/O in the atmospheres of carbon stars. *ApSS*, **202**, 155–160.

[Engel *et al.* 1990] Engel, M. H., Macko, S. A., and Silfer, J. A., 1990. Carbon isotope composition of the individual amino acids in the Murchison meteorite. *Nature*, **348**, 157–160.

[Engels *et al.* 1983] Engels, D., Kreysa, E., Schultz, G. V., and Sherwood, W. A., 1983. The nature of OH/IR stars: I. Infrared Mira variables . *A&A*, **124**, 123–138.

[Feast *et al.* 1984] Feast, M. W., Whitelock, P. A., Catchpole, R. M., Roberts, G., and Overbeek, M. D., 1984. Variable circumstellar obscuration of the carbon star R Fornacis. *MNRAS*, **211**, 331–337.

[Feuchtinger *et al.* 1993] Feuchtinger, M. U., Dorfi, E. A., and Höfner, S., 1993. Radiation hydrodynamics in atmospheres of long–period variables. *A&A*, **273**, 513–523.

[Fleischer *et al.* 1990] Fleischer, A. J., Gauger, A., Sedlmayr, E., and Gail, H.-P., 1990. Dynamical models of dust shells around Mira variables. In Cacciari, C. and Clementini, G., editors, *Confrontation between stellar pulsation and evolution*, pages 431–434. Astronomical Soc. Pac. Conf. Ser., Vol. 11.

[Fleischer *et al.* 1991] Fleischer, A. J., Gauger, A., and Sedlmayr, E., 1991. Generation of shocks by radiation pressure on newly formed circumstellar dust. *A&A*, **242**, L1–L4.

[Fleischer *et al.* 1992] Fleischer, A. J., Gauger, A., and Sedlmayr, E., 1992. Circumstellar Dust shells around Long-period Variables. I. Dynamical models of C-stars including dust formation, growth and evaporation. *A&A*, **266**, 321–339.

[Fletcher 1991] Fletcher, C. A. J., 1991. *Computational Techniques for Fluid Dynamics*, volume I: Fundamental and General Techniques of *Series in Computational Physics*. Springer Verlag, 2^{nd} edition.

[Frantsman and Eglitis 1988] Frantsman, Y. L. and Eglitis, I. E., 1988. The C / O – ratio in N stars: observations and theory. *SvA*, **14**, L109 – L111.

[Frenklach and Feigelson 1989] Frenklach, M. and Feigelson, E. D., 1989. Formation of polycyclic aromatic hydrocarbons in circumstellar envelopes. *ApJ*, **341**, 372–384.

[Fujita 1970] Fujita, Y., 1970. *Interpretation of Spectra and Atmospheric Structure in Cool Stars*. University of Tokyo Press.

[Gail 1990] Gail, H.-P., 1990. Winds of late type stars. *Rev. Mod. Astron.*, **3**, 156–173.

[Gail and Sedlmayr 1985] Gail, H.-P. and Sedlmayr, E., 1985. Dust formation in stellar winds. II. Carbon condensation in stationary, spherically expanding winds. *A&A*, **148**, 183–190.

[Gail and Sedlmayr 1987a] Gail, H.-P. and Sedlmayr, E., 1987. Dust formation in stellar winds. In Morfill, G. E. and Scholer, M., editors, *Physical Processes in Interstellar Clouds*, pages 275–303. D. Reidel Publ. Comp.

[Gail and Sedlmayr 1987b] Gail, H.-P. and Sedlmayr, E., 1987. Dust formation in stellar winds. III. Self-consistent models for dust-driven winds around C-stars. *A&A*, **171**, 197–204.

[Gail and Sedlmayr 1987c] Gail, H.-P. and Sedlmayr, E., 1987. Dust formation in stellar winds. V. The minimum mass loss rate for dust-driven winds. *A&A*, **177**, 186–192.

[Gail and Sedlmayr 1988] Gail, H.-P. and Sedlmayr, E., 1988. Dust formation in stellar winds. IV. Heteromolecular carbon grain formation and growth. *A&A*, **206**, 153–168.

[Gail *et al.* 1984] Gail, H.-P., Keller, R., and Sedlmayr, E., 1984. Dust formation in stellar winds. I. A rapid computational method and application to graphite condensation. *A&A*, **133**, 320–332.

[Gauger *et al.* 1990] Gauger, A., Gail, H.-P., and Sedlmayr, E., 1990. Dust formation, growth and evaporation in a cool pulsating circumstellar shell. *A&A*, **235**, 345–361.

[Gauger *et al.* 1993] Gauger, A., Fleischer, A. J., Winters, J. M., and Sedlmayr, E., 1993. Dynamical models of dust shells around LPVs: Effects of time–dependent postshock cooling. *AG Abstract Series*, **9**, 127.

[Gauger *et al.* 1994a] Gauger, A., Fleischer, A. J., and Sedlmayr, E., 1994. Circumstellar Dust shells around Long-period Variables. Effects of post shock cooling. *A&A*, **in preparation**.

[Gauger *et al.* 1994b] Gauger, A., Fleischer, A. J., Winters, J. M., and Sedlmayr, E., 1994. Circumstellar shells of long–period variables: Dust formation and optical appearance. In Clegg, R. E. S., Meikle, P., and Stevens, I., editors, *Circumstellar Media in the late stages of Stellar evolution*, page in press, Cambridge University Press, Cambridge.

[Gehrz 1972] Gehrz, R. D., 1972. Infrared radiation from RV Tauri Stars. I. An infrared survey of RV Tauri stars and related objects. *ApJ*, **178**, 715–725.

[Gehrz 1989] Gehrz, R. D., 1989. Sources of stardust in the galaxy. In Allamandola, L. J. and Tielens, A. G. G. M., editors, *Interstellar Dust*, pages 445–453, Kluver Academic Publishers, Dordrecht.

[Gehrz and Woolf 1971] Gehrz, R. D. and Woolf, N. J., 1971. Mass loss from M stars. *ApJ*, **165**, 285–294.

[Gillet 1988] Gillet, D., 1988. The shock wave velocity in Mira stars. *A&A*, **190**, 200–214.

[Gillet 1992] Gillet, D., 1992. On the origin of the alternating deep and shallow light minima in RV tauri stars: R Scuti and AC Herculis. *A&A*, **259**, 215–226.

[Gillet *et al.* 1989] Gillet, D., Duquennoy, A., Bouchet, R., and Gouiffes, C., 1989. Shock phenomena in the atmosphere of the RV Tauri star, R Scuti. *A&A*, **215**, 316–330.

[Gillet *et al.* 1990] Gillet, D., Burki, G., and Duquennoy, A., 1990. The pulsation of the photosphere of the RV Tauri stars: AC Herculis and R Scuti. *A&A*, **237**, 159–168.

[Glassgold and Huggins 1986] Glassgold, A. E. and Huggins, P. J., 1986. *The M-type stars*, chapter 6, pages 291–323. NASA SP-492.

[Goeres 1993] Goeres, A., 1993. The formation of PAHs in C–type star environments. *Rev.Mod.Astron.*, **6**, 165–177.

[Goeres *et al.* 1988] Goeres, A., Henkel, R., Sedlmayr, E., and Gail, H.-P., 1988. Non-equilibrium chemistry in Circumstellar Shells. *Rev.Mod.Astron.*, **1**, 231–248.

[Goldreich and Scoville 1976] Goldreich, P. and Scoville, N., 1976. OH-IR Stars. I. Physical properties of circumstellar envelopes. *ApJ*, **205**, 144–154.

[Goldsmith *et al.* 1987] Goldsmith, M. J., Evans, A., Albinson, J. S., and Bode, M. F., 1987. Optical and infrared observations of RV Tauri stars. *MNRAS*, **227**, 143–159.

[Gow 1977] Gow, C., 1977. Spectrophotometry of cool carbon stars. *PASP*, **89**, 510–518.

[Greenberg 1989a] Greenberg, J. M., 1989. *From Interstellar dust to comet dust and interplanetary particles*, volume 8 of *Highlights of Astronomy*, pages 241–250. Kluwer Academic Publ.

[Greenberg 1989b] Greenberg, M. J., 1989. The core–mantle model of interstellar grains and the cosmic dust connection. In Allamandola, L. J. and Tielens, A. G. G. M., editors, *Interstellar Dust*, pages 345–355.

[Griffin 1990] Griffin, I. P., 1990. A model for the infrared and radio spectral energy distribution of IRC +10216 . *MNRAS*, **247**, 591–605.

[Groenewegen *et al.* 1992] Groenewegen, M. A. T., deJong, T., van der Bliek, N. S., Slijkhuis, S., and Willems, F. J., 1992. A flux-limited sample of galactic carbon stars. *A&A*, **253**, 150–172.

[Gustafsson 1989] Gustafsson, B., 1989. Chemical analyses of cool stars. *ARA&A.*, **27**, 701–756.

[Guthnick 1901] Guthnick, P., 1901. Neue Untersuchungen über den veränderlichen Stern *o* (Mira) Ceti. *Nova Acta der Kaiserl. Leop. Carol. Akademie der Naturforscher*, **79**(2), 17–261.

[Guthnick 1919] Guthnick, P., 1919. Künstliche Lichtkurven. *Astron. Nachr.*, **209**, 1–8.

[Habing 1987] Habing, H. J., 1987. IRAS results on circumstellar shells. In Appenzeller, I. and Jordan, C., editors, *Circumstellar Matter*, pages 197–213, Reidel Publishing, Dordrecht.

[Habing 1990] Habing, H. J., 1990. The evolution of Red Giants to White Dwarfs, a review of the observational evidence. In Mennessier, M. O. and Omont, A., editors, *From Miras to Planetary Nebulae: Which path for stellar evolution?*, pages 16–40, Editions Frontières, Gif sur Yvette Cedex - France.

[Hagen and Stein 1921] Hagen, J. G. and Stein, J., 1921. *Die Veränderlichen Sterne.* Herder, Freiburg.

[Hartmann and MacGregor 1980] Hartmann, L. and MacGregor, K. B., 1980. Momentum and energy deposition in late–type stellar atmospheres and winds. *ApJ*, **242**, 260–282.

[Heske 1989] Heske, A., 1989. A multifrequency study of circumstellar envelopes of cool giants and supergiants. *A&A*, **208**, 77–90.

[HESKE 1990] Heske, A., 1990. Circumstellar CO emission and pulsational properties of cool giants and supergiants. *A&A*, **229**, 494–503.

[HICKS *et al.* 1972] Hicks, T. R., May, B. H., and Reay, N. K., 1972. MgI emission in the night sky spectrum. *Nature*, **240**, 401–402.

[HICKS *et al.* 1974] Hicks, T. R., May, B. H., and K., R. N., 1974. An investigation of the motion of zodiacal dust particles I. Radial velocity measurements on Fraunhofer line profiles. *MNRAS*, **166**, 439–448.

[HILL AND WILLSON 1979] Hill, S. J. and Willson, L. A., 1979. Theoretical velocity structures of long-period variables star photospheres. *ApJ*, **229**, 1029–1045.

[HOFFMEISTER *et al.* 1990] Hoffmeister, C., Richter, G., and Wenzel, W., 1990. *Veränderliche Sterne*. Johann Ambrosius Barth, Leipzig, 3^{rd} edition.

[HÖFNER AND DORFI 1992] Höfner, S. and Dorfi, E. A., 1992. Dust formation in winds of long-period variables. II. Dust energetics, optical properties, chemistry, time scales. *A&A*, **265**, 207–215.

[HOLLENBACH AND MCKEE 1979] Hollenbach, D. and McKee, F., 1979. Molecule formation and infrared emission in fast interstellar shocks. I. Physical processes. *ApJS*, **41**, 555–592.

[HOLZER 1987] Holzer, T. E., 1987. Theory of winds from cool stars. In Appenzeller, I. and Jordan, C., editors, *Circumstellar matter*, pages 289–305. Reidel, Dordrecht.

[HOLZER AND MACGREGOR 1985] Holzer, T. E. and MacGregor, K. B., 1985. Mass loss mechanisms for cool, low-gravity stars. In Morris, M. and Zuckerman, B., editors, *Mass Loss from red giants*, pages 229–255. D. Reidel Pub. Com.

[HOLZER *et al.* 1983] Holzer, T. E., Flå, T., and Leer, E., 1983. Alfvén waves in stellar winds. *ApJ*, **275**, 808–835.

[IBEN 1981] Iben, I. J., 1981. The Carbon star mystery: Why do the low mass ones become such, and where have all the high mass ones gone? *ApJ*, **246**, 278–291.

[IBEN 1984] Iben, I. J., 1984. On the frequency of planetary nebula nuclei powered by Helium burning and on the frequency of white dwarfs with hydrogen–deficient atmospheres. *ApJ*, **277**, 333–354.

[Iben 1987] Iben, I. J., 1987. Helium shell flashes and their consequences. In Kwock, S. and Pottasch, S. A., editors, *Late stages of stellar evolution*, pages 175–195. D. Reidel Publ. Comp.

[Iben 1991] Iben, I., 1991. Single and binary star evolution. *ApJS*, **76**, 55–114.

[Iben and Renzini 1983] Iben, I. and Renzini, A., 1983. Asyptotic Giant Branch evolution and beyond. *ARA&A*, **21**, 271–342.

[Icke *et al.* 1992] Icke, V., Frank, A., and Heske, A., 1992. Weak chaos in long-period variables. *A&A*, **258**, 341–356.

[Jeans 1929] Jeans, J. H., 1929. *Astronomy and Cosmogony*. Cambridge University Press.

[Jones *et al.* 1990] Jones, T. J., Bryja, C. O., Gehrz, R. D., Harrison, T. E., Johnson, J. J., Klebe, D. I., and Lawrence, G. F., 1990. Photometry of variable AFGL sources. *ApJS*, **74**, 785–817.

[Jørgensen and Johnson 1992] Jørgensen, U. G. and Johnson, H. R., 1992. Radiative force on molecules and its possible role for mass loss in evolved AGB stars. *A&A*, **265**, 168–176.

[Jura 1986a] Jura, M., 1986. Mass loss from carbon stars. *ApJ*, **303**, 327–332.

[Jura 1986b] Jura, M., 1986. RV Tauri stars as post-asymptotic Giant Branch Stars. *ApJ*, **309**, 732–736.

[Jura 1986c] Jura, M., 1986. The Role of dust in mass loss from late-type stars. *Irish astr. J.*, **17**, 322–330.

[Jura and Kleinmann 1989] Jura, M. and Kleinmann, S. G., 1989. Dust–enshrouded asymptotic giant branch stars in the solar neighborhood. *ApJ*, **341**, 359–366.

[Jura *et al.* 1989] Jura, M., Joyce, R. R., and Kleinmann, S. G., 1989. High–luminosity carbon stars in the galactic anticenter. *ApJ*, **336**, 924–936.

[Keeley 1970] Keeley, D. A., 1970. Dynamical models of long–period variable stars. *ApJ*, **161**, 657–667.

[Keller 1987] Keller, R., 1987. Polyaromatic hydrocarbons and the condensation of carbon in stellar winds. In Léger, A., d'Hendecourt, L., and Boccara, N., editors, *Polycyclic Aromatic Hydrocarbons and Astrophysics*, pages 387–397. Reidel Publ. Comp.

[Keller and Sedlmayr 1983] Keller, R. and Sedlmayr, E., 1983. Entstehung von Kohlestaub in Sternhüllen. *Mitt. Astron. Ges.*, **60**, 312.

[KERSCHBAUM AND HRON 1992] Kerschbaum, F. and Hron, J., 1992. Semiregular variables of type SRa and SRb. Basic properties in the visual and the IRAS-range. *A&A*, **263**, 97–112.

[KHOLOPOV *et al.* 1985] Kholopov, P. N., Samus, N. N., Frolov, M. S., Goranskij, N. A., Kireeva, N. N., Kurkarkina, N. P., Kurochkin, N. E., Medvedena, G. I., Perova, N. B., and Shugarov, S. Y., 1985. *General Catalogue of Variable Stars*. Nauka, Moscow, 4^{th} edition.

[KNAPP 1985] Knapp, G. R., 1985. Mass Loss from evolved stars. IV. The dust-to-gas ratio in the envelopes of Mira variables and carbon stars. *ApJ*, **293**, 273–280.

[KNAPP AND MORRIS 1985] Knapp, G. R. and Morris, M., 1985. Mass loss from evolved stars. III. Mass loss rates for 50 Stars from CO $J = 1 - 0$ observations. *ApJ*, **292**, 640–669.

[KNAPP *et al.* 1982] Knapp, G. R., Phillips, T. G., Leighton, R. B., Lo, K. Y., Wannier, P. G., Wooten, H. A., and Huggins, P., 1982. Mass Loss from evolved stars. I. Observations of 17 stars in the CO $(2 - 1)$ line. *ApJ*, **252**, 616–634.

[KNAPP *et al.* 1993] Knapp, G. R., Sandell, G., and Robson, E. I., 1993. The dust content of evolved circumstellar envelopes and the optical properties of dust at submillimeter to radio wavelengths. *ApJS*, **88**, 173–197.

[KOIKE *et al.* 1980] Koike, C., Hasegawa, H., and Manabe, A., 1980. Extinction coefficients of amorphous carbon grains from $2100\mathring{A}$ to 340μm. *Ap&SS*, **67**, 495–502.

[KONINX AND HEARN 1992] Koninx, J. P. M. and Hearn, A. G., 1992. The role of sound waves in Be–star winds. *A&A*, **263**, 208–218.

[KONINX AND PIJPERS 1992] Koninx, J. P. M. and Pijpers, F. P., 1992. The applicability of the linearized theory of sound waves driven winds. *A&A*, **265**, 183–194.

[KOVÁCS AND BUCHLER 1988] Kovács, G. and Buchler, J. R., 1988. Regular and irregular non–linear pulsations in Population II Cepheid models . *ApJ*, **334**, 971–994.

[KOVÁCS AND BUCHLER 1993] Kovács, G. and Buchler, J. R., 1993. Double–mode pulsation in radiative RR Lyrae models . *ApJ*, **404**, 765–772.

[Kowalsky *et al.* 1986] Kowalsky, P. A., Percy, J. R., Mattei, J. A., and Waagen, E. O., 1986. AAVSO observations of long–period variable stars 1900–1975: maximum and minimum magnitudes and O–C diagrams. *J. Am. Assoc. Variable Star Obs.*, **15**, 236–238.

[Kozasa *et al.* 1984] Kozasa, T., Hasegawa, H., and Seki, J., 1984. Grain formation in the expanding gas flow around cool luminous stars. *Ap&SS*, **98**, 61–79.

[Kwan and Linke 1982] Kwan, J. and Linke, R. A., 1982. Circumstellar molecular Emission of evolved stars and Mass Loss: IRC +10216. *ApJ*, **254**, 587–593.

[Lafon and Berruyer 1991] Lafon, J.-P. and Berruyer, N., 1991. Mass loss mechanisms in evolved stars. *A&AR*, **2**, 249–289.

[Lafont *et al.* 1982] Lafont, S., Lucas, R., and Omont, A., 1982. Molecular abundances in IRC +10216. *A&A*, **106**, 201–213.

[Lambert *et al.* 1986] Lambert, D., Gustafsson, B., Eriksson, K., and Hinkle, K. H., 1986. The chemical composition of carbon stars. I. Carbon, Nitrogen, and Oxygen in 30 cool carbon stars in the galactic disk. *ApJS*, **62**, 373–425.

[Landau and Lifshitz 1987] Landau, L. D. and Lifshitz, E. M., 1987. *Fluid Mechanics*, volume 6 of *Course of Theoretical Physics*. Pergamon Press, 2^{nd} edition.

[Lattanzio 1989] Lattanzio, J. C., 1989. Carbon dredge-up in low-mass stars and solar metallicity stars. *ApJ*, **344**, L25–L27.

[LeBertre 1992] LeBertre, T., 1992. Carbon-star lightcurves in the 1-20 μm range. *A&AS*, **94**, 377–398.

[LeBertre 1993] LeBertre, T., 1993. Oxygen-rich late-type star lightcurves in the 1-20 μm range. *A&AS*, **97**, 729–753.

[Lèbre and Gillet 1991a] Lèbre, A. and Gillet, D., 1991. The bright RV tauri star R Scuti during an exceptional irregular light phase. *A&A*, **246**, 490–502.

[Lèbre and Gillet 1991b] Lèbre, A. and Gillet, D., 1991. The multicomponent motion of the very high atmosphere of thet RV tauri star: R Scuti. *A&A*, **251**, 549–559.

[Ledoux and Walraven 1958] Ledoux, P. and Walraven, T., 1958. *Variable stars*, volume LI, Astrophysik II of *Handbuch der Physik*, pages 353–604. Springer, Berlin.

[Léger and Puget 1984] Léger, A. and Puget, J. L., 1984. Identification of the unidentified IR emission features of interstellar dust? *A&A*, **137**, L5–L8.

[Lockwood and Wing 1971] Lockwood, G. and Wing, R., 1971. Light curves of Mira variables at 1.04 microns. *ApJ*, **169**, 63–86.

[Loup *et al.* 1993] Loup, C., Forveille, T., Omont, A., and Paul, J. F., 1993. CO and HCN observations of circumstellar envelopes. A catalogue – mass loss rates and distributions. *A&AS*, **99**, 291–377.

[Lucy 1971] Lucy, L. B., 1971. The formation of resonance lines in extended atmospheres. *ApJ*, **163**, 95–110.

[Lucy 1976] Lucy, L. B., 1976. Mass loss by cool carbon stars. *ApJ*, **205**, 482–491.

[Ludendorff 1928] Ludendorff, H., 1928. *Die Veränderlichen Sterne*, volume VI of *Handbuch der Astrophysik*, chapter 2, pages 49–250. Springer.

[Maron 1990] Maron, M., 1990. Optical properties of fine amorphous carbon grains in the infrared region. *Ap&SS*, **172**, 21–28.

[Mathis 1990] Mathis, J. S., 1990. Interstellar Dust and Extinction. *ARA&A*, **28**, 37–70.

[Mattei *et al.* 1990] Mattei, J. A., Cannizzo, J. K., and Goodings, D. A., 1990. AAVSO data files on pulsating stars and chaos studies on three long period variables. In Cacciari, C. and Clementini, G., editors, *Confrontation between stellar pulsation and evolution*, pages 461–463. ASP Conf. Ser. 11.

[McCray and Snow 1979] McCray, R. and Snow, T. P., 1979. The violent interstellar Medium. *ARA&A*, **17**, 213–240.

[Mendoza and Johnson 1965] Mendoza, E. E. and Johnson, H. L., 1965. Multicolor photometry of Carbon stars. *ApJ*, **141**, 161–169.

[Menietti and Fix 1978] Menietti, J. D. and Fix, J. D., 1978. Models of mass flows from cool, luminous stars. *ApJ*, **224**, 961–968.

[Mihalas 1978] Mihalas, D., 1978. *Stellar Atmospheres*. W. H. Freeman and Company, San Francisco, 2^{nd} edition.

[Mihalas and Hummer 1974] Mihalas, D. and Hummer, D. G., 1974. Theory of extended stellar atmospheres. I. Computational method and first results for static spherical models. *ApJS*, **28**, 343–372.

[Mihalas and Weibel Mihalas 1984] Mihalas, D. and Weibel Mihalas, B., 1984. *Foundations of Radiation Hydrodynamics*. Oxford University Press.

[Müller and Hartwig 1918] Müller, G. and Hartwig, E., 1918. *Geschichte und Literatur des Lichtwechsels der bis Ende 1915 als sicher veränderlich anerkannten Sterne nebst einem Katalog der Elemente ihres Lichtwechsels*, volume I. Poeschel & Trepte, Leipzig.

[Nyman *et al.* 1992] Nyman, L.-A., Booth, R. S., Carltröm, U., Habing, H. J., Heske, A., Sahai, R., Stark, R., van der Veen, W. E. C. J., and Winnberg, A., 1992. A survey of circumstellar CO emission from a sample of IRAS point sources. *A&AS*, **93**, 121–150.

[Nyman *et al.* 1993] Nyman, L.-A., Hall, P. J., and Le Bertre, T., 1993. Infrared and SiO maser observations of OH/IR stars. *A&A*, **280**, 551–566.

[O'Keefe 1939] O'Keefe, J. A., 1939. Remarks on Loreta's Hypothesis concerning R Coronae Borealis. *ApJ*, **90**, 294–300.

[Olofsson *et al.* 1987] Olofsson, H., Eriksson, K., and Gustafsson, B., 1987. CO ($J = 1 - 0$) observations of bright carbon stars. *A&A*, **183**, L13 – L16.

[Olofsson *et al.* 1993a] Olofsson, H., Eriksson, K., Gustafsson, B., and Carlström, U., 1993. A study of circumstellar envelopes around bright carbon stars. I. Structure, kinematics, and mass loss rate. *ApJS*, **87**, 267–304.

[Olofsson *et al.* 1993b] Olofsson, H., Eriksson, K., Gustafsson, B., and Carlström, U., 1993. A study of circumstellar envelopes around bright carbon stars. II. Molecular abundances. *ApJS*, **87**, 305–330.

[Omont 1991] Omont, A., 1991. Circumstellar chemistry. In Greenberg, J. M. and Pirronello, V., editors, *Chemistry in Space*, pages 171–199. Kluwer Academic Publishers.

[Ostlie and Cox 1986] Ostlie, D. A. and Cox, A. N., 1986. A linear survey of the mira variable star instability region of the hertzsprung–russell diagram. *ApJ*, **311**, 864–872.

[Owocki 1990] Owocki, S. P., 1990. Winds from Hot stars. *Rev. Mod. Astron.*, **3**, 98–123.

[Owocki *et al.* 1988] Owocki, S. P., Castor, J. I., and Rybicki, G. B., 1988. Time-dependent models of radiatively driven stellar winds. I. Nonlinear evolution of instabilities for a pure absorption model. *ApJ*, **335**, 914–930.

[Pasquini *et al.* 1990] Pasquini, L., Brocato, E., and Pallavicini, R., 1990. Chromospheric activity of evolved late-type stars: Chromospheric activity in evolved stars. *A&A*, **234**, 277–283.

[Patzer *et al.* 1993] Patzer, A. B. C., Winters, J. M., Beck, H. K. B., and Sedlmayr, E., 1993. Carbon–rich Circumstellar shells: Chemistry and Dust formation. *AG Abstract Ser.*, **9**, 125.

[Pijpers 1990] Pijpers, F. P., 1990. A model for the wind of the M supergiant VX Sagittarii. *A&A*, **238**, 256–264.

[Pijpers and Habing 1989] Pijpers, F. P. and Habing, H. J., 1989. Driving the stellar wind of AGB stars by acoustic waves; exploration of a simple model. *A&A*, **215**, 334–346.

[Pijpers and Hearn 1989] Pijpers, F. P. and Hearn, A. G., 1989. A model for the stellar wind driven by linear acoustic waves. *A&A*, **209**, 198–210.

[Raveendran 1989] Raveendran, A. V., 1989. Dust envelopes around RV Tauri stars. *MNRAS*, **238**, 945–953.

[Richtmyer and Morton 1967] Richtmyer, R. D. and Morton, K. W., 1967. *Difference methods for initial-value problems.* John Wiley & Sons, New York, 2^{nd} edition.

[Ridgway and Keady 1988] Ridgway, S. T. and Keady, J. J., 1988. The IRC +10216 circumstellar envelope. II. Spatial measurements of the dust. *ApJ*, **326**, 843–858.

[Ridgway *et al.* 1980a] Ridgway, S. T., Jacoby, G. H., Joyce, R. R., and Wells, D. C., 1980. Angular diameters by the lunar occultation technique. III. *AJ*, **85**, 1496–1504.

[Ridgway *et al.* 1980b] Ridgway, S. T., Joyce, R. R., White, N. M., and Wing, R. F., 1980. Effective temperatures of late–type stars: The field giants from K0 to M6. *ApJ*, **235**, 126–137.

[Robertson and Feast 1981] Robertson, B. S. C. and Feast, M. W., 1981. The bolometric, infrared and visual absolute magnitudes of Mira variables. *MNRAS*, **196**, 111–120.

[Rowan-Robinson and Harris 1983] Rowan-Robinson, M. and Harris, S., 1983. Radiative transfer in dust clouds. IV. Circumstellar dust shells around carbon stars . *MNRAS*, **202**, 797–811.

[Rybicki 1987] Rybicki, G. B., 1987. Radiation driven instabilities. In Lamers, H. J. G. L. M. and deLoore, C. W. H., editors, *Instabilities in luminous early type stars*, pages 175–190. D. Reidel Publishing.

[Scholz and Tsuji 1984] Scholz, M. and Tsuji, T., 1984. The effects of spherical extension upon the photospheric structure and spectrum of red giants: comparison of M and C stars. *A&A*, **130**, 11–18.

[Schönberner 1990] Schönberner, D., 1990. Mass loss and evolution of Planetary Nebulae. In Mennessier, M. O. and Omont, A., editors, *From Miras to Planetary Nebulae: Which path for stellar evolution?*, pages 355–367, Editions Frontières, Gif sur Yvette Cedex - France.

[Sedlmayr 1989] Sedlmayr, E., 1989. Dust condensation in stellar outflows. In Allamandola, L. J. and Tielens, A. G. G. M., editors, *Interstellar Dust*, pages 467–477. Kluwer Academic Publishers, Dordrecht.

[Sedlmayr 1994] Sedlmayr, E., 1994. From molecules to grains. In Jørgensen, U. G., editor, *IAU Colloquium 146: Molecules in the Stellar Environment*, pages 163–185, Springer–Verlag, Berlin.

[Serrin 1959] Serrin, J., 1959. *Mathematical principles of classical fluid mechanics*, volume VIII/1 of *Handbuch der Physik*, chapter 2, pages 125–263. Springer.

[Shenton *et al.* 1992] Shenton, M., Albinson, J. S., Barrett, P., Davies, J. K., Evans, A., Goldsmith, M. J., Hutchinson, M. G., Maddison, R. C., and Weight, A., 1992. Multiwavelength observations of RV Tauri stars. I. AC Herculis. *A&A*, **262**, 138–152.

[Sopka *et al.* 1985] Sopka, R. J., Hildebrand, R., Jaffe, D. T., Gatley, I., Roelling, T., Werner, M., Jura, M., and Zuckerman, B., 1985. Submillimeter observations of evolved stars. *ApJ*, **294**, 242–255.

[Stein and Leibacher 1974] Stein, R. and Leibacher, J., 1974. Waves in the solar atmosphere. *ARA&A*, **12**, 407–435.

[Struve 1955] Struve, O., 1955. Dust and related phenomena in stars. *Mém. Soc. Roy. Sci. Liège, Sér. IV*, **15**, 193–222.

[Thompson and Stewart 1986] Thompson, J. M. T. and Stewart, H. B., 1986. *Nonlinear Dynamics and Chaos*. John Wiley and Sons.

[Thronson *et al.* 1987] Thronson, H. A., Latter, W. B., Black, J. H., Bally, J., and Hacking, P., 1987. Properties of evolved mass–losing stars in the Milky Way and variations in the interstellar dust composition. *ApJ*, **322**, 770–786.

[Tscharnuter and Winkler 1979] Tscharnuter, W. M. and Winkler, K.-H., 1979. A method for computing selfgravitating gas flows with radiation . *Comp.Phys.Comm.*, **18**, 171–199.

[Tsuji 1981] Tsuji, T., 1981. Intrinsic properties of Carbon stars. I. Effective temperature scale of N-type Carbon stars. *J. Astrophys. Astr.*, **2**, 95–113.

[Tuchman 1991] Tuchman, V., 1991. The mode of pulsation in Mira Variables determined by the observed acceleration data. *ApJ*, **383**, 779–783.

[Tuchman *et al.* 1993] Tuchman, Y., Lèbre, A., Mennessier, M. O., and Yarri, A., 1993. Linear analysis of RV Tauri stars: the resonance hypothesis . *A&A*, **271**, 501–507.

[Turner 1989] Turner, B. E., 1989. Recent Progress in Astrochemistry. *Space Sci. Rev.*, **51**, 235–337.

[Vassiliadis and Wood 1993] Vassiliadis, E. and Wood, P. R., 1993. Evolution of low- and intermediate– mass stars to the end of the asymptotic giant branch with mass loss. *ApJ*, **413**, 641–657.

[Veen and Rugers 1989] van der Veen, W. E. C. J. and Rugers, M., 1989. A comparison between CO-, OH- and IR-mass-loss rates of evolved stars. *A&A*, **226**, 183–202.

[Weidemann and Schönberner 1990] Weidemann, V. and Schönberner, D., 1990. Stellar evolution theory: Up to and on the AGB. In Mennessier, M. O. and Omont, A., editors, *From Miras to Planetary Nebulae: Which path for stellar evolution?*, pages 3–15, Editions Frontières, Gif sur Yvette Cedex - France.

[Werner *et al.* 1980] Werner, M. W., Beckwith, S., Gatley, I., Sellgren, K., and Berriman, G., 1980. Simultaeous far–infrared, near–infrared, and radio observations of OH/IR stars. *ApJ*, **239**, 540–548.

[Whitelock *et al.* 1991] Whitelock, P. A., Feast, M. W., and Catchpole, R. M., 1991. IRAS sources and the nature of the galactic bulge. *MNRAS*, **248**, 276–316.

[Whittet and Chiar 1993] Whittet, D. C. B. and Chiar, J. E., 1993. Cosmic evolution of the biogenic elements and compounds. *A&AR*, **5**, 1–35.

[Willems and deJong 1988] Willems, F. J. and de Jong, T., 1988. IRAS low resolution spectra of cool carbon stars. IV. A scenario for carbon star evolution. *A&A*, **196**, 173–184.

[Willson 1976] Willson, L. A., 1976. Shock-wave interpretation of emission lines in LPV stars. I. The velocity of the shock. *ApJ*, **205**, 172–181.

[Willson and Bowen 1985] Willson, L. A. and Bowen, G. H., 1985. Atmospheric structure and mass loss for pulsating stars. In Stalio, R. and Zirker, J., editors, *Relations between chromosperic-coronal heating and mass loss in stars*, pages 127–176. Trieste Workshop Series.

[Willson and Hill 1979] Willson, L. A. and Hill, S. J., 1979. Shock wave interpretation of emission lines in long period variable stars. II. Periodicity and mass loss. *ApJ*, **228**, 854–869.

[Willson *et al.* 1993] Willson, L. A., Struck-Marcell, C., and Bowen, G., 1993. Winds from pulsating stars. In ???, editor, *???*, page in press, ???, ???

[Winters 1994] Winters, J. M., 1994. *Internal structure and optical appearance of circumstellar dust shells around cool carbon giants.* PhD thesis, Technische Universität, Berlin, FRG.

[Winters *et al.* 1993] Winters, J. M., Fleischer, A. J., Gauger, A., and Sedlmayr, E., 1993. Circumstellar Dust shells around Long-period Variables. II. Theoretical lightcurves of C–stars. *A&A*, **submitted**.

[Winters *et al.* 1994a] Winters, J. M., Dominik, C., and Sedlmayr, E., 1994. Theoretical spectra of circumstellar dust shells around carbon-rich asymptotic giant branch stars. *A&A*, **in press**.

[Winters *et al.* 1994b] Winters, J. M., Fleischer, A. J., Gauger, A., and Sedlmayr, E., 1994. Circumstellar Dust shells around Long-period Variables. Brightness distributions and visibilities of C-stars. *A&A*, **in preparation**.

[Witteborn *et al.* 1980] Witteborn, F. C., Strecker, D. W., Erickson, E. F., Smith, S. M., Goebel, J. H., and Taylor, B. J., 1980. The spectrum of IRC+10216 from 2.0 to 8.5 microns. *ApJ*, **238**, 577–584.

[Woitke *et al.* 1993] Woitke, P., Dominik, C., and Sedlmayr, E., 1993. Dust destruction in the transition region between stellar wind and interstellar medium. *A&A*, **274**, 451–464.

[Wood 1976] Wood, P. R., 1976. Red Variables. In Fitch, W. S., editor, *Multiple Periodic Stars*, pages 69–85. Reidel, Dordrecht.

[Wood 1979] Wood, P. R., 1979. Pulsation and mass loss in Mira variables. *ApJ*, **227**, 220–231.

[Wood 1986] Wood, P., 1986. Long-Period Variables. In Cox, A. N., Sparks, W., and Starrfield, S., editors, *Stellar Pulsation*, pages 250–259. Springer Lecture Notes in Physics No. 274.

[Wood 1990] Wood, P. R., 1990. Mira variables: Pulsation, Mass Loss and Evolution. In Cacciari, C. and Clementini, G., editors, *Confrontation between stellar pulsation and evolution*, pages 355–364. Astronomical Soc. Pac. Conf. Ser., Vol. 11.

[Woolf and Ney 1969] Woolf, N. J. and Ney, E. P., 1969. Circumstellar infrared emission from cool stars. *ApJ*, **155**, L181–L184.

[Yorke 1988] Yorke, H. W., 1988. . In Chmielewski, Y. and Lanz, T., editors, *Radiation in moving gaseous media*, page 193, Swiss Soc. for Astrophys. and Astron., Saas-Fee.

[Zel'dovich and Raizer 1966] Zel'dovich, Y. B. and Raizer, Y. P., 1966. *Physics of Shock Waves and High–Temperature Hydrodynamic Phenomena*, volume 1. Academic Press.

[Zuckerman and Aller 1986] Zuckerman, B. and Aller, L. H., 1986. Origin of planetary nebulae; Morphology, Carbon - to - oxygen abundance ratios, and central star multiplicity. *ApJ*, **301**, 772–789.

[Zuckerman and Dyck 1986a] Zuckerman, B. and Dyck, H. M., 1986. Carbon Monoxide Emission from Stars in the IRAS and Revised AFGL Catalogs. I. Mass Loss driven by Radiation pressure on Dust grains. *ApJ*, **304**, 394–400.

[Zuckerman and Dyck 1986b] Zuckerman, B. and Dyck, H. M., 1986. Dust grains and gas in the circumstellar envelopes around luminous red giants. *ApJ*, **311**, 345–359.

[Zuckerman and Dyck 1989] Zuckerman, B. and Dyck, H. M., 1989. Outflow velocities from carbon stars. *A&A*, **209**, 119–125.

[Zuckerman *et al.* 1986] Zuckerman, B., Dyck, H. M., and Claussen, M. J., 1986. Carbon Monoxide Emission from Stars in the IRAS and Revised AFGL Catalogs. II. Massive Carbon stars. *ApJ*, **304**, 401–408.

Index

Danksagung – Acknowledgement

Mein Dank gilt zunächst Prof. Dr. E. Sedlmayr für die Betreuung meiner Promotion. Er hat mir die Möglichkeit eröffnet, in die Astrophysik zu wechseln und in einem modernen, sich rasch entwickelnden Forschungsgebiet zu arbeiten. Seine Bemerkungen und Anregungen haben mich oft aus dem Verstricktsein in Details wieder auf die wirklich großen Zusammenhänge, nicht nur der Astrophysik, geleitet.

Ich danke Priv. Doz. Dr. J.P. Kaufmann, daß er sich der Mühe des Schreibens eines Zweitgutachtens unterzogen hat.

Ein besonderer Dank geht auch an Prof. Dr. S. Hess, der sich trotz eines Forschungssemesters sofort bereiterklärt hat, den Vorsitz in der Prüfungskomission zu übernehmen.

Ich danke meinen Kollegen aus dem Zimmer PN 801, Andreas Gauger und Jan Martin Winters. Was soll ich Euch sagen, Männer? Ihr seid mir einiges mehr als nur Kollegen. Jan Martin, wenn Du damals nicht in Neukölln gewohnt hättest, hätte ich diese Arbeit niemals geschrieben. Ohne Dich, Andreas, hätte *CHILD* niemals das Licht der Welt erblickt. Eure Anregungen, Aufmunterungen und Tips, die Diskussionen mit Euch, Sprüche und Witzeleien, aber auch Sarkasmus und Zynismus sind Dinge, die ich nicht missen möchte.

Mein herzlicher Dank gilt auch Uwe Bolick, für den Hinweis auf Brian May. Aber bestimmt nicht nur *dafür*. Ohne Deine Kenntnisse z.B. als TeXnician und als CRAYzy Computerspezialist wäre ich wohl längst verzweifelt.

Je voudrais remercier chaleureusement Thierry Allain pour la traduction en français du résumé (Abstract).

Allen anderen Institutsmitgliedern danke ich dafür[4], daß sie dazu beigetragen haben, ein Klima zu schaffen, das wahrscheinlich einmalig ist und in dem es Freude macht zu arbeiten, auch wenn es manchmal etwas anders aus PN 801 klingt . . . , sorry. Es ist bestimmt nicht überall so, daß es immer jemanden gibt, der hilft, der noch die letzten Kopien macht, die Sachen nachts zur Post bringt, Targetlisten komplettiert, oder der sich einfach nur die neuesten krausen Gedanken anhört und Fragen beantwortet.

Meiner Lebensgefährtin Christina Köhlen danke ich für ihre Geduld, die sie mit mir gehabt hat, gerade während der letzten Zeit, in der sie auf so vieles verzichten mußte, . . . und für Dein Verständnis, das Du (meistens ☺) zeigtest, auch wenn ich wieder einmal die meiste Zeit an der Uni verbracht hatte.

The calculations were performed on the CRAY computers of the Konrad-Zuse-Zentrum für Informationstechnik Berlin and the Höchstleistungsrechenzentrum, HLRZ, Jülich. A generous grant of computing time is greatly acknowledged.

This work has been partly supported by the Deutsche Forschungsgemeinschaft, *DFG*-Schwerpunkt "Theorie kosmischer Plasmen".

[4]Ich schließe hier auch ausdrücklich die nicht biertrinkenden oder nur teetrinkenden mit ein!

Lebenslauf

Name	Axel Joachim Fleischer
Geburtsdatum	01.06.1962
Geburtsort	Berlin
Eltern	Gertrud Fleischer, geb. Lemke Joachim Fleischer, RegR i.R.
Staatsangehörigkeit	deutsch
Familienstand	ledig

Schulbesuch

1968–1974	Grundschule „Unter den Kastanien“, Berlin–Lichterfelde
1974–1980	Tannenberg–Oberschule(Gymnasium), Berlin–Lichterfelde
Dez. 1980	Abitur (Allgemeine Hochschulreife)

Studium

1981–1989	Studium der Physik am Fachbereich 04 der Technischen Universität Berlin
Okt. 1986–März 1989	Studentische Hilfskraft mit Lehraufgaben (Tutor) am Institut für Theoretische Physik
Feb. 1989	Diplom in Physik, Diplomarbeit bei Prof.Dr. K.-E. Hellwig (Inst. für Theoretische Physik) über das Thema *Zur Regularisierung der Feldgleichungen und Dynamik von Bianchi–Kosmologien*
April 1989–März 1992	Wissenschaftlicher Mitarbeiter in der Arbeitsgruppe von Prof.Dr. E. Sedlmayr (Inst. für Astronomie und Astrophysik, TU Berlin) in einem von der DFG geförderten Forschungsvorhaben
seit Mai 1992	Wissenschaftlicher Mitarbeiter am Institut für Astronomie und Astrophysik

Berlin, den 7. März 1994